Non-Heme Iron Oxygenases: An Investigation of the Protein Ligand Effects on the Chemical Reactivity in MiaE and Cysteamine Dioxygenase

by

Philip Palacios

Presented to the Faculty of the Graduate School of

The University of Texas-Arlington in Partial Fulfillment

of the requirements of the Degree of

DOCTOR OF PHILOSOPHY

THE UNIVERSITY OF TEXAS-ARLINGTON

August 2019

Acknowledgements

Firstly, I want to express my sincere gratitude to my P.I. and friend, Dr. Brad Pierce, for his patience and support throughout these five years. It has been greatest honor to have worked under your guidance.

I want to also thank my thesis committee members Dr. Rasika Dias, Dr. Robin Macaluso, and Dr. Jongyun Heo for their feedback throughout my graduate career.

I want to thank all my coworkers that I've had the pleasure of working with throughout my graduate career; Josh, Sinjinee, Nick, Jared, Pender, Bender and the rest of the group. All of you made the experience of going to work enjoyable. We started out as lab mates and ended up as lifelong friends. I cannot think of a more perfect group of delinquents to spend these past five years with.

Lastly, I want to thank my family and friends. To my family, you've always been a huge support of my dreams and I am not the person I am today without all that you have done and continue to do for me today. To my wonderful girlfriend, Diane, you've been the greatest gift in my life. I am not here without all your love and support throughout these years. You've pushed me to be better and always encouraged me to do what I love.

September 3rd, 2019

Table of Contents

Abstract

Non-Heme Iron Oxygenases: An Investigation of the protein ligand effects on the chemical reactivity in MiaE and cysteamine dioxygenase

Philip Palacios, PhD

The University of Texas-Arlington, 2019

Supervising Professor: Brad S. Pierce

Considerable research interest has focused on the non-heme oxygenase/oxidase enzyme family because of vast array of chemically diverse O_2-depedent oxidations they participate in. For example, the bacterial multicomponent monooxygenases (sMMOH and ToMOH) are bacterial diiron enzymes that are involved in the oxidations of simple carbon sources (methane and toluene) for nutrition and other cellular cycles. Investigations of the BMM systems have significant implications for the research and development in greenhouse emissions. The hydroxylase component of the BMM superfamily is coordinated by 2-Histidine-4-carboxylate ligands (Asp or Glu) [2H4C]. The [2H4C] configuration is the typical moiety for the 2-electron oxidation in the monooxygenases. Following reduction, the diferrous cluster is able to catalyze the O_2-depedent oxidation of the respective substrate by 2-electrons. Much like the bacterial multicomponent monooxygenase (BMM) superfamily, the binuclear site of *Salmonella typhimurium* MiaE is coordinated by 2-His-4-carboxylate (Asp or Glu) residues (2H4C). The Pierce group has extensively characterized the *wild-type* MiaE and its native, 2-electron *t*RNA-hydroxlase activity with a variety of spectroscopic and analytical methods

(EPR, ^{57}Fe Mössbauer, Circular dichroism (CD), UV-vis, X-ray diffraction (XRD), HPLC/LCMS, steady-state kinetics). With recent discoveries of the arylamine *N*-oxygenases, AurF and CmlI, the interests shifted toward the potential functionality of MiaE as a model for arylamine *N*-oxygenase chemistry. Comparisons of crystal structures with AurF suggests that the MiaE L199H variant can re-create the 3-His-4-carboxylate (3H4C) environment in the binuclear site. DFT studies on the *wild-type* MiaE revealed the shift in the F181 side chain for incorporation of the histidine residue and does not significantly affect the geometry of the active-site. Spectroscopic studies (UV-vis, EPR, and Mössbauer) of the L199H variant show good agreement with spectroscopic values reported for other arylamine *N*-oxygenases. Reactivity studies showed successful incorporation of molecular oxygen into an arylamine substrate with expected mass shift through HPLC and LC-MS. Together, this research has shown the potential for MiaE to serve as the framework for further investigation into arylamine *N*-oxygenase chemistry biologically inspired designed for catalyst development.

Our research group has had significant interests in the role of thiol dioxygenases (TDOs) in the role of sulfur regulation. Clinical studies have shown a correlation between sulfur imbalances and the development of neurodegenerative diseases. TDOs are involved in the first irreversible step in the oxidation of sulfur-containing amino acid derivatives. The mammalian enzyme, cysteamine dioxygenase (ADO), is a non-heme iron enzyme that catalyzes the O_2-depedent oxidation of cysteamine to produce hypotaurine. Hypotaurine and taurine biosynthesis are important metabolites for brain and cellular development. Extenstive studies have been dedicated to the mammalian counterpart cysteine dioxygenase (CDO). Consequently, ADO remains a relatively uncharacterized member of the non-heme iron family. Sequence homology between CDO and ADO show a conserved first-coordination sphere suggesting comparable mechanistic features for catalysis and substrate binding. Steady-state and NMR studies on ADO shows a proclivity for the native substrate, cysteamine (***ca***) with little reactivity toward L-cysteine (***cys***). Additionally, key ionization events in k_{cat}

and k_{cat}/K_M suggests a different collection of residues involved in catalysis that differs from what is seen in other thiol dioxygenases. The complementary X-band EPR studies suggests the substrate does not bind directly to the Fe-site. Together, these studies suggest potential deviations in mechanistic steps during catalysis from what is classically observed in thiol dioxygenases.

Chapter 1 Introduction

Analytical applications of Electron Paramagnetic Resonance

Electron paramagnetic resonance (EPR) is a magnetic resonance spectroscopic method use for interrogation of species with unpaired electrons. This spectroscopic technique relies on the Larmor precession of magnetic pole by the unpaired electron (and magnetic nuclei) in the presence of an external magnetic field (**B**). The precession of the electronic and nuclear spins can be inverted through the application of an oscillating magnetic field at the resonance frequency for the unpaired electron. The energy gap for the resonance frequency is diagnostic information about the number of unpaired electrons, the orbital the electron may reside in, and the interaction with adjacent magnetic nuclei that couples with the unpaired electron. EPR measurements are most commonly performed at room temperature however, transition metal systems are examined under cryogenic conditions. Cryogenic EPR is necessary for transition metals because of the increased relaxation rates which leads to line broadening at elevated temperatures. The relaxation rates of transition metals are enhanced due to increased spin-orbit coupling of the d-electrons. The spin-orbit coupling (SOC) effect arises from the interaction between the spin and orbital motion of an electron.[6] In biological systems, fast forming transient species can be trapped by rapid freeze quench methods and analyzed by cryogenic EPR.

For transition metals, the d-orbitals can adopt various oxidation states and therefore a variety of spin-states. Consequently, the d-orbitals exhibit a larger perturbation under various conditions related to substrate, coordination environment, and oxidation state unlike their organic radical counterparts.[7] In this work, EPR has been an essential tool for probing and quantifying the concentration of species in metalloproteins and various transition metal complexes. A brief review into the role of quantitative measurements by EPR will be discussed further in this chapter.

In isolated systems where the total spin of the molecule is $S = {}^{1}/_{2}$, the measurement of the interaction between the unpaired electron and an external magnetic field can be described by Equation 1.1, where β is the Bohr's magneton (9.274 x 10^{-24} J/T), **B** is the applied magnetic field, **g** is the *g*-tensor and **S** is the spin angular momentum of the electron.

$$\mathcal{H} = \beta \mathbf{B} \cdot \mathbf{g} \cdot \mathbf{S} \qquad (\mathbf{1.1})$$

When an external field is applied to the paramagnetic substance, the degenerate m_s levels are linearly split allowing for measurement of excitation spin-states in a sample. Under $S = {}^{1}/_{2}$ conditions, the integration of the area under the curve is a direct calculation of the number of spins contributing to the EPR signal. The measurement of the spin-spin interactions can be calculated and reveals the EPR parameters of the species analyzed.

For systems with more than one unpaired electron ($S > 1/2$), additional mathematical terms are needed to account for the spin-spin interactions. In the absence of an applied magnetic field, the interaction of the increased number of unpaired electrons breaks the degeneracy of the m_s eigenstates and is referred to as zero field splitting (zfs). Under octahedral ligand field conditions, the zfs contributions can be designated by the axial (***D***) and rhombic (***E***) terms which describe the electron-electron interactions along the z-axis and xy-plane. In integer-spin systems, the non-Kramer's doublets exhibit non-degeneracy and the application of the zfs terms are necessary for accounting for the spin-spin interactions. Another component that is accounted for in the expanded Hamiltonian is the hyperfine splitting interactions. Hyperfine splitting is the magnetic interaction of electron (S) and nuclear (***I***) angular momentum. The hyperfine multiplicity follows the 2n+ 1 rule, and transitions must satisfy the selection rules: $\Delta m_S = \pm 1$ and $\Delta m_I = 0$. Hyperfine interactions have

equally spaced EPR peaks and measurement of these values (MHz) can be a diagnostic tool for distinguishing between metal centers. The hyperfine contribution in the Hamiltonian can be described as S·A·I. As seen in Equation 1.2, the expanded Hamiltonian is more complex but thorough mathematical expression for the total spin-spin interactions.

$$\mathcal{H} = \mathbf{D}\left[\hat{S}_{\mathbf{Z}}^{2} - \frac{S(S+1)}{3}\right] + \mathbf{E}\left(\hat{S}_{\mathbf{X}}^{2} + \hat{S}_{\mathbf{Y}}^{2}\right) + \beta\mathbf{B}\cdot\mathbf{g}\cdot\mathbf{S} + \mathbf{S}\cdot\mathbf{A}\cdot\mathbf{I} \qquad (\mathbf{1.2})$$

A look into the Mononuclear Non-Heme Metalloproteins

Genomic analysis across phylogenic domains have revealed that approximately one-third of all expressed proteins require a metal ion or cofactor for proper protein assembly and functionality. For nearly 50 years, the enzymes that are involved in aerobic oxidative reactions have garnered considerable attention because of their selective oxidation of organic substrates. The oxidation of organic substrates by molecular oxygen (combustion reactions) are exergonic therefore thermodynamically favorable. However, the two unpaired electrons in the π* in oxygen result in a *S* = 1 ground state that results in a triplet multiplicity ($^3O_2$). In contrast, majority of organic substrates (R) are diamagnetic compounds (no unpaired electrons) that result in a *S* = 0 ground state configuration therefore results in a singlet multiplicity (^{1}R). The conservation of angular moment for substrates and products must be maintained and with differing spin-states with molecular oxygen and the combustion products, such reactions are designated as spin-forbidden and are kinetically slow.

To overcome this kinetic barrier for organic substrate oxidation, nature has employed the use of transition metals to balance angular moment of oxygen-dependent reactions.[8, 9] The inclusion of several first-row transition metals provides an avenue for substrate oxidation to occur with relative ease and under less stringent conditions. This first chapter provides contextual background

about the expansive reactions catalyzed by O_2-dependent metalloproteins as well as highlight the structural designs utilized for metal incorporation and the influence by the protein ligand environment.

The O_2-dependent oxidation of organic substrates are designated as either mono- or di-oxygenase based on the number of oxygen atoms incorporated into the substrate (1 or 2). In contrast, enzymes that reduce oxygen into water without incorporate of O-atoms into the product are termed oxidases. In totality, the O_2-dependent enzymes are designated as the oxygenase/oxidase family. The work presented here focuses on the non-heme mono- and bi-nuclear iron oxidase/oxygenase enzymes and presented below is a brief summary of their characteristics.

The mononuclear non-heme Fe(II)/O_2 enzyme family is a diverse collection of metalloproteins that are involved in critical chemical reactions such as aromatic ring cleavage, hydroxylation, and C-C double bond epoxidation through the activation of dioxygen. The reactions that are catalyzed are integral components for the biosynthesis of antibiotics and amino-acids.[10] Consequently, the non-heme Fe(II) family have been researched considerably because of their participation in critical biosynthetic pathways as well as the rational design of natural products and industrial catalysts. Research efforts into the heme and non-heme oxygenases/oxidases have shown overlapping mechanistic features for substrate oxidation and O_2-binding. However, the structural framework and divergent chemical steps illustrate the diversity of these Fe-dependent enzymes.[11-13]

The non-heme iron enzyme family

The non-heme iron enzymes can be classified as mononuclear or binuclear that is coordinated by a combination of histidine and carboxylate residues as seen by the non-heme diiron enzyme toluene monooxygenase in Figure 1.1 (panel B).[14] The structural frame of the non-heme iron enzymes are not hampered by the rigidity of a macrocyclic ring like that of its heme counterparts.

Consequently, the newly adopted framework has more open binding sites to coordinate directly to substrate, cofactors, or dioxygen.[15-17] The additional binding modes effectively acts to tune the chemical reactivity of Fe-site and expands the diverse collection of products synthesized.[12, 13]

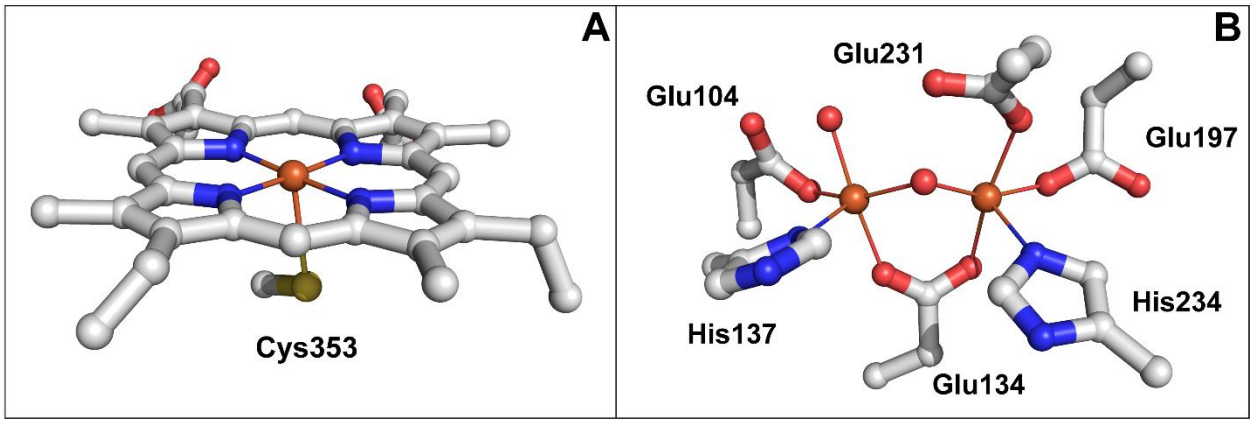

Figure 1.1 X-ray crystal structures of Fe-bound active sites for the heme and non-heme iron oxygenase. A) Cytochrome P450 (PDB: 2D0E)[13] from Streptomyces coelicolor. B) Hydroxylase component of toluene monooxygenase (ToMOH) (PDB:1T0Q)[9] from Pseudomonas stutzeri.

Mechanistically, these enzymes share many overlapping pathways and chemical intermediate despite the wide array of reactions and substrates utilized.[12, 13, 15, 16, 18] In general, the binding process begins by a obligated order of addition where the resting Fe(II)-active site is chemically unreactive to molecular oxygen. Oxygen activation begins by the binding of the substrate or cofactor the iron active site.[18] This process of precise, sequential bindings is critical due to the harmful effects that can incur on the enzyme if oxygen binds prior to substrate as reactive oxygen species (ROS) can be produced and harm the organism. The precise order of substrate binding and oxygen activation ensures that the substrate can be adequately oxidized by molecular oxygen. At this time, there are two chemical routes for substrate oxidation to occur either by 1) substrate activation or 2) oxygen activation.[16] For oxygen activation, the O-O bond undergoes homolytic cleavage that results in the formation of a high-valent Fe(IV)-oxo species that will subsequently be used for

substrate oxidation. Numerous studies on the taurine/α-ketoglutarate-dependent dioxygenases, hydroxylases, and halogenases have shown evidence for the high valent Fe(IV)-oxo species being the catalytic species for substrate oxidation.[19-22] In contrast, the substrate activation mechanism the oxidizing species is a Fe(III)-superoxo that is formed by the heterolytic cleavage of the O-O bond and a rapid electron transfer from the Fe(II). Spectroscopic studies into the formation of the Fe(III)-superoxo species has been identified and trapped in several non-heme iron enzymes such as isopenicilin N-synthase and homoprotocatechuate 2,3-dioxygenase.[23, 24]

Non-heme iron enzymes with the 2-His-1-carboxylate moiety

Among the non-heme mononuclear iron oxygenase/oxidases, the active-site is composed of a single ferrous iron that is coordinated by two protein derived histidine residues and one carboxylate ligand (Glu or Asp) along one side of the octahedral face as seen in Figure 1.2[15, 25]

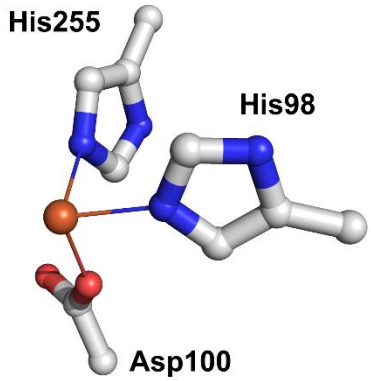

Figure 1.2 X-ray crystal structure of the Fe(II)/α-ketoglutarate dependent enzyme TauD from Myobacterium marinum (PDB: 3SWT)[22]

This 2-His-1-carboxylate motif has been identified in numerous enzymes and is found to be a conserved active-site domain.[15] The 2-His-1-carboxylate motif serves a wide variety of substrate oxidations as described previously and is employed by a diverse set of enzymes in the non-heme iron family.[11, 13] In below, the classification of the 2-His-1-carboxylate enzymes can be seen. A brief discussion on these classes will be described further along in this chapter.

Table 1.1 Classification of 2-His-1-carboxylate enzymes

Enzyme Group	Enzymes	Function
Catechol Dioxygenases	2,3-HPCD, 4,5-HPCD, BphC	C-C bond cleavage
Riseke Dioxygenases	NDO	Cis-dehydroxlation of arenes
A-ketoglutarate-depedent oxygenases	TauD, DAOCS, HPPD	C-H bond activation
Pterin-dependent Hydoyxlases	PheOH, TyrOH, TryOH	Amino-acid biosynthesis
Others	ACCO, IPNS	Antibiotic biosynthesis

HPCD, homeoprotocatechuate dioxygenase; BphC, polychlorinated-biphenyl dioxygenase; NDO, naphthalene dioxygenase; TauD, taurine dioxygenase; DAOCS, deacetoxycephalosporin C synthase; HPPD, 4-hydroxyphenylpyruvate dioxygenase; PheOH, phenylalanine hydroxylase; TyrOH, tyrosine hydroxylase; TryOH, tryptophan hydroxylase; ACCO, 1-Aminocyclopropane-1-carboxylic acid oxidase; IPNS, isopenicilin N-synthase

The Catechol Dioxygenase Enzymes

The catechol dixoxygenases use dioxygen to catalyze the cleavage of the C-C bond in the catechol ring. This reaction can be subdivided into two types of cleavage based on the regioselectivity of the C-C bond. For intradiol cleavage involves the breaking of the C-C bond that resides between the two hydroxyl groups while the extraodiol cleavage reaction involves the

breaking of the C-C bond adjacent to the hydroxyl substituents.[26-28] The general mechanism for the extradiol dioxygenase can be seen in Scheme 1.1.

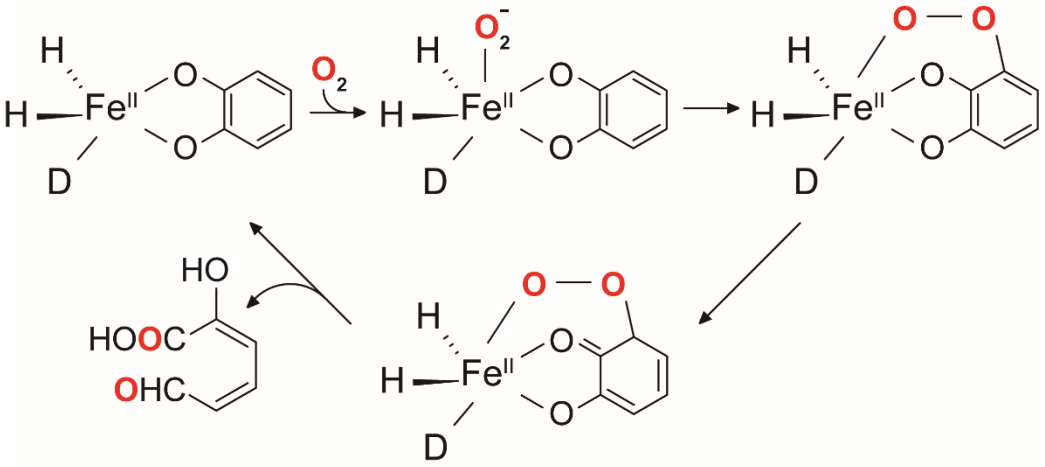

Scheme 1.1 The proposed pathway for catechol dioxygenase catalysis.

The α-ketoglutarate-dependent enzymes

The α-ketoglutarate-depedent oxygenases is the largest group within the 2-His-1-carboxylate enzyme family. These enzymes use α-ketoglutarate as an electron source for catalysis through the decarboxylation of α-ketoglutarate as seen in Figure 1.1. This group of enzymes are heavily involved in crucial biochemical pathways that are related to antiobiotic biosynthesis, DNA/RNA repair, and oxygen detection.[15, 19-22]

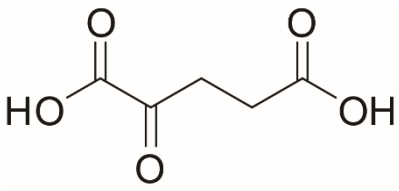

Figure 1.3 Structure of the α-ketoglutarate cofactor.

The proposed mechanism has been studies extensively and begins with the resting ferrous iron active-site that is situated in the 2-His-1-carboxylate moiety. The available binding sites are used for bidentate coordination to the α-ketoglutarate cofactor with one site open for molecular oxygen binding. Interestingly, the substrate is not directly coordinated to the iron active site much like the other enzymes in the non-heme iron family. Despite this change in substrate binding, the α-ketoglutarate dependent enzymes still follow the obligated addition of substrate prior to dioxygen binding. The proposed mechanism for the α-ketoglutarate-dependent oxygenases can been seen in Scheme 1.2. The binding of oxygen and the rapid electron transfer from the ferrous iron leads to the formation of a Fe(III)-superoxo species. The Fe(III)-superoxo swings over binds to the α-ketoglutarate cofactor to form a bicyclic ring-like structure which consequently weakens the O-O for cleavage. This leads to the formation of a high-valent Fe(IV)-oxo species that abstracts a hydrogen atom from the nearby substrate resulting in a Fe(III)-hydroxo and radical substrate species. The final step in the catalytic cycle is the hydroxylation of the substrate and subsequent release.[29]

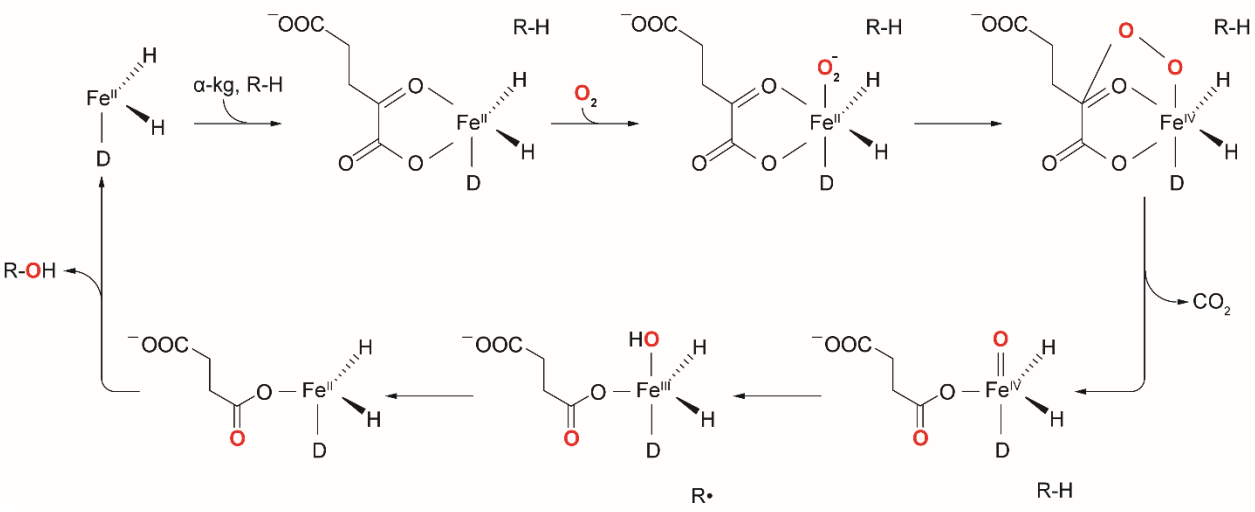

Scheme 1.2 Proposed mechanism for α-ketoglutarate dioxygenase catalysis.

The newly discovered 3-His facial triad

The 2-His-1-carboxylate moiety has been the dominant configuration in this family of enzymes and has been extensively examined with numerous structures solved elucidating crucial mechanistic information.[11, 13] However, a largely uncharacterized subset of enzymes have been identified that utilize a 3-His facial triad that deviates from the conical 2-His-1-carboxlyate motif. To date, there are only four solved crystal structures that illustrate this 3-His facial triad.[25, 30-33] The role of the 2-His-1-carboxylate structural configuration allows for stabilization of high-valent Fe-oxo intermediates, therefore it is reasonable that the transition to the 3-His moiety would have consequential effects on the catalytically relevant species formed during turnover.

Non-heme iron enzymes involved in sulfur catabolism

The development of life on Earth is defined by the utilization of the six primordial elements (H, C, N, O, P and S). For brevity, the focus will be on the sulfur biochemical pathway in cellular systems. Sulfur is an essential element to life and is critical to many biochemical pathways that are involved in amino acid synthesis and Fe-S clusters.[34-37] Numerous studies into the biochemical cycle of sulfur has shown a complex network of reactions that are not fully understood. A closer look into the stability of various redox states (-II to +VI) shows the remarkable capabilities of sulfur to be utilizied in various chemical reactions.[38]

The discovery of thiol dioxygneases (TDOs) that can oxidize sulfur containing amino acids has been known for nearly 40 years.[39] These O_2-depedent, non-heme iron enzymes are responsible for the catalytic conversion of thiols to sulfinic acid products. To date, there are two known mammalian enzymes involved in thiol oxidation, cysteine dioxyngease and cysteamine dioxygenase (CDO and ADO, respectively) of which CDO being the most extensively studied. An intense research effort has been made to shed light on the mechanistic pathway for thiol oxidation as medical studies into the disruption of cysteine regulaton has been linked to numerous diseases and ailments.[40-42] The CDO cycle converts cysteine to cysteinesulfinic acid that serves as a source for other sulfur regulatory steps in the cycle as seen in Scheme 1.3.

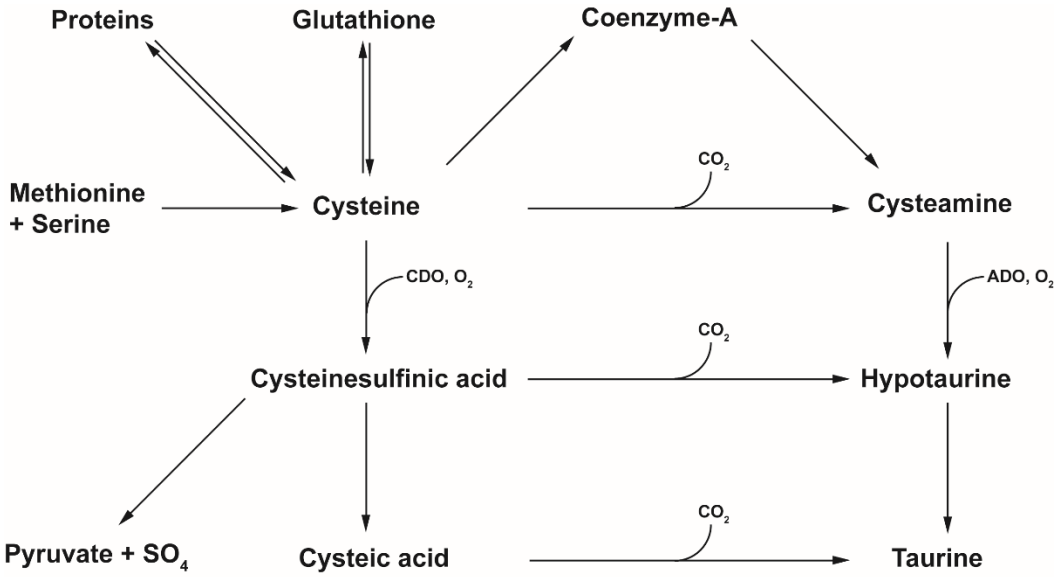

Scheme 1.3 The role of cysteine in the sulfur biochemical pathway.

Cysteine serves a critical role in metabolism of several important metabolites for cellular stability and regulation. Free cysteine exists in an equilibrium established by the glutathione and methionine biochemical pathways. Glutathione (GSH) is a critical component for maintaining healthy cellular function and monitoring oxidative stress. Nearly 90% of all available glutathione (1-10 mM) is located in the cytosol and represents the largest reservoir of readily-available antioxidants for detoxification of free radical and reactive oxgen species.[43, 44] Unde oxidative stress, reduced glutathione reacts with radical species to form oxidized glutathione (GSSG) which is can be re-reduced with the assistance of gluthathione reductase (GR) as seen in Scheme 1.4.[45]

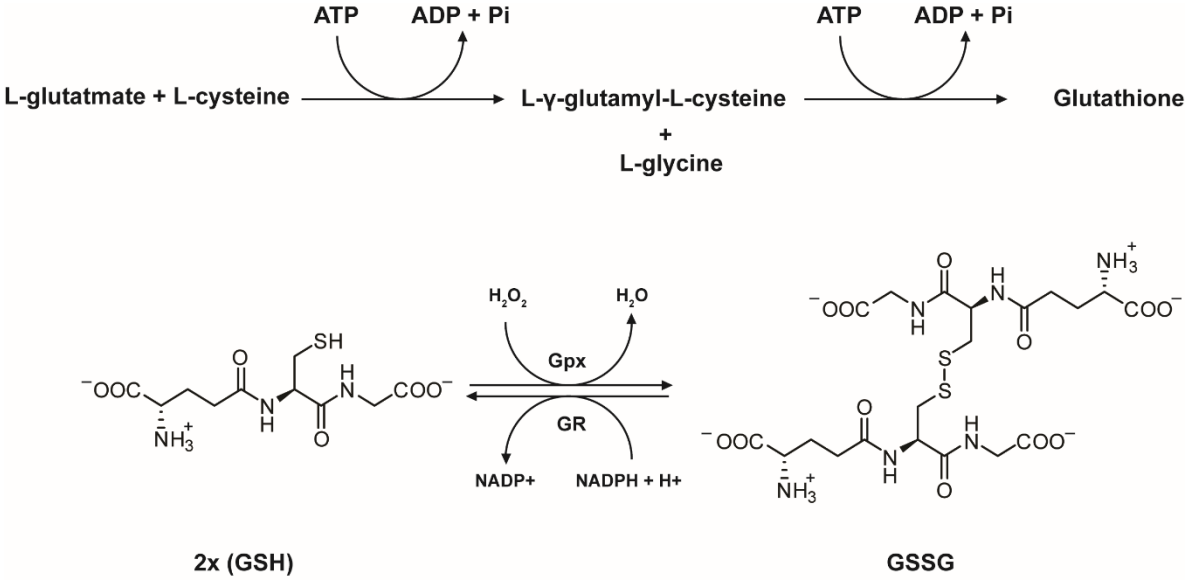

Scheme 1.4 Glutathione biochemical pathway.

The synthesis of cysteine is also regulated by methionine catabolism. Methionine is converted to *S*-adenosylmethionine (SAM) by the ATP-dependent synthatase, methionine adenosyltransferase (MAT). SAM is a crucial component for methylation in other biochemical pathways that such as DNA/RNA and protein methylation.[46] Methyl transfer from SAM leaves the *S*-adenosylhomocysteine (SAH) product. Hydrolysis of SAH by adenosylhomocysteinase (AHC) removes the adenosyl ligand and produces homocysteine. Homecysteine can either be recycled for methionine biosynthesis with 5-methyltetrahydrofolate or by the transsulfuration pathway that irreversibly converts homocysteine into cysteine as seen in Scheme 1.5.

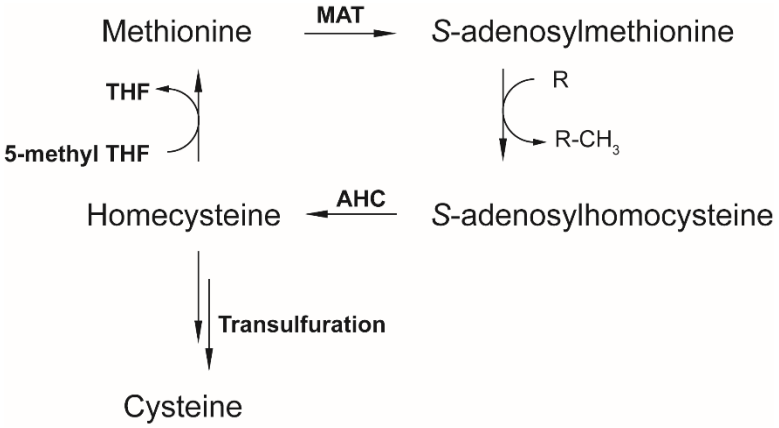

Scheme 1.5 Cysteine synthesis by methionine.

As seen above, the pathways that maintain cysteine levels are in some fashion reversible to maintain a healthy equilibrium. However, CDO is involved in the first irreversible step of cysteine consumption to product cysteinesulfinic acid (CSA). The production of CSA plays several roles as this metabolite can be further processed for production of pyruvate and inorganic sulfate or undergo decarboxylation to produce hypotaurine and eventually taurine as seen in Scheme 1.3.[47] CDO has been researched extensively due to it's importance in strict regulation of cysteine in biochemical pathways. However, little information has been available into the investigation of role of hypotuarine production in mammals.

The role of hypotaurine to date has shown to serve as the prerequiste metabolite to taurine biosynthesis.[39, 48] This biochemical pathway is initiated by the formation of the starting substrate, cysteamine (CA). Cysteamine is one the by-products of coneyzme-A catabolism.[49, 50] The thiol dioxygenase, cysteamine dioxygenase (ADO), is an O_2-dependent non-heme iron enzyme responsible for the conversion of cysteamine to hypotaurine as seen in Scheme 1.6.[48] The medical importance of

cysteamine has been investigated as a treatment for Huntington's and cystinosis, which is a uncontrolled buildup of cystine leading to organ failure.[51-53]

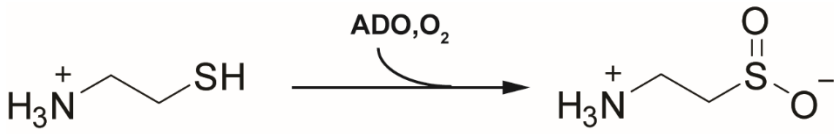

Scheme 1.6 ADO-catalyzed formation of hypotaurine.

ADO is a member of the newly identified 3-His facial triad enzymes. Examination of the amino-acid sequence shows that ADO is a member of the cupin superfamily of proteins. The cupin sequence motif are composed of β-barrel folds that house the metal active site region of the protein.[54, 55] Sequence homology between ADO and CDO show a low (~15%) identity however share the conserved 3-His facial triad found in CDO. Structural studies have shown that CDO exhibits an unusually rare post-translation modification (PTM) that involves the formation of a covalent crosslink between Cys93 and Tyr157 forming the C93-Y157 modified CDO. This modified pair has been postulated to aid in substrate orientation as well as proper stereo-selectivity of the substrate. Work by Liu *et. al.* found through ^{19}F NMR spectroscopy and high-resolution LC-MS reported a Cys-Tyr crosslink in the ADO protein that is found in CDO and suggests this post-translational cofactor may play a role in catalytic efficiency and substrate binding.[50] Various studies on the ADO protein report increased difficulty in crystal formation for X-ray diffraction and remains a largely uncharacterized biological system.

The non-heme diiron proteins

The non-heme, diiron enzymes are a functionally diverse collection of O_2-depedent oxygenases that are heavily involved in many critical biochemical reactions throughout the biological

kingdom as seen in Scheme 1.7.[17] The structural configuration of the active site houses the diiron metal cofactor and the nature of the transient speices is heavily influenced by the nature of the coordinating residues. Typically, the first-coorination sphere of the diiron core is surrounded by 2-histidine residues and 4-carboxylate ligands either in the form of aspartate or glutamate [2-His/4-carboxylate]. Among this family, the hydroxylase diiron enzymes of the bacterial multicomponent (BMM) diiron oxygenase superfamily (I.e. methane monooxygenases (MMOH), phenol hydroxlase (PH) and the R2 subunit of ribonucleotide reductase (RNR-R2) have attracted considerable interest due to their role in green chemistry, DNA synthesis, and degradation of toxic aromatic products.[56-58] Characterization of the myo-inositol (MIOX), *p*-aminobenzoate arylamine oxygenase (AurF), and chloramphenicol oxygenase (Cml I) have shown the addition of another histidine residue to the diiron active-site which results in 3-His/4-carboxylate configuration. These diiron enzymes are involved in extended oxdations (4-electron and 6-electron, respectively) and suggest that the coordination environment around the diiron core heavily influences the mechanistic approach and number of substrate oxidations.

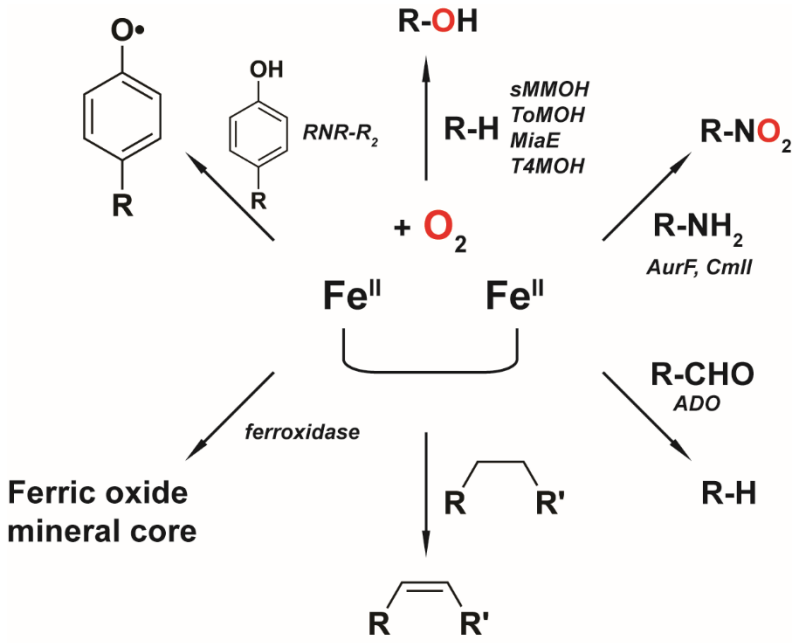

Scheme 1.7 Reactions carried out by diiron oxygenases.

This hypothesis is supported by the design and examination of the 4-helix bundle synthetic protein models known as *"Due Ferri"* proteins which houses the diiron core in a 2-his/4-carboxylate or 3-His/4-carboxylate environment.[59] Reactivity studies demonstrated that 4-aminophenol (4-AP) was oxidized in a manner that is comparable to other 2-His/4-carboxylate oxygenases. Furthermore, the 3-His/4-carboxylate *DF* proteins were exposed to 4-AP and showed evidence for production of arylnitro products much like that of AurF and Cml I.[60, 61]

Mechanistically, the initial step for substrate oxidation begins with the 2-electron reduction of the resting diferric enzyme that primes the diiron core for O_2-binding. The reductive process is aided by an external source of electrons typically in the form of NADH or NADPH. In the BMM, there are other enzymatic components utilized for electron delivery to the hydroxylase portion of the enzyme complex. The binding of dioxygen facilitates the formation of a peroxo intermediate. Several

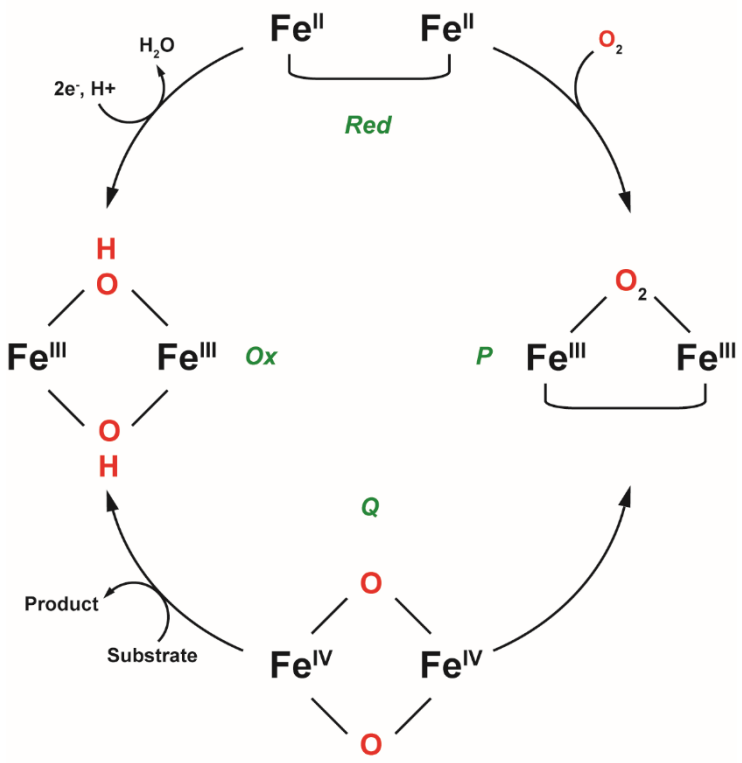

Scheme 1.8 Cycle for diiron intermediate formation

peroxo intermediates have been postulated and isolated for a variety of diiron oxygenases.[62] In Scheme 1.8, the transient species formed during O_2-binding in several diiron proteins in illustrated.

Structurally, the diiron enzyme family adopts a multimeric protein deisgn that houses that diiron active-site (hydroxylase component), electron transfer subunit, and an effector subunit for substrate binding and oxidation.[63] This dynamic multimeric protein structure immediately creates complications spectroscopically because each protomer of the enzyme houses a diiron core. This makes the assignment of spectroscopic features ambiguous at best. Additionally, these complexes

are tethered together and present the possibility for communication between protomers that can enable half-site reactivity suggesting that substrate oxidation is not limited to one portion of the protein. Together, these present significant hurdles when undertaking characterization of this family of enzymes.

This presents an excellent opportunity for the utilization of the *t*RNA-modifying monooxygenase, MiaE, to serve as the framework for studying the effects of the Fe-coordination sphere in tuning reactivity and transient species selectivity. MiaE is a non-heme diiron enzyme , from *Salmonella* typhimurium, that catalyzes the O_2-dependent hydroxylation of adenosine$_{37}$ in *t*RNA ($ms^2i^6A_{37}$) to produce 2-methylthio-*N*^{6}-(4-hydroxylisopenentyl)-adenosine ($ms^2io^6A_{37}$).[64, 65] The diiron core is situated similarly to that of the BMM diiron proteins with a 2-His/4-carboxylate environment. However, protein analytics and X-Ray crystallography have shown that the MiaE protein exists as a monomeric protein. The minimalist design that MiaE has adopted allows for strict assignments of spectroscopic signals and eliminates the potential for inter-protomer communication. The utilization of MiaE presents a “top-down” enzymatic approach for studies into arylamine oxdidation. With MiaE, the complications of designing the substrate channel, reductase subunit, and electron delivery mechanism are removed. This allows for an in-depth investigation of the catalytic cycle of arylnitro product formation.

Chapter 2 Mutation in tRNA-modifying monooxygenase, MiaE, leads to viable enzymatic model for arylamine oxidation.

Introduction

In metalloproteins, nature has made use of the first-row transition metals and conserved protein moieties to carry out a wide range of biochemical processes. The non-heme, diiron family encompasses a large, diverse set of O_2-dependent enzymes that can be found throughout the biological landscape. The various organic substrates utilized highlights the remarkable use of available biomolecules in the surrounding environment for cellular homeostasis and proliferation. The diiron metal cofactor buried in the active site cavity serves as the centerpiece for O_2 activation in oxidative processes. The binding and subsequent molecular arrangement of dioxygen in the diiron core is an integral component for transient species formation and has significant impact on the mechanistic route for oxidation. Numerous X-ray crystal structures have been solved for a variety of diiron oxygenases and show the generally conserved metal cofactor surrounded by varying number of histidine and carboxylate residues. The subtle change in the number of coordinated ligands has a significant impact on the chemical tuning of the diiron site and suggests an avenue to study the chemical reactivity of diiron oxygenases through structural alterations.[62,66]

A variety of classifications can be used for categorizing the non-heme diiron family of enzymes but for this purpose, I will focus primarily on the role of the first-coordination sphere and its impact on chemical tuning for reactivity toward non-native substrates.

Arylnitro containing compounds are a sought-after industrial product that can be found in pharmaceuticals, food dyes, and explosives. Like many industrial processes, the preparatory methods for arylnitro products require harsh reaction conditions and are less than satisfactory in terms of regioselectivity.[67, 68] Recently, a small subset of diiron enzymes have been identified to play a role in

oxidation of arylamine metabolites for arylnitro product synthesis. The antibiotic, pyrrolnitrin from *Pseudemonas fluorescens*, is biosynthetically produced by the Prn enzymatic pathway where Pyrrolnitrin *N*-oxygenase (PrnD) serves as the arylamine oxygenase to doubly oxidize aminopyrrolnitrin to pyrrolnitrin.[69] Protein studies confirmed that the PrnD enzyme utilizes a [2Fe-2S] cluster that aids in the electron delivery network for catalysis and was subsequently designated as a Riseke dioxygenase.[70] In contrast , two newly isolated diiron enzymes, CmlI and AurF, were recently identified and characterized as non-heme diiron aryl-*N*-oxygenases for their role in chloramphenicol and *p*-nitrobenzoate biosynthesis.[71,72] The overall 6-electron oxidation is a significant shift in oxidative capacity for the diiron metalloproteins for a variety of reasons. Evolutionarily, a majority of the diiron oxygenases identified are involved in modest 2-electron, monooxygenase chemistry. Additionally, the mechanistic process for extended oxidation requires the framework that allows the substrate to remain within the active site long enough for oxidative targeting. Overall, there is significant interest in understanding the unusual uptick in substrate oxidation of arylamines for practical applications of potential catalysts for arylnitro products in industrial production.[73]

The characterization of these enzymes began with synthetic 4-helix bundle development with the diiron metal cofactor incorporated with the appropriate ligand set for biomimicry to the arylamine oxygenase system.[59,61,60] While the bottom-up approach for modeling arylamine oxidation showed promise, the initial 2-electron oxidation of the arylamine substrate but was unable to fully convert the substrate into the arylnitro product. The “top-down” approach proposed here takes advantage of the highly conserved nature of the diiron metal cofactor that is unique to this family of enzymes. Using a fully functional enzyme we can bypass the synthetic route and utilize an intact protein environment for understanding arylamine oxidation.

The enzyme 2-methylthio-N^6-isopentenyl-adenosine (37)-tRNA monooxygenase (MiaE) is a non-heme diiron enzyme that is involved in the O_2-dependent conversion of 2-methylthio-N^6-isopentyl-

adenosine ($ms^2i^6A_{37}$) into 2-methylthio-*N*^{6}-(4-hydroxyisopentenyl)-adenosine ($ms^2io^6A_{37}$) as seen in Scheme 2.1.[66,74]

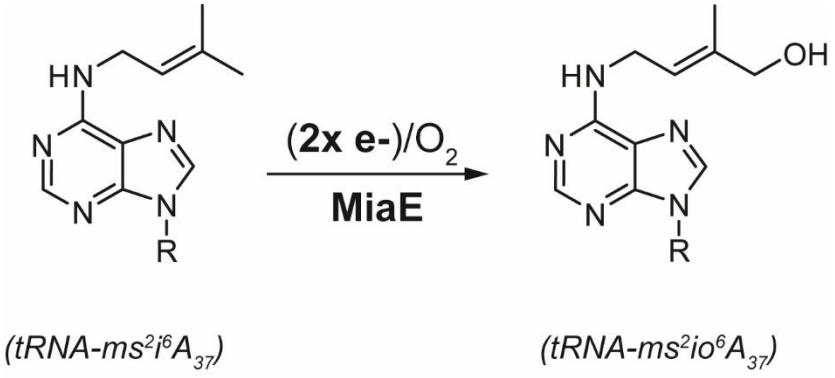

Scheme 2.1 Hydroxylation reaction by MiaE in synthesis of 2-methylthio-N6-(4-hydroxyisopentyl)-adensosine ($ms^2io^6A_{37}$)

Structural alignments of the first-coordination sphere show the major component that distinguishes these enzymes lies in the coordination of the nearby histidine/carboxylate residues.[75] MiaE has a nearly symmetrical distribution of ligands with each Fe site bound to a nearby histidine and further coordinated to four glutamate residues much like other non-heme diiron enzymes in this family. There is appended water/hydroxo ligand on the Fe site closest to Leu^{199} that lies 6.1 Å away as seen in Figure 2.1 (panel A). MiaE is classified as monooxygenase with a 2-His-4-carboxylate [2H4C] frame and is a classic design with other monooxygenases. X-ray crystallography of the arylamine *N*-oxygenase, AurF, shows a similar distribution of ligands however, there is an additional histidine residue bound to one of the Fe-sites as seen in Figure 2.1 (panel B). This classifies the AurF metalloprotein with a 3-His-4-carboxylate [3H4C] moiety and is a common feature among the other arylamine *N*-oxygenase, CmlI. The elegant arrangement of residues to the diiron core is further expanded in other systems like hemerythrin and myo-inositol oxygenase. The changes that are introduced by the variation in coordinated protein ligands

can aid in classification of diiron enzymes and show a pattern that relates to extent of oxidation as seen in Figure 2.2.

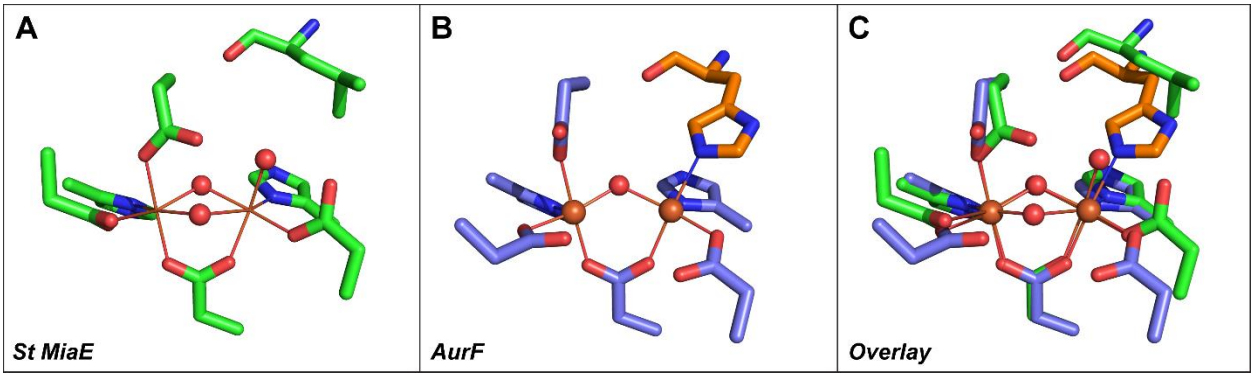

Figure 2.1 X-ray crystal structures of two diiron oxygenases, MiaE and AurF. A) Crystal structure of MiaE from Salmonella typhimurium at 1.7 Å. B) Crystal structure of AurF from Streptomyces thioluteus at 2.0 Å (PDB: 3CHH)[70]. C) Overlay of crystal structures between MiaE and AurF.

The rather subtle changes in the first-coordination sphere illustrate how nature has taken a general conserved protein region and is able to tune the reactivity of the diiron center for propagation of diversity in chemical reactivity. Analysis of the crystal structures of AurF and MiaE draws attention to the

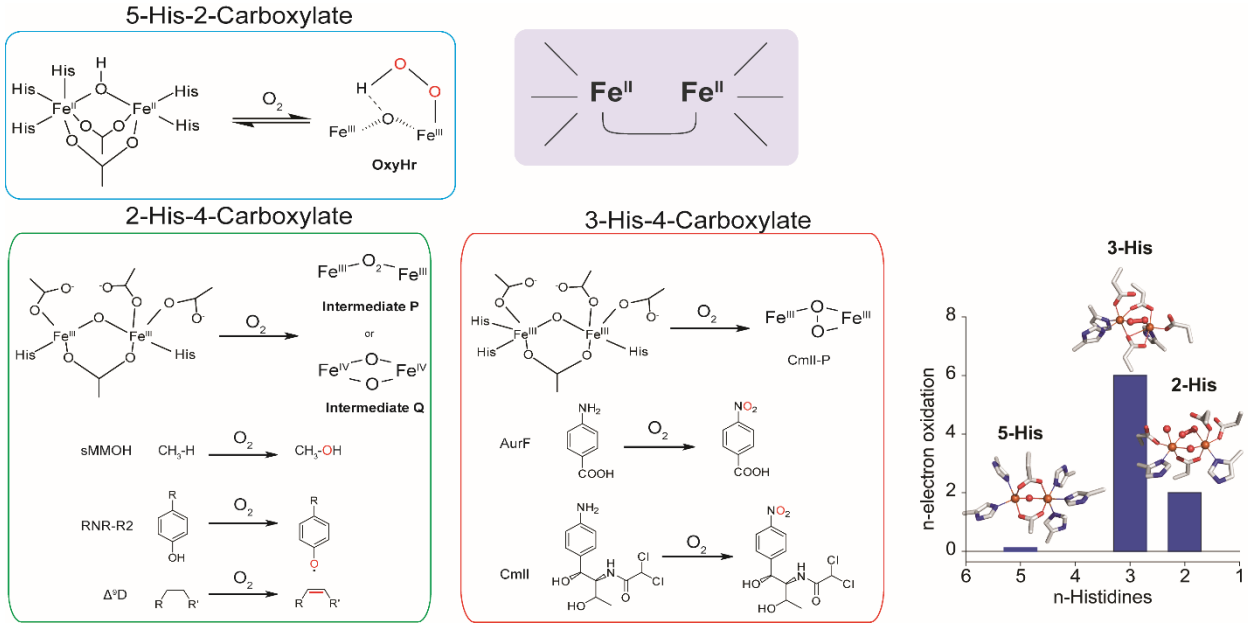

Figure 2.2 Classification of non-heme diiron enzymes by structural arrangement of first-coordination sphere ligands and net change in extent of oxidation by bound histidine residues in active-site.

significant overlap between active-site configurations with the major difference in the additional histidine residues in AurF and the innocent Leu199 residue as seen in Figure 2.1 (panel C).

In theory, this particular arrangement can be altered and probed using site-directed mutagenesis to mimic the 3H4C moiety with MiaE as the system to house the newly created configuration. This provides a unique opportunity to study the effects of protein ligands on the tuning of chemical reactivity but also the avenue to explore the arylamine *N*-oxygenase pathway and elucidate further mechanistic information that relates to transient species formation and the critical peroxo-intermediate that is necessary for catalysis.

In this work, we present evidence for the use of the L199H MiaE variant as a model for studying arylamine oxygenase chemistry in a non-native system. Experimental results show the L199H variant participates in arylamine reactivity with the substrate aniline (**NH_2-Ar**) to form nitrobenzene (**NO_2-Ar**). Additionally, arylamine activity studies showed that L199H variant can bypass the first oxidation step through the '*hydroxylamine-shunt*' and proceed to form **NO_2-Ar** through a 4-electron process. Together these results provide strong evidence for the use of MiaE as a functional model to extrapolate information related to the arylamine oxidation pathway as well as further understand the role of the first-coordination sphere in this family of enzymes.

Materials and Methods

Site-Directed Mutation of MiaE wild-type. The L199H variant was prepared with the QuikChange Lightning Site-Directed Mutagenesis kit (Agilent Technologies). Primers for mutagenesis were designed and purchased from Integrated DNA Technologies (http://idtdna.com), and sequence verification of the single-amino acid mutation was carried out by Sequetech (Mountain View, CA).

Protein Purification of MiaE L199H Variant. Procedures for expression, transformation and protein purification for MiaE are described elsewhere and were carried out for both *wild-type* and the

L199H variant.[66,76] Briefly, 25g of cell paste was thawed and stirred gently in lysis buffer (20 mM HEPES, 50 mM NaCl, pH 8.0) in an ice bath with 10 μg/mL each of deoxyribonuclease I, ribonuclease, and lysozyme. The suspended cells were sonicated in an on/off 30 s pulse cycle for 10 min. The cell free extract was centrifuged (JA 20 rotor) at 40,000 X *g* for 60 min at 4°C. The supernatant was loaded on a pre-equilibrated fast-flow DEAE column and the protein was eluted on a linear NaCl gradient (25 mM to 350 mM NaCl in 20 mM HEPES, 0.3 mM Tris[2-carboxylethyl] phosphine (TCEP), pH 8.0). Fractions containing MBP-L199H variant, verified via SDS-PAGE, were pooled and concentrated with an Amicon N_2 stir cell equipped with an YM 30 ultrafiltration membrane. The TEV protease was used to cleave the MBP-tagged protein overnight at 4°C. Determination for protein concentration was carried out with a standard Bio-Rad protein assay (Bio-Rad Laboratories Inc.).

Fe Content Quantification*.* The total iron in the protein sample was quantified with UV-vis spectroscopy according to previous studies.[77] Generally, 500 μL protein sample was denatured in 250 µL each of trichloroacetic acid (20%) and 2N hydrochloric acid. The iron released after denaturation was reduced via 100 µL hydroxylamine hydrochloride (10% w/v) along with 100 μL 2,4,6-tripyridyl-*S*-triazine (TMTP) (4 mM) and 200 μL ammonium acetate (50% w/v). A UV-vis spectrophotometer was used to measure the colored solution (ε_{596} = 22, 600 $M^{-1}cm^{-1}$).

EPR and UV-Visible Spectroscopy*.* X-band (9 GHz) EPR spectra were recorded on a Bruker (Billerica, MA) EMX Plus spectrometer equipped with a bimodal resonator (Bruker model 4116DM). Low-temperature measurements were made using an Oxford ESR900 cryostat and an Oxford ITC 503 temperature controller. A modulation frequency of 100 kHz was used for all EPR spectra. All experimental data used for spin-quantitation were collected under non-saturating conditions. For simulations of the reduced diiron cluster, it was assumed that the exchange coupling constant (J) is comparable in energy to (or larger) than the zero-field splitting (D) of the diferrous cluster. Under this constraint, the S = 4 Hamiltonian takes the form illustrated in Equation 2.1.

$$\mathcal{H} = \mathbf{D}\left[\hat{S}_Z^2 - \frac{S(S+1)}{3}\right] + \mathbf{E}\left(\hat{S}_X^2 + \hat{S}_Y^2\right) + \beta \boldsymbol{B} \cdot \mathbf{g} \cdot \mathbf{S} \quad (\mathbf{2.1})$$

where ***D*** and ***E*** are the axial and rhombic zero-field splitting(zfs) parameters and g is the g-tensor.[78] EPR spectra were simulated and quantified using Spin Count (v 4.0.30319), written by Professor M. P. Hendrich at Carnegie Mellon University. The simulations were generated with consideration of all intensity factors, both theoretical and experimental, to allow for determination of species concentration. The only unknown factor relating the spin concentration to signal intensity was an instrumental factor that is specific to the microwave detection system. However, this was determined by the spin standard, Cu(EDTA), prepared from a copper atomic absorption standard solution purchased from Sigma-Aldrich.

UV-visible measurements were carried out on an Agilent 8453 photodiode array spectrometer. Samples were measured with ES quartz cuvettes (NSG Precision Cells, Farmingdale, NY).

Analysis of oxidized arylamine products. 100 μM of L199H variant was reduced in aerobic conditions with 5 equivalents of ascorbic acid. 500 μM **NH_2-Ar** in methanol was spiked into reduced L199H variant and allowed to mix for 10 minutes. 150 μL of the assay was removed at selected time points and acid-quenched with 15 μL of 0.2 mM HCl for HPLC analysis. All aliquoted samples were spin-filtered through a 0.22 μm cellulose acetate centrifuge tube filter. Samples were analyzed either immediately or frozen in liquid N_2 and stored in -80°C.

For the hydroxylamine shunt pathway assay, 500 μM *N*-phenylhydroxylamine (**NPH**) was added to 100 μM of L199H variant and allowed to mix for 10 minutes. 150 μL aliquots were removed at selected time points and acid-quenched with 15 μL of 0.2 mM HCl for analysis. All aliquots were filtered

through a 0.22 μm cellulose acetate centrifuge tube. Assay samples were analyzed immediately or frozen and stored in -80°C.

HPLC Assay for arylamine oxidation products. A Shimadzu dual pump liquid chromatograph (LC-20AD) with an equipped photodiode array detector (SPD-M20A) was used for analysis. The column used was a Phenomenex, Luna 5μ, C18(2) 100 Å, 250 mm x 4.60 mm. The mobile phase consisted of (A) methanol and (B) water. The injection volume was 10 μL at a flow rate of 0.5 mL/min. The column temperature was 25°C. The UV-visible detection was monitored at 242 nm (λ_{max} of **NH_2-Ar**), 268 nm (λ_{max} of **NO_2-Ar**), and 282 nm (λ_{max} of **NO-Ar**). The concentrations of **NH_2-Ar**, nitrosobenzene (**NO-Ar**), and **NO_2-Ar** were determined by comparison to calibration curves with primary standards (0.01 – 0.5 mM) analyzed under the same conditions.

LCMS/MS assay for arylamine oxidation products. Verification of the product of the enzymatic assay was done by multiple-reaction monitoring (MRM) using a Shimadzu triple-quadrupole LC-MS/MS (LCMS, 8040). The molecular ions (M^+) of the enzyme substrate (93 m/z) and product (123 m/z) were selected for secondary fragmentation. Secondary fragmentation of nitrobenzene produces secondary ions of 105.0 m/z and 87.0 m/z which correspond to the loss of two water molecules. MRM optimization was employed to maximize intensity and sensitivity for each fragment allowing for quantification of product ions. The MRM method was used to verify both substrate and product by direct injection of enzymatic assays. The results were then compared to direct injections of primary standards.

^{18}O Isotope Incorporation Assays. For verification of ^{18}O incorporation with $H_2{}^{18}O$, L199H variant was placed in anaerobic chamber and reduced with excess sodium dithionite and methyl viologen. Exchange with $H_2{}^{18}O$ was done by three treatments of dilution and concentration of reduced L199H variant. The enzyme-$H_2{}^{18}O$ was removed from the chamber and 500 μM **NH_2-Ar** was spiked and the assay was allowed to mix for 10 min. Aliquots were removed and acid-quenched for LCMS-MS analysis.

Detection of ^{18}O into the substrate via $^{18}O_2$, L199H variant was placed into an anaerobic chamber and reduced with stoichiometric sodium dithionite and methyl viologen. The vessel was removed from the chamber and purged with Ar gas for 30 min on a Schlenk line. $^{18}O_2$ was streamed into the vessel for several minutes and allowed to sit for 30 mins on ice. Positive pressure of $^{18}O_2$ was kept inside the vessel and transferred to the anaerobic chamber. Anaerobic substrate **NH_2-Ar** was spiked into the enzyme and allowed to mix for 30 min. Aliquots were removed and acid-quenched and filtered for LCMS-MS analysis.

Results

Purification of MiaE wild-type and L199H variant. The recombinant L199H variant was purified and analyzed for Fe-content as described in the Materials and Methods. The MBP-L199H fusion protein displays the ~70 KDa apparent molecular weight through SDS-PAGE. The overnight TEV-cleavage of the fusion protein results in two bands ~40 KDa and ~29 KDa (MBP-tag and L199H, respectively). Comparative analysis of the SDS-PAGE bands between *wild-type* MiaE and the L199H variant shows comparable bands and density for pre- and post-cleavage with TEV.

The Fe-content of iron in the L199H variant was confirmed with 2,4,6-tripyridyl-*s*-triazine (TPTZ), Bradford assay, and UV-vis spectroscopy described in previous works.[79] Briefly, a 100 µL aliquot of purified enzyme was denatured by the addition of 250 µL of 2 N HCl, 250 µL of trichloroacetic acid (20% w/v), and 400 µL of Milli-Q H_2O. The hydrolyzed sample was placed in a table-top centrifuge and spun down at 14,000 rpm for 10 min. After centrifugation, 750 µL of the pelleted sample was added to 300 µL of 1.0 M TPTZ, ammonium acetate (50% w/v), and hydroxylamine (10% w/v). The solution was allowed to react for 10 min at room temperature to fully reduce all ferric iron to the ferrous state. The quantification of ferrous iron in the sample was carried out in the absence of hydroxylamine (NH_2OH).

The total iron content in the sample was measured spectrophotometrically at 596 nm (ε = 22.6 mM^{-1} cm^{-1}). For clarity, all reported concentrations are related to the ferrous content in the enzyme sample.

UV-visible and X-band EPR Spectroscopy. The Fe-associated bands of *wild-type* MiaE have been well-documented in previous studies.[66,74] Numerous spectroscopic studies on the non-heme, diiron family have found the nature of the Fe-oxo bridge is a distinguishable feature amongst the family.[62] Studies with the as-isolated MiaE protein exhibits an Fe-associated charge transfer band at 370 nm.[66,74] In Figure 2.3 (panel A), the comparative absorptive features in the *wild-type* enzyme (black trace) and L199H variant (red trace) are shown.

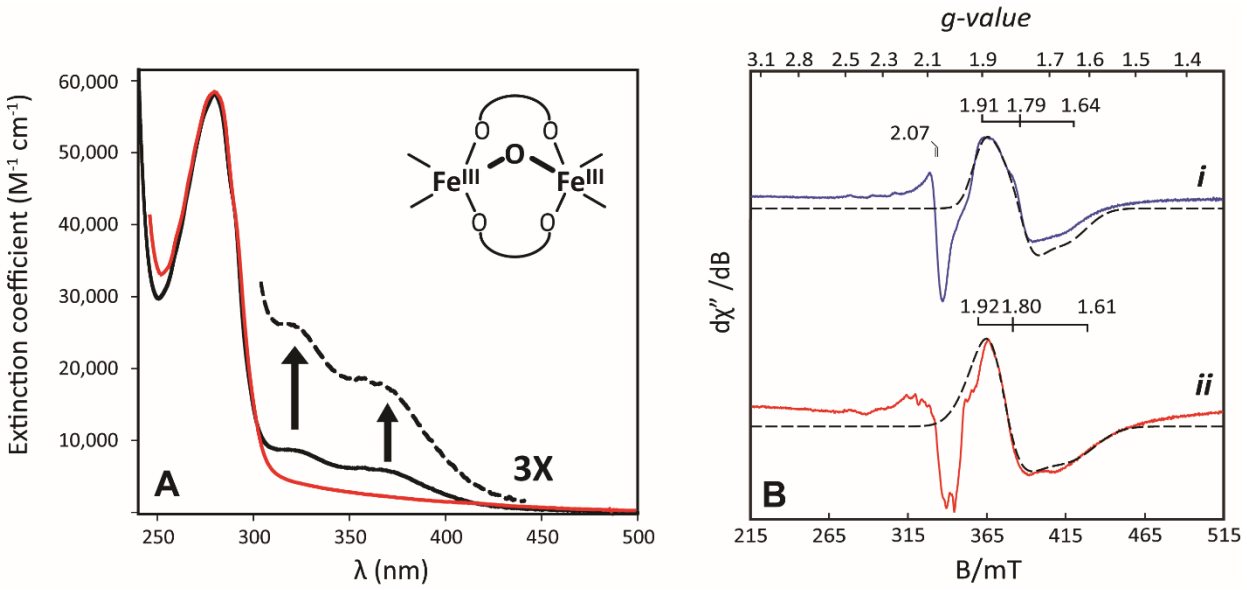

Figure 2.3 A) UV-vis comparison of as-isolated wt MiaE and L199H variant. A) Optical spectra of the as-isolated oxidized MiaE (black) and L199H variant (red). B) 5.0 K perpendicular (⊥) X-band EPR spectra of purified wt MiaE and L199H variant. (***i***) perpendicular X- band EPR spectra of purified wt MiaE (0.97 mM) chemically reduced with 0.5 molar equivalents of sodium dithionite and catalytic methyl viologen; (***ii***) perpendicular X-band EPR spectra of purified L199H variant (0.56 mM) chemically reduced with 0.5 molar equivalents of sodium dithionite and catalytic methyl viologen. EPR simulations are overlaid on spectra with dashed lines. EPR instrumental parameters: microwave frequency, (⊥) 9.644 GHz; microwave power, (***i*** and ***ii***)6.325 mW; modulation amplitude; 0.92 mT; temperature; 5.0 K. EPR simulation parameters. i: S = 1⁄2, gz = 1.91, gy = 1.79, gx = 1.64; σgz = σgy = 0.04, σgx = 0.05. ii: S = 1⁄2, gz = 1.93, gy = 1.82, gx = 1.62; ; σgz = σgy = 0.06, σgx = 0.05.

As seen in Figure 2.3 (panel A), there are two distinct shoulders in the oxidized MiaE protein at ~320 and ~370 nm. The absorption feature at 320 nm has been attributed to potentially a distinct binuclear site separate from the μ-oxo bridge that is traditionally seen in the diiron enzymes. Mössbauer studies on the oxidized MiaE have shown a small portion of the signal that is comparable to a μ-hydroxo bridged ligand and thus is possibly the 320 nm feature.[76]

The UV-vis studies with the newly purified L199H variant shows the absence of discernable signals that may be related to the LMCT bands found in the *wild-type* enzyme. In the diiron enzyme family, many of the isolated oxygenases have been spectroscopically analyzed and shown to generally contain at least one oxo bridge in the binuclear site. However, exceptions to the general trend exist in the bacterial multicomponent enzymes of methane monooxygenase (sMMOH) and toluene monooxygenase (ToMOH).[80,81] The diiron cluster found in these enzymes lends itself for examination by spectroscopy and provide distinguishable details that describe the local environment around the metal center.

The diiron family of enzymes have been known to stabilize a variety of oxidation states such as the differic, mixed-valent Fe^{III}-Fe^{II}, and diferrous species.[82] The spectrum of oxidation states allows the electronic structure of these clusters to be probed with a variety of spectroscopic techniques. In perpendicular X-band EPR, many of these enzymes have features at $g_{avg} < 2$ which has been verified as the mixed-valent species of the diiron site.[81,83] The mixed-valent species can be used as a diagnostic tool to confirm the presence of a diiron cluster as well as give insight into the local environment around the diiron core.[82] The chemically induced mixed-valent species is generated by titration of electrons into the diiron site under sub-stochiometric conditions. The mixed-valent species is a unique electronic configuration where the two iron centers are coupled (S = $5/2$, Fe(III) and S = 2, Fe(II)) antiferromagnetically. The resulting coupled system generates an overall spin of S = $1/2$. The newly

generated electronic form is unique species that is distinguishable from other EPR-active species generated by the diiron site.

The broad, axial signal at $g \sim 2.07$ is remnants of a Cu(II) contaminant. Copper signals in EPR can be saturated and spectroscopically attenuated with changes in the power parameters in the EPR software. While changes in power input generally affect many of the EPR signals, the mixed-valent species is relatively unaffected. Spincount simulations can isolated and similar the copper signal and be subtracted out. The total spin of the mixed-valent species aids in the simulation calculations as the more complex Hamiltonian terms from Equation 2.1 are only necessary for systems with $S > {}^{1}/_{2}$. As seen in Figure 2.3 (panel B), the broad feature at $g < 2$ in the *wild-type* MiaE (dashed lines) illustrates the simulated mixed-valent species. At 5K, the calculated *g-values* of 1.90, 1.79, and 1.63 are comparable values for what are generally seen in other diiron systems and model complexes.[82]

At $g \sim 2.11$, there is a residual signal related to a Mn(II) contaminant which has a characteristic 6-line hyperfine pattern ($\boldsymbol{I} = 5/2$). Much like the copper signal in the *wild-type* spectra, the Mn(II) signal was saturated with increased power settings and subtracted out from the experimental spectrum. The L199H variant exhibits a comparable broad feature at $g < 2$ with *g-values* of 1.92, 1.81, and 1.61 which are comparable to the *g*-values found in the *wild-type* enzyme. The comparative *g*-values between the L199H variant, *wt* MiaE, and AurF is shown in *Table 2.1*. EPR data sets for MiaE and L199H variant would suggest the presence of at least one hydroxyl bridged ligand which supports what is seen in the Mössbauer and crystallographic studies for *wild-type* MiaE.[76, 82]

Table 2.1. Effective g-values for mixed-valent species found in diiron enzymes.

$Fe^{II}Fe^{III}$-state (S = ½)	$g_{x,y,z}$		
MiaE	1.90	1.79	1.63
L199H	1.94	1.79	1.70
AurF	1.92	1.81	1.61

For the non-heme diiron enzymes, the binuclear site can be probed in with parallel mode X-band EPR spectroscopy. The perpendicular mode for EPR spectroscopy is used for analysis of half-integer spin species (S = $^1/_2$, $^3/_2$,…). In contrast, parallel mode is more affiliated with integer-spin (S = 1, 2…) systems and present more complicated spectral features. The non-heme diiron enzymes exhibit a low-field signal at $g \sim 16$ in the fully-reduced, diferrous form.[58, 84-86] The weak ferromagnetic exchange coupling between the iron sites results in a S = 4 ground state. Comparisons between model complex and other diiron monooxygenases show a fairly intense response at minimal concentrations. In the L199H variant, the $g \sim 16$ signal is significantly attenuated relative to the intense signal in *wild-type* MiaE. Regardless, the exhibited $g \sim 16$ signal with the L199H variant further confirms the incorporated of the diiron cluster.

$^{18}O_2$/$H_2{}^{18}O$ Isotopic Studies. To verify the source of oxygen incorporated into nitrobenzene, the catalytically active form of the L199H variant, **P**, was formed under an $^{16}O_2$ or $^{18}O_2$ atmospheric environment to react with aniline. Reactions were initiated with 5.0 equivalents of **NH_2-Ar** at ambient temperature (22 ± 1°C) for 30 mins and acid-quenched for analysis as described in the experimental protocol. Substrate additions presented here and in further experiments were calculated with respect to concentration of **P**. When $^{18}O_2$-L199H variant reacted with **NH_2-Ar**, the resulting nitrobenzene formation was observed by a +4 m/z shift in the parent ion peak from 123.0 to 127.0, indicating the incorporation of two ^{18}O atoms into the substrate. Furthermore, the fragmentation peak at 105.0 represents the loss of a water molecule from the product (under $^{16}O_2$ conditions) and this pattern is consistent in the $^{18}O_2$ assay with a fragmentation peak at 107.0. Collectively, the LCMS results indicate that both incorporated oxygen atoms into aniline are derived from $^{18}O_2$-**P** and therefore from atmospheric oxygen and not from nearby water molecules in the solvent. To verify this result, reduced L199H variant was exchanged with

$H_2{}^{18}O$ and exposed to an $^{16}O_2$ environment to form $^{16}O_2$-**P**. Reactions with aniline were analyzed and produced only ^{16}O-product.

Arylamine reactivity observed in L199H variant with NH_2-Ar. Arylamine reactivity with **NH_2-Ar** was carried out with purified recombinant MiaE L199H variant that was reduced with L-ascorbate (***asc***) to form the catalytically active diferrous cluster. For detection of nitrobenzene, HPLC traces of the L199H-catalyzed reactions were measured at 268 nm. As shown in the HPLC trace Figure 2.4 (panel A), the addition of **NH_2-Ar** to reduced L199H variant results in the formation of a new peak at 17.2 min (black circle). The substrate, aniline, has two UV bands (235 and 282 nm) that can be measured spectroscopically in HPLC and used for monitoring of product formation. The end-product, nitrobenzene, has a UV absorption band at 268 nm under aqueous conditions. The UV-vis spectra of both compounds can be seen in Figure 2.4 (panel B) In reactions with aniline, copious amounts of substrate remained in solution was observed. Substrate detection allows for measuring the rate of substrate loss to determine the kinetics for arylamine consumption. Reactions with *wild-type* MiaE and aniline were analyzed as a control to verify that MiaE did not exhibit arylamine reactivity. Additionally, reactions where enzyme was omitted verified that aniline did not spontaneously oxidize into nitrobenzene.

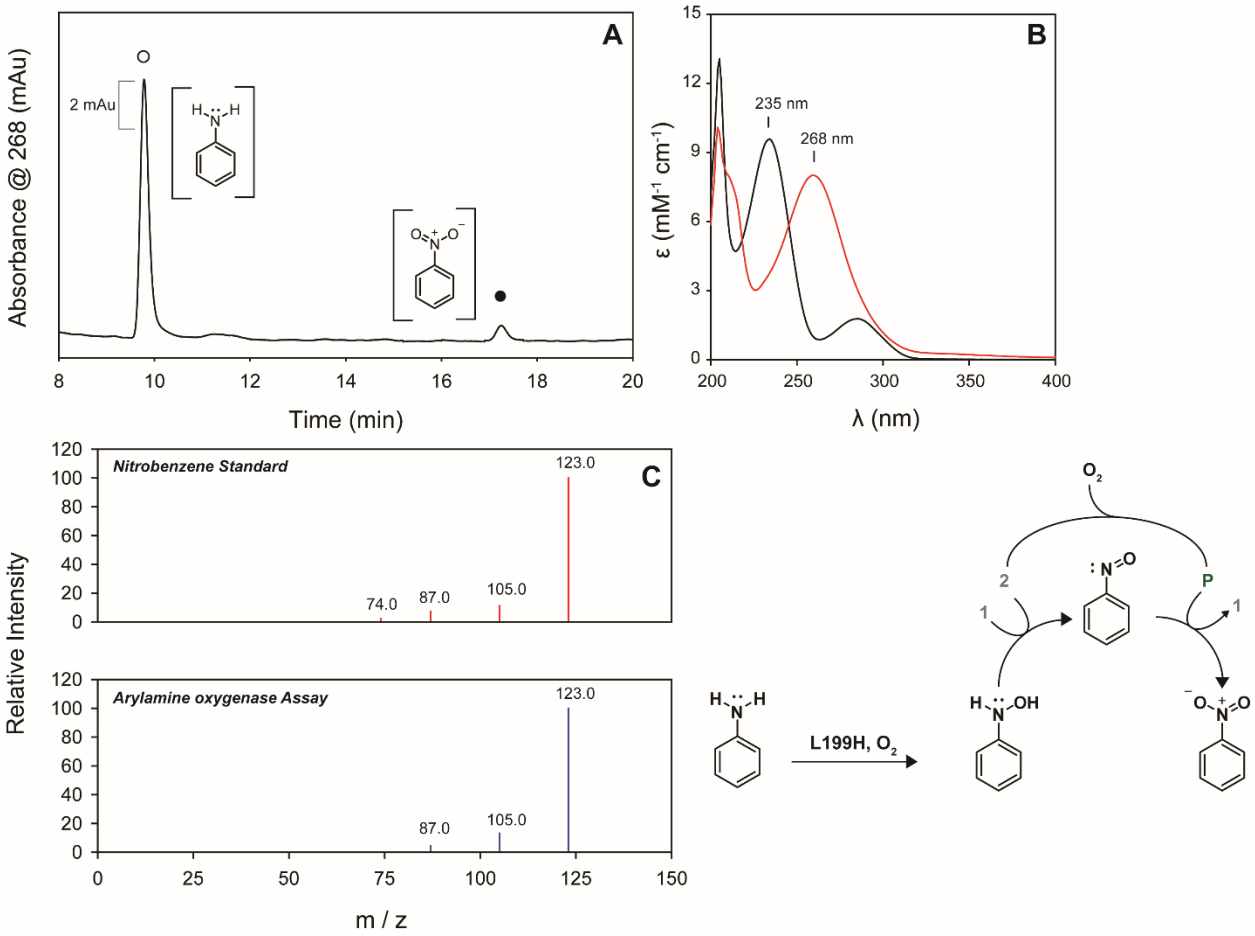

Figure 2.4 Representative chromatogram of aniline oxidation in L199H reaction (product detected spectrophotometrically at 268 nm). A) Chromatogram shows the nitrobenzene peak (black circle, 17.5 min) produced by the reaction of aniline with the L199H variant in presence of excess reductant. The remaining substrate aniline is observed as well (white circle, 9.7 min). B) UV-vis spectra of substrate aniline (black) and product nitrobenzene (red). C) Comparative LC-MS of primary standard nitrobenzene (top panel) and L199H-catalyzed nitrobenzene formation (bottom panel).

The quenched samples were analyzed with LCMS with multiple-reaction monitoring to confirm the arylnitro product. Standards of the nitrobenzene product were analyzed by direct injection and used to compare product peaks from the L199H reaction. The nitrobenzene product underwent further fragmentation and selected peaks were chosen for comparisons. As seen in Figure 2.4 (panel C), the nitrobenzene standard has a molecular ion peak of 123.0 m/z with other selected peaks of 105.0, 87.0,

and 74.0. For enzymatic reactions, the fragmentation pattern has peaks that correspond to 123.0, 105.0, and 87.0. The newly generated peak matches the retention time, UV/Vis absorption features, and MRM of the nitrobenzene standard. The L199H variant with aniline plateaus after 180 s of reaction time. Single-turnover reaction conditions lend themselves to a myriad of variables and pitfalls in relation to product formation and stability. The presence of excess reductant can invariably interact with the highly reactive oxidative species in the diiron site. The diferric peroxo-intermediate may be quenched by the electron-rich environment. Additionally, the L199H-catalzyed reactions are more than likely to be uncoupled in product formation. The production of harm species (ROS) can interact and destroy the enzyme from the inside.

Arylhydroxylamine shunt pathway studies*.* Winkler and company first proposed the biosynthetic pathway for the conversion of *p*-aminobenzoate (PABA) that involves the formation of an arylhydroxylamine intermediate and Lipscomb *et. al.* showed the use of the arylhydroxylamine substrate as an intermediate in the metabolic pathway.[73, 87] Verification that the arylhydroxylamine is involved in aniline conversion in the L199H variant, *N*-phenylhydroxylamine (**NPH**), was used as the substrate for the viability of a '*hydroxylamine shunt'* pathway. Shunt pathways have been identified in the ToMOH system and *wild-type* MiaE where hydrogen peroxide provides the electron source for chemical oxidation of the substate.[66, 88] The addition of **NPH** directly to oxidized L199H variant serves two chemical functions for the reaction. Firstly, the diferric cluster is reduced by **NPH** through the hydroxylamine moiety which generates the oxidative species for oxygen incorporation**.** During this process, **NPH** subsequently oxidized and generates nitrosobenzene (**NO-Ar**). The nitrosobenzene becomes the substrate for oxidation and is oxygenated by the L199H variant generating nitrobenzene. Additionally, **NPH** decomposes into nitrosobenzene under aqueous conditions and can be followed spectroscopically for the rate of decay and account for during turnover. As seen in Figure 2.5 (panel A), two new peaks form at 17.5 and 19.3 min.

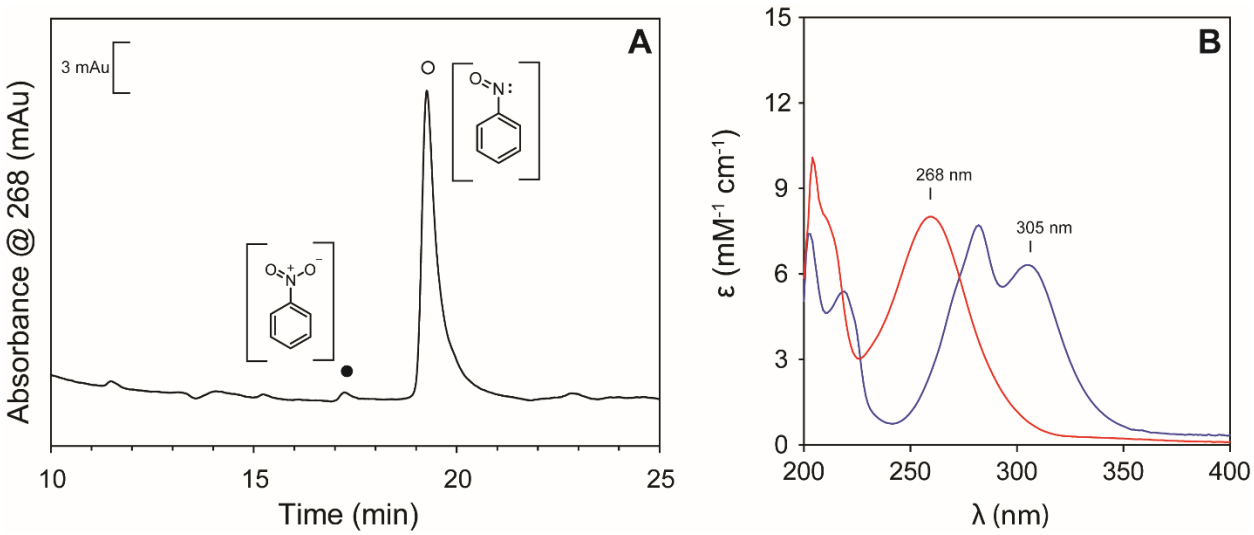

Figure 2.5 Representative chromatogram of nitrosobenzene oxidation in L199H reaction (product detected spectrophotometrically at 268 nm). A) HPLC Chromatogram illustrates the nitrobenzene peak (black circle, 17.5 min) produced by the reaction of N- phenylhydroxylamine with the oxidized L199H variant. The remaining N-phenylhydroxylamine decomposes spontaneously in aqueous solvent and forms the nitrosobenzene peak (white circle, 19.2 min). B) UV-vis spectra of by-product nitrosobenzene (blue) and the product nitrobenzene (red).

In Figure 2.5 (panel B), the UV-vis spectra of nitrosobenzene and nitrobenzene is illustrated. With only an oxygen atom distinguishing these species, each compound has a unique UV-vis spectral fingerprint that allows for measurement of each species. The peak at 17.5 min matches the retention time, UV/Vis pattern, and LCMS/MS of the nitrobenzene standard. Spike recovery experiments provided confirmation that the newly formed peak is nitrobenzene. The second peak that forms at 19.3 min matches the retention time, UV/Vis spectra, and LCMS/MS of nitrosobenzene which can be attributed to the decay of **NPH** in aqueous solvent.

Discussion

Significant efforts have been made for rational design of protein inspired models for biomimetic studies. For arylamine *N*-oxygenase chemistry, the goal of artificially creating the 3-His-4-carboxylate moiety was explored with the *t*RNA-modifying monooxygenase MiaE.

In the wild-type MiaE enzyme, site-directed mutagenesis of Leu199 was done to induce a structural change to the first-coordination sphere of the binuclear iron site. The mutation placed the newly inserted histidine residue in the vicinity of the Fe-site and theoretically coordinate thus "tuning" the diiron core toward arylamine oxidation. While sequence analysis showed the newly inserted residue was successful, the L199H variant showed decreased incorporation of Fe into the active site. The decreased Fe-content is predictable as mutations especially when so close to the active-site can cause problems with metal incorporation.

The design and purification of the L199H variant was successful in transforming MiaE into a functional arylamine *N*-oxygenase. The production of **NO_2-Ar** with oxidation of aniline by L199H, there is significant evidence that the first-coordination sphere of the binuclear site heavily influences the extent of oxidation and "tuning" the Fe-site. While mutagenesis in enzymes have been found in the past to create unusual reactivity toward non-native substrates, the affinity for chemical reactivity toward aniline is profound and highly unusual for the simple monooxygenase MiaE. The net 6-electron process is a significant increase in oxidation capacity and highlights the unique capabilities of the first-coordination

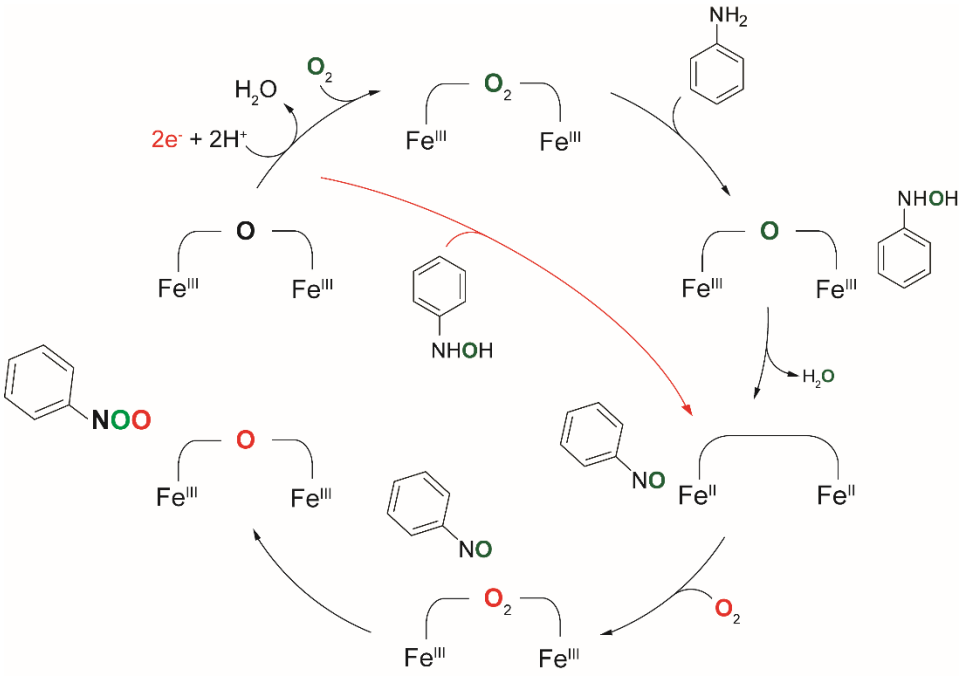

Scheme 2.2 Proposed biochemical synthesis of nitrobenzene with L199H variant.

sphere and its interaction with the diiron site to drive chemical reactivity and effectively diversify the diiron family of enzymes.

As seen in Scheme 2.2, the reactive pathway for biosynthesis of nitrobenzene begins with the resting diferric enzyme. In single-turnover experiments, ***asc*** was used in lieu of the electron delivery machinery to prime the diiron core. The diferrous cluster can now bind molecular oxygen and synthesize the catalytically relevant oxidative species, **P**. The transient peroxo-intermediate has been characterized in many other diiron oxygenases and has been confirmed to be the oxidative component for oxygen incorporation into the product. In the MiaE arylamine *N*-oxygenase pathway, **P** interacts with aniline to form the proposed hydroxylamine intermediate. Here the hydroxylamine intermediate acts the 2-electron source to regenerate **P** to continue the oxidation of the arylamine. The oxidation of the arylhydroxylamine leads to the formation of the nitrosobenzene intermediate where this species becomes the new target for oxygen incorporation. The conversion of the nitrosobenzene substrate to nitrobenzene is the final step in the production of nitrobenzene.

X-band EPR analysis of the wild-type and variant in the mixed-valent oxidation state shows comparable values to what is seen in other non-heme, diiron enzymes.[72,82,81] The mixed-valent signal has been shown to provide evidence for the nature of the bridged ligand for diiron enzymes. Davydov and Que found through comparisons of various diiron protein and model complexes that the bridged ligand perturbs the observed *g*-values of the mixed-valent response.[82] The data would suggest that the wild-type and variant contain a hydroxo-bridged ligand. The ^{57}Fe Mössbauer experiments on the *wild-type* enzyme have suggested minor contributions from a hydroxyl-bridged ligand. These studies in conjunction with the complementary X-band EPR spectroscopy provide further evidence for the incorporation of the hydroxyl-ligand but also provides the evidence for the potential loss of the LMCT bands in the MiaE variant. The electron transfer across the Fe-OH-Fe bridge is weaker than what is

perceived for the μ-oxo bridge found in the *wild-type* and would show a structural proclivity for the incorporation of the hydroxyl-bridged ligand.

In totality, these nzymatic assays with L199H and the *"hydroxylamine shunt"* provides evidence and validity for the framework of the MiaE L199H variant for arylamine oxygenase chemistry. While investigative studies have been unable to identify the peroxo-intermediate formed during O_2-binding, the prospect of the development of a fully-functional enzyme model for diiron oxygenases has provided the avenue for investigations into potential new systems and isolated of key mechanistic steps. Additionally, studies into the potential enhancement of chemical turnover with the MiaE L199H variant with the addition of electron-transfer proteins (ferrodoxin) may provide an avenue for better understanding of the role of the ETC component for the diiron enzymes and how these components connect and communicate between each other. Although chemical reprogramming is not uncommon, it is fascinating that such a dramatic change is observable by a single substitution. This newly discovered feature offers a new avenue to explore and further elucidate information about the catalytic and mechanistic processes that occur during arylamine oxidation.

Chapter 3 The steady-state kinetics and spectroscopic features of the mammalian thiol dioxygenase, cysteamine dioxygenase

Introduction

Cysteine dioxygenase is a non-heme, mononuclear iron enzyme that is involved in the O_2-dependent oxidation of L-cysteine (***cys***) to produce cysteinesulfinic acid (***csa***).[89-91] Cysteine dioxygenase (CDO, EC 1.11.13.20) and cysteamine [2-aminoethanethiol] dioxygenase (ADO, EC 1.13.11.19) are the only known mammalian thiol dioxygenases. While CDO has been extensively studied by spectroscopic, kinetic, and X-ray crystallographic methods, limited reports are available for ADO.[48, 92, 93] The TDOs catalyzes the first irreversible step in sulfur-containing amino acid derivatives and is a critical component of the sulfur biochemical cycle. Various medical studies and investigations have suggested correlations between the development of neurodegenerative diseases and sulfur imbalances.[94-97] Disruption in the ***cys*** metabolic cycle has been linked to Parkinson's, Alzheimer's, and other degenerative ailments suggesting a potential correlation between dysregulation in cysteine metabolism and these neurological diseases.[98, 99] The crystal structure for the substrate-bound *Rattus nervegicus* CDO shows the bidentate coordination of L-cysteine (***cys***) to the mononuclear Fe-site through the thiolate and neutral amine.[33] While the bacterial thiol dioxygenase, 3-mercaptopropionic acid (***3mpa***) dioxygenase, remains unsolved, investigations through spectroscopic and kinetic methods have suggested a monodentate coordination for substrate binding in *Av* MDO through the thiolate.[100] The outer-sphere coordination of the MDO and CDO enzymes have shown a conserved "catalytic triad" (Ser-His-Tyr) that is key for catalysis. However, ADO is the only known thiol dioxygenases that does not contain this triad moiety. Therefore, it remains unclear if a common mechanistic paradigm exists between these enzymes despite the same type of O_2-depedent oxidation of thiols.

The non-heme mononuclear iron enzymes have been studied extensively and X-ray crystal structures have shown the 2-His-1-carboxylate active-site configuration as the dominating moiety for metal coordination in this class of enzymes. However, a largely uncharacterized subset of this enzyme family has been found to adopt a 3-His facial triad that is able to successfully incorporate a mononuclear metal ion into the active-site and carry out O_2-depedent oxygenase chemistry.

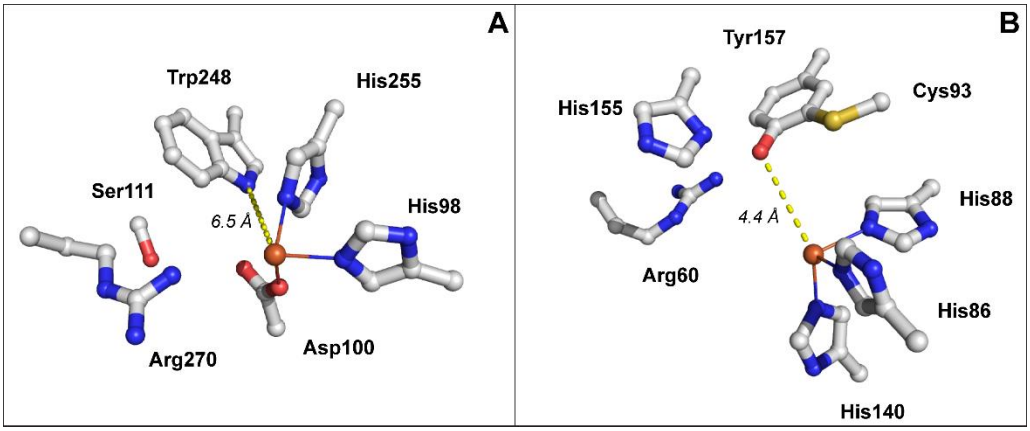

Figure 3.1 X-ray crystal structures of CDO and TauD. A) Active site of the Fe(II)/α-ketoglutarate-dependent enzyme TauD from Myobacterium marinum (PDB: 3SWT)[22]. B) Active site of CDO enzyme from Rattus norvegius (PDB: 4IEV)[28].

As shown in Figure 3.1 (panel A), the active-site for the α-ketoglutarate-dependent enzyme TauD houses a mononuclear iron atom that is coordinated by 2 protein-derived histidine residues and an aspartate ligand . In contrast, the active site of the *Rattus norvegicus* CDO is composed of a mononuclear iron bound to three nearby residues: H86, H88, and H140. The bond distances for the two coordinated N_{ε}- and O-atoms are within 2.3 Å and the bond angles for the Fe-O-N_{ε} are ~ 45°. The CDO active site with the three bound N_{ε} atoms, share comparable bond distances and angles. The comparable geometries highlights the unique nature of the divergent active-site moiety and the influence of the first- and second-coordination sphere on non-heme mononuclear oxygenase chemistry.[25] To date, only a select few of the 3-His active site moiety has been crystallographically characterized (CDO, diketone dioxygenases (Dke1)[31], and gentisate 1,2-dioxygeanse (GDO)[30]). A unique feature of the mammalian CDO enzyme is the post-translation modification located 3.3 Å from the Fe-

site in which Cys93 and Tyr157 are covalently linked, producing a crosslinked Cys93-Tyr157 pair. Sequence homology has shown the Tyr157 to be a conserved amino-acid across phylogenic domains, however the C93-Y157 crosslink has been found only in eurkaryotes.[101] The role of the post-translation modification has been investigated and suggested to play a role in catalytic efficiency and substrate orientation.

The extensive enzymatic studies into CDO has left its counterpart, cysteamine dioxygenase (ADO), largely uncharacterized. Since its discovery in the 1960s, the enzyme has relatively been minorly investigated and remains an elusive biochemical pathway.[93] 2-aminoethanethiol (cysteamine [***ca***]) is the by-product of the degradation of coenzyme A and the decarboxylated product of L-cysteine as seen in Scheme 3.1 The mammalian thiol dioxygenase cellular biochemical route. Left side) The CDO-catalyzed pathway of L-cysteine to cysteinesulfinic acid. Right side) The ADO-catalyzed pathway of cysteamine to hypotaurine.. [49, 50]

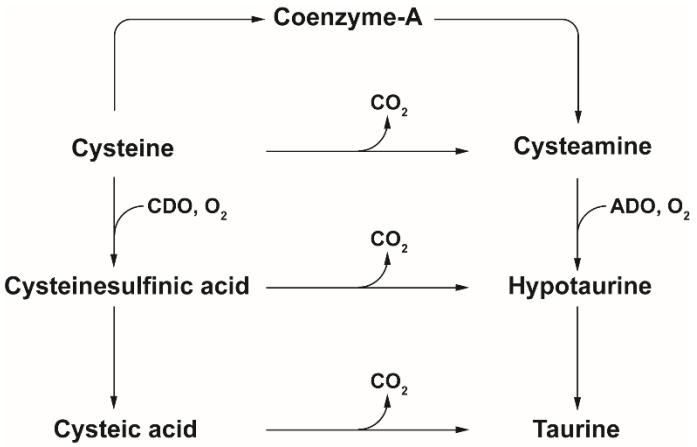

Scheme 3.1 The mammalian thiol dioxygenase cellular biochemical route. Left side) The CDO-catalyzed pathway of L-cysteine to cysteinesulfinic acid. Right side) The ADO-catalyzed pathway of cysteamine to hypotaurine.

Cysteamine is the precursor for hypotaurine (***ht***) and in turn the starter for taurine biosynthesis.[48, 93] The biochemical production of hypotaurine and taurine are necessary pathways for brain, heart and cellular homeostasis. Medical studies have also highlighted the role of cysteamine is treatment of cystinosis, an uncontrolled accumulation of cystine in the cell.[49, 52, 53] Genomic analysis of the protein sequences of ADO and several other CDOs have shown low sequence (~15%), however ADO has the conserved cupin regions for metal incorporation and capacity for thiol oxidation. It is reasonable to hypothesize that these two proteins share some mechanistic features. Additionally, several clinical studies have shown a correlation to mitigated effects of Huntington's disease and cysteamine, therefore pressing the need to investigate the mechanistic pathway of this enzyme.[51, 52] The growing interest in the effects of cysteamine and hypotaurine synthesis shows the pressing need to explore and elucidate more information related to the mechanistic and kinetic parameters of this enzyme.

Presented here is the steady-state and spectroscopic characterization of the thiol dioxygenase, ADO, isolated from *Mus musculus*. The steady-state kinetics of ADO were evaluated with several thiol containing substrates to investigate affinity to non-native substrates as this phenomenon has been seen in other TDOs. Complementary ^{1}H NMR spectroscopy was carried out to compare kinetic rates between oxygen electrode and NMR measurement of product accumulation. Additionally, complementary X-Band EPR experiments utilizing nitric oxide (NO) as a surrogate for O_2-binding was also explored to investigate the effects of substrate binding to the local environment surround the Fe-site.

Materials and Methods

Cloning. For *in vivo* ADO activity assays, the *m*RNA construct was cloned into the commercially available pF1K flexi-vector (Promega). PCR primers: S*gf I*-forward; 5' –(AAA AGC GAT CGC CAT GCC CCG CGA CAA CAT GGC CT)-3'; *PME I*-reverse; 5'-(AAA AAG TTT AAA CTC AAG GTA GGA CCT TGG GGC CTG GAT)-3'. Forward and reverse restriction sites are underlined for clarity. Sequence verification was

verified by Sequetech (Mountain View, CA). Expression of soluble protein (28 kDa) was confirmed by SDS-PAGE.

Media and Growth conditions. The pADOF1K vector was transformed using the chemically competent BL21(DE3) *E. coli* cell line through heat-shock and was grown overnight on a lysogeny broth (LB) agar plate in the presence of 25 μg/mL Kanamycin antibiotic at 37°C. The next day, an isolated colony was used for growth in sterile liquid LB with antibiotic for cellular training prior to the inoculation of a 10L bioreactor at 37°C. The cell growth cycle was monitored via optical density at 600 nm (OD_{600}) using a table-top UV-visible spectrophotometer. At OD_{600} ~ 4.0, the induction cycle was initiated by the addition of 20g of casamino acids, 1 mM ferrous ammonium sulfate, and 0.5 mM IPTG. Additionally, the temperature for the bioreactor was lowered to 25°C. After 4 h of induction, the cells were harvested and pelleted by centrifugation at 17,700 x g for 8 min. The paste was collected and stored in an -80°C freezer. Verification of ADO expression was carried out by SDS-PAGE of lysed cells before and after induction.

Protein Purification of ADO enzyme. Approximately 20 g of cell paste was suspended in 100 mL of lysis buffer (20 mM HEPES, 50 mM NaCl, pH 8.0) and thawed in an ice-bath with 10 µg/ml each of deoxyribonuclease I, ribonuclease, and lysozyme with gentle stirring for 45 min. The cell suspension was sonicated on a 30 s off/on pulse cycle for a total of 30 min. The cell free extract was centrifuged (JA-20 rotor) at 40,000 x g for 60 min at 4°C. The supernatant was decanted and loaded onto a fast-flow DEAE column that was pre-equilibrated with lysis buffer. The protein was eluted on a linear NaCl gradient (25 mM to 350 mM NaCl in 20 mM HEPES, pH 8.0). Fractions containing the ADO enzyme were verified via SDS-PAGE and concentrated via an Amicon N_2 stir cell equipped with YM 10 ultrafiltration membrane.

ADO Activity Assay via TLC. After column purification, fractions containing the ADO protein were selected based on activity with substrate by thin-layer chromatography (TLC). A 100 μL sample was removed from the desired fraction and placed into a preset 37°C incubator. A buffered solution

cysteamine (2-aminoethanethiol) was added to the protein sample for a final concentration of 5 mM. At selected time points, a 2 μL was removed and spotted onto a silica gel 60 F254 TLC plate (EMD Millipore). In addition, 5 mM cysteamine and hypotaurine standards were spotted on the TLC plate. The TLC plate was allowed to dry in air before elution for 20 min in a mobile phase of 25:20:55 (v/v) H_2O, glacial acetic acid, and *n*-butanol respectively. After elution, the TLC plate was removed from the mobile phase and dried by a heat gun. The TLC plate was stained using a ninhydrin solution (200 mL of ethanol, 6 mL of glacial acetic acid, and 3 g of ninhydrin) and dried using the heat gun.

Iron Quantitation. The total iron content in the protein was analyzed by using UV-visible spectrophotometer according to previous methods (insert citation CDO 2007). In a typical preparation, a 500 μL enzyme sample was denatured with 250 μL each of 2 N hydrochloric acid and trichloroacetic acid (20% w/v) and centrifuged at 14,000 rpm for 10 min. The iron released was reduced with 100 μL of hydroxylamine (10% w/v). In addition, 200 μL of 4 mM 2,4,6-tripyridyl-*S*-triazine (TPTZ) and 100 μL of ammonium acetate (50% w/v) was added. The intense blue color produced via the TPTZ reaction (ε_{596} = 22,600 M^{-1} cm^{-1}) was used to quantify the amount of ferrous iron within the sample.

Oxygen Electrode. The O_2 concentration was determined using a standard Clark electrode (Hansatech Instruments, Norfolk, England) within a jacketed 2.5 mL cell at 22 ± 2 °C. The electrode was bathed in a saturated solution of KCl (50% w/v) and separated from the buffer in the cell using a gas-permeable membrane. The Clark electrode was calibrated by measurement of the response factor by the addition of sodium dithionite to aerobic buffer. For enzymatic reactions, the addition of 1 mL of reaction buffer (25 mM Good's buffer and 50 mM NaCl) containing either ***ca*** or ***cys*** (0.1 – 5 mM) to the cell under continuous mixing in an aerobic environment. Each reaction was initiated by the addition of ADO to a final concentration of 1 μL.

Nitric oxide inhibitory studies. The measurement of inhibitory effects on the *Mm* ADO-catalyzed reactions with ***ca*** were carried out on a standard Clark electrode. In a typical reaction, a

buffered solution of ***ca*** was added to a final concentration of 5 mM to the stir cell. As a control, the measurement of k_{cat} was determined prior to the addition of nitric oxide to the cell. Nitric oxide (NO) was titrated (0.001 – 0.2 mM) into the buffered substrate solution prior to the addition of enzyme. The rate of O_2 consumption was measured and fit to an exponential decay equation by SigmaPlot version 11.0 (Systat Software Inc. Chicago, IL).

Data Analysis. The steady-state kinetics parameters for *Mm* ADO were solved by fitting the kinetic data to the Michaelis-Menten equation using SigmaPlot version 11.0 (Systat Software Inc., Chicago, IL). This analysis calculated both k_{cat} and K_M as well as the error associated with each value by nonlinear regression. In reactions where the pH dependent kinetic parameters are "bell-shaped" in that the activity of the enzyme is decreased at low and high pH values, the data was fit to Equation 3.1.[102-104]

$$\log Y = \log\left[\frac{C}{\left(1+\frac{[H]}{K_1}\right)\left(1+\frac{K_2}{[H]}\right)}\right] \quad (\mathbf{3.1})$$

where Y is defined as either k_{cat} or k_{cat}/K_M. The terms [H], K_1, and K_2 represent the hydrogen ion concentration and the two observable dissociation constants related to the steady-state curve. The overall mathematical expression is scaled by the constant (C) that is defined as the maximal k_{cat} or k_{cat}/K_M. In an alternative fashion, the steady-state pH-dependent curves that decreased only at low or high pH, the data set was fit to Equation 3.2.[101-103] Much like eq 1, this expression is scaled by a constant scalar quantity (C) that represents the maximal kinetic rate (k_{cat} or $k_{cat}/K_{M)}$. The error associated with each kinetic value (k_{cat}, k_{cat}/K_M, pKa$_1$, and pKa$_2$) extrapolated from these fits can be seen in Table 1.

$$\log Y = \log\left(\frac{C}{1+\frac{[H]}{K_1}}\right) \quad (\mathbf{3.2})$$

^{1}H NMR Studies. NMR kinetic studies were executed on a 500 JEOL nuclear magnetic resonance spectrometer (Pleasanton, CA). All NMR measurements were made in Wilmad NMR tubes (standard wall, 5 mm O.D., precision 507-PP-7). For each reaction, the *Mm* ADO protein (2-10 μM) was added to a buffered substrate solution in D_2O (sodium phosphate 25 mM, 50 NaCl, pD 8.0) to initiate catalysis at ambient temperature (21 ± 2 °C). Sample aliquots were removed and terminated by heat shock at 95 °C for 2 min followed by spin-filtration to remove the denatured protein. As an internal standard, trimethylsilyl propanoic acid (TMSP) was added to a final concentration of 0.1 mM. NMR spectral data was integrated using JEOL USA Delta NMR data processing software (v. 5.1.3). For corrected values of pD, 0.4 pD units were added to value of the observed pH via the pH electrode (Mettler Toldeo InLab Expert Pro)[105]

Spectroscopy. All UV-visible measurements were conducted on an Agilent 8453 photodiode array spectrophotometer (Santa Clara, CA) using ES Quartz cuvettes. X-Band (9 GHz) EPR spectra were recorded on a Bruker EMX Plus spectrometer equipped with a bimodial resonator (Bruker model 4116DM). Cryogenic temperature measurements were taken using an Oxford ESR900 cryostat and an Oxford ITC 503 temperature controller. A modulation frequency of 100 KHz was used for all spectra. All experimental data used for spin quantifications were collected under non-saturating conditions.

The analysis of the EPR spectra utilized the general spin Hamiltonian

$$\mathcal{H} = \mathbf{D}\left[\hat{\mathrm{S}}_{\boldsymbol{Z}}^{\mathbf{2}} - \frac{S(S+1)}{3}\right] + \mathbf{E}\left(\hat{\mathrm{S}}_{\boldsymbol{X}}^{\mathbf{2}} + \hat{\mathrm{S}}_{\boldsymbol{Y}}^{\mathbf{2}}\right) + \beta \boldsymbol{B} \cdot \mathbf{g} \cdot \mathbf{S} \qquad (\mathbf{3.3})$$

where ***D*** and ***E*** are the axial and rhombic zero-field splitting (zfs) parameters, respectively, and **g** is the g-tensor (oxford citation). EPR spectra were simulated and quantified using SpinCount (v. 6.3.7115.22108),

written by M. P. Hendrich at Carnegie Mellon University (Pittsburgh, PA). The simulations were generated with consideration for all intensity factors, both theoretical and experimental, to determine species concentrations. In addition to quantitation, the instrumental factor was determined for the microwave detection system. This was carried out by a known spin standard, Cu(EDTA), that was prepared by a copper atomic absorption standard solution purchased through Sigma-Aldrich.

Nitric Oxide Sample Additions. For the preparation of FeNO EPR samples, initial *Mm* ADO was assayed for iron content at ~300 μM Fe(II). EPR samples were prepared by varying the concentrations of each substrate (***ca*** and ***cys***) to ferrous iron from 0.5-10 molar equivalents. Prior to the addition of NO, substrate was added to anaerobically reduced *Mm* ADO and allowed to equilibrate in a glovebox for 15 min prior to being frozen in liquid N_2.

For NO additions, stock solutions of NO were prepared with by dissolving 5 mg of PROLI-NONOate (Cayman Chemical, 178948-42-0) in a 1.0 mL solution of anaerobic 10 mM sodium hydroxide. Aliquots of degassed stock PROLI-NONOate (20-50 µL) were diluted 1:1 with deoxygenated buffer and allowed to react for 5 min. At pH 7.4, 2 mols of NO are released with each mol of NONOate at a half-life of 6 s at ambient temperature.[106, 107] Samples of (substrate/NO)-bound enzyme were prepared anaerobically by the addition of 10 mol equivalents of 22 mM stock NONOate solution to enzyme pre-incubated with 10 mol equivalents of substrate. Samples were allowed to equilibrate on ice for 10 min prior to freezing in liquid N_2. Following the addition of NO and substrate to the ferrous *Mm* ADO solution, the final concentration of protein in the EPR samples is 285 μM.

Results

Purification of *Mm* ADO. The mammalian enzyme from *M*. *musculus* (*Mm* ADO) was purified and analyzed for iron content per the details in the materials and methods section above. The IPTG-inducible protein exhibits an observed band of ~28 kDA. The SDS-PAGE band is in good agreement with

the calculated mass of the ADO protein (28,241 Da). The fractions containing the *Mm* ADO protein were pooled based on the activity of cysteamine turnover via thin-layer chromatography (TLC) and SDS-PAGE. Much like the mammalian cysteine dioxygenase (*Mm* CDO), the *Mm* ADO protein exhibits the double-band feature that is suggested to result from the pre- and post-translational Cys-Tyr crosslink. The Cys-Tyr covalent crosslink has been investigated by Liu *et. al*. and most likely resides between Cys220-Tyr222 located on the backside of the Fe-site.[50]

The TDOs are Fe-dependent enzymes with the cupin genomic motifs for metal incorporation. The iron stoichiometry within the ADO protein were determined through TPTZ, Bradford, and UV-Visible spectroscopic assays as described in previous studies. Measurement of iron occupancy in ADO shows sub-stochiometric Fe-incorporation (~60%) that highlights the lack of full incorporation of metal ions into the active site. This behavior is seen in the *Mm* CDO form as well. However, purified ADO shows nearly all (~90%) iron present in solution was in the ferrous state and was not prone to auto-oxidation during the protein purification process.

Steady-state Kinetics of *Mm* ADO-catalyzed reactions. Previous studies into the reactivity have confirmed that cysteamine (***ca***) is the native substrate of the *Mm* ADO protein.[48] However, it has been observed in other TDOs the promiscuity toward other thiol-containing substrates.[79, 101] With L-cysteine as a readily-available thiol source in the cell and the recently discovered 3-mercaptopropion acid dioxygenase, the potential promiscuity of ADO toward ***cys*** and 3-mercaptopropionic acid (***3mpa***).[79, 108, 109]

For all steady-state kinetic assays, the apparent initial rate was normalized as a function of the concentration of Fe(II) in the purified *Mm* ADO (v_0/[E]). The kinetic parameters were analyzed for substrates that exhibited O_2-consumption in the presence of ADO. In the dioxygenase reactions, molecular oxygen serves as a co-substrate, in addition to product formation, the rate of O_2 consumption was measured using a calibrated Clark-type electrode O_2 electrode. The methodology for these

experiments is described in the materials and methods section previously stated and in previous studies.[100, 110] For each substrate, k_{cat}, K_M, and the errors associated with each value were determined by fitting the data to a standard Michaelis-Menten equation at 22 ± 2 °C and pH 8.0.

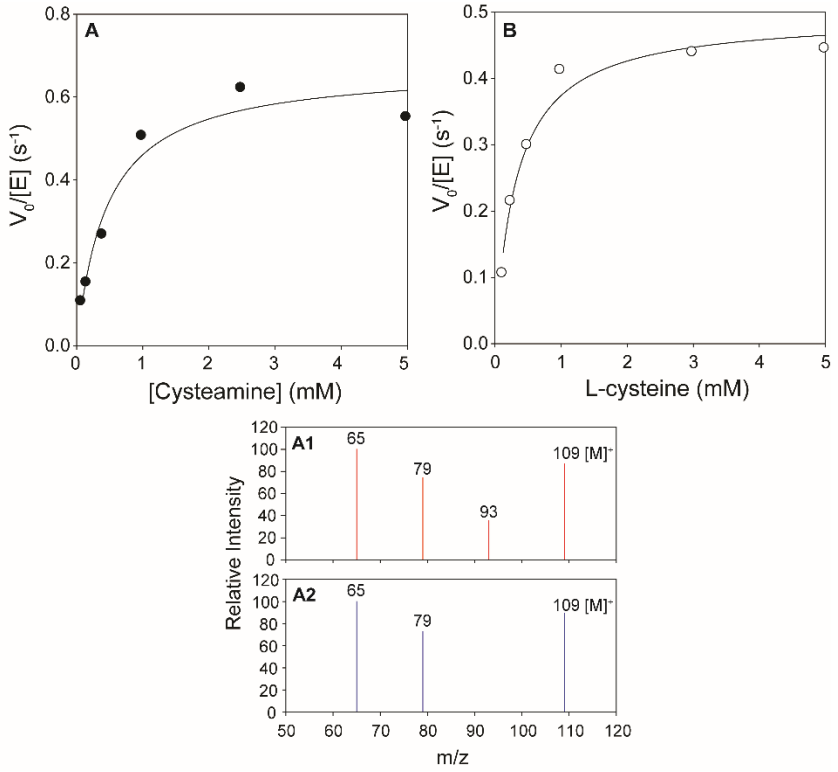

Figure 3.2 Steady-state kinetics of Mm ADO-catalyzed ca (A, black circle) and cys (B, white circle) consumption. In both panels, the maximal velocities (kcat) for O2-consumption (circles) were determined by the best fit to the standard Michaelis-Menten equation. Assay conditions: 22 °C and pH 8.0. LC-MS/MS of ht (A) MRM response for standards (1, top) compared to direct injection of enzymatic reactions (2, bottom).

In Figure 3.2 (panel A), the steady-state curve for O_2-consumption is shown with ***ca*** as the substrate. Maximal k_{cat} behavior was observed in excess of 5 mM substrate. The observed k_{cat} (0.69 ± 0.06 s^{-1}) and K_M (0.5 ± 0.1 mM) were determined by the initial rate of O_2-consumption (●). From these values, the catalytic efficiency for ADO with ***ca*** is 1400 ± 400 M^{-1} s^{-1}.

In the reactions that utilized ***cys*** as a substrate (Figure 3.2 [panel B]), k_{cat} and K_M values were obtained from the initial rate of O_2 consumption (○) and determined to be 0.63 ± 0.07 s^{-1} and 1.1 ± 0.2 mM, respectively. From these results, the catalytic efficiency is 1530 ± 400 M^{-1} s^{-1}. Enzymatic assays that used ***3mpa*** as the substrate, detectable O_2-consumption was not observed and was determined to not affinity towards.

The detection of the enzymatic product of this reaction was followed-up by LC-MS/MS utilizing multiple reaction monitoring (MRM) as described in materials and methods. In these assays, the parent ion $[M + H]^+$ for each thiol-product (***ht***, *m/z* 109; ***csa***, *m/z* 154) were selected for secondary fragmentation. The optimized MRM methodology was used to verify the sulfinic acid products formed during turnover via direct injection. The data for the enzymatic products were compared to primary standards of the products for identification. For the ***ht*** detection, the parent ion peak of *m/z* 109 was detected as well as three other ion peaks *m/z* 93, 79, and 65 were detected. The fragmentation patterns and relative intensities detected in the enzymatic assays (Figure 3.2 [panel A1]) virtually match those observed in the ***ht*** standard (Figure 3.2 [panel A2]).

LC-MS/MS experiments with direct injections from enzymatic reactions that utilized ***cys***, did not show comparable fragmentation patters for ***csa*** formation. The observed O_2-consumption behavior with ***cys*** suggests oxidation has taken place but is not related to ***csa*** catalysis.

pH Effects on enzymatic activity. Mechanistic details involving the ionizable groups necessary for catalysis can be determined from the pH-dependent kinetics of k_{cat} and k_{cat}/K_M. For *Mm* ADO, the influence of pH effects was measured for ***ca*** and ***cys*** over a broad pH range (5-10). Figure 3.3 illustrates the (A) log(k_{cat})-pH and (B) log(k_{cat}/K_M)-pH dependent profiles obtained from the initial rate data for *Mm* ADO reactivity utilizing ***ca*** as the substrate. Each point within the data sets (Figure 3.3 [panels B and D]) were obtained by fitting the steadt-state kinetic data to the standard Michaelis-Menten equation. Error associated with these results are included graphically in the fits.

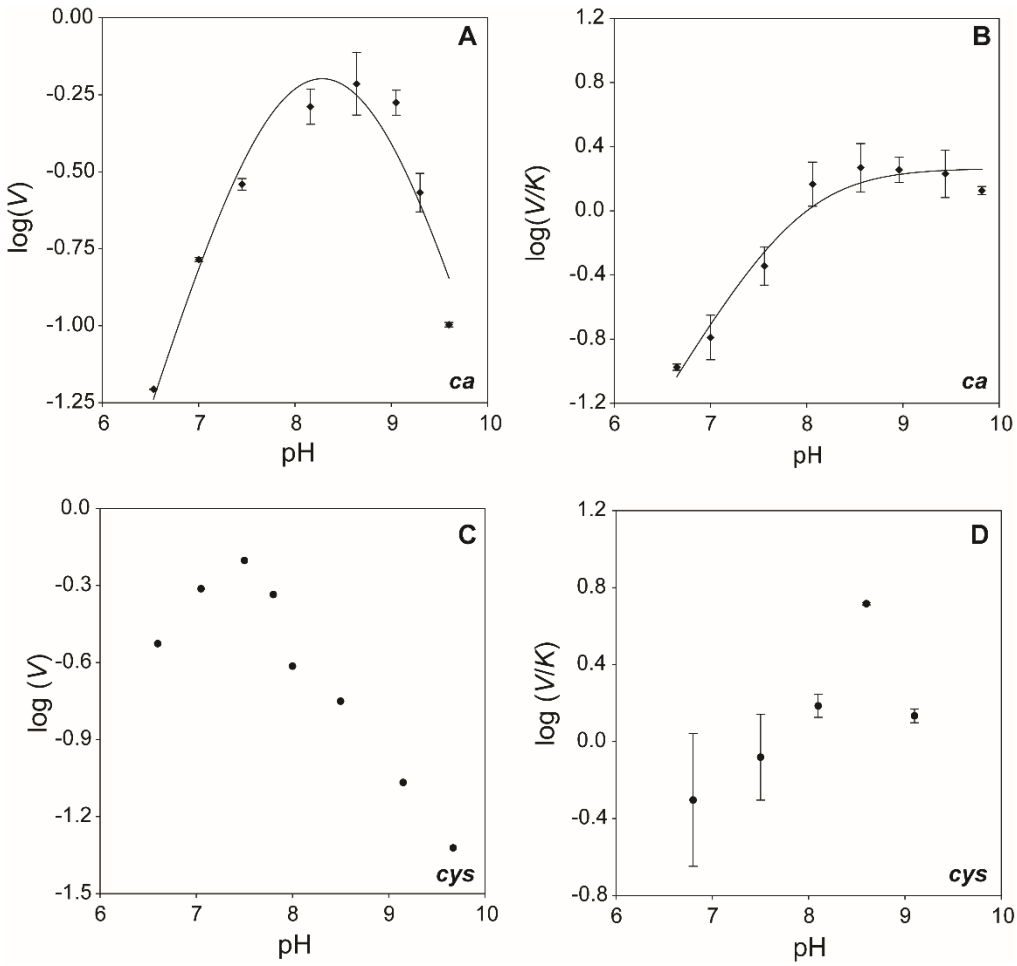

Figure 3.3 pH dependence of kcat and kcat/KM for the ADO-catalyzed reactions with ca (A and B) and cys (C and D) at 22°C. Error within steady-state results were obtained by fitting the kinetics at each pH point to a standard Michaelis-Menten equation. The pKa values were determined by best fit of each kcat- and kcat/KM¬-pH dependent profiles to eqs 1 and 2. The summary of the steady-state parameters for Mm ADO, Av MDO, and Mm CDO can be seen in

Enzymatic assays using ***ca***, the k_{cat}-pH profile exhibits a "bell-shaped" curve with two observable p*K*a values. In the acidic limit (pH 5-8), both the k_{cat} and k_{cat}/K_M data sets increase to an observable maximum at ~pH 8.2. However, beyond the acidic limit (pH 8-10) the observable activity in the k_{cat} pH-profile decreases while in k_{cat}/K_M the activity is unaffected. The log(k_{cat}) kinetic curve can be fit to Equation 3.1, and the apparent pK_a values can be extrapolated. Two observable pK_a values were calculated (7.78 ± 0.3 and 8.78 ± 0.3) for the k_{cat}-pH dependent profiles in the ***ca*** reactions. The maximal k_{cat} value obtained from the fit was 0.61 ± 0.1 s^{-1} at pH 8.64. For the log(k_{cat}/K_M), the kinetic data was fit to Equation 3.2

that accounts for plateaued activity in the basic regime of the kinetic fit. One observable pK_a value was obtained from the k_{cat}/K_M-pH kinetic fit (7.93 ± 0.1) with reactions that used ***ca***. Here, the maximal k_{cat}/K_M (1400 ± 420 M^{-1} s^{-1}) was observed in this plot. The maximal value obtained (1856 ± 673) was observed at pH 8.56.

Table 3.1 Comparison of steady-state kinetic parameters for thiol dioxygenases Mm ADO, Mm CDO, and Av MDO

Enzyme	kinetic parameter	***cys***	***3mpa***	***ca***
Mm ADO (22°C)	k_{cat} (s^{-1})	0.63 ± 0.07	-	0.7 ± 0.06
	K_M (mM)	1.1 ± 0.2	-	0.5 ± 0.1
	k_{cat}/K_M (M^{-1} s^{-1})	572	-	1400
	log(k_{cat})			
	pK_a1	-	-	7.78 ± 0.3
	pK_a2	-	-	8.78 ± 0.3
	log(k_{cat}/K_M)			
	pK_a1	-	-	7.93 ± 0.1
	pK_a2	-	-	not observed
Mm CDO (20°C)	k_{cat} (s^{-1})	0.6 ± 0.1	-	not observed
	K_M (mM)	2.3 ± 0.3	-	not observed
	k_{cat}/K_M (M^{-1} s^{-1})	260 ± 30	-	<0.01
	log(k_{cat})			
	pK_a1	7.42 ± 0.1	-	-
	pK_a2	10.30 ± 0.08	-	-
	log(k_{cat}/K_M)			
	pK_a1	8.0 ± 0.2	-	-
	pK_a2	not observed	-	-
Av MDO (25°C)	k_{cat} (s^{-1})	1.2 ± 0.1	1.0 ± 0.1	0.29 ± 0.08
	K_M (mM)	11.4 ± 0.9	0.013 ± 0.005	26 ± 5
	k_{cat}/K_M (M^{-1} s^{-1})	110 ± 20	72000 ± 9000	11 ± 2
	log(k_{cat})			
	pK_a1	5.6 ± 0.1	6.9 ± 0.1	0.29 ± 0.12
	pK_a2	9.9 ± 0.1	9.5 ± 0.1	0.29 ± 0.13
	log(k_{cat}/K_M)			
	pK_a1	5.1 ± 0.1	7.6 ± 0.2	0.29 ± 0.15
	pK_a2	9.7 ± 0.1	8.2 ± 0.2	0.29 ± 0.16

The pH-dependent profiles were determined for *Mm* ADO with ***cys*** as a substrate for comparison. Steady-state reactions with ***cys*** exhibited a comparable maximal k_{cat} values for the k_{cat}-pH profile (0.63 ± 0.22 s^{-1}) at pH 7.5. The skewed shape of the kinetic plot did not satisfy the conditions for fits to Equation 3.1. In the log(k_{cat}/K_M) kinetic plot, the irregular shape was not able to fit to either Equations 3.1 or 3.2. However, the observed maximal k_{cat}/K_M (1500 ± 400) observed at pH 8.1. A summary of all pH-dependent kinetic results is provided in Table 3.1.

NMR studies on *Mm* ADO reactivity. The measurement of sulfinic acid catalysis in previous studies utilized a combination of analytical techniques including HPLC, O_2-electrode, and LC-MS.[110, 111] However, the use of NMR spectroscopy allows for a greater range in monitoring the catalysis of sulfinic acid products in thiol dioxygenases.[101] NMR samples conditions bypass the optimization of mobile phases and assay conditions for individual substrates under HPLC conditions. The NMR spectra for cysteamine and hypotaurine standards in a sodium phosphate buffer in D_2O can be seen in Figure 3.4 (panel A).

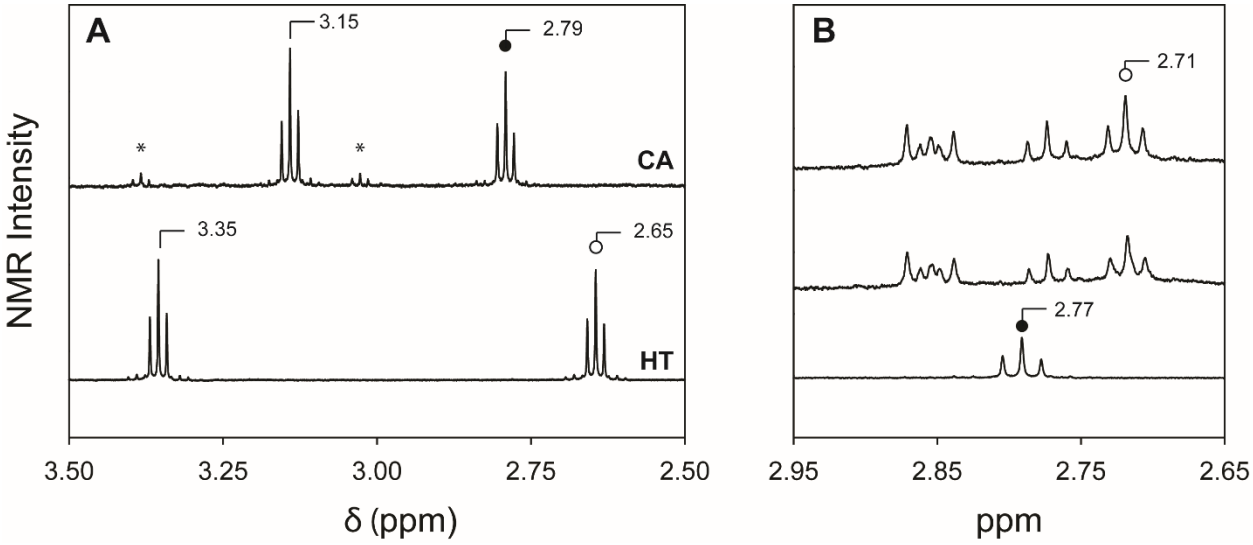

Figure 3.4 A) NMR spectrum of cysteamine and hypotaurine representing the α- and β-carbon protons. The time course formation and decay of ht and ca by integration of the β-carbon protons (CA, black circle; triplet centered at 2.79 ppm [2H, t, J1 = J2 = 6.7 Hz].; HT, white circle, triplet centered at 2.65 ppm [2H, triplet, J1 = J2 = 6.7 Hz]). NMR peaks labelled with (*) are trace levels of oxidized cysteamine originating from the disulfide bridge (cystamine); [δ = 3.03 ppm; 2H, t, J1 = J2 = 6.7 Hz] and [δ = 3.38 ppm; 2H, t, J1 = J2 = 6.7 Hz]. B) Representative NMR spectra that

In the spectral window (2.50 – 3.50 ppm), the peaks are related to the non-exchangeable α- and β- protons within the substrate and product standards. The resolved resonances allowed for monitoring of substrate loss and product formation during an enzymatic assay. In the NMR spectra of ***ca***, two sets of resonances are observed as triplets centered at 2.79 and 3.15 ppm. By comparison, the resonances in the product standard, ***ht***, has two sets of triplet resonances centered at 2.65 and 3.35 ppm. The end-product of ***ht*** exhibits greater shift in the chemical shift relative to substrate due to the nearby sulfinic acid moiety. Since the α-protons slightly overlap between the substrate and product, the β-protons for ***ca*** and ***ht*** (2.79 and 2.65, respectively) were used for measuring rate of product formation.

Each reaction was initiated by the addition of ADO (10 μM) to a buffered D_2O solution (25 mM sodium phosphate, 50 mM NaCl, pD 8.4) at 22°C containing 5 mM ***ca***. At select time points, samples were removed and quenched by heat shock, spin-filtered, analyzed by NMR spectroscopy. The internal standard trimethylsilyl propanoic acid (TMSP) was added for normalization of the signal intensity as

described previously in materials and methods. In Figure 3.4 (panel B), the time course measurement of the β-protons for ***ht*** formation. Quantitation of each species was carried out by integration of peak area relative to freshly prepared substrate and product standards of known concentrations.

Inhibition of ADO-catalyzed reactions by NO. Investigations into the effects of nitric oxide (NO) on the kinetics of cysteamine conversion were carried out on a standard Clark electrode as previously stated in the Materials and methods. The addition of NO to aerobic stirring of ADO and ***ca*** showed decreased k_{cat} values compared to *wild-type* ADO controlled reactions.

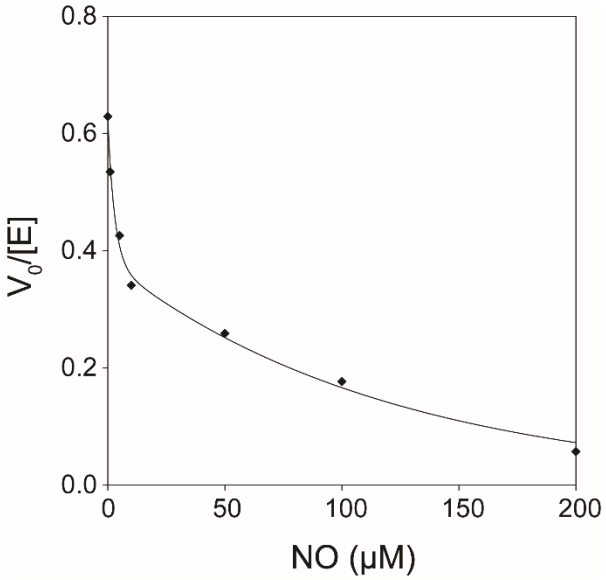

*Figure 3.5 Inhibitory effects by NO on the ADO-catalyzed reaction with **ca**. The k_{cat} values observed were fit to an exponential decay function.*

As seen in Figure 3.5, the decreased rate of O_2-consumption was plotted and fit to an exponential decay function. This kinetic behavior suggests an unusual interaction that occurs between the ADO protein and NO. In the absence of NO, the ADO-catalyzed reaction with ***ca*** exhibits comparable k_{cat} values (0.63 s^{-1}) to steady-state kinetic parameters mentioned previously. After 10 mol equivalent additions of NO, the observed kcat drops precipitously (0.63 to 0.34 s^{-1}). This downward trend continues with more additions of NO but to a lesser degree. The observable kcat at significant excess (200 mol

equiv) is 0.06 s^{-1}, a mere 10% of the uninhibited reaction. This observed kinetic hinderance by NO on ADO further highlights the unusual catalytic nature of ADO and perhaps a deviated mechanism than what is reported for *Mm* CDO.

EPR Spectroscopy of the Substrate-bound *Mm* ADO FeNO. The non-heme iron enzymes have been extensively studied in the last 20 years to lay out a general mechanism that describes the catalytic cycle involved in substrate oxidation.[15-17] In a typical reaction, the mononuclear iron site is housed within a 6-coordinate environment with multiple solvent-bound ligands. Under reduced conditions, the ferrous active site is generally unreactive towards molecular oxygen until the substrate and/or cofactor are bound.[15] In this process, the substrate "gates" the binding of O_2 during catalysis. In an effort to probe the binding of molecular oxygen to the iron-substrate complex, nitric oxide (NO) is often employed as a spectroscopic probe as it assumed that NO and O_2 behave in a similar fashion in the binding motif for the ES-O_2 complex. Since NO is presumably thought to bind to the substrate-bound complex, this allows for measurements of the binding affinity of substrates to the active site.

The addition of NO to the ES-complex of a mononuclear non-heme iron enzyme generally results in the formation of a $FeNO^7$ ($S = {}^3/_2$) species that is characterized by an axial EPR spectrum with *g*-values of 4, 4, and 2. The Feltham-Enemark notation describes the ground-state of the $S = {}^3/_2$ manifold as antiferromagnetically coupling between the high-spin Fe(III) ($S = {}^5/_2$) and the bound NO^- anion (S = 1). [112-114]

Samples of the as-isolated protein and substrate-bound of *Mm* ADO (*Mm* **ES**) were treated under anaerobic conditions with NO to verify if the *Mm* ADO shows the formation of the obligated-ordered addition of substrate (***ca***) prior to the addition of NO. In the absence of ***ca***, no $FeNO^7$ (S = 3/2) signals were observed by EPR upon excess addition of NO. This suggests the ferrous Fe-site is incapable of binding NO in the absence of substrate. As mentioned previously, this is typical behavior for the non-

heme mononuclear iron enzymes and is consistent with reports *Mm CDO* and the bacterial *Av* MDO.[79, 115] As seen in Figure 3.6, the ES-NO complexes formed by *Av MDO, Mm* CDO, and *Mm* ADO are illustrated. The addition of NO to the ES complex of MDO shows a new EPR signal that correlates to a high spin Fe(III) *S* = 3/2 complex. In contrast, the *Mm* CDO *and* ADO enzymes when pre-complexed with

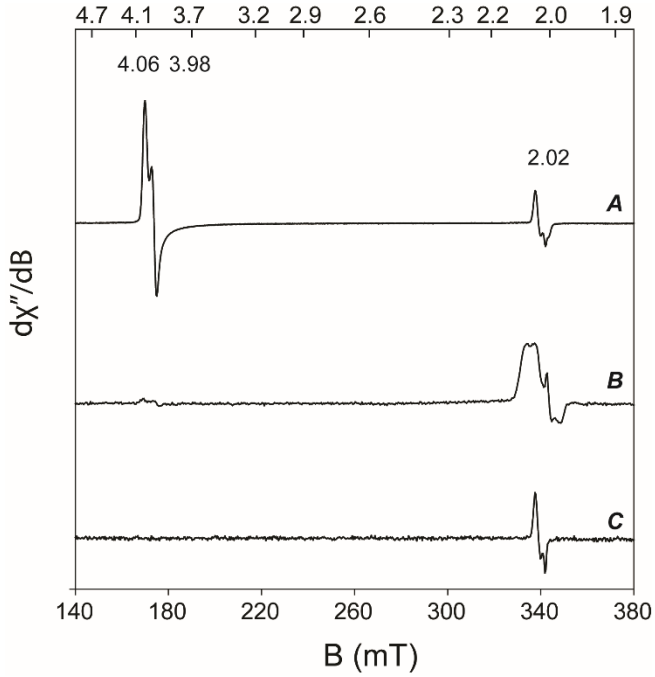

Figure 3.6 Comparative X-band EPR of Av MDO, Mm CDO, and Mm ADO of ES-NO complex. A) ES-NO complex of Av MDO with 3mpa. Observed g-values represents a S = 3/2 spin-state from the addition of NO. B) ES-NO complex of Mm CDO with L-cys. Observed g-values represent a S = 1/2 spin-state from the addition of NO. C) ES-NO complex of Mm ADO with ca. Observed g-values represent the S = 1/2 spin-state.

substrate and then exposed to NO produce a low spin Fe(III) *S* = 1/2 species. The EPR signal at *S* = 1/2 for the substrate-bound $(FeNO)^7$ species has observable *g*-values of 2.04, 2.02, and 2.00. This signal is only produced upon additions of NO to samples equilibrated with ***ca***.

Discussion

The cloning and purification of the ADO protein is in good agreement with what has been reported about for the molecular size of the ADO protein. The double-band feature that is commonly observed with *Mm* CDO purifications is also exhibited with ADO purification studies. This highlights the unusual post-translation modification that is observed between the nearby Cys-Tyr pair and may play a role in substrate catalytic efficiency and orientation of the substrate-binding model. Further investigations into the kinetic behavior of each protein forms may elucidate information related to substrate binding and show related features with the *Mm CDO* protein.

The steady-state kinetics and complementary NMR studies are in good agreement with the observed kinetic parameters and confirm the presence of hypotaurine formation by ADO. Observed k_{cat} values for the ADO protein are in good agreement with what has been reported other studies.[48, 50] The k_{cat}/K_M values determined show a 10-fold magnitude difference in in K_M. One of the unusual behaviors amongst the TDOs is the allowance for accommodation of multiple substrates in the substrate binding pocket. The investigations into the *Mm* CDO has shown the capability to catalyze the conversion of multiple sulfur-containing thiol substrates (L-cys, D-cys, L-homocysteine).[101] Remarkably, the steady-state results would suggest the binding of ***cys*** to the active-site but no detectable formation of ***csa***. The k_{cat} values for ***cys*** are comparable with ***ca*** showing the accommodation of both substrates into the active site. The K_M calculated by steady-state plots show a 10^1 magnitude difference between ***cys*** and ***ca***.

Further verification by LC-MS/MS experiments for each substrate showed that only ***ca*** was converted into the sulfinic acid product. Therefore, the O_2-consumption observed is more likely related to the formation of the disulfide-bridged molecule, cystine. Presumably, the formation of cystine leads to the undesired product of reactive oxygen species (ROS) such as H_2O_2, $O_2^{\bullet-}$, and $OH^{\bullet}$. The accumulation of cystine has been linked to cystinosis and would be evolutionarily a hinderance for proper cell development if the ADO protein catalytically formed this compound. However, studies have shown

cysteamine an effective remedy for cystine build-up and suggests a built-in failsafe for accidental cystine formation.

Mechanistic information can be extrapolated for *Mm* ADO by inspection of the k_{cat}-pH and k_{cat}/K_M-pH profiles. For instance, the acidic pK_a value in the k_{cat}-pH profiles generated using ***ca*** (7.78 ± 0.3) deviates from what is seen in the acidic limits for *Mm* CDO which highlights a different protein-derived residue related to the chemical processes in catalysis. The basic regime shows a pK_a (8.78 ± 0.3) also deviates from the values reported for *Mm* CDO and *Av* MDO suggesting another alteration to the catalytic process. While reported values for protein residues are available in literature, the pK_a of these amino acids can drift from their free-amino acid values. The acidic pK_a could be related to a histidine or cysteine residue and the basic pk_a could be related to a thiol residue as well. However, these assignments need to be further investigated and clarified through X-ray crystallography studies to determine the framework of the second-coordination sphere.

In steady-state reactions with NO as a surrogate for O_2-binding, the additions of NO in the ADO-catalyzed reactions with ***ca*** exhibited significant inhibitory effects on k_{cat}. The relatively low additions of NO hampered the capability for O_2-consumption at saturating substrate conditions (5 mM). This behavior is unusual and has not been reported in other TDOs. This unusual interaction could be from the interactions of 1) with the substrate ***ca***, 2) the Fe-site or 3) protein-derived residue. In the first case, the additions of NO were significantly lower than the presence of substrate in the reactions. This would eliminate the possibility the interaction arises from ***ca*** and NO. For the second case, if the NO is binding directly the Fe-site and preventing the substrate-binding complex this would support the decreased activity at low concentrations. The third case relates to the interaction between NO and a nearby protein necessary for either substrate binding or catalysis. It has been known that NO can bind to active-thiols and this would suggest that there exists an active thiol in the active-site that is related to the binding of ***ca***. Presumably, this active-thiol may be related to one of the pK_s values determined from the

steady-state pH-profiles. Further investigations into the interactions of NO and the ADO protein are needed to assign these interactions and further elucidate information that is related to the role of binding for substrate.

EPR spectroscopy of the ADO **ES-NO** complex exhibited the low-spin features that is observed in the *Mm* CDO enzyme. However, only a small percentage of NO is bound to the **ES** complex which is an unusual characteristic. Previous studies have shown the proclivity for nitric oxide to bind to the ferrous center in the presence of substrate. The inhibitory effects by NO previously stated show that NO is interacting in some fashion with the enzyme-substrate complex. Therefore, the lack of iron-nitrosyl formation suggests either NO is not bound to the Fe-site or is bound but exists in a non-paramagnetic state. Further investigations into the nature of NO and its interactions in the active-site are needed to determine how NO is binding to the Fe-site. Additionally, efforts for crystallization are underway for proper designation of the active-site as well as the outer-sphere coordination environment to clarify the ambiguity in the covalent Cys-Tyr crosslink and the potential substrate orientation during catalysis.

The results presented here highlight the unusual nature of ADO and show why the largely uncharacterized thiol dioxygenase proves to be a challenging biological system. Despite the conserved chemical oxidation of a thiol, the spectroscopic features and lack of “catalytic triad” for substrate orientation and binding prove the deviated mechanistic nature that occurs in this enzyme.

Chapter 4 Collaboration Works with Analytical EPR

Spectroscopic and solid-state evaluations of tetra-aza macrocyclic cobalt complexes with parallels to the classic cobalt(II) chloride equilibrium

*Johnston, H. M., **Palacios, P. M**., Pierce, B. S., and Green, K. N. *Spectroscopic and solid-state evaluations of tetra-aza macrocyclic cobalt complexes with parallels to the classic cobalt(II) chloride equilibrium. J. Coor. Chem. 69*, (11-13), 1979-1989.

Contribution in collaboration

The Pierce lab has participated in many collaborations that deal with the application of EPR for quantitative measurement of transition metal complexes and biological systems. In collaborative efforts with the Green group, the cobalt complexes, **L1a** and **L1b**, was designed, synthesized, and analyzed. In this complex, a mononuclear cobalt ion was incorporated into the tetra-aza macrocyclic ring and was exposed to select solvents for preparation of different complexes based on solvent effects. Each complex was frozen and analyzed with X-band EPR spectroscopy for quantitation of the incorporation of the cobalt ion and determination of the oxidation state of the ion as the complex transitioned from solid to liquid phase.

As seen in **Figure S. 1**, the EPR signal for **L1a** is consistent with a nearly axial $S = 3/2$ spin-state with the observed *g*-values (5.5 and 2.04) in good agreement with a 5- or 6-coordinate Co(II) complex. Temperature-dependent studies showed the $m_s = \pm 1/2$ is the ground state within the $S = 3/2$ manifold.

In the samples prepared in DMF, **L1b** exhibited *g*-values different from the aqueous sample. Observed *g*-values for **L1b** suggested presence of two species (***i*** and ***ii***). The multiline hyperfine features were

simulated and revealed the ***i*** EPR spectrum is comparable to a 5- or 6-coordinate complex with a tetrahedral Co(II) complex that exhibits the more resolved hyperfine.

Abstract

The Co(III) complex of 3,6,9,15-tetra-azabicyclo[9.3.1]penta-deca-1,11,13-triene (**L1**) has been synthesized in DMF and isolated as a blue solid (**1**) ([**L1**$Co^{III}ClX]^{n+}$, X = Cl^- or DMF, *n* = 1 or 2). Complex **1** exhibits solution behavior similar to the classic cobalt(II) chloride equilibrium. When **1** is dissolved in water, the solution is pink and this complex exists as **1a**, which consists of a cobalt(III) bound to **L1** and two *cis*-chlorides with a perchlorate counter-ion to balance the complex charge ([**L1**$Co^{III}Cl_2][ClO_4]$). In contrast, when **1** is dissolved in DMF or other organic solvents the solution is blue and is observed as **1b**. The **1b** complex salt contains two cobalt centers. One cobalt(III) is bound to **L1**, Cl^-, and DMF. Charge balance is accomplished by the second cobalt center: $[Co^{II}Cl_4]^{2-}$, thus making **1b** (**L1**$Co^{III}Cl(DMF)][Co^{II}Cl_4]$). This equilibrium was confirmed using UV-visible spectroscopy, EPR, and X-ray crystallography.

Introduction

From crown ethers to N-heterocyclic amines, macrocycles are integral to coordination chemistry and can bind to a multitude of transition-metal ions.[116] Along with having a variety of donors, these ligands have a range of sizes. The smallest macrocycles have as few as 3 donor atoms forming rings with 9 atoms in the macrocycle, while larger macrocycles can have as many as 11 donor atoms forming rings with 33 atoms.[116] However, more common examples are synthetic 12- to 16-membered rings which are often utilized to mimic biologically important and naturally occurring macrocycles, such as porphyrins and corrins.[116-122] A vast array of macrocyclic transition-metal complexes have numerous potential uses;

applications range from use as biomimetic models, therapeutic agents, and catalysts in various organic reactions.[116-126] The kinetic and thermodynamic stabilities of these diverse ligands have played a major role in their popularity in inorganic and bioinorganic chemistry. Macrocyclic complexes exhibit enhanced kinetic and thermodynamic stability when compared to non-cyclic analogs; Margerum and Cabbiness term this large increase in stability as the *macrocyclic effect*.[116, 119, 123, 126, 127] The large amalgamation and inherent stability of complexes derived from macrocycles have made these ligands ubiquitous in the field of coordination chemistry.

Transition-metal ions incorporated in the Irving-Williams series, based on increasing stability of metal complex formed (Mn(II) < Fe(II) < Co(II) < Ni(II) < Cu(II) > Zn(II)), are particularly popular choices for forming macrocyclic metal complexes.[128] Within our group, the properties of the complexes of Fe(III), Ni(II), Cu(II), and Zn(II) with 12-membered pyridine- and pyridol-containing tetra-aza macrocycles have been characterized and studied in depth.[120, 129, 130] In continuation with the studies on macrocyclic complexes of first-row late transition metal ions, we have performed characterization on a 12-membered pyridine-containing tetra-aza macrocyclic cobalt (III) complex.

Surprisingly, cobalt(III) complexes with 12-membered tetra-aza macrocycles are not prevalent in the literature, but there are a few examples.[123, 131, 132] The majority of the chemical literature is dominated by 12-membered Co(II) tetra-aza macrocyclic complexes or planar 14-membered Co(II)/Co(III) tetra-aza macrocyclic complexes.[117, 118, 122, 124, 125, 133, 134] Although examples of Co(III) tetra-aza macrocyclic complexes are sparse, there are many Co(II)/Co(III) coordination complexes derived from monodentate and open chain chelates that are historically significant and ubiquitous in chemical literature.[132] When new heterocycles are synthesized, the complexes formed with Co(II)/Co(III) ions can be compared to these more classic coordination compounds in order to delineate the observed reactivity.[132] One specific example of a classic Co(II) coordination complex is the equilibrium between

pink cobalt(II) hexahydrate and blue cobalt(II) tetrachloride (scheme 1); this well-characterized demonstration is often used to illustrate le Chatelier's Principle.[135-141]

Solid-state and spectroscopic methods were used to characterize the 12-membered tetra-aza macrocyclic Co(III) compound. The solution behavior was similar to the classic Co(II) equilibrium. The color change in organic *versus* aqueous solvents, as well as the presence of a cobalt, led us to examine the classic cobalt(II) chloride equilibrium to determine if there were any parallels to our ligand system.[135-141]

Electronic absorption spectra of cobalt(II) chloride in both water and DMF lead to an important parallel that helped to confirm our system was undergoing a similar equilibrium in these two solvents. Electronic absorption spectroscopy and X-ray diffraction measurements were obtained to further investigate this phenomenon. Through this work, it was observed that solvent choice could be used to produce two derivatives of **1** (**1a** and **1b**). Depending on solvent choice one of the *cis*-bound ligands of **1** change (Cl^- or DMF) as well as the overall complex charge (+1 or + 2) and counter-ion ($[ClO_4]^-$ or $[Co^{II}Cl_4]^{2-}$). The spectroscopic and solid-state characteristics of these two systems and the parallels to the classic cobalt(II) chloride demonstration used to illustrate le Chatelier's principle will be discussed.

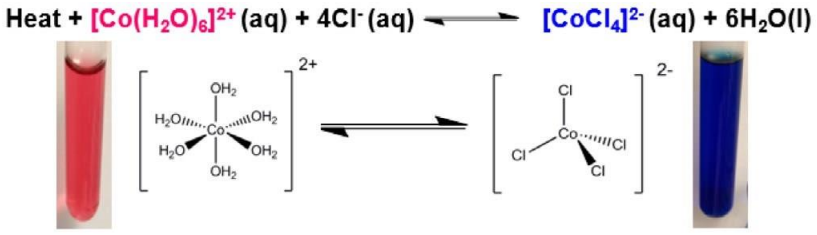

Scheme 4.1 Equilibrium reaction between cobalt(II) hexahydrate and cobalt(II) tetrachloride used to demonstrate le Chatelier's Principle.[130-136]

Materials and Measurements

Caution! Perchlorate salts are explosive and should be handled with care; such compounds should never be heated as solids. All chemical reagents were purchased from either Sigma-Aldrich or Alfa Aesar and used without purification. The 12-membered tetra-aza macrocycle (**L1**) was isolated as the hydrochloride salt prior to metal-ion complexation in accord with standard practices.[120, 142] The yield reported for **1** ([**L1**$Co^{III}ClX]^{n+}$, X = Cl^- or DMF; *n* = 1 or 2) was calculated from an average of three trials and based on elemental analysis results; each reaction was carried out in DMF. Elemental analyses were performed by Canadian Microanalytical Services ltd. Electronic absorption spectra were collected between 190 nm and 1100 nm using a 8453 UV–vis spectrophotometer (Agilent) and a 3-ml quartz cuvette with a path length of 1.0 cm. Molar extinction coefficients were calculated utilizing the Beer-lambert law (A = εbc).

Preparation of 12-membered tetra-aza macrocycle (**L1**)

The 12-membered pyridine-based tetra-aza macrocycle [3,6,9,15-tetra-azabicyclo[9.3.1]penta-deca1(15),11,13-triene (**L1**)] was synthesized by (1 + 1) condensation between a nosyl (Ns) protected amine and the respective benzyl chloride. Upon cyclization of the ligand, the amines were deprotected based on a modified published procedure using thiophenol and potassium hydroxide.[142] A full description for the synthesis of **L1** is available.[120]

Preparation of $[L1Co^{III}ClX]^{n+}$ (**1**)

Cobalt(II) perchlorate hexahydrate (89.0 mg, 0.243 mmol) was dissolved in 10 ml of DMF, resulting in a bright pink solution. Subsequently, **L1**·3HCl (100 mg, 0.317 mmol) was added in one

portion. The solution color changed immediately from bright pink to deep blue (figure S1) upon addition of **L1**·3HCl. This reaction mixture was stirred at room temperature for 24 h. The resulting deep blue solution was filtered through a 0.45-µm filter syringe to remove excess unreacted ligand. Excess diethyl ether was added to the filtered solution, causing a deep blue powder to precipitate. The powder and diethyl ether mixture were transferred to Eppendorf tubes and centrifuged for 5 min at 4000 rpm. The supernatant was decanted, and more diethyl ether was added to the blue powder in the Eppendorf tube; this process was repeated four to six times in order to remove traces of DMF. Finally, the blue powder, along with a small amount of diethyl ether, was transferred to a 6-ml vial and dried by vacuum on a Schlenk line to afford **1** as a light blue solid (106 mg, 0.122 mmol, 39% yield). Electronic absorption λ_{max}/nm (ε/M^{-1} cm^{-1}); water: 376 (144), 535 (133); DMF: 380 (318), 535 (320), 680 (886) nm. Elemental analysis for **1** [**L1**$Co^{III}Cl$: DMF][$Co^{II}Cl_4$]·2HCl·3DMF Found (Calculated): C, 31.89 (31.87); H, 4.57 (5.58); N, 12.78 (12.93); O 7.95 (7.38) %.

X-ray crystallographic structure determination

A leica MZ 75 microscope was used to identify the samples suitable for X-ray analysis. A Bruker Apex 2 X-ray (three-circle) diffractometer was employed for crystal screening and unit-cell determination. The data collections were obtained at 100 K. The goniometer was controlled using APEX2 software suite, v. 2008–6.0.[143] The samples were optically centered with the aid of a video camera so that no translations were observed as the crystal was rotated through all positions. The X-ray radiation utilized was generated from a Mo sealed X-ray tube (K_α = 0.70173 Å with a potential of 40 kV and a current of 40 mA) fitted with a graphite monochromator in the parallel mode (175 mm collimator with 0.5 mm pinholes). Crystal data and structure refinement parameters for **1a** and **1b** are provided in tables 1 and 2, respectively.

Table 4.1 Crystal data, intensity collections, and structure refinement parameters for [L1CoiiiCl(dmf)][CoiiCl4] (1b).

molecular formula	$[C_{14}H_{25}ClCoN_5][CoCl_4]$
empirical formula	$C_{14}H_{25}Cl_5Co_2N_5O$
formula weight	574.5
temperature (K)	100
Crystal system	orthorhombic
space group	Pbca
a (Å)	13.042(2)
b (Å)	16.735(3)
c (Å)	20.520(4)
α (°)	90
β (°)	90
γ (°)	90
Volume (Å^3)	4478.7(14)
Z	8
*ρ*calc (g cm^{-3})	1.704
μ (mm^{-1})	2.093
F(0 0 0)	2328
Crystal size (mm^3)	0.464 × 0.272 × 0.086
radiation	mo K*α* (*λ* = 0.71073)
2Θ range for data collection (°)	6.116 to 70.13
index ranges	$-21 \le h \le 20$, $-26 \le k \le 26$, $-33 \le l \le 33$
reflections collected	59,090
independent reflections	9867 [R_{int} = 0.0426, R_{sigma} = 0.0323]
data/restraints/parameters	9867/0/258
Goodness-of-fit on F^2	1.046
final *R* indexes [$I >= 2\sigma(I)$]	R_1 = 0.0329, wR_2 = 0.0673
final *R* indexes [all data]	R_1 = 0.0542, wR_2 = 0.0746
largest diff. peak/hole (e Å^{-3})	0.99/−0.40

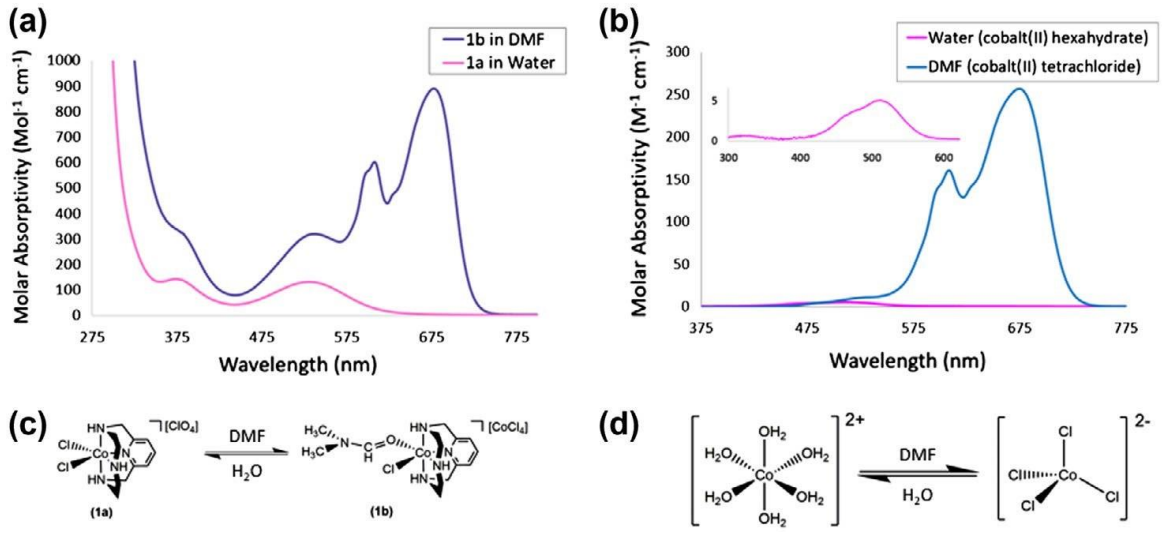

Figure 4.1 Comparison of the electronic absorption spectra of (a) 1a and 1b and (b) cobalt(ii) chloride in water vs. dmf. the conversion process observed for (a) and (b) is noted in (c) and (d), respectively.

[L1Co^{III}Cl$_2$][ClO$_4$] **(1a).** Crystals of **1a** suitable for X-ray analysis were obtained by dissolving several mg of the blue powder of **1** in H_2O to provide a pink solution. Slow evaporation of this solution at room temperature afforded a translucent dark red-pink, plate-like crystal of **1a** (0.101 × 0.262 × 0.303 mm^3) which was mounted on a 0.5-mm cryo-loop and used for X-ray crystallographic analysis. The crystal-to detector distance was set to 50 mm, and the exposure time was 10 s per degree for all data-sets at a scan width of 0.5°. A total of 1304 frames were collected, and the data collection was 99.8% complete. The frames were integrated with the Bruker SAINT Software package[143] using a narrow frame algorithm. The integration of the data using a monoclinic unit cell yielded a total of 139,761 reflections to a maximum ϑ angle of 38.63° (0.57 Å resolution) of which 26,110 were independent with R_{int} = 6.72%. Data were corrected for absorption effects using the multi-scan method (SADABS).[144] Structural refinements were performed with XShell (v. 6.3.1) by full-matrix least-squares.[145] All hydrogen and non-hydrogen atoms were refined using anisotropic thermal parameters. The thermal ellipsoid molecular plots (50%) were produced using XP, which is included in the XShell suite.[145]

***[L1Co^{III}Cl(DMF)][Co^{II}Cl$_4$]* (1b).** Crystals of **1b** suitable for X-ray analysis were obtained via vapor diffusion of diethyl ether into DMF. An intense dark blue-purple plate-like crystal of **1b** (0.086 × 0.272 × 0.464 mm^3) was mounted on a 0.5 mm cryo-loop and used for X-ray crystallographic analysis. The crystal-to-detector distance was set to 50 mm, and the exposure time was 10 s per degree for all data-sets at a scan width of 0.5°. A total of 772 frames were collected, and the data collection was 99.6% complete. The frames were integrated with the Bruker SAINT Software package[143] using a narrow frame algorithm. The integration of the data using a monoclinic unit cell yielded a total of 59,090 reflections to a maximum ϑ angle of 35.06° (0.62 Å resolution) of which 9867 were independent with the R_{int} = 4.26%. Data were corrected for SADABS.[144] Structural refinements were performed with XShell (v. 6.3.1) by full-matrix least-squares.[145] All hydrogen and non-hydrogen atoms were refined using anisotropic thermal parameters. The thermal ellipsoid molecular plots (50%) were produced using XP, which is included in the XShell suite.[145]

Results and Discussion

*Synthesis of [L1Co^{III}ClX]$^{n+}$ (**1**) and equilibrium behavior in organic and aqueous solvents*

Complexation between cobalt(II) perchlorate hexahydrate and the hydrochloride salt of **L1** in DMF yielded [**L1**Co^{III}ClX]$^{n+}$ (X = Cl$^-$ or DMF; *n* = 1 or 2) (**1**) (scheme 2). Upon addition of the ligand to the

Table 4.2 Electronic absorption bands and transition assignments for 1 in dmf and h2o, λmax/nm (ε/m−1 cm−1).

Solvent	DMF	Transitions in DMF	H_2O	Transitions in H_2O
	380 (236)	oh Co(iii): 1a1 g → 1t2 g oh	376 (144)	oh Co(iii): 1a1 g → 1t2 g
	535 (320)	Co(iii): 1a1 g → 1t1 g t_d	535 (133)	oh Co(iii): 1a1 g → 1t1 g
	680 (886)	Co(ii): $^4a_2$ → $^4t_1$(P)	530 (5)	oh Co(ii): 4t1 g(f) → 4t1 g(P)

stirred cobalt(II) perchlorate hexahydrate solution, the color changed immediately from bright pink to deep blue (figure S1). After reaction completion, **1** was isolated as a periwinkle blue solid. In order to characterize this ligand-cobalt complex, **1** was dissolved in several different solvents, including DMF and water. Upon complex dissolution in DMF, the solution remained blue. Conversely, when the complex was dissolved in water, the resulting solution was pink. The color changes observed, suggested the cobalt coordination was modified in DMF *versus* H_2O solutions. Electronic absorption spectroscopy was utilized in order to further investigate this phenomenon in solution.

Electronic absorption spectra of **1** *in aqueous and organic solvents*

The electronic absorption spectrum of **1** was measured in DMF and H_2O in order to investigate the color changes observed upon complex dissolution in organic and aqueous solvents. A comparison of the spectra confirmed that cobalt coordination depended upon the nature of the solvent (i.e. organic *versus* aqueous). For instance, in H_2O, the solution of **1** is bright pink and contains two absorbance bands at 376 and 535 nm (figure 1(a), table 3). The spectrum of **1** in H_2O is consistent with a limited number of reported Co(III) 12-membered tetra-aza macrocyclic complexes.[131, 132, 146] When **1** is dissolved in H_2O the solution is bright pink and it exists as **1a** ([**L1**$Co^{III}Cl_2$][ClO_4]) and cobalt(II) hexahydrate. Whereas, when **1** is dissolved in DMF the solution is deep blue and it exists as **1b** ([**L1**Co^{III}Cl(DMF)][$Co^{II}Cl_4$]). The following spectroscopic results support these assignments.

Most known octahedral cobalt(III) complexes are diamagnetic and have a ground state of $^1A_{1g}$. The visible absorption spectra of these octahedral cobalt(III) complexes consist of two spin allowed transitions, $^{1A}{}_{1g} \rightarrow {}^{1T}{}_{1g}$ and $^{1A}{}_{1g} \rightarrow {}^{1T}{}_{2g}$.[147-150] In a perfectly symmetric octahedral complex [Co^{IIIX}_6], there is

no splitting observed in the $^1A_{1g} \rightarrow {}^1T_{1g}$ transition, but in asymmetric octahedral complexes $[Co^{III}X_4y_2]$ there can be splitting of the $^1T_{1g}$ state.[147] The magnitude of $^1T_{1g}$ splitting is dependent upon the nature of $[Co^{III}X_4y_2]$, which can exist in both the *cis* and *trans* configurations.[147] *Trans*-$[Co^{III}X_4y_2]$ complexes have large splitting in the $^1T_{1g}$ state, resulting in an electronic absorption spectrum with three absorbance bands.[147-150] In contrast, *cis*-$[Co^{III}X_4y_2]$ complexes have a lesser degree of splitting in the $^1T_{1g}$ state, resulting in only two observed absorbance bands, with one absorbance band being slightly asymmetric.[147, 150] **1a** has a geometry consistent with *cis*-$[Co^{III}X_4y_2]$. In water, the absorption band at 376 nm is assigned to the higher energy transition, $^1A_{1g} \rightarrow {}^1T_{2g}$. The absorption band observed at 535 nm is assigned to the lower energy transition, $^1A_{1g} \rightarrow {}^1T_{1g}$.

In DMF, the solution of **1b** is deep blue with a shoulder at 380 nm and two absorbance bands at 535 and 680 nm. The lower energy absorbance at 680 nm has multiple shoulders due to spin-orbit coupling (figure 1(a), table 3). The absorbance bands at 380 and 535 nm can once again be assigned to the transitions $^{1A}{}_{1g} \rightarrow {}^{1T}{}_{2g}$ and $^{1A}{}_{1g} \rightarrow {}^{1T}{}_{1g}$, respectively, of the octahedral diamagnetic Co(III) complex. Upon careful examination of the additional absorbance band (680 nm), it was determined that it resembled the spectrum of a cobalt(II) chloride species in solution.[136, 141] The electronic absorption spectrum of cobalt(II) chloride hexahydrate was obtained under the same experimental conditions (figure 1(b)) because of this intriguing similarity of the absorbance band to **1b** in DMF solution. It is established that cobalt(II) chloride dissolved in H_2O, or aqueous solvents, exists as the complex ion, cobalt(II) hexahydrate. Alternatively, when cobalt(II) chloride is dissolved in DMF (or organic solvents) it exists as cobalt(II) tetrachloride. The cobalt(II) chloride dissolved in DMF exhibited a complex absorbance band at 680 nm, consistent with a cobalt(II) tetrachloride ion present in solution.[136, 141] This absorbance is in agreement with the higher energy band observed in the spectrum of the deep blue DMF solution containing **1b**.

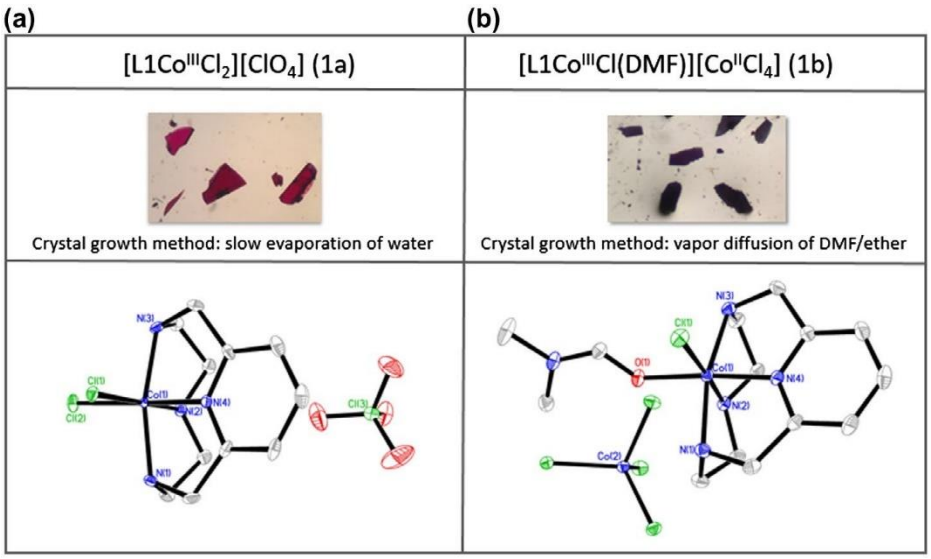

Figure 4.2 Comparison of 1a and 1b growth methods, crystal morphology, and solid-state structures (orteP views 50% probability). hydrogens were omitted for clarity.

The cobalt(II) tetrachloride ion has been well characterized using electronic absorption spectroscopy.[136, 147-150] Because this complex has a tetrahedral geometry, with no center of symmetry, very intense absorbance bands are observed when compared to octahedral cobalt(II) hexahydrate.[151] Assigning transitions for cobalt(II) tetrachloride can be somewhat difficult. In the visible region, the absorbance at 680 nm can be assigned to the highest energy transition $^4A_2 \rightarrow {}^4T_1(P)$.[147, 149, 150] This absorbance is very complex (containing multiple shoulders and peaks) due to other transitions to doublet excited states that occur in the same region of wavelengths.[147, 150]

Based on this parallel between the electronic absorption spectra of cobalt(II) chloride and **1**, the DMF solution (figure 1(a)) contained **1b** with cobalt(II) tetrachloride and the H_2O solution contained **1a** with cobalt(II) hexahydrate. EPR methods were in agreement with a four-coordinate Co(II) in DMF and six-coordinate Co(II) in water as well (figure S4). To verify this hypothesis and determine the exact nature of the cobalt coordination sphere, the two salt congeners of **1** were analyzed using solid-state methods.

Solid-state evaluation of **1a** *and* **1b**

Following spectroscopic evaluation, crystallizations of **1** were carried out separately in H_2O and DMF (figure 2). Two crystal growth methods were used in order to continue the investigation of how solvent type changed cobalt coordination. Both methods afforded X-ray quality crystals of **1** (**1a** and **1b**), respectively. Through evaluation of the solid-state structures, the cobalt coordination spheres were identified.

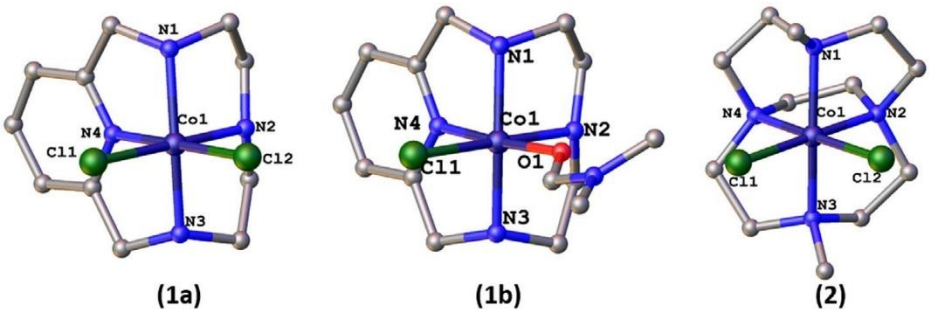

Figure 4.3 Comparison of the solid-state structures of 1a, 1b, and 2; hydrogens were omitted for clarity.[127]

Alternatively, deep-blue crystals of **1b** suitable for X-ray analysis were obtained via vapor diffusion of diethyl ether into DMF (figure 2(b)). The asymmetric unit of **1b** consisted of one independent [**L1**$Co^{III}Cl(DMF)][Co^{II}Cl_4]$. The resulting structure was derived from an orthorhombic *Pbca* system. **1b** also has a pseudo-octahedral geometry; the cobalt(III) ion is ligated by four N-donors of **L1**, a *cis* chloride, and a *cis* DMF, making it six coordinate. In contrast to **1a**, [**L1**$Co^{III}Cl(DMF)]^{2+}$ is balanced by $[Co^{II}Cl_4]^{2-}$. The second cobalt is Co(II). It is this $[Co^{II}Cl_4]^{2-}$ anionic coordination complex that is responsible for the solvent-dependent equilibrium behavior of **1**.

The [**L1**$Co^{III}ClX]^{n+}$ (X = Cl^- or DMF; *n* = 1 or 2) units of **1a** and **1b** show little deviation in the cobalt(III) coordination environment. For example, the largest deviation derived from the **L1**-Co coordination is observed with the Co(1)–N(1) interaction, with the bond length decreasing from 1.992(2) Å to 1.9703(12)

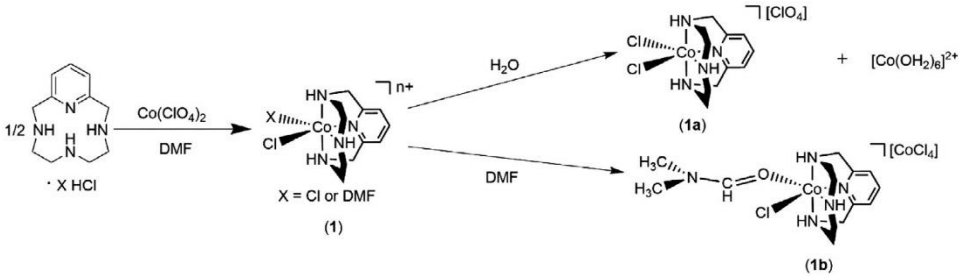

Scheme 4.2 Synthesis of 1; equilibrium of 1b and 1a in aqueous and organic solvents.

Å in **1a** and **1b**, respectively. likewise, the Co(1)–Cl(1) distance decreases from 2.2823(8) Å to 2.24115(5) Å in **1a** and **1b**. This is consistent with the change in Cl^- *versus* DMF donors to Co(III). The bond angles change very little (table 4) between **1a** and **1b**.

Complexes with a similar coordination environment to **1a** and **1b** are limited.[132] One particular Co(III) complex synthesized by Hubin *et al.* (denoted **2**)[132] offered connectivity parallels to **1a** and **1b**. **2** is a 12-membered ethylene cross-bridged macrocycle bound to Co(III) and is shown in figure 3. This complex, like **1a** and **1b**, is a 5–5-5–5 ring structure with Co(III) ligated by four N-donors, as well as two *cis* ligands to complete the octahedron. When comparing **1a** and **1b** with **2** some differences in bond angles were noted, specifically when comparing axial *versus* equatorial bond angles. In **1a** and **1b** the N(3)–Co(1)–N(1) bond angles are 165.25(11)° and 165.33(5)°, but in **2** the N(3)–Co(1)–N(1) bond angle is 168.8(14)°; this axial bond angle in **2** is more linear than **1a** and **1b** (figure 3, table 4).[132] The equatorial bond angles N(4)–Co(1)–N(2) in **1a** and **1b** are 93.40(11)° and 94.56(5)°, while this same bond angle is

only 87.2(4)° in **2** (figure 3, table 4).[132] Inspecting the axial and equatorial bond angles of these three structures revealed that both **1a** and **1b** have deviations from octahedral geometry in the axial coordination, whereas **2** modifies the equatorial cobalt(III) interactions. The slight difference in axial and equatorial bond angles is due to the structures of the two ligands. **L1** is a 12-membered, pyridine-containing tetra-aza macrocycle; the presence of the pyridine ring constrains the axial N(3)– Co(1)–N(1) bond angle causing more deviation from linearity in **1a** and **1b** than in **2**. In contrast, **2** contains a 12-membered ethylene cross-bridged tetra-aza macrocycle; this ethylene cross-bridge restrains the axial N(4)–Co(1)–N(2) bond angle in **2**.

Equilibrium behavior of **1a** *and* **1b**

When dissolved in DMF, or organic solvents, **1** exists as **1b** ([**L1**$Co^{III}Cl(DMF)][Co^{II}Cl_4]$), but when dissolved in H_2O, it exists as **1a** ([**L1**$Co^{III}Cl_2][ClO_4]$). The solid-state structure of **1b** contains cobalt in two different oxidation states, whereas the solid-state structure of **1a** contains only cobalt(III). This indicates that **1** remains intact throughout. Although in the solid-state **1a** contains only one cobalt ion, when **1a** is in solution $[Co^{II}(OH_2)_6]^{2+}$ could also be present. This complex ion is not observed in the solid state, because it does not balance the charge of the ligand-cobalt complex [**L1**$Co^{III}Cl_2]^+$, instead $[ClO_4]^-$ is the counter-ion (scheme 1). With the ligand-cobalt complex, cobalt(II) tetrachloride present in DMF and cobalt(II) hexahydrate present in H_2O, the solution behavior of these macrocyclic ligand complexes mimicked the classic cobalt(II) chloride equilibrium. This was further confirmed when the spectra of **1b** and cobalt(II) chloride were obtained in concentrated HCl and compared (figure S3). Although neither complex was dissolved in an organic solvent, both exhibited the characteristic cobalt(II) tetrachloride absorbance bands. Because chloride ions were present in such excess that the equilibrium was shifted from cobalt(II) hexahydrate to cobalt(II) tetrachloride. The same complex ions present in this classic

demonstration were also present within the coordination sphere of the cobalt-macrocyclic ligand complexes (scheme 1). There are several instances reported where ligand-cobalt complexes have changed color drastically upon dissolution, but never before has this equilibrium been investigated in the depth described here.[132]

Conclusion

Utilizing various spectroscopic and solid-state techniques, coordination of the ligand-cobalt complex was identified. In different solvents, ions bound to the Co center and counter-ions underwent an equilibrium. When dissolved in DMF, **1** is **1b** with two cobalt metal centers, one bound to **L1**, Cl^-, and DMF and the other bound to four chlorides ([**L1**$Co^{III}Cl$(DMF)][$Co^{II}Cl_4$]). This cobalt(II) tetrachloride species serves as the counter-ion. In contrast, when **1** is dissolved in water, it exists as **1a**, consisting of a cobalt(III) bound to **L1** and two *cis* chlorides with a perchlorate counter-ion to balance the charge, ([**L1**$Co^{III}Cl_2$] [ClO_4]). **1b** and **1a** undergo an equilibrium (scheme 2) and when **1a** is dissolved in water it only has one cobalt center present within the complex, but cobalt(II) hexahydrate may also be present. Investigation of this phenomenon utilizing electronic absorption spectroscopy and solid-state methods showed that this ligand cobalt complex parallels the behavior of the classic cobalt (II) chloride equilibrium.

Isolation and identification of the pre-catalyst in iron-catalyzed direct arylation of pyrrole with phenylboronic acid

*Brewer, S. M., **Palacios, P. M**., Johnston, H. M., Pierce, B. S., and Green, K. N. Isolation and identification of the pre-catalyst in iron-catalyzed direct arylation of pyrrole with phenylboronic acid. *Inorg. Chim. Acta.,* **2018**, 478, 139-147.

Contribution to collaboration

The quantitative measurement of the tetra-aza Fe-complexes were analyzed by EPR spectroscopy. As seen in the Co-complexes previously mentioned, various complexes were analyzed for validation of Fe incorporation and oxidation state. The Fe-complexes were measured in cryogenic temperatures and exhibited signals that are related to a mononuclear Fe(III) ion incorporated into the macrocyclic ring. Further details into EPR parameters of the spin-state, zero-field splitting, and verification of the ground-state are discussed in the text below.

Abstract

Herein we describe the synthesis, characterization, and role of three dichloric iron(III) complexes, **[L1Fe (III)$(Cl)_2$]ClO_4 (L1Fe)**, **[L2Fe(III)$(Cl)_2$]ClO_4 (L2Fe)**, and **[L3Fe(III)$(Cl)_2$]ClO_4 (L3Fe)** [**L1** (Pyclen) = 1,4,7,10tetra-aza-2,6-pyridinophane; **L2** = 1,4,7,10-tetra-aza-2,6-pyridinophane-14-ol; **L3** = 1,4,7,10-tetra-aza-2,6-pyridinophane-13-ol, in the coupling of pyrrole and phenylboronic acid to form 2-phenylpyrrole. The oxidation- and spin state of the iron complexes were characterized using X-ray crystallography, UV–vis absorbance spectroscopy, electron paramagnetic resonance spectroscopy, cyclic voltammetry, and mass spectrometry. Electrochemistry results rank ligand **L1–L3** as moderate tetra-

azamacrocycle donors to iron between **cyclen** and **Me_2EBC-12**. Characterization of the iron(III) complexes and subsequent catalytic testing indicates that the complexes enter the C–C coupling catalytic cycle in the high spin iron(III) oxidation state. Furthermore, the results indicate that the iron(III) complexes are essential for catalytic and regioselective production of the 2-phenylpyrrole product.

Introduction

C-C cross-coupling reactions catalyzed by transition metals are invaluable components in a chemist's toolbox.[152] Paradoxically, the precious metal palladium is commonly used to facilitate such transformations despite its low natural abundance, high cost, and high toxicity.[152-158] In response to this limitation, there has been a growing interest in replacing palladium with a more each abundant metal catalysts such as iron.[157, 158] While iron catalysts are indeed making strong contributions to the field of cross-coupling reactions, mechanistic insights and thorough catalyst characterizations are much more challenging than the palladium counterparts due to the strong reactivity of iron complexes, unpaired electrons complicating NMR spectroscopy, and transient nature of intermediate species.[152-158] Regardless, iron complexes have proven useful in the syntheses of organic compounds[151-168] and as model complexes of metalloenzymes.[169-171] Indeed, such complexes have been crucial for elucidating the reactivity and spectroscopic properties of key iron-oxo intermediates such as Fe(III)OOH, Fe(IV)=O, or Fe(V)=O.[167, 170, 172] As a result of these studies, the key mechanistic elements driving oxidative iron catalysis are becoming increasingly well understood. However, the studies that investigate iron catalysts for C-C bond formation focus largely on the scope of the catalysts and less on the properties of the active metal center. A compliment to studies of substrate scope would focus on the identification of catalyst oxidation state and spin state (which may be tuned by the ligand scaffold[173, 174]) needed for the desired organic transformation to take place. Thorough understanding of ligand effects on the metal

center will aid in designing more efficient catalysts.[152, 156-158] For example, the White-Chen [Fe(S,S-PDP)] catalyst has been studied for C-H bond activation.[175] This work focused on regioselectivity derived from substrate properties such as electronics, steric bulk, and directing groups. Talsi *et. al*. have separately probed the nature of the active species in this process using electron paramagnetic resonance spectroscopy (EPR) and enantioselectivity studies to show that the oxygen transfer occurs by an Fe(V)-oxo species.[176] Insight into a previously unknown mechanism resulted from the detailed characterization in this work.[177] Furthermore, multi-dentate N-containing ligands have been used to obtain stable Fe(IV)-oxo species, providing invaluable spectroscopic comparisons to metalloenzymes in nature.[161, 169, 170, 178-180]

Interestingly, Bedford and co-workers reported that iron catalysts derived from rigid tetra-azamacrocycles, such as **Me_2EBC-12**, resulted in poor yields for the cross-coupling of 4-tolyl magnesium bromide with cyclohexylbromide.[156] However in 2010, Wen et al. reported that the tetra-azamacrocycles shown in

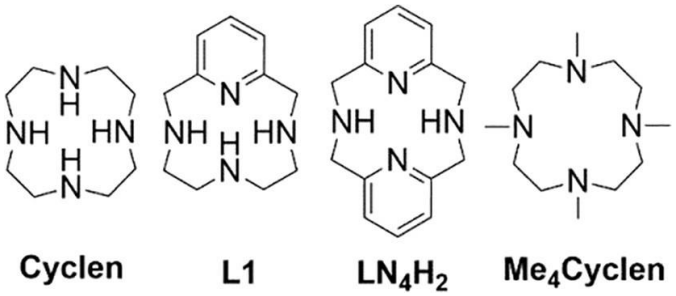

Figure 4.4 Tetra-azamacrocycles studied by Wen et al. in combination with iron(II) salts to facilitate the coupling of pyrrole and phenylboronic acid to produce 2phenylpyrrole.[176]

Fig. 1, when mixed with iron(II) salts in the presence of oxygen, facilitate direct arylation of pyrrole with phenylboronic acid to form 2-phenylpyrrole.[181] A preliminary mechanism was proposed in which an iron-oxo species acts as the active catalyst; however, no metal oxidation states were assigned or catalyst

characterization reported aside from a mass spectrum that proved to be tenuous in its assignment. Since the publication of this manuscript, it has been cited over 70 times.[159, 162, 166, 174, 182-247] Interestingly, to date the synthesis and characterization of iron complexes derived from two of the four ligands in this original report, **LN_4H_2 and cyclen**, have been reported (Fig. 2). Both complexes **$[(LN_4H_2)Fe(Cl)_2]^+$** and **$[(cyclen)Fe(Cl)_2]^+$** were identified as high-spin iron(III) systems.[1, 248-250] Of the four mixtures tested for catalytic ability by Wen and co-workers, the mixture containing **L1** afforded the highest yield. Therefore and reported here, we have identified the spin-state and oxidation state of the complex formed by **L1** and iron(II) in the presence of oxygen and compared the structural and electronic properties to **$[(LN_4H_2)Fe(Cl)_2]^+$**, **$[(cyclen)Fe(Cl)_2]^+$**, and others. We have previously explored **L1** and its derivatives (**L2** and **L3**, Fig. 3) as chelates for Cu(II), Ni(II), and Zn(II); the donor capacity of the ligand was affected by the presence and position of the hydroxyl group.[129] Therefore, the iron complexes of **L2** and **L3** were also isolated, characterized, and compared within the series described above. The bona fide iron(III) high-spin complexes derived from **L1**, **L2**, and **L3** were identified as pre-catalysts for direct Suzuki-Miyaura coupling of pyrrole and phenylboronic acid to yield 2-phenylpyrrole. Finally, further experiments show that **L2** and **L3** can promote a small amount of background reactivity yielding multiple products, but the iron(III) pre-catalysts are critical for focusing the reactivity to produce only 2-phenylpyrrole, thus validating the need for the intact iron complex as a catalyst.

Materials and Methods

Iron(II) perchlorate was freeze dried prior to use, all other reagents were obtained from commercial sources and used as received, unless noted otherwise. NMR spectra were obtained on a 400-MHz Bruker Advance spectrometer, using deuterated solvents ($CDCl_3$). NMR spectra were referenced using the corresponding solvent resonance (in parts per million; $CDCl_3$ d = 7.26).[251] The

following abbreviations were used for proper identification of the NMR signals: s = singlet, d = doublet, t = triplet,

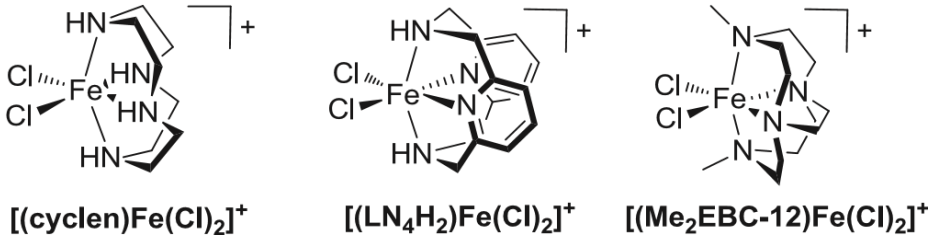

Figure 4.5 Iron(III) complexes derived from cyclen, LN4H2, and Me2EBC-12.

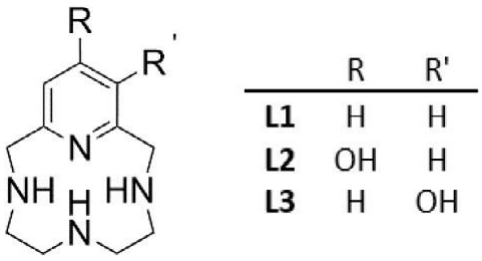

	R	R'
L1	H	H
L2	OH	H
L3	H	OH

Figure 4.6Chemical structure of ligands L1–L3 (L1 = 1,4,7,10-tetra-aza-2,6-pyridinophane[113, 115], L2 = 1,4,7,10-tetra-aza-2,6-pyridinophane-14-ol, L3 = 1,4,7,10tetra-aza-2,6-pyridinophane-13-ol.[124]

m = multiplet. ESI-MS experiments were carried out using an Agilent 6224 Accurate-Mass Time-of-Flight (TOF) mass spectrometer using 175 V to ionize the complexes. Elemental analysis was performed by Canadian Microanalytical Service Ltd. Electronic absorption spectra were recorded on a DU 800 UV–vis spectrophotometer (Beckman Coulter) using a 3 mL quartz cuvette with a 1 cm path length. GC–MS analysis was carried out using a Bruker Scion 436-GC–MS equipped with an auto sampler 8410 and a Br-5 ms column 29.9 m. **Caution!** *Perchlorate salts are explosive and should be handled in small quantities. In particular, such compounds should never be heated as solids.*

Synthesis of ligands

Stability of transition-metal complexes containing a tetra-azamacrocycle are facilitated by the macrocyclic effect. The ease with which these processes occur depends upon ring size, the number of donor atoms, electronic characteristics, and other factors.[116, 118] The formation of 14-membered tetra-azamacrocyclic ligands, for example, typically involves the use of transition metal-ions to template the cyclization step between two independent units to form the ligand. The product of this reaction is, therefore, a transition metal macrocyclic complex. However, tetraazamacrocyclic amines, comprised of 12 atoms in the ring, form through metal-independent cyclization pathways.[252-258] Therefore, for the work described herein, the 12-membered pyridine and pyridol based tetra-azamacrocyclic amines ligands, **L1**– **L3**, were produced previously reported procedures developed in our group and isolated as the corresponding HCl salts.[120, 129]

[L1Fe(III)(Cl)$_2$]ClO$_4$ (**L1Fe**): Ligand (**L1·3HCl**) (101.1 mg, 0.3216 mmol) and Fe(ClO$_4$)$_2$ (83.7 mg, 0.330 mmol) were dissolved in 3 mL DI water; the solution was adjusted to pH = 6 using 1 M KOH. The resulting red solution was allowed to stir open to air for 15 h at 40 C. After 15 h, a tan precipitate was removed by centrifugation followed by filtration using a 0.45 μm PTFE filter. The water was removed using an azeotrope formed with acetonitrile. The resulting solid was taken up in CH_3CN and dried with Na_2SO_4. The addition of Et_2O to the CH_3CN solution, followed by centrifugation yielded the product as a brown powder. Yield: 62% (92.8 mg, 0.198 mmol). Yellow X-ray quality crystals were obtained by slow diffusion of ether into DMF at 4 C, CCDC# 1422489. ESI-MS (m/z) Found: 260.1515, [L1Fe(III)-2H$^+$]$^+$, (34%); 296.1360, [L1Fe(III)Cl-H$^+$]$^+$, (58%), 332.1209, [L1Fe(III)2Cl]$^+$, (14%). Theoretical: 260.0724, [L1Fe(III)-2H$^+$]$^+$, 296.0491, [L1Fe(III)Cl-H$^+$]$^+$, 332.0258, [L1Fe(III) 2Cl]$^+$. UV–vis, $k_{max,}$ e (M^1cm^1): 261 nm

(3,600), 311 nm (800), 416 nm (170). Elemental analysis: **[L1Fe(III)(Cl)$_2$]ClO$_4$** (Formula:$C_{11}H_{18}N_4FeO_4Cl_3$); Found (Calculated): C, 30.66 (30.50); H, 4.09 (4.20); N, 13.04 (12.95).

[L2Fe(III)(Cl)$_2$]ClO$_4$ (L2Fe): Ligand (**L2·3HCl**) (65.0 mg, 0.208 mmol) was dissolved in 2.5 mL DI water. The pH of the solution was adjusted to 5 using 1 M KOH. $Fe(ClO_4)_2$ (53.6 mg, 0.211 mmol) was dissolved in 1 mL DI water and added dropwise to the ligand solution; the pH was maintained between 3.5 and 5.2. After all iron(II) solution was added, the pH was adjusted to 5.3. The solution was allowed to stir open to air 2 days resulting in precipitation of a brown solid that was isolated by centrifugation. Yield: 30% (27.4 mg, 0.061 mmol). Yellow crystals suitable for XRD analysis were obtained by slow evaporation of water at room temperature, CCDC # 1422490. ESI-MS (m/z) Found: 276.1529, [L2Fe(III)-$2H^+]^+$ (35%); 312.1377, [L2Fe(III)Cl-$H^+]^+$ (45%). Theoretical: 276.0674, [L2Fe(III)-$2H^+]^+$; 312.0440 [L2Fe(III)Cl-$H^+]^+$. UV–vis, $k_{max,}$ e (M^1cm^1): 249 nm (6,700), 306 nm (4,000), 356 nm (2,700). Elemental analysis**: [L2Fe(III)(Cl)$_2$]ClO$_4$** (Formula: $C_{11}H_{18}N_4FeO_5Cl_3$); Found (Calculated): C, 29.88 (29.46); H, 4.08 (4.05); N, 11.75 (12.49).

[L3Fe(III)(Cl)$_2$]ClO$_4$ (L3Fe): Ligand (**L3·3HCl**) (206.4 mg, 0.6223 mmol) was dissolved in 20 mL DI water and the pH was adjusted to 5 using 1 M KOH. $Fe(ClO_4)_2$ (164.0 mg, 0.6155 mmol) was dissolved in 10 mL DI water, added drop wise to ligand, and the pH was readjusted to 5. The solution was allowed to stir open to air for 2 days at 40 C. The solvent was removed under reduced pressure. The resulting dark brown solid was dissolved in DMF, dried with Na_2SO_4, and filtered. Ether was added to the DMF solution and a red-brown powder was isolated by centrifugation. Yield = 63.2% (235.6 mg, 0.3932 mmol). Brown crystals suitable for XRD analysis were obtained by slow evaporation from water at room temperature, CCDC # 950048. ESI-MS (m/z) Found: 276.1481, [L3Fe(III)$2H^+]^+$ (30%), 312.1322, [L3Fe(III)Cl-$H^+]^+$ (55%). Theoretical: 276.0674, [L3Fe(III)-$2H^+]^+$, 312.0440 [L3Fe(III)Cl-$H^+]^+$. UV–vis, k_{max}, e (M^1cm^1): 205 nm (14,000), 219 nm (10,000), 284 nm (5,600), 458 nm (300). Elemental analysis: [L3Fe(III)(Cl)$_2$]ClO$_4$ (Formula: $C_{11}H_{18}N_4FeO_5Cl_3$); Found (Calculated): C, 29.03 (29.46); H, 4.05 (4.05); N, 12.57 (12.49).

X-ray diffraction analysis

Crystal diffraction data were collected at 100 K on a Bruker D8 Quest Diffractometer. Data collection, frame integration, data reduction (multi-scan), and structure determination were carried out using APEX2 software.[259] Structural refinements were performed with XSHELL (v 6.3.1), by the full-matrix least-squares method.[260] All non-hydrogen atoms were refined using anisotropic thermal parameters, while the hydrogen atoms were treated as mixed. The ORTEP molecular plots (50%) were produced using APEX2 (Version 2014.9–0).

Electrochemistry

Cyclic voltammetry experiments were obtained using 2.2 mM complex and 100 mM tetrabutylammonium tetrafluoroborate as the supporting electrolyte in DMF. The electrochemical cell was composed of a working glassy carbon electrode, a Pt auxiliary electrode, and a silver wire as the reference electrode. To facilitate solubility, all samples were first dissolved in 1 M HCl, thoroughly dried, and then dissolved in DMF for electrochemical analysis. The potential was scanned in the negative direction at a rate of 100 mV/s, starting at the open circuit potential. The potential values presented here have been normalized to the half-wave potential of the Fc/Fc^+ redox couple set equal to 0.00 V. For comparison purposes half-wave potential in cited references were converted to reflect $Fc/Fc^+ = 0.00$ mV**;** **[(Me$_2$EBC-12)Fe(Cl)$_2$]PF$_6$**, ($Fc/Fc^+ = 400$ mV), and **[(cyclen)Fe(Cl)$_2$]Cl**, ($Fc/Fc^+ = 515$ mV).[1-3]

X-band EPR spectroscopy and analytical simulations

X-band (9 GHz) EPR spectra were recorded on a Bruker EMX Plus spectrometer equipped with a bimodal resonator (Bruker model 4116DM). Low-temperature measurements were made using an

Oxford ESR900 cryostat and an Oxford ITC 503 temperature controller. A modulation frequency of 100 kHz was used for all EPR spectra. All experimental data used for spin-quantitation were collected under non-saturating conditions. Analysis of the EPR spectra utilized the general spin Hamiltonian,

$$\mathcal{H} = \boldsymbol{D}\left[\hat{\mathrm{S}}_{\mathbf{Z}}^{\mathbf{2}} - \frac{\mathrm{S(S+1)}}{3}\right] + \boldsymbol{E}\left(\hat{\mathrm{S}}_{\mathbf{X}}^{\mathbf{2}} + \hat{\mathrm{S}}_{\mathbf{Y}}^{\mathbf{2}}\right) + \beta\mathbf{B}\cdot\mathbf{g}\cdot\mathbf{S} \qquad (\mathbf{4.1})$$

where ***D*** and ***E*** are the axial and rhombic zero-field splitting parameters and **g** is the g-tensor.[261] EPR spectra were simulated and quantified using Spin Count (ver. 5.8.6218.29549), written by Professor M.P. Hendrich at Carnegie Mellon University. The simulations were generated with consideration of all intensity factors, both theoretical and experimental, to allow concentration determination of species. The only unknown factor relating the spin concentration to signal intensity is an instrumental factor that depends on the microwave detection system. However, this factor is determined by the spin standard, Cu(EDTA), prepared from a copper atomic absorption standard solution purchased from Sigma–Aldrich.

Yield determination of 2-Phenylpyrrole

Phenylboronic acid (24 mg, 0.2 mmol) and crystalline material of the iron complex (0.02 mmol) were added to a 5 or 10 mL flask equipped with a stir bar. Pyrrole (1 mL) was added to flask, the mixture was heated to 130 °C for 10 h. The reaction was cooled to room temperature and the pyrrole was removed under vacuum until no visible liquid was present. Increasing the time, the reaction was kept under reduced pressure decreased yields. The product mixture was dissolved in a minimum amount of $CDCl_3$, 5 mL of dimethyldiphenylsilane was added to the solution. The solution was filtered through a 0.2 μm nylon filter and a known amount of sample was added to a pre-weighed NMR tube. Yield determinations were performed using three resonances 6.875, 6.532, and 6.307 ppm corresponding to

2-phenylpyrrole and a resonance at 0.533 ppm corresponding to dimethyldiphenylsilane. The reported values are averages of all resonances; each measurement was run in triplicate.

Control reactions

Phenylboronic acid (24 mg, 0.2 mmol) and ligand (0.02 mmol), if used, were added to a 2 mL flask equipped with a stir bar, the system was then placed under an atmosphere of nitrogen. Pyrrole (1 mL) was added to flask and the mixture was heated to 130 °C for 15 min, if used, 10 mL O_2 was injected directly into the pyrrole, the system was closed, and heated for 10 h. Yields were determined as stated above.

GC–MS details

Method: 80 °C 2 min, ramp 5 °C/min to 170 °C, ramp 20 °C/min to 300 °C, hold 5 min.

GC–MS Compound identification **L3** coupling: 3-methyl-4phenylfuran-2(5H)-one: (trace) RT. 14.909 min. Found (Cal.): M^+ 174.1 (174.1); (6%) 3-phenylpyrrole: RT. 15.002 min. Found (Cal.) M^+ 142.9 (143.0); (trace) 3-methyl-5-phenylfuran-2(4H)-one: 16.330 min. Found (Cal.) 174.1 (174.1); (16%) 2-phenylpyrrole: RT: 16.460 min Found (Cal.): M^+ 142.9 (143.0).

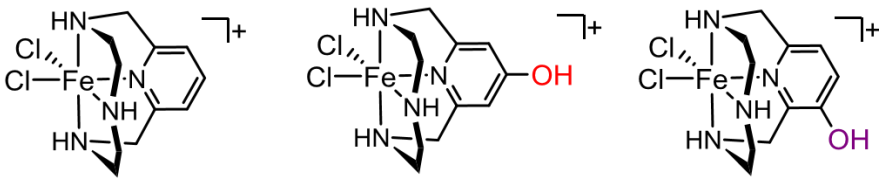

Figure 4.7 Pictorial representation of [L1Fe(III)(Cl)2]+ (L1Fe), [L2Fe(III)(Cl)2]+ (L2Fe), and [L3Fe(III)(Cl)2]+ (L3Fe).

Results and discussion

Synthesis and characterization

The corresponding iron complexes of **L1**–**L3**, shown in Fig. 4, were synthesized in water at pH 5 to compensate for the protonation of the isolated ligands. The iron(II) salt was used in metalation of **L1**–**L3** and was oxidized in air to iron(III) prior to isolation of the **L1Fe**–**L3Fe** complexes. The iron(II) perchlorate salt was exploited to facilitate the growth of X-ray quality crystals, discussed below. Attempts to form complex using $Fe(ClO_4)_3$ did not afford product in water. The presence and position of the hydroxyl group on the aromatic ring of the ligand affected the metalation efficiency and solubility of the resulting complexes; therefore, divergent synthetic strategies were developed for each complex produced. For example, mixtures of CH_3CN/Et_2O or DMF/Et_2O were used to isolate metal complexes **L1Fe** (62% yield) and **L3Fe** (63% yield), respectively, as solids precipitates. **L2Fe** was easily isolated as a precipitate from the aqueous reaction mixture, albeit with a low yield (30%). Nevertheless, the resulting ferric complexes of **L1**–**L3** were stable to both air and light and can be stored indefinitely once isolated as dark red (**L3Fe**) or light brown (**L1Fe**, **L2Fe**) solids.

X-ray crystallography

Fig. 5 shows the results of single crystal diffraction analysis on crystalline solids of **L1Fe**, **L2Fe**, and **L3Fe**. Yellow, X-ray quality crystals of **L1Fe** were obtained through vapor diffusion of ether into a solution of DMF; yellow **L2Fe** and brown **L3Fe** crystalline

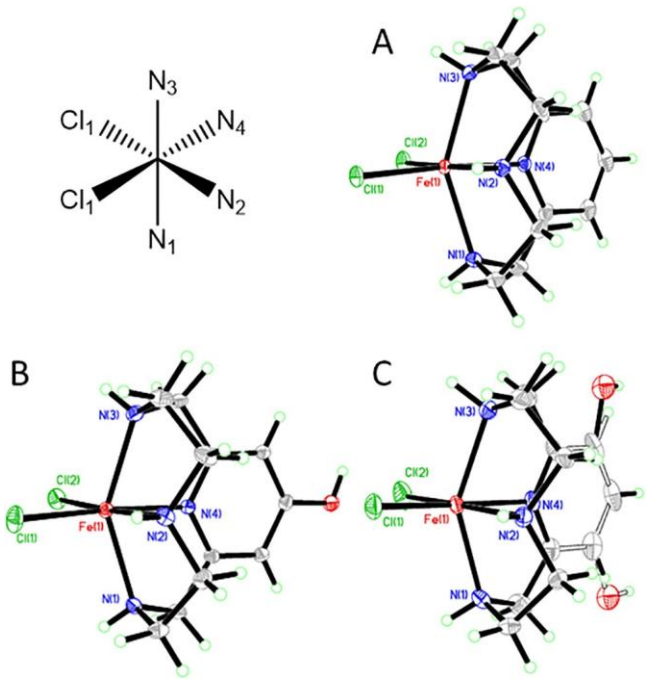

Figure 4.8 ORTEP (50%) representations of L1Fe (A), L2Fe (B), and L3Fe (C). The perchlorate anion has been omitted for clarity; modelling of disorder for L3Fe is shown in grey. All complexes take on a cis-folded distorted octahedral geometry. The Fe-N bond lengths are greater than 2.0 Å, consistent with other high-spin ferric systems.[1, 3, 250] A full list of bond lengths and angles are available in Tables S2–7.

materials were isolated by slow evaporation of aqueous solutions. Table S1 contains the crystal data, intensity collections, and structure refinement parameters; a full list of bond lengths and angles are also located in the supporting information. The structures determined through X-ray diffraction analysis show that each complex adopts a six coordinate, distorted octahedral geometry (N(2)–Fe–N(4), 85°; N(1)–Fe–N(3), 147°). The coordination sphere consists of four nitrogen donors from the ligand set and two chloride ions. Each complex adopts a *cis*-folded geometry due to the rigidity of the 12-membered ligand set in which one chloride is *cis* and the other is *trans* to the pyridol ring.[166] This finding is consistent with previous structure determination of **[L1Fe]BF_4**, reported by Alcock *et al*.[262] The charge of the $[L_xFe\ (III)(Cl)_2]^+$ systems are balanced by one perchlorate counter ion within the asymmetric unit. The position of the hydroxyl group and the flexibility of the aliphatic portion of the ligand results in an

enantiomeric mixture of **L3Fe**. The hydroxyl group was modeled for disorder to account for both enantiomers, as shown in Fig. 5c.

The geometry of complexes **L1Fe–L3Fe** can be compared to other macrocycles in the literature. For example, N(1)–Fe–N(3) bond angles have been reported for two 12-membered macrocycles (Fig. 2), **[(LN$_4$H$_2$)Fe(Cl)$_2$]$^+$** (142.41°) and **[(cyclen)Fe(Cl)$_2$]$^+$** (146.40°), where the latter complex provides the closest bond angle to the **L1Fe–L3Fe** systems.[2, 250, 263] The **L2Fe** complex provides slightly longer Fe-N bonds compared to **L1Fe** and **L3Fe**. For example, the Fe-N(2) bond of **L2Fe** was determined to be 2.2023(10) Å, while **L1Fe** and **L3Fe** were slightly shorter with 2.2001(6) and 2.181(2) Å, respectively. The only exception was observed with the Fe-N(4) bond, which was slightly shorter in **L2Fe** (2.0967(10) Å) compared to **L1Fe** (2.1074(5) Å) and L3Fe (2.107(2) Å). The difference in the equatorial Fe-N(4) pyridinederived bond length is consistent with a stronger interaction between the pyridol nitrogen of **L2** vs **L1** and **L3**. Throughout the series, the equatorial Fe–N(2) (pyridine atom) bond is the longest and thus the weakest Fe-N interaction. The Fe-N bond lengths of **L1Fe–L3Fe** are greater than 2.00 Å (Tables 1 and 2 and Fig. 5) and are consistent with an iron(III) high-spin system.[264] For example, the iron center of **[(LN$_4$H$_2$)Fe(Cl)$_2$]$^+$** was assigned as a high-spin iron(III) by EPR, and the Fe-N bond lengths within the high-spin complex were measured as 2.128 and 2.221 Å.[2, 265] Altogether, the results indicate that ligands **L1–L3** stabilize the high-spin iron(III) in similar manners and that **L2** is a slightly stronger donor to iron(III) compared to **L1** and **L3**. However, the differences in bond lengths and angles within **L1Fe– L3Fe** is much smaller than the nickel(II), copper(II), and zinc(II) congeners of **L1–L3**[129] (see Table 1).

Mass spectrometry

Mass spectrometry further confirmed the oxidation state of the iron(III) in **L1Fe–L3Fe**. The mass spectrum obtained for L1Fe consisted of three isotopic envelopes that correspond to the complex:

260.1519 m/z = [L1Fe(III)–2H$^+$]$^+$, 296.1358 m/z = [L1Fe(III)Cl-H$^+$]$^+$, and 322.1209 m/z = [L1Fe(III)2Cl]$^+$ (Fig. S4). Similar fragmentation patterns were obtained for complexes **L2Fe** and **L3Fe** and are

Table 4.3 Selected bond lengths (Å) and angles (°) of complxes L1Fe and L3Fe.

Bond	**L1Fe**	**L2Fe**	**L3Fe**
Fe(1)–N(1)	2.1641(6)	2.1787(11)	2.162(2)
Fe(1)–N(2)	2.2001(6)	2.2023(10)	2.181(2)
Fe(1)–N(3)	2.1676(6)	2.1812(11)	2.172(2)
Fe(1)–N(4)	2.1074(5)	2.0970(10)	2.107(2)
N(1)–Fe(1)–N(3)	147.25(2)	146.70(4)	147.17(8)
N(2)–Fe(1)–N(4)	85.56(2)	85.47(4)	85.72(8)

Table 4.4 Comparison of spin-state and bond lengths within iron(III) complexes derived from 12-membered tetra-azamacrocyclic ligands. [162, 163]

Complex	Spin State (S)	Fe–N4 (Å)	Fe–N2 (Å)	N1–Fe–N3 (°)	Ref.
[(cyclen)Fe(Cl)$_2$]Cl	2-May	–	2.1461(16)	146.40(6)	[1]
[(LN$_4$H$_2$)Fe(Cl)$_2$]Cl	*	2.094(1)	2.189(1)	142.41(7)	[2, 250, 263]
[(Me$_2$EBC-12)Fe(Cl)$_2$]PF$_6$	2-May	–	2.163 (2)	153.2	[3]
[(L1)Fe(Cl)$_2$]ClO$_4$	2-May	2.1074(5)	2.2001(6)	147.25(2)	
[(L2)Fe(Cl)$_2$]ClO$_4$	2-May	2.0967(10)	2.2023(10)	146.71(4)	
[(L3)Fe(Cl)$_2$]ClO$_4$	2-May	2.107(2)	2.181(2)	147.19(8)	

detailed in experimental methods related to each complex. Mass spectrometry analysis of the coupling reaction performed by Wen. et al. revealed three isotopic envelopes: m/z = 207.1532, 353.1956, and 369.1956.[181] The isotopic envelopes were assigned as [L1]$^+$, [L1 + Fe + C_2O_4]$^+$, and [L1 + Fe + C_2O_4 + O]$^+$, respectively, with no indication of iron oxidation states or charge balance. The isotopic envelope observed at *m/z* = 207.1532 indeed corresponds to the singly protonated free ligand [L1+H$^+$]$^+$, which we observe as well with studies of free ligand **L1**. However, the assignment of m/z = 353.1965 as [L1 + Fe + C_2O_4]$^+$ is incorrect, as the exact mass the expected species is modeled to have *m/z* = 350.0672, three mass units less than the observed ion reported. Similarly, the assignment of *m/z* = 369.1897 as [L1 + Fe +

$C_2O_4 + O]^+$ (Theoretical *m/z* = 366.0621) as a component of the catalytic reaction does not correlate as well. Therefore, the results reported herein serve as the first validation of the composition and oxidation state of the iron pre-catalyst involved in the C-C coupling chemistry, to be described later.

The spin and oxidation states of complexes **L1Fe–L3Fe** were also validated at low temperature via electron paramagnetic resonance (EPR) spectroscopy. As shown in Fig. 6(*left*), the EPR spectra(*solid lines*) for all complexes (**L1Fe–L3Fe**) exhibit features typical of high-spin ferric iron (S = 5/2). For analytical purposes, all data were recorded under non-saturating microwave power. The simulations overlaid on each spectrum (*dashed lines*) consist of contributions from two separate doublets. As indicated by the energy diagram shown in Fig. 6(*right*), the dominant transition for these complexes arises from the ground $m_s = \pm 1/2$ doublet of a S = 5/2 spin state with near axial symmetry (*E/D*= 0.07). Transitions within this doublet yield the observed *g*-values of 7.6, 4.3, and1.7. The linewidth of this transition can be reasonably simulated by assuming a Gaussian distribution in rhombicity (*E/D*)[designated $\sigma_{E/D}$], which broadens the g ~ 1.7 resonance significantly. The lower intensity features observed at *g* ~ 5.8 and 1.97 are nearly absent at low temperature (4 K) but reach a maximal intensity near ~ 8 K before decreasing again as temperature approaches 20 K. The alternating temperature dependence of these features confirm that this signal must originate from the middle $m_s = \pm 3/2$ doublet of the S = 5/2 spin state. The magnitude of the zero-field splitting parameter ($|D| = 0.7 \pm 0.2$ cm1) was determined by plotting the EPR signal intensity of the $m_s = \pm 1/2$ doublet versus 1/T and fitting the data to a Boltzmann population distribution for a 3-level system. Additional corroboration of the axial zero-field splitting term was obtained by simultaneous simulation of EPR spectra collected at temperatures ranging from 4 to 20 K (n = 5). Within this temperature regime, all simulations accurately reproduce the relative intensity for each transition (±1/2 and ± 3/2 m_s-states) using a $|D|$-value of 0.7 ± 0.2 cm^{-1}. Within error, all complexes (**L1Fe–L3Fe**) exhibited equivalent temperature dependence and thus all EPR simulations shown in Fig. 6 utilized the same axial zero field splitting term. Indeed, with the exception of

minor perturbations in the extent of *E/D*-distribution ($\sigma_{E/D}$), all complexes **L1Fe–L3Fe** exhibit nearly equivalent EPR spectroscopic properties.

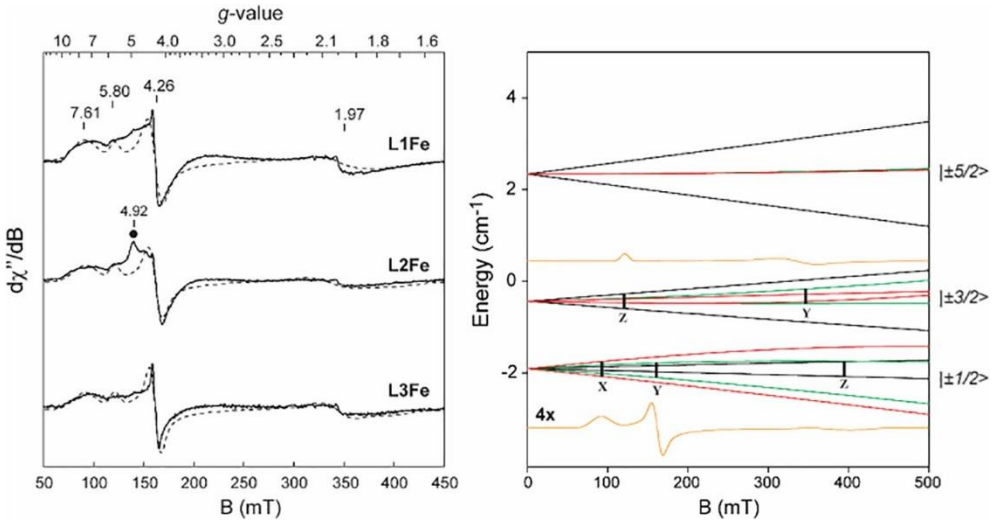

Figure 4.9 X-band EPR spectra of L1Fe–L3Fe (left). Quantitative simulations (dashed lines) are overlaid on each spectrum for comparison. The black circle observed at g ~ 4.92 in L2Fe is from a minor (< 10%) high-spin iron(III)-impurity. Instrumental parameters: frequency, 9.643 GHz, microwave power, 6 µW; modulation amplitude, 0.9 mT; temperature, 10 K. Simulation parameters: S = 5/2; $g_{1,2,3}$ ~ 2.0; |D|, 0.7 ± 0.2 cm^{1}; E/D, 0.07; $\sigma_{E/D}$, 0.01; σ_B, 0.9 mT. Energy level diagram (right) illustrating the splitting of doublets within the S = 5/2 spin state along each principle axis (X, red; Y, green; Z, black). (For interpretation of the references to color in this figure legend, the reader is referred to the web version of this

The near equivalent of EPR spectra observed for these complexes is understandable given the close agreement in Fe-coordination sphere bond length and coordination geometry observed crystallographically (Table 1).

Electrochemistry

Cyclic voltammetry was used to evaluate the electrochemical behavior of **L1Fe–L3Fe**. The cyclic voltammograms corresponding to the iron(III/II) couple of **L1Fe–L3Fe** are shown in Fig. 7. Of the three complexes, **L2Fe** ($E_{1/2}$ = 486 mV) has the most negative half potential, followed by **L3Fe** ($E_{1/2}$ = 468 mV) and **L1Fe** ($E_{1/2}$ = 465 mV) (Table 3). The difference in the half potentials indicated derivatization of the pyridine ring effects the electron density around the iron center, specifically, **L2** is the most donating. Fig. 8 compares the electrochemical potentials of iron complexes containing 12-membered tetra-azamacrocycles; a wide range (865 mV to 20 mV) of half potentials is achieved by changing the donor capacity of the ligand set, **LN_4Me_2** < **Me_2EBC-12** < **L1** ≈ **L3** < **L2** < **cyclen**.[4, 244, 264, 266]

The reversibility of the redox process was investigated by determining the ΔE_p and I_{pa}/I_{pc}. The iron(III/II) redox processes are

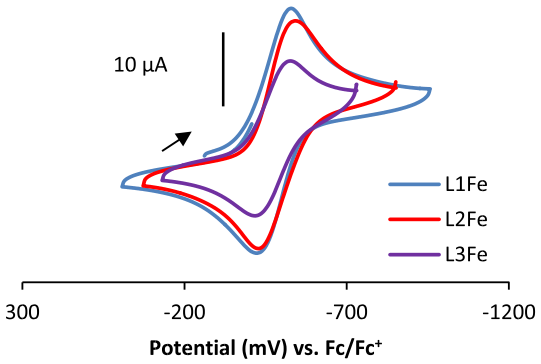

Figure 4.10 Cyclic voltammogram overlay of the FeIII/II couple measured for L1Fe–L3Fe in DMF containing 0.1 M [Bu4N][BF4] as electrolyte, Ag/Ag+ reference electrode, glassy carbon working electrode, and platinum auxiliary electrode at a scan rate of 100 mV/s. All scans were referenced to Fc/Fc+ = 0.00 mV.

quasi-reversible (ΔE_p, I_{pa}/I_{pc}): **L1Fe** (105 mV, 1.2583), **L2Fe** (112 mV, 0.7264), and **L3Fe** (101 mV, 0.7485). Lastly, the electrochemical events are diffusion controlled for all three iron complexes, as shown by the linear relationship between I_p and the square-root of the scan rate (Fig. S6).[267]

It should be noted that an additional ligand-based oxidation event around 900 mV is observed in the full solvent window (1.4 to -1.2 mV, Fig. S5) for **L1Fe–L3Fe**. We have previously postulated that this event was ligand derived, based on electrochemical analysis of the corresponding zinc(II) complexes providing a similar behavior.[129] Electrochemical analysis of **L1**–**L3** in DMF solvent with TBAP electrolyte provide direct confirmation that this positive oxidation wave is ligand based (Fig. S5).

Electronic absorption spectroscopy

The spectrophotometric behaviors of L1Fe–L3Fe are shown in Fig. 9. The aromatic components of the ligands (sans metal) result in absorbance bands between 210 and 290 nm when measured in 1 M HCl. The iron(III) complexes showed no appreciable shift in the p?p* region (210–300 nm). Instead, the appearance of MLCT bands were observed at wavelengths greater than 300 nm: L1Fe (311 nm), L2Fe (306 and 356 nm), L3Fe (458 nm), which is

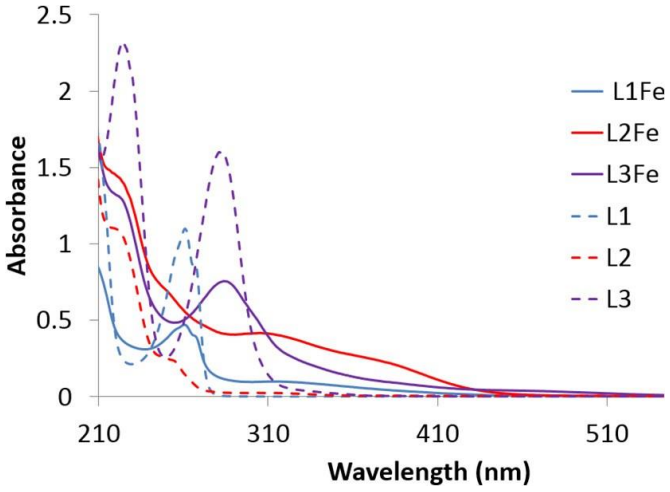

Figure 4.11 The electronic absorbance spectra of ligands L1–L3 and complexes L1Fe– L3Fe obtained in 1 M HCl.

Table 4.5 The anodic wave potential (Epa), cathodic wave potential (Epc), peak potential separation (DEp), and halfway potential (E1/2) of L1Fe–L3Fe. L2Fe contains the most stable iron(III) ion in the series according to the E1/2 values.

Complex	E_{pc} (mV)	E_{pa} (mV)	E1/2 (mV)	ΔE_p (mV)	I_{pc} (µA)	I_{pa} (µA)	Ipa/Ipc
L1Fe	-517	-412	-465	105	10.5837	-13.3181	1.2583
L2Fe	-542	-430	-486	112	18.4176	-13.3791	0.7264
L3Fe	-519	-418	-468	101	11.9661	-8.957	0.7485

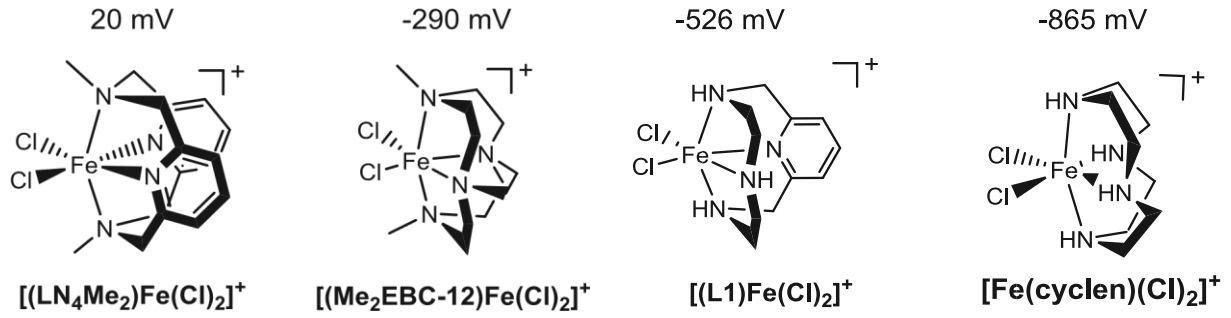

Figure 4.12 Iron(III)/(II) halfway potentials of iron complexes in literature containing 12-membered tetra-azamacrocycles. The potentials are reported as referenced to Fc/Fc^+ = 0.00 mV.[1-5]

consistent with high-spin d^5 complexes.[268] These metal based assignments are supported by comparison to the 12-membered macrocycle, **$[(cyclen)Fe(NCMe)_2]^{3+}$** that Hua et al. reported to have absorbance bands at 259 and 358 nm and corresponding extinction coefficients below 500 $M^1\,cm^1$.[268] Furthermore, the difference in the absorbance spectra of **L1Fe**, **L2Fe**, and **L3Fe** is reflected in the visible color of the complexes. The **L1Fe** and **L2Fe** complexes are light brown solids, while **L3Fe** is a red solid; in solution **L1Fe** and **L2Fe** are yellow and **L3Fe** is brown. Low solubility of the complexes in other solvents precluded a full study of solvent effects or at other pH values. Therefore, it should be noted that the iron complex responsible for catalytic activity may vary in the degree of ligand protonation, but the coordination sphere around the iron within the complex does not change. The electronic absorption differences between **L3Fe** compared to the **L1Fe** and **L2Fe** complexes could be attributed to the lack of symmetry originating from the hydroxyl moiety in the meta-position of the pyridine ring of the ligand.

Catalytic activity of iron(III) complexes

Motivated by the report that addition of a tetra-azamacrocycle, iron(II) salt, and oxygen to phenylboronic and pyrrole results in the formation of 2-phenylpyrrole[181], we explored the oxidation state of the pre-catalyst by testing **L1Fe**, **L2Fe**, and **L3Fe** for catalytic activity. Yields are shown in Table 4. In this series of experiments each catalyst was tested at 10% loading, open to air. The ferric complexes afforded 2-phenylpyrrole in yields of 57% (**L1Fe**), 58% (**L2Fe**), and 52% (**L3Fe**), thereby identifying the oxidation state of the pre-catalyst as an iron(III) species. The realization that the iron(III) complexes enter the catalytic cycle will allow for a better foundation to determine the oxidation state and identity of the active catalytic species. The following discussion focuses on the experiments used to validate that the iron + ligand catalyst species is solely responsible for providing the selective reactivity observed, showing the ligand can catalyze baseline reactions with no regioselectivity, and components necessary for the reaction to proceed.

Control reactions were performed to ensure that the catalytic reactivity observed with **L1Fe**, **L2Fe**, and **L3Fe** was due only to the iron complexes. The substrates, pyrrole and phenylboronic acid, were heated to 130 °C in both the absence and presence of oxygen (Table 5). No reaction was observed under either of these conditions. This indicates that the reaction requires a catalyst to proceed. Additionally, four control reactions consisting of iron(III) perchlorate, **L1**, **L2**, and **L3** were performed in the presence of 10 mL O_2. Yield of 2-phenylpyrrole was determined by both GC–MS and NMR due to the low quantities observed. Iron(III) perchlorate and **L1** did not afford 2-phenylpyrrole, however, **L2** and **L3** produced trace amounts of 2-phenylpyrrole. Interestingly GC–MS analysis of the control reaction, which included pyrrole,

Table 4.6 Catalytic efficiency of iron complexes to obtain 2-phenylpyrrole from pyrrole and phenylboronic acid, achieved using 10% catalyst loading in the presence of air.

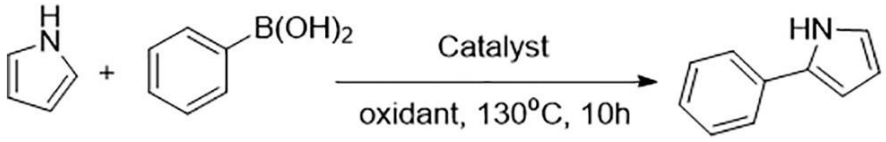

Catalyst	Yield
L1Fe	57 ± 3
L2Fe	58 ± 7
L3Fe	52 ± 7

Table 4.7 Control reactions used to determine the yield of product in the absence of the highspin iron(III) complexes.

Test compound	Oxidant	Yield
*	*	0
*	20 eq. oxygen	0
$Fe(ClO_4)_3$	20 eq. oxygen	0
L1	20 eq. oxygen	0
L2	20 eq. oxygen	Trace
L3	20 eq. oxygen	Trace
L3	Atmosphere	Trace

*Not present

phenylboronic acid, **L3**, and atmospheric air also showed the formation of trace amounts of 2-phenylpyrrole, 3-phenylpyrrole, and two butenolides. The formation of 3-phenylpyrrole and butenolides was previously observed by Campi *et al*. when 3-phenylprop-2-yn-1-amine is exposed CO/H_2 at 400 psi at 70 °C for 20 h in the presence of a rhodium catalyst. These results indicate that the ligand is capable of background reactivity producing a pyrrole derivative. Additionally, it indicates that the derivatives produced are controlled by the composition of the oxidant (O_2 and CO_2) used in the reaction. Importantly, comparison of the products formed in the presence of **L3** vs **L3Fe** and atmosphere show that the use of the iron complex is *essential* to obtain catalytic and regioselective production of 2-phenylpyrrole product.

Conclusion

The addition of iron(II) perchlorate to the tetra-azamacrocycles **L1**, **L2**, and **L3** in the presence of oxygen yields high-spin iron(III) complexes **L1Fe**, **L2Fe**, and **L3Fe** as shown by X-ray crystallography and EPR spectroscopy. Furthermore, it was demonstrated that the high-spin iron(III) complexes participate in the coupling of pyrrole and phenylboronic acid to produce 2-phenylpyrrole. Although a small amount of background reactivity was overserved with **L3**, the results show that the iron complexes are responsible for controlling the reaction to produce 2-phenylpyrrole alone. A full study involving a large library of iron macrocyclic derived complexes focused on understanding features of catalytic activity is the topic of a forth coming report. Finally, the characterization of the complexes using electrochemistry, UV–vis spectroscopy and mass spectrometry lays a foundation for mechanistic investigations concerning the oxidation state of the iron center throughout the catalytic process.

Structural and Electronic Responses to the Three Redox Levels of $Fe(NO)N_2S_2$-$Fe(NO)_2$

*Ghosh, P., Ding, S., Quiroz, M., Bhuvanesh, N., Hsieh, C. H., **Palacios, P. M**., Pierce, B. S., Darensbourg, M. Y., Hall, M. B. Structural and Electronic Responses to the Three Redox Levels of $Fe(NO)N_2S_2$ – $Fe(NO)_2$. *Chemistry*, **2018**, 24 (60), 16003-16008.

Contribution to the *collaboration*

In collaboration with the Darensbourg group, the analytical quantitation of the iron-nitrosyl complexes was measured with X-band EPR spectroscopy. The iron-nitrosyl complexes were synthesized, and chemical treated for addition of an electron from the resting $\mathbf{1^0}$ state. Further details into the EPR parameters of the iron-nitrosyl complexes are discussed further below. In summation, the reductive state of the $\mathbf{1}^-$ shows an integer spin signal (S = 1) that correlates to the insertion of an additional electron. Integer spins are more complex due to the absence of degeneracy in the spin manifolds (S = 0, 1, 2,…), however simulations and quantitation of the $\mathbf{1}^-$ exhibited nearly stoichiometric conversion from the S = 1/2 species to the S = 1 integer spin complex. Tabulated results can be seen in Table S1 in the appendix.

Abstract

The nitrosylated diiron complexes, $Fe_2(NO)_3$, of this study are interpreted as a mono-nitrosyl Fe(NO) unit, MNIU, within an N_2S_2 ligand field that serves as a metallodithiolate ligand to a dinitrosyl iron unit, DNIU. The cationic $Fe(NO)N_2S_2{\cdot}Fe(NO)_2^+$ complex, $\mathbf{1}^+$, of Enemark–Feltham electronic notation $Fe(NO)^7$-$Fe(NO)_2^9$, is readily obtained via myriad synthetic routes, and shown to be spin coupled and diamagnetic. Its singly and doubly reduced forms, $Fe(NO)\}^7$-$Fe(NO)_2^{10}$, $\mathbf{1}^0$, and $Fe(NO)^8$-$Fe(NO)_2\}^{10}$, $\mathbf{1}^-$,

were isolated and characterized. While structural parameters of the DNIU are largely unaffected by redox levels, the MNIU readily responds; the neutral, S = $^1/_2$, complex, $\mathbf{1}^0$, finds the extra electron density added into the DNIU affects the adjacent MNIU as seen by the decrease its Fe-*N*-O angle (from 171° to 149°). In contrast, addition of the second electron, now into the MNIU, returns the Fe-*N*-O angle to 171° in $\mathbf{1}^-$. Compensating shifts in Fe_{MNIU} distances from the N_2S_2 plane (from 0.518 to 0.551 to 0.851 Å) contribute to the stability of the bimetallic complex. These features are addressed by computational studies which indicate that the MNIU in $\mathbf{1}^-$ is a triplet-state Fe(NO)$\}^8$ with strong spin polarization in the more linear FeNO unit. Magnetic susceptibility and parallel mode EPR results are consistent with the triplet state assignment.

Introduction

With its easily accessible one-electron, reduced (NO^-), and one electron-oxidized (NO^+) forms, nitric oxide ($NO^{\cdot}$) as a ligand shows extensive electronic interplay in metal-nitrosyl fragments, resulting in considerable structural and bonding intricacies especially in M(NO) and $M(NO)_2$ units.[269-272] Complexes containing the dinitrosyl iron units, $Fe(NO)_2$ or DNIUs, increasingly gain attention as physiologically important products of NO overload or NO storage.[273, 274] Nevertheless, the predominant chemical relevance of NO in biology stems from various heme-type Fe(NO)$^{6/7/8}$ species of distinctive IR and EPR spectral features and solid state metric parameters.[275] While the Fe(NO)^7 species is most prevalent, rare illustrations of the reduced Fe(NO)^8 have been noted in synthetic porphyrins decorated with electron-withdrawing groups.[276-279] Examples are also known for non-heme, cyclam-based macrocycles and in a tetracarbene binding scaffold.[280-283] In the latter, Meyer et al. presented X-ray crystal structures in three redox levels.[283]

Contiguous N_2S_2 donor sites are efficient and versatile tetradentate ligands, creating MN_2S_2 units whose S-based nucleophilicity has yielded a wide range of di- and poly-heterometallic complexes.[284] While mostly explored with $M{=}Ni^{2+}$, other dications such as $[Fe(NO)]^{2+}$, $[Co(NO)]^{2+}$, and $[V{\equiv}O]^{2+}$ are also included in this new class of metallo-ligands.[16] A notable biological N_2S_2 site in Acetyl-coA Synthase (ACS) is constructed of a Cys-Gly-Cys tripeptide motif that securely binds a catalytically inactive Ni^{II}.[285, 286] A second, kinetically labile nickel is attached to the NiN_2S_2 moiety via the cis-dithiolate sulfurs, is presumed to orchestrate the C-C coupling processes in ACS.[285]

An ACS-related structure, $[Fe(NO)N_2S_2{\cdot}Fe(NO)_2]^{+/0}$ was revealed by us during studies of metallodithiolates as ligands in dinitrosyliron complexes, DNICs, Figure 1.[287] The redox activity of this diiron complex, centered at both iron atoms, and exhibiting two fully reversible electrochemical events, encouraged its exploration as a proton reduction electrocatalyst in mimicry of the [FeFe]-H_2ase active site.[287-289] Specifically, redox reactivity in the NO of the Fe(NO) unit might mimic the 4Fe4S cluster of the H-cluster. Generally, the diiron complex offers opportunity to examine the mutual influence of redox active units as mediated by sulfur bridges.

As indicated in Figure 1, multiple chemical routes led to the cationic, oxidized form, $Fe(NO)^7$-$Fe(NO)_2^9$, that is, $\mathbf{1}^+$ or $\mathbf{1}^{*+}$, implicating particular thermodynamic stability and a self-assembly process. Herein we will give distinguishing properties

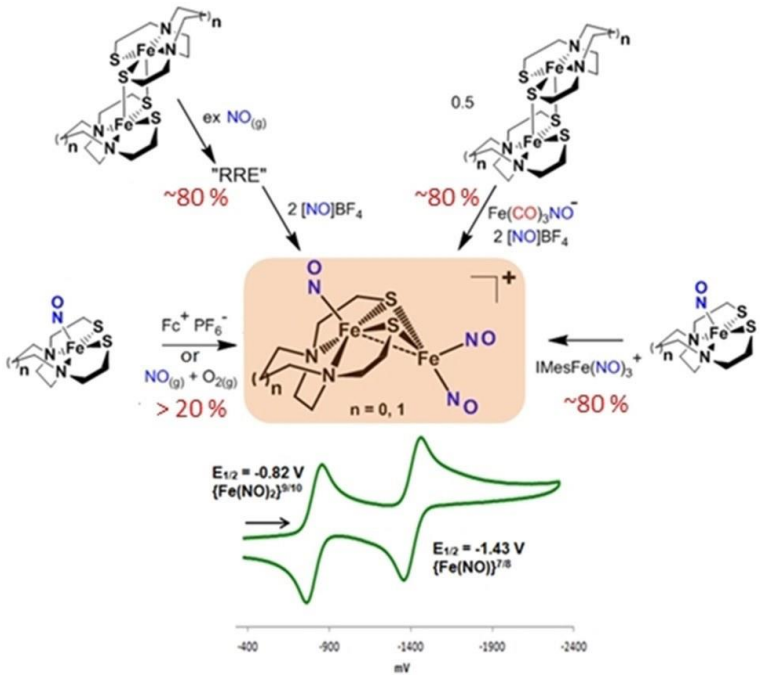

Figure 4.13 A selection of synthetic routes for the formation of the oxidized diiron-trinitrosyl complex, Fe(NO)N2S2·Fe(NO)2+, with N2S2 ligands, bis-mercaptodiazamethyl-ethane, bme-dame (n = 0), complex 1+, and bis-mercaptodiazacycloheptane, bme-dach (n = 1), complex ***1*+****. The cyclic voltammogram of* ***1+*** *was recorded in CH_2Cl_2 at a scan rate of 200 mV sec^{-1} and referenced to $Fc^{+/0}$ =0.00 V.*

of $Fe(NO)\}^{7/8}$ within a diiron complex containing the mononitrosyl in N_2S_2 binding that acts as a metalloligand to a $Fe(NO)_2$ unit, which itself is stable in two redox levels, $Fe(NO)_2^{9/10}$.

Initial studies of the $[Fe(NO)N_2S_2{\cdot}Fe(NO)_2]^{+/0}$ construct made use of an N_2S_2 ligand containing a moderately rigid diazamesocycle grafted to bis-mercaptoethylene arms, complexes **1*+** and **1*0** as indicated in Figure 1.[287] Difficulties in the isolation of the doubly-reduced, anionic **1*-**, $Fe(NO)^8$-$Fe(NO)_2^{10}$, prompted adjustment to a more flexible, open-chain, bmedame (bis-mercaptoethyl-diazamethylethane) ligand,[290] to prepare the mononitrosyliron complex, (bme-dame)Fe(NO).[291] This MNIC is used as the metallodithiolate ligand in the $\mathbf{1}^+$, $\mathbf{1}^0$ and $\mathbf{1}^-$ complexes of this study.

Synthesis and Characterization

The key precursor to the MNIU of the bimetallic complex is dimeric ($[FeN_2S_2]_2$), readily cleaved by NO(g).[291] The most selective route to the $Fe(NO)N_2S_2{\cdot}Fe(NO)_2^+$ complex, three o'clock position in Figure 1, is found to be the reaction of an N-heterocyclic-carbenestabilized, trinitrosyliron complex (TNIC), $[(IMes)Fe(NO)_3]^+$,[292] with $Fe(NO)N_2S_2$ as nucleophile, displacing an NOC radical, as well as the NHC, to form oxidized diiron complex $\mathbf{1}^+$. At one o'clock in Figure 1, the "one-pot" synthesis, involved in situ generation of NOC and the putative $[Fe(CO)_2(NO)_2]^+$ to serve as a $Fe(NO)_2^+$ source,[293] derived from $[Fe(CO)_3(NO)]$@ and two equivalents of $[NO][BF_4]$. The in situ generated NOC and $Fe(NO)_2^+$ react with the $[FeN_2S_2]_2$ dimer to yield the target trinitrosyl bimetallic. Such synthetic routes, using the bme-dame and bme-dach ligands, gave isolated yields of ≈ 80%.

In contrast to the reaction of the $[FeN_2S_2]_2$ dimer with a stoichiometric amount of NO(g) that forms $Fe(NO)N_2S_2$, addition of excess NO(g), leads to a Roussin's Red Ester (RRE) derivative,[294] indicated by position and separation of the signature ν(NO) bands at 1780 and 1754 cm^{-1}. Although this species has not been structurally characterized, it is likely a (precedented) dimeric structure in which two *S*-*N*-*N*-*S* dithiolate ligands span two RRE units.[295] Subsequent oxidation of this species by [NO] $[BF_4]$ formed complex $\mathbf{1}^+$ or $\mathbf{1}^{*+}$ in ≈ 80% yields. Oxidation of the $[FeN_2S_2]_2$ dimer by aerial O_2, or Fc^+, in the presence of excess NO(g) also generated $\mathbf{1}^+$ and $\mathbf{1}^{*+}$, albeit in yields <20%. Formation of $Fe(NO)^7$-$Fe(NO)_2^9$ was repeatedly observed in various reactivity studies with $Fe(NO)N_2S_2$, under oxidizing conditions. The isolated yields for these reactions were marginal, as expected from the low atom economy in such circuitous routes. Full experimental descriptions and characterizations are provided in the Supporting Information.

The cyclic voltammogram of complex $\mathbf{1}^+$ in CH_2Cl_2 displayed two-single-electron, fully reversible events at $E_{1/2}$ = -0.82 V and -1.43 V, assigned as the $Fe(NO)^7$-$Fe(NO)_2)^{9/10}$, and the $Fe(NO)^{7/8}$-$Fe(NO)_2)^{10}$

couples, respectively, Figures 1 and S1. Thus, the reduced species, $Fe(NO)^7$-$Fe(NO)_2)^{10}$ and $Fe(NO)^8Fe(NO)_2)^{10}$, were targeted for isolation. Treatment of $\mathbf{1}^+$ with 1 equiv of K^+ (or Na^+) $HBEt_3^-$ in THF at 0 °C, showed a color change from dark brown to green with a concomitant blue shift in all three ν(NO) stretching frequencies by ca. 110 cm^{-1}, Figure 2. The air sensitive neutral compound, $\mathbf{1}^0$, was isolated as a green solid by layering a THF solution with pentane.

An extra 1.3 equiv of K^+HBEt_3@ added to $\mathbf{1}^0$ at -40 °C showed a further, but less dramatic, 30 cm^{-1} shift in the ν(NO) stretching frequencies to lower values, Figure 2. Notably, while the site of reduction is reasonably assigned to the separate components of the $Fe_2(NO)_3$ complex, the three nitrosyls in both reduced levels conjointly respond to the added electrons; the first added electron, largely on the $Fe(NO)_2$, evincing a greater response. The anionic complex, $\mathbf{1}^-$, was isolated at ≈ 40 °C as its K^+/18-Cr-6 salt; reddish-brown plates, suitable for XRD, were obtained from THF/pentane and stored at -35 °C.

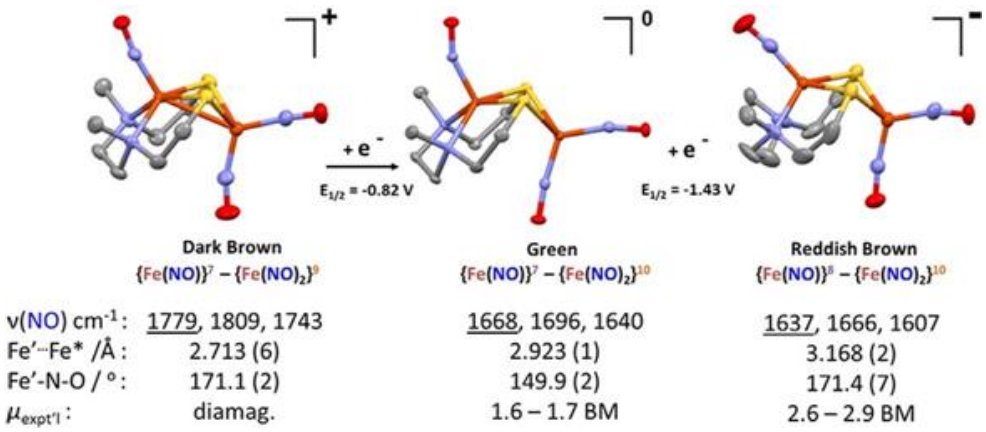

*Figure 4.14 Sequential reduction of **1**⁺ to **1⁰** and to **1**⁻ within(NO) IR values (THF solution), and XRD structures (Fe'···Fe* distances and Fe'-N-O angles shown); Fe" refers to Fe(NO) and Fe* to Fe(NO)₂. Other metric parameters are listed in Table 1 and in the Supporting Information. Magnetic susceptibility and $m_{expt'l}$ determined by Evans method using $CF_3C_6H_5$ as shift agent.*

*Table 4.*8 Comparison of experimental and computed parameters of the $Fe(NO)^{7/8}$ moieties in **1**⁺, **1⁰**, and **1**⁻.

	1⁺		**1⁰**		**1⁻**	
multiplicity	BS singlet		Double		Triplet	
E-F count	$Fe(NO)^7$		$Fe(NO)^7$		$Fe(NO)^8$	
d electron configuration	$(d_z^2)^1(d_{xy})^0$		$(d_z^2)^1(d_{xy})^0$		$(d_z^2)(d_{xy})^1$	
Measureable	**Expt.**	**Calcd**	**Expt.**	**calcd**	**Expt.**	**calcd**
d(Fe'-N) [Å][a]	1.666(2)	1.676	1.709(5)	1.681	1.720(7)	1.728
Fe'disp [A][b]	0.518	0.515	0.531	0.517	0.851	0.864
(N2S2) [A][c]	0.094	0.118	0.114	0.103	0.058	0.114
τ value [192]	0.18	0.21	0.21	0.18	0.11	0.2
∠ (Fe'-N-O) [°]	171.1(2)	161.6	149.9(4)	149.4	171.4(7)	170.0
ν(NO) [cm^{-1}][d]	1779	1868	1668	1734	1637	1675

[a] Fe" to N distance in MNIU. [b] The distance between apical Fe" and the mean place of the N_2S_2 chelating ligand of the MNIC. [c] The (un-signed) average displacement of two sulfur and two nitrogen atoms from the N_2S_2 mean place. [d] Calculated numbers are unscaled.

EPR Studies

The transverse mode EPR spectra shown in Figure S6 (panel **A**) confirm that the *g* = 2.024 (*S* = 1/2) species observed for **1⁰** (trace [***α***]), is abolished upon reduction of the complex. Instead, two new

signals are observed with *g*-values near 2.0, albeit at significantly reduced intensity relative to the starting $\mathbf{1^0}$ complex. Both signals follow Curie law behavior and collectively account for <13% of initial $\mathbf{1^0}$ concentration. Further discussion of these $S = 1/2$ species is given in the EPR spectroscopy section in the Supporting Information.

As the anticipated spin for $\mathbf{1}^-$ is an integer value ($S = 1$), EPR data were also collected with the microwave polarization parallel to the static magnetic field ($B_1 \parallel B_0$) using a Bruker bimodal resonator (4116DM). As shown in Figure S6, panel **C** (trace [***d***]), a broad signal can be observed in samples of $\mathbf{1}^-$ with an observed *g*-value of 4.0. This signal is consistent with the presence of an $S = 1$ spin-state.[261, 296] The temperature-normalized signal intensity shown in Figure S7 illustrates that the greatest intensity occurs at the lowest temperature (4.2 K) and decreases with increasing temperature. Therefore, this transition must originate from within a ground state doublet of a "non-Kramers" center. Within the "good quantum number" regime,[84, 297-299] this is represented by the $|\ m_s > = \pm 1$ eigen states. The value of the axial zero field splitting term ($D = -35 \pm 3\ cm^{-1}$) was determined by fitting this data to a Boltzmann population distribution for a 2-level system (Figure S7, solid line). Figure S6C (trace [***d***], dashed line) illustrates the simulated parallel mode EPR spectrum for $\mathbf{1}^-$ utilizing the experimental determined *D*-value and a small rhombic distortion near the axial limit (*E/D*, 0.003). This simulation also includes distributions in *E/D* ($\sigma_{E/D} = 0.02$) in order to accurately reproduce the spectral line width. From this analysis, the concentration of 1^- determined by simulation is 19 ± 5 mM. After subtraction of the afore-mentioned $S = 1/2$ impurities, the calculated concentration of this triplet signal accounts for nearly 90% of the expected $\mathbf{1}^-$ concentration based on mass balance. These studies indicate nearly stoichiometric formation of a triplet spin-state upon reduction of $\mathbf{1^0}$. This conclusion is supported by magnetic susceptibility measurements, which indicate a range of 2.56–2.92 BM for the effective magnetic moment, Figures S8–S9. A summary of all EPR data is provided in Table S1.

X-ray Diffraction Analysis

The molecular structures of the bme-dach analogue of the cationic **1*$^{+}$** and the neutral, singly reduced **1*^{0}** complexes were reported earlier.[287] Using the bme-dame N_2S_2 ligand, crystals suitable for X-ray diffraction analysis of **1**$^{+}$, **1**^{0} and **1**$^{-}$ were obtained; detailed procedures and crystallographic reports are in the Supporting Information, Figures S10–S15 and Tables S2–S5. Selected metric parameters are listed in Figure 2 and Table 1. Note especially the Fe'-*N*-O angle within the square pyramidal MNIU (τ values of 0.1 to 0.2) increases from the unbound metallodithiolate ligand (ca. 155.2°)[291] to 171.1° in **1**$^{+}$ as electron density is withdrawn on binding to the cationic DNIC unit. Consistent with conventional perception of M-*N*-O angles, on reduction of the DNIC unit the added electron density found in **1**^{0} diminishes the Fe'-*N*-O angle of the MNIU to 149.9°; the displacement of Fe from the best N_2S_2 plane increases by 0.013 Å. As the second electron is added, and largely localized on the MNIU, vide infra, a much larger Fe_{disp} of 0.32 Å is concomitant with much smaller shifts in ν(NO). Notably, the Fe-*N*-O angle increases in **1**$^{-}$, in fact it returns to 171° as seen for **1**$^{+}$. That is, the anionic $Fe(NO)^8$-$Fe(NO)_2^{10}$ complex showed marked linearity in the Fe'-*N*-O angle of the MNIU which is a rare example of a high spin, non-heme, linear $Fe(NO)^8$ species. It is further distinctive in that the reduced iron nitrosyls are adjacent within a diiron complex.

Computational Modeling

Density functional theory (DFT) calculations were applied to **1**$^{+}$, **1**^{0} and **1**$^{-}$ to clarify the electron partitioning between iron and nitrosyl(s), and to correlate this partitioning with the geometric changes, particularly the changes in the Fe'-*N*-O angle. All energies reported are Gibbs free energy, calculated for CH_2Cl_2 solvation.

The MNIU and DNIU electronic states, energies and structural consequences

Consistent with the diamagnetism of complex **1**$^{+}$, computations predict a singlet ground state with the broken-symmetry[300] (BS) singlet, 2.0 kcalmol^{-1} more stable than the triplet and 10.0 kcalmol^{-1} more stable than the closed-shell (CS) singlet. The BS singlet features anti-ferromagnetically coupled $Fe(NO)^7$ and $Fe(NO)_2^9$ spin centers[287] with the iron atoms separated by 2.834 Å.

Two successive reductions of **1**$^{+}$ produce **1**^{0} and **1**$^{-}$, respectively, with the added electrons assigned to the $Fe(NO)_2^{9/10}$ and the $Fe(NO)^{7/8}$ moieties, respectively. In agreement with the experimental results, the calculations show that complex **1**^{0} is a doublet with one unpaired electron in the $Fe(NO)^7$ moiety, while complex **1**$^{-}$ is a triplet, with two unpaired electrons in the $Fe(NO)^8$ unit. The calculations also corroborate changes in the Fe-*N*-O angle: 170.0° (expt.: 171.4°) in **1**$^{-}$, 149.4° (expt.: 149.9°) in **1**^{0}, and 161.6° (expt.: 171.2°) in **1**$^{+}$. The SP structure of the $Fe(NO)(N_2S_2)$ fragment is maintained throughout the three redox levels (τ values[301] in Table 1). The largely linear $Fe(NO)^8$ moiety in square pyramidal geometry is reproduced, along with the displacement of Fe from the mean N_2S_2 plane: 0.864 Å (expt.: 0.851 Å) in **1**$^{-}$, 0.517 Å (expt.: 0.531 Å) in **1**^{0}, and 0.515 Å (expt.: 0.518 Å) in **1**$^{+}$. The Fe'-*N*-O angle and the Fe'_{disp} are closely coupled and related to the electronic structures of **1**$^{+}$, **1**^{0} and **1**$^{-}$, vide infra.

The $Fe(NO)^7$ moiety in **1**$^{+}$ and **1**^{0} have one unpaired electron in the d_z2 orbital with a d-configuration of $(d_{x^2-y^2})^2(d_{xz})^2(d_{yz})^2(d_{z^2})^1(d_{xy})^0$.[302] (The electrons are arbitrarily assigned to the iron regardless of the electron partitioning between Fe and NO; note the coordinate definition in Figure 3C.) In the subsequent reduction of **1**^{0}, the incoming electron is added to the Fe(NO) fragment's d_{xy} orbital, that is, the antibonding orbital from N_2S_2 s-donations. This reduction results in an overall configuration of $(d_{x^2-y^2})^2(d_{xz})^2(d_{yz})^2(d_{z^2})^1(d_{xy})^1$ in the Fe(NO)8 moiety of **1**$^{-}$. The d_{xy} has no direct overlap with the nitrosyl, this assignment justifies the small shift of NO vibrational frequency of the Fe(NO) moiety, 59 cm^{-1} (expt.: 31 cm^{-1}) after reduction of **1**^{0}, in contrast to the shift of the mononitrosyl by 134 cm^{-1} (expt.: 111 cm^{-1}), from

$\mathbf{1}^{+}$ to $\mathbf{1}^{0}$ given that the reduction happens on the $Fe(NO)_2$ moiety. However, because the d_{xy} is strongly destabilized, the Fe(NO) system further changes its structure to better accommodate the added electron; see next Section.

Spin Polarization, Orbital Overlap in π-Back-Bonding and the Interplay between Electronic and Geometric Structures

Although the unpaired electron on the $\mathbf{1}^{0}$ is formally on the iron of the $Fe(NO)^7$ moiety, the spin polarizes such that both iron atoms share the same spin alignment, Figure 3A. For the $Fe(NO)^8$ moiety of $\mathbf{1}^{-}$, significant spin polarization (Figure 3B, also see Figure S16) occurs in the p-back-bonding orbitals formed by the overlap of the d_{xz} and d_{yz} orbitals on Fe and the $2p_x$ and $2p_y$ orbitals of NO, such that the Fe's spin density is 3.0, while the spin density of its NO is -1.2. Although the $Fe(NO)_2^{10}$ moiety is saturated, it also shows Fe/NO spin-polarization (Figure 3B) as well. Such spin-polarization indicates that the nitrosyls withdraw electron density, of one spin preferably, from the iron atoms to stabilize the electron-rich system and the electrons of the opposite spin localize on each iron to take advantage of iron's high exchange energy. The corresponding singlet of $\mathbf{1}^{-}$, which eliminates the spin-polarization and pairs the two above-mentioned unpaired electrons in the d_{z^2} orbital of the $Fe(NO)^8$ unit, is 16.5 $kcalmol^{-1}$ higher than the triplet.

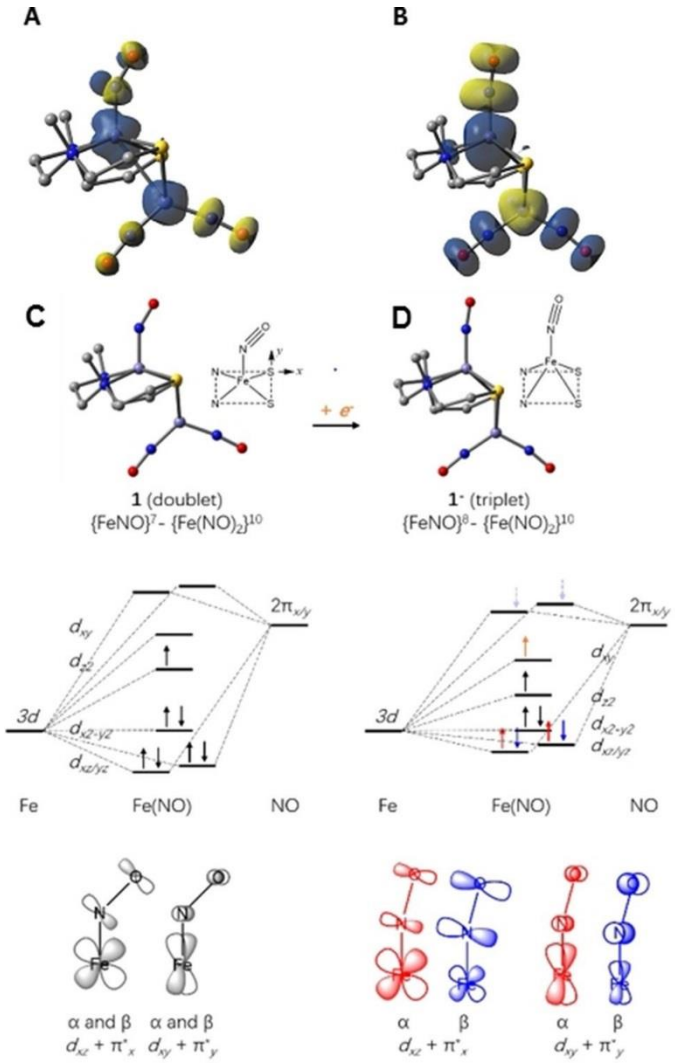

Figure 4.15 Spin density plots (isovalue=0.005 a.u.) of A) 1^0 and B) 1^-; C),D) The geometric and electronic structure changes after the reduction of 1^0 into 1^-.

Figure 4 sketches how individual d orbitals of a metal in the SP geometry interact with orbitals of an axial NO and their geometric preferences.[32] The d_{xz}, d_{yz} orbitals, if occupied, prefer a linear NO (180°) to maximize their p-back-bonding. Such a linear structure also helps the NO donate electron density from its 5s into the iron's d_z^2, should it be empty. In contrast, a doubly-occupied d_z^2 would benefit from a bend in the NO, typically 120°-130° for the doubly-occupied d_z^2, so that the over- lap between d_z^2 and NO's 2p can be established to conduct s back-bonding. In addition, this bending of NO also helps stagger

the occupied d_{z^2} away from NO's 5s donor orbital. The same preference, though less prominent, is applicable to a singly occupied d_{z^2}.

The cationic $\mathbf{1}^{+}$ and neutral $\mathbf{1}^{0}$, featuring a $Fe(NO)\}^{7}$ unit with only one electron in d_{z^2} and no electrons on d_{xy}, show subtle changes of the Fe-*N*-O angle. In $\mathbf{1}^{+}$, the singly occupied d_{z^2} would prefer a bent Fe-*N*-O angle. However, it is spin paired with the electron on the $Fe(NO)_2^{9}$ and delocalizes *away* from the attached NO, which results in a wider angle of 161.6° (expt.: 171.1°). The incoming electron in the reduction of $\mathbf{1}^{+}$ is accepted by the $Fe(NO)_2^{9}$ moiety, which eliminates the spin-pairing between two iron atoms and, in response, the now more electron rich $Fe(NO)\}^{7}$ bends the Fe-*N*-O angle to 149.4° (expt.: 149.9°). When the next electron is added to the high-lying d_{xy} of $\mathbf{1}^{0}$, the Fe moves further out of the N_2S_2 plane by 0.347 Å (expt. 0.32 Å) with elongated Fe-N(N_2S_2) and Fe-S(N_2S_2) bond lengths to stabilize the d_{xy} orbital. The NO also responds to the now elevated electron density in the $Fe(NO)^{8}$ moiety of $\mathbf{1}^{-}$ by restoring a more linear Fe-*N*-O angle (170.0°, expt.: 171.4°), which helps achieve the maximal back-bonding from the doubly occupied d_{xz} and d_{yz} instead of the singly occupied d_{z^2}, and relieve the electron crowdedness on the iron. Significant spin-polarization was observed between Fe and NO as part of the efforts to stabilize the electron-rich system, Figure 3B. It verifies the idea that the d orbital preference over the Fe-*N*-O angle (Figure 4) is biased by its occupancy number. The computationally modelled singlet state $\mathbf{1}^{-}$ with doubly occupied d_{z^2} and vacant d_{xy}, shows a sharply bent Fe-*N*-O angle of 131.0° and a smaller Fe displacement from the N_2S_2 plane (0.585 Å, as compared to 0.864 Å of the triplet). Many $Co(NO)^{8}$ moieties inscribed in SP environments prefer a doubly occupied d_{z^2} (i.e. the same configuration as singlet $Fe(NO)^{8}$) and were experimentally characterized to have bent Co-*N*-O.[303]

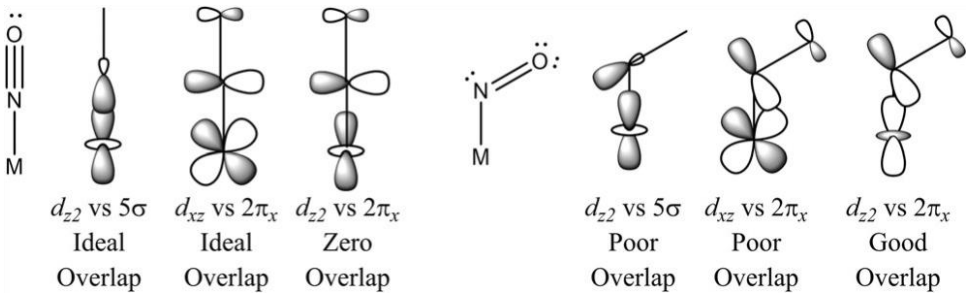

Figure 4.16 Fe'-N-O angle preferences of individual d orbitals with sketches of orbital overlap.

Comments on Another Linear Singlet Fe(NO)^8 System

There could be additional factors stabilizing the M(NO)^n moieties. A linear (169.1°) singlet Fe(NO)^8 moiety in the SP environment was reported in 2016 by DeBeers, Meyer and coworkers.[283] Their Fe(NO) is coordinated by four equatorial carbene carbons from a cyclic chelating $(NHC)_4$ ligand. On reproducing their calculations, we found the doubly occupied d_z^2 orbital is stabilized by π* orbitals of the four N-heterocarbenes, which tilt below the equatorial plane to achieve orbital overlap, Figure S17. Because of this stabilization of the d_z^2, the 2p orbitals of NO interact exclusively with the d_{xz}, d_{yz} orbitals, which lead to a linear Fe-*N*-O angle, despite the singlet configuration.

Remarks

The isolation and characterization of three redox levels of a diirontrinitrosyl complex, **1**$^{+/0/-}$, has revealed important and unanticipated structural changes of the Fe(NO) fragment during redox events. The XRD analysis, solid-state structures, and IR data are consistent with data from EPR spectroscopy, magnetic susceptibility and computational modeling that define the electronic structures of these species. The iron atoms and their bound nitrosyls are capable of reorganizing their orbitals in cooperative structural alterations, and subtle tuning of back-bonding to the NO's so as to rebalance the

electron density. The intriguing interplay again emphasizes the role of the π-acid ligand, nitrosyl, as a buffer of electrons. It is noteworthy that the bimetallic $\mathbf{1}^{+}$ and $\mathbf{1}^{*+}$ are electrocatalysts for H_2 generation; in this regard, the electron buffering capacity of NO was earlier highlighted in the details of our mechanistic study.[287-289] We introduced NO into models of the [FeFe]-hydrogenase enzyme active site with the expectation that it might reproduce the function of the electron reservoir $[Fe_4S_4]$sub-cluster in the H-cluster. Clearly the binding capability of the N_2S_2 unit to both Fe(NO) and $Fe(NO)_2$ persists through two reductions increasing the overall electron count by two. The burden of the redox changes is shared throughout the nitrosylated iron complex, including shifts in the orientation of the N_2S_2 ligand donor orbitals. These results emphasize the importance of the holistic or entire molecular framework.

Nitroxyl Modified Tobacco Mosaic Virus as a Metal-Free High-Relaxivity MRI and EPR Active Superoxide Sensor

*Madushani, D. *et. al.* Nitroxyl Modified Tobacco Mosaic Virus as a Metal-Free High-Relaxivity MRI and EPR Active Superoxide Sensor. *Mol. Pharm.* **2018**, 15, 2973-2983.

Contribution to the collaboration

In collaboration with the Gassensmith group, analytical measurements of the Tobacco Mosaic Virus (TMV) was modified by TEMPO and measured by X-band EPR spectroscopy. In these experiments, verification of attachment of TEMPO to the TMV protein tubule was done by measurement in the anisotropy in the observed *g*-values and hyperfine features of the nitrogen radical species in TEMPO. Comparisons between the free radical and bound TEMPO showed considerable broadening and anisotropy from interactions between the unpaired electron and the change in the local environment of the TEMPO molecule. As presented below, the observed EPR features shifted and shows evidence for the bound interaction between TEMPO and TMV. These signals were simulated and quantitated the effectiveness of TEMPO to attached the TMV surface.

Abstract

Superoxide overproduction is known to occur in multiple disease states requiring critical care; yet, noninvasive detection of superoxide in deep tissue remains a challenge. Herein, we report a metal-free magnetic resonance imaging (MRI) and electron paramagnetic resonance (EPR) active contrast agent prepared by “click conjugating” paramagnetic organic radical contrast agents (ORCAs) to the surface of tobacco mosaic virus (TMV). While ORCAs are known to be reduced in vivo to an MRI/EPR

silent state, their oxidation is facilitated specifically by reactive oxygen species in particular, superoxide and are largely unaffected by peroxides and molecular oxygen. Unfortunately, single molecule ORCAs typically offer weak MRI contrast. In contrast, our data confirm that the macromolecular ORCA-TMV conjugates show marked enhancement for T_1 contrast at low field (<3.0 T) and T_2 contrast at high field (9.4 T). Additionally, we demonstrated that the unique topology of TMV allows for a "quenchless fluorescent" bimodal probe for concurrent fluorescence and MRI/EPR imaging, which was made possible by exploiting the unique inner and outer surface of the TMV nanoparticle. Finally, we show TMV-ORCAs do not respond to normal cellular respiration, minimizing the likelihood for background, yet still respond to enzymatically produced superoxide in complicated biological fluids like serum.

Introduction

The upregulation of reactive oxygen species (ROS), in particular, superoxide, is associated with certain cancers,[1,2 304, 305] neurodegenerative disorders[1,3,4 304, 306, 307] such as Parkinson's disease,[5 308] diabetes,[6,7 309, 310] mitochondrial diseases such as Friedreich ataxia,[8 311] Leber's hereditary optic neuropathy (LHON),[9 312] mitochondrial encephalomyopathy, lactic acidosis, stroke-like episodes (MELAS),[10 313] myoclonic epilepsy with ragged red fibers (MERRF),[11 314] and Leigh syndrome (LS).[3,4,12,13 306, 307, 315, 316] The detection of superoxides, both extra and intracellularly, has consequently become an area of research interest in efforts to study and target diseased tissues.[14,15 317, 318] Superoxide sensing in biological tissues has focused mainly on fluorescent imaging, as many dyes are easily quenched in the presence of ROS,[16,17 319, 320] and superoxide in particular.[18 321] Moreover, the superoxides produced by people with diabetes can cause serious health complications such as heart injuries, and sensing of superoxide overproduction in these situations is also done using fluorescence imaging.[19,20 322, 323] An

unavoidable issue with fluorescence imaging in general, however, is limited tissue penetration, making it problematic for tissue imaging but ideal in guided surgery applications. Consequently, the need to detect cellular and biological events in deep tissue noninvasively has driven the development of "smart" probes for magnetic resonance imaging (MRI)[21–23 324-326] or electron paramagnetic resonance (EPR) modalities.[14,24 317, 327] On the MRI front, paramagnetic chemical exchange saturation transfer (paraCEST) and other stimuli-responsive contrast agents have begun to generate considerable interest for their ability to detect changes in extracellular pH or production of specific biological markers like lactate.[25–27 328-330] While redox active paraCEST agents based on lanthanides have emerged as potential sensors of singlet oxygen[28 331] and peroxide,[29 332] none have clearly emerged as candidates for superoxide.[25 328] Paramagnetic nitroxide organic radical contrast agents (ORCAs), on the other hand, have been making inroads toward superoxide detection in vivo and in vitro.[14,30–32 317, 333-335] While sterically unencumbered nitroxide radicals like TEMPO (Figure 1b)

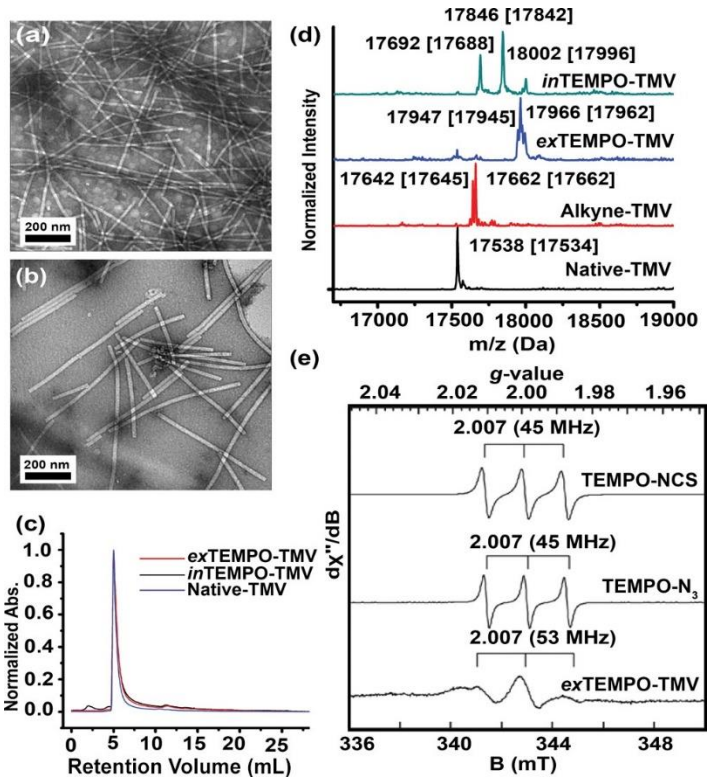

Figure 4.17 Characterization of TMV after bioconjugation reactions. The TEM images of (a) exTEMPO-TMV and (b) inTEMPO-TMV shows the expected rod-like morphology. (c) A single peak in the SEC chromatogram (at 260 nm) of modified TMV confirms that the solution dispersity was unchanged. (d) Bioconjugation of the TEMPO radical to the TMV was characterized by ESI-MS. Native TMV has a peak at 17 538 m/z. The loss of this peak and emergence of a new peak at 17 662 m/z confirms that TMV was completely modified to alkyne-TMV. ESI-MS of exTEMPO-TMV shows complete conjugation of TEMPO-N_3 to the alkyne-TMV. The peak at 17 966 m/z represents the attachment of the TEMPO radical to the TMV coat protein, whereas the peak at 17 942 m/z is the attachment of the TEMPO radical to the alkyne group with an unidentified elimination first noted by Francis (see ref 44) that has taken place during diazonium reaction. The interior surface of TMV consists of several glutamate residues, and three sites were modified via EDC coupling with TEMPO・one (17 692 m/z), two (17 846 m/z), or three (18 002 m/z) TEMPO molecules were installed. (e) X-band EPR spectra of exTEMPO-TMV. The exTEMPO-TMV sample was prepared in a capillary tube to minimize interaction between high dielectric aqueous solvent and the electric field of the incident microwave radiation.

are easily reduced to diamagnetic hydroxylamines in biological media, making their use as long-lived MRI contrast agents problematic, this property has been utilized to map redox activity in tumors ex vivo and in vivo.[33 336] On the other hand, reoxidation is kinetically favored by superoxide, while less reactive ROS, and in particular hydrogen peroxide, do not significantly oxidize hydroxylamines back.[1 304] Consequently, TEMPO can serve as a "turn-on" MRI sensor for superoxide.

The benefit of "turn-on" over "turn-off" sensors is that they can have nearly infinite contrast against background.[34 337]

Nevertheless, ORCAs have historically suffered from low proton relaxation rates compared to metal-based contrast agents. These poor relaxivities have been cleverly addressed using polymeric systems,[33,35–39 336, 338-342] as these multivalent scaffolds allow for high local concentrations of paramagnetic ORCAs. While such multimeric polymeric scaffolds allow for attachment of both MRI and fluorescence agents on the same platform, ORCAs are well-known and potent quenchers of adjacent fluorophores.[33 336] This quenching process means that when an ORCA is MRI/EPR active, adjacent fluorophores are typically quenched. While this has been elegantly exploited,[32,33,40,41 335, 336, 343, 344] a true ratiometric sensor capable of assessing the probe concentration by fluorescence and the relative ROS levels by EPR/MRI signal would require a constant fluorescence emission regardless of the oxidation state of the ORCA.

Viral nanoparticles (VNPs) provide distinct structural features that make them well-suited to resolving some of these issues. For instance, they contain spatially well-defined functionalities, are rigid and monodisperse, and contain discrete topological surfaces that provide a distinct "outer" and "inner" surface.[42 345] These distinctions are well-suited for EPR active spin systems prone to spin pairing and relaxation when in close contact with other radical species.[25 328] Tobacco mosaic virus (TMV) is a 300 × 18 nm rod-shaped RNA virus that contains 2130 individual coat proteins.[43–45 346-348]

Each of these coat proteins contains an easily functionalizable tyrosine residue (Y139) on the exterior surface, which is spatially separated from the next closest accessible tyrosine[46 349] by 2.3−2.6 nm.[47,48 350, 351] Furthermore, TMV contains a 4 nm narrow pore lined with glutamic acid residues (E97 and E106), likewise easily functionalized, and electronically inaccessible to the exterior surface.[49–51 352-354] These features provide two distinct advantages over existing polymeric nanostructures containing nitroxide radicals: (i) radical systems on the surface are spaced far enough apart so that spin−spin coupling is minimized even if 100% of the available functional groups are utilized, and (ii) fluorophores placed on the interior of the capsid will not be quenched by electron transfer processes from radical TEMPO moieties placed on the exterior surface. Previous studies have shown that VNPs and virus-like particles (VLPs) decrease the T_1 and T_2 relaxation times of attached metal-based MRI contrast agents.[41,48,52–63 161, 344, 351, 355-365] The increase in r_1 ($1/T_{1p}$, p = paramagnetic contribution; $mM^{-1}{\cdot}s^{-1}$) relaxivity in these systems has been attributed to an increase in molecular diffusion and translation correlation times brought about by attachment to the surface of relatively massive, rigid, and slowly diffusing protein ensembles.

Here we present a method to create a sensitive EPR/MRI probe for superoxide detection in vitro with enhanced r_1 and r_2 relaxivities that rival clinically used molecular lanthanide-based MRI probes. The observed r_2/r_1 ratio allows TEMPO- conjugated TMV probes to operate as both a T_1 and T_2 contrast agent, making these probes valuable for both clinical (<3 T) and preclinical (>3 T) MRI scanners. We have also designed a bimodal TEMPO-TMV probe for ratiometric fluorescence experiments that is functionalized with a fluorescent dye on the interior and with an ORCA for MRI/ EPR imaging on the exterior. The unique topology of the VNP scaffold allows for the insertion of an internal fluorescent probe as a concentration marker that is insensitive to the oxidation state of the ORCA probe. Finally, we present the evaluation of these probes in both cells and serum.

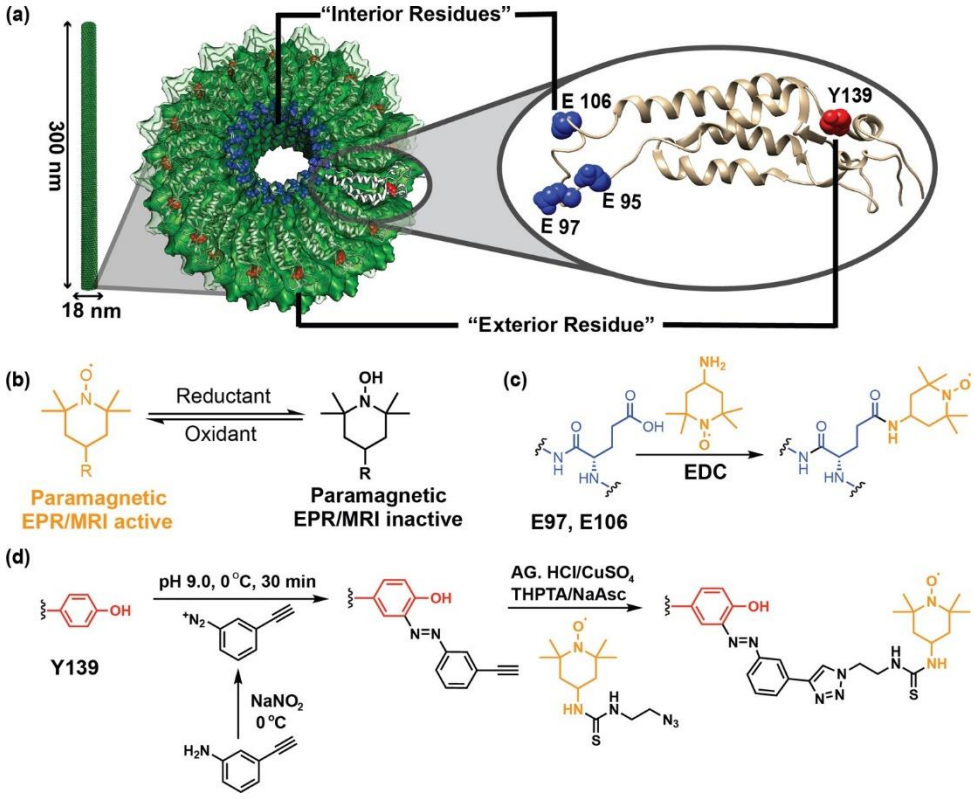

Scheme 4.3 Representations of a Single TMV Nanoparticle[a] and a Single TMV Coat Protein Highlighting Solvent Exposed Amino Acid Residues Available for Bioconjugation Reactions, (b) Oxidation States of Nitroxide Radicals,[b] (c) Bioconjugation to the Interior Surface of TMV via EDC Coupling Reaction To Make inTEMPO-TMV, and (d) TMV Bioconjugation on the Exterior via Stepwise Diazonium Coupling Followed by a CuAAC Reaction To Make exTEMPO-TMV. [a]Created in Chimera using PDB ID of 2tmv. [b]Paramagnetic radical species can be detected by both EPR and MRI, whereas the reduced diamagnetic species is neither MRI nor EPR active.

Results and Discussion

Attaching ORCA to the Surfaces of TMV. As shown in Scheme 1a, TMV contains two distinct surfaces: (i) an outer surface with few charged functional groups and uninhibited access to bulk water and (ii) a 4 nm narrow inner channel with a net negative surface charge and less access to diffusing bulk water. We thus first set to determine if there would be any difference in measured relaxivities if ORCAs were placed on the inner vs the outer surface of TMV. The interior surface of TMV contains solvent exposed glutamic acid residues, which we functionalized via EDC coupling with TEMPO-NH_2 (Scheme 1c). High-performance liquid chromatography/electron spray ionization mass spectroscopy (HPLC/ESI-MS) confirms that three sites were modified following the EDC coupling reaction to yield inTEMPO-TMV. As shown in Figure 1d, peaks at 17 692 Da, 17 846 Da, and 18 002 Da represent the attachment of one, two, and three molecules of TEMPO, respectively, to the coat protein monomers of TMV. While only glutamate residues E97 and E106 have been identified as reactive sites,[49 352] the third peak at 18 002 Da likely corresponds to E95. Though three conjugations to this inner channel have been observed[55 357] before, the residue of the third modification site has never been identified. Separately, the exterior surface of TMV was functionalized initially using a diazonuim coupling reaction[49 352] (alkyne-TMV) with in situ prepared 3-ethynylphenyldiazonium salt. This quantitative reaction was followed by a coppercatalyzed azide−alkyne cycloaddition[64 366] (CuAAC) with TEMPO-N_3 to yield exTEMPO-TMV (Scheme 1d).

The TEMPO radical is known to be reduced in the presence of sodium ascorbate, so we modified a procedure initially described by Finn[65 367] by forming Cu^{I}(THPTA) separately by mixing a 1:5:1 molar ratio of Cu^{II} sulfate, the ligand THPTA, and sodium ascorbate in water. Starting with Cu^{II} sulfate as opposed to directly using a Cu^{I} source to form the Cu^{I}(THPTA) complex provided consistently high yields, likely because of the more favorable aqueous solubility of Cu^{II} sulfate. This solution was transferred quickly in open air to an aqueous solution of TMV under N_2. Degassing of solutions were not necessary,

and the successful attachment of the new functional groups was again confirmed by HPLC/ESI-MS. As shown in Figure 1d, after the quantitative diazonium coupling reaction, all of the TMV coat protein monomers were modified to the azo adduct (17 666 Da) in line with previous literature reports.[66 368] The CuAAC reaction on the alkyne-TMV with TEMPO-N_3 proceeded quantitatively, evidenced by the loss of the alkyne peak at 17 666 Da. The morphology and dispersity of TMV were checked after each bioconjugation reaction and were found unchanged by transmission electron microscopy (TEM) and size exclusion chromatography (SEC), respectively (Figures 1a−c and S11).

Finally, EPR spectroscopy was used to characterize the presence of paramagnetic species on the TMV surface. As shown in the Figure 1e, small molecule TEMPO radicals

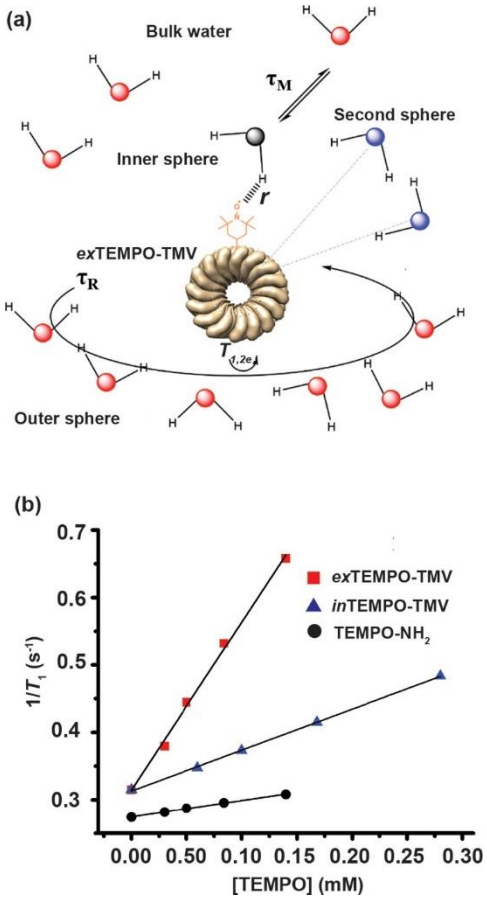

Figure 4.18 (a) Schematic representation of the exTEMPO-TMV with one coordinated water molecule (inner-sphere water, its oxygen is colored black) in solution (bulk water, oxygens are red). Second sphere water molecules (water oxygens are blue). The parameters that govern the relaxivity are also represented: NO−H distance (r), the mean lifetime (τ_m) of the water molecule(s) in the inner sphere, the rotational correlation time (τ_R), and the electronic spin relaxation times (T_{1e} and T_{2e}). (b) Plot of $1/T_1$ (s^{-1}) versus TEMPO concentration (mM) for exTEMPO-TMV, inTEMPO-TMV, and TEMPO-NH_2 at 23 MHz in 0.1 M pH 7.4 KP buffer and 310 K.

showed a characteristic ^{14}N-triplet (I = 1; A ~ 45 MHz) centered at a g-value of 2.007, which is typical of the nitrogencentered radical. The sharp line width and isotropic g/A-values are consistent with rotational averaging. By contrast, the exTEMPO-TMV (Figure 1e) and inTEMPO-TMV (Figure S12) results in significantly broader and more anisotropic EPR spectra. The distributed g/A-values and attenuated signal intensity are attributed to decreased rotational and translational mobility of the radical. This significantly increases the observed line width of the mobilized radical. High density of radicals can also result in dipolar spin−spin exchange, which also contributes to the increased line width.

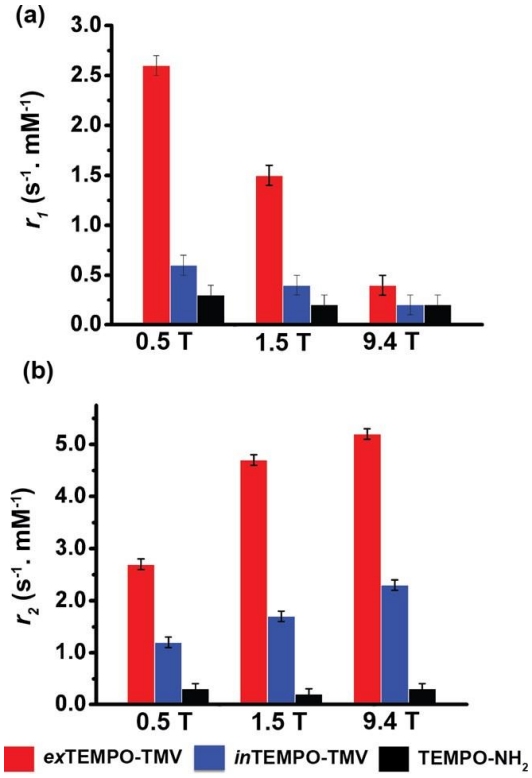

Figure 4.19 Determined (a) r_1 and (b) r_2 relaxivities for the agents exTEMPO-TMV, inTEMPO-TMV, and TEMPO-NH_2 at different fields in 0.1 M pH 7.4 KP buffer and 310 K.

Proton Relaxation Properties of ORCA Loaded TMV Rods.

To characterize the relaxation behavior of the TEMPO-TMV particles, we performed proton relaxometric measurements at different fields. It is worth noting that nitroxide radicals normally bind noncovalently

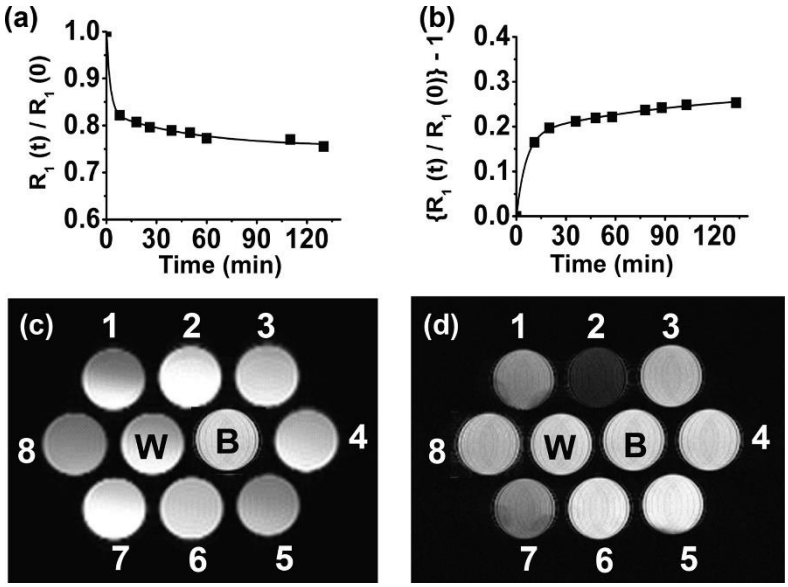

Figure 4.20 (a) Evolution of the relative water proton paramagnetic relaxation rate of a 0.14 mM aqueous solution of exTEMPO-TMV in the presence of 100-fold molar excess of ascorbate. Plot normalized to the initial value $R_1^{(t)}/R_1^{(0)}$ as a function of the time (min) and measured at 23 MHz, 0.1 M pH 7.4 KP buffer, 310 K. (b) Evolution of the relative water proton paramagnetic relaxation rate of a 0.14 mM aqueous solution of exTEMPO-TMV (reduced) in the presence of 100-fold molar excess of KO_2. Plot normalized to $(R_1^{(t)}/R_1^{(0)} - 1)$ as a function of the time (min) and measured at 23 MHz, 0.1 M pH 7.4 KP buffer, 310 K. The solid lines through the data points represent the pseudo-first-order reaction fits. (c) T_1-weighted and (d) T_2-weighted fast spin−echo images (TE = 200 ms) of (1) exTEMPO-TMV oxidized with KO_2, (2) exTEMPO-TMV (0.14 mM/TEMPO), (3) exTEMPO-TMV reduced with ascorbate, (4) ascorbate in PBS, (5) TEMPO-NH_2 (1.4 mM), (6) TEMPO-NH_2 (0.14 mM), (7) inTEMPO-TMV (0.14 mM/TEMPO), (8) KO_2 in PBS, (W) water at pH 7.0,

to at least one water molecule,[67 369] which is similar to that found with metal-based complexes with one or more water molecules coordinated to the inner sphere of the metal centers.[34,68 337, 370] The overall proton relaxation behavior is determined by the sum of the inner-sphere and outer-sphere contributions.[34 337] While the outersphere contributions cannot be neglected, the inner-sphere

contributions are typically dominant.[69 371] For nitroxide radicals, under the extreme narrowing condition,[70,71 372, 373] the primary innersphere relaxation mechanism is determined by dipolar and Curie dipolar contributions.[72,73 374, 375] However, at higher magnetic fields, line broadening predominantly originates from Curie spin relaxation processes. The dipolar and Curie mechanisms from the inner- and outer-sphere contributions can be modeled as described in previous detailed reports.[73–75 375-377] Large macromolecules, like the TMV presented here, are characterized by slow rotation dynamics in solution[33,35 336, 338] commonly represented by the rotational correlation time (τ_R). Other factors that have a high impact on the relaxation processes for T_1 and T_2 are the electronic relaxation rates ($1/T_{ei}$; i = 1, 2) and solvent exchange lifetimes (τ_m) as defined by the correlation times (τ_{ci}; i = 1, 2)

$$\tau_{ci} = \frac{1}{T_{\mathrm{ei}}} + \frac{1}{\tau_{\mathrm{m}}} + \frac{1}{\tau_{\mathrm{R}}}, i = 1, 2 \qquad (\mathbf{4.2})$$

We can make several simplifying assumptions. In systems where T_e is short, as is the case of TEMPO radicals ($T_{ei} \geq 20$ ns),[39 342] the molecular rotation and water exchange dominate τ_{ci}.The water exchange rate ($k_{ex} = 1/\tau_m$) for nitroxide radicals has been estimated to be quite slow ($k_{ex} \sim 2 \times 10^{-4}$ s),[39 342] and it is expected from theory[76 378] that the low-field total transverse relaxivity (T_2) will be small and similar to the longitudinal relaxivity, since it is modulated by T_e. At higher magnetic fields, the r_2 relaxivity is mostly affected by the square of the field (not r_1) and increases with field strength. As shown in Table S2, exTEMPO-TMV, the most efficient system (Figure 2b), shows a significant increase in r_2 at 9.4 T to 5.2 s^{-1} mM^{-1} per TEMPO compared to lower fields where r_1 and r_2 were similar.

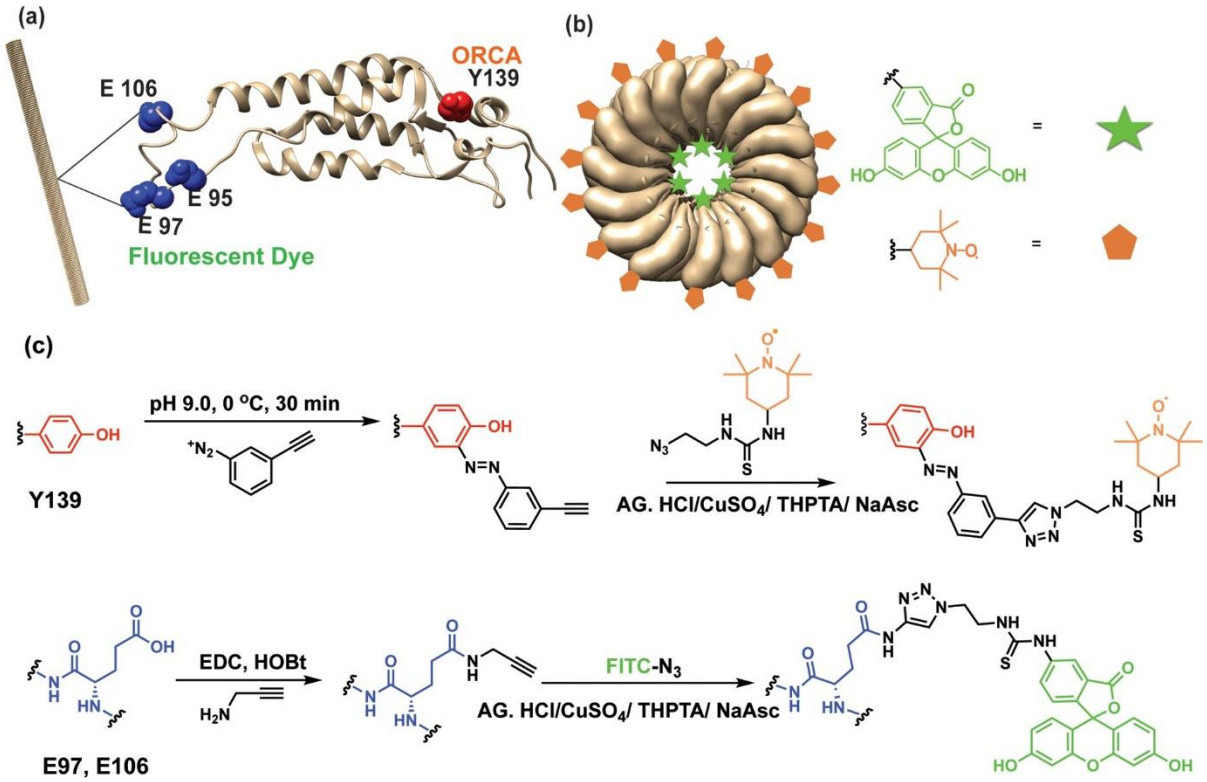

Scheme 4.4 (a,b) inFITC-exTEMPO-TMV Bimodal Imaging Probe and (c) Diagram of TMV Showing the Relative Placement of the Fluorescent Dye on the Interior Residues and the ORCAs on the Exterior[a] The exterior surface was first modified with TEMPO radicals via diazonium coupling followed by a CuAAC reaction, and then, the interior surface of TMV was modified by EDC coupling with propargylamine followed by a CuAAC reaction.

Our data show that the TEMPO-TMV conjugates are efficient T_1 and T_2 contrast agents at low field and present remarkable properties as T_2 agents at high field,[35 338] with the greatest enhancement seen for exTEMPO-TMV (Table S2). Indeed, exTEMPO-TMV shows an enhancement of r_1 and r_2 at low field nearly 1 order of magnitude higher than that of the corresponding small molecule TEMPO-NH_2, and at high-field, the r_2 shows a 13-fold increase compared to that of TEMPONH_2. A comparison of $r_1$and r_2 values for exTEMPO-TMV and inTEMPO-TMV (Figure 3a,b) show that the exterior functionalization yields higher relaxivity values at all fields and both r_1 and r_2 relaxivities compare very favorably to existing polymeric ORCAs and small molecule contrast agents (Table S3).These data suggest that the TEMPO spins located on the inner cavity of the TMV macromolecule may have less access to bulk water

preventing optimal exchange between the innersphere water molecules and those in the close vicinity of the TEMPO spin.[77 379]

Nitroxide-based ORCAs typically undergo rapid reduction to diamagnetic hydroxylamines in the presence of reducing agents such as ascorbate.[78,79 380, 381] Relaxometric studies of exTEMPOTMV, shown in Figure 4a, confirm that, in the presence of an equimolar amount of ascorbate, about 20% of the paramagnetic TEMPO spins on the exTEMPO-TMV are reduced within a few minutes. This was also confirmed by EPR spectroscopy (Figure S13a). As proof of principle that TEMPO-TMV compounds could be used as potent indicators of strong ROS, we performed the relaxometric experiments over the same time span, but in the presence of an excess of KO_2 at 0.4 T. In this case, the T_1 of water protons recovered to nearly the original values (Figure 4b). This same reoxidation experiment was confirmed using EPR spectroscopy (Figure S13b).We investigated the rate of reduction of the exTEMPO-TMV under pseudo-first-order conditions using a 100-fold excess of ascorbate in pH 7.4 phosphate-buffered saline (PBS). Fits were obtained for relaxometric data collected over a 2 h period. Pseudo-first-order rate constants, k', were obtained by following the decay of the $R_1^{(t)}/R_1^{(0)}$ determined by proton relaxometry. Excellent agreement with literature values was found for exTEMPO-TMV and other macromolecules (k' = $17 \times 10^{-4} \pm 0.1\ s^{-1}$) as shown in the Table S4.[33,35,39 336, 338, 342] Conversely, the oxidation of the reduced exTEMPO-TMV hydroxylamine with an excess of KO_2 also showed a quite extensive reaction with a k' = $16 \times 10^{-4} \pm 0.1\ s^{-1}$.

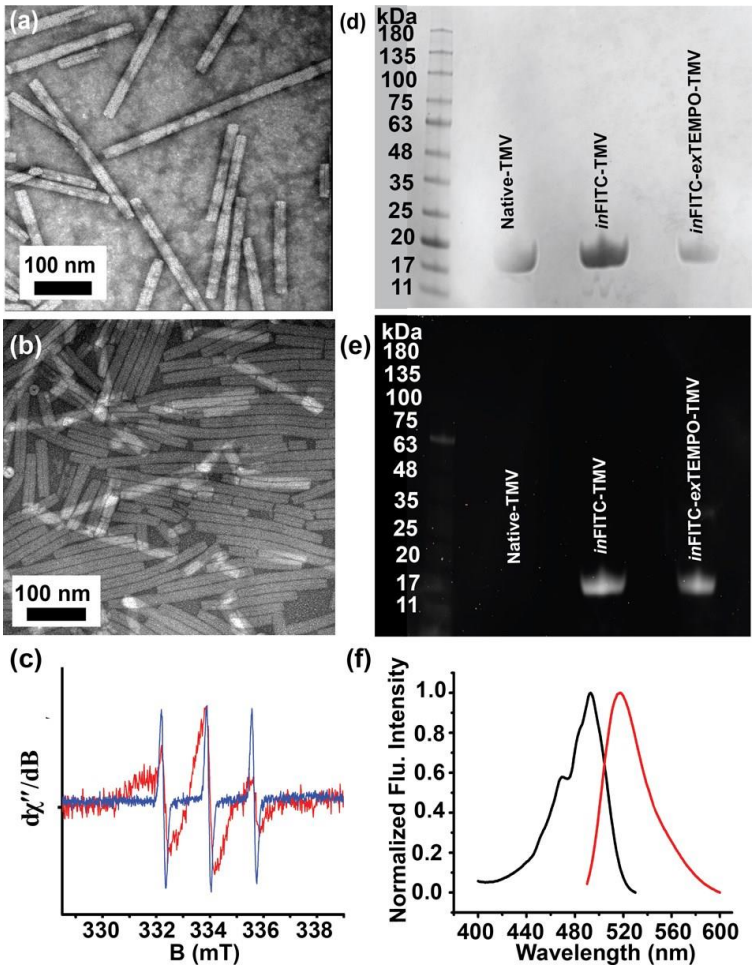

Figure 4.21 Synthesis and characterization of inFITC-exTEMPO-TMV; TEM images: (a) inFITC-TMV, (b) inFITC-exTEMPO-TMV. (c) EPR spectrum of inFITC-exTEMPO-TMV (red) and TEMPO-NH_2 (blue). SDS-PAGE to confirm that FITC has been successfully attached to TMV; SDS-PAGE was visualized by (d) Coomassie brilliant blue and (e) UV. (f) Excitation (black line) and emission (red) spectra of inFITC-exTEMPO-TMV.

In Vitro MR Imaging. In support of these experimental observations, we have performed phantom imaging on several samples containing exTEMPO-TMV, inTEMPO-TMV, reduced exTEMPO-TMV, oxidized exTEMPO-TMV, and standards. T_2-weighted MR imaging at 9.4 T showed that among the 10 tubes, only those containing the nonreduced TMVTEMPOs showed enhanced T_2 contrast, whereas

the free TEMPO (Figure 4d, wells 5 and 6) do not show any contrast difference even when we doubled the concentration of free TEMPO sample (Figure 4d, well 6). While contrast enhancement is evident in the T_1-weighted images (Figure 4c, wells 8 vs 2), the greatest contrast at this field strength comes from the T_2-weighted images (Figure 4d, wells 8 vs 2).These results suggest that these TEMPO macromolecular derivatives can detect changes in superoxides at millimolar concentrations. It also shows the potential of using exTEMPO-TMV as a high- field (T_2) contrast agent.

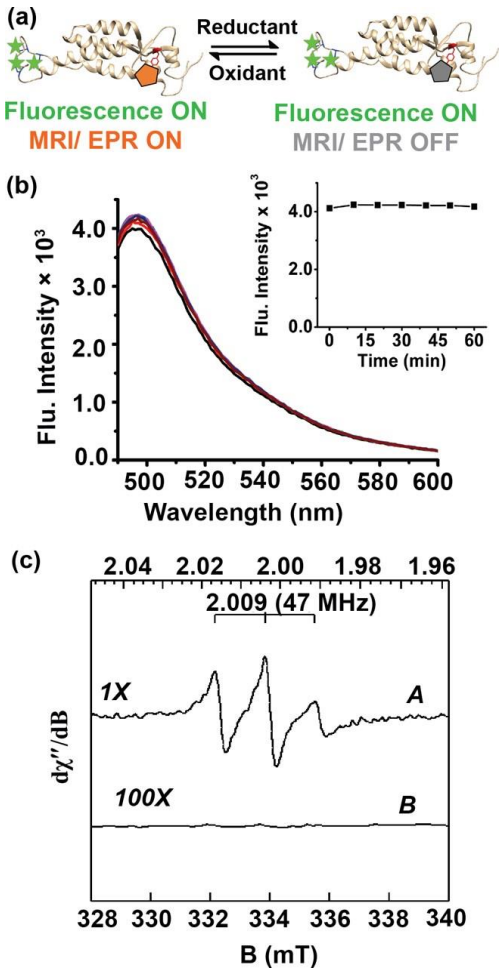

Figure 4.22 Bimodal imaging characteristics of the inFITC-exTEMPOTMV redox probe. (a) Protein crystal structure of a single coat protein of TMV showing the attachment of FITC and TEMPO to the inner (glutamate) and outer (tyrosine) surfaces, respectively. (b) Time dependent emission behavior of inFITC-exTEMPO-TMV redox probe upon addition of 100 eq of ascorbate in 0.1 M pH 7.4 KP buffer. (c) EPR spectra of inFITC-exTEMPO-TMV redox probe before (A) and 60 min after (B) addition of 100 eq of ascorbate in 0.1 M pH 7.4 KP buffer. An identical experiment on Cy5 was conducted, and details are in Figure S13.

This is particularly relevant, because most of clinical MR scanners operate at low fields (0.4−3 T), though implementation of clinical high-field scanners is progressing.

inFITC-exTEMPO-TMV for Bimodal Molecular Imaging.

After confirming that exTEMPO-TMV exhibits better T_1 and T_2 relaxation characteristics compared to inTEMPO-TMV, this compound was used for all additional studies. A second goal of using TMV as a platform was to install a fluorophore for bimodal imaging in a position where it would not be quenched by the TEMPO radicals (Scheme 2). The order of the bioconjugation reactions to the TMV virus surface is important to minimize the redox chemistry on the attached TEMPO. We first functionalized the interior surface with FITC using standard CuAAC conditions and then functionalized the exterior surface with TEMPO radicals using our modified procedure. After each bioconjugation reaction, the integrity of the particle was characterized by SEC and TEM (Figure 5a,b). Moreover, TEMPO radical attachment to the exterior surface was confirmed by EPR spectroscopy (Figure 5c). The attachment of FITC to the interior surface of TMV was confirmed by UV−vis spectroscopy (Figure S14), SDS-PAGE (Figure 5d,e), and fluorescence spectroscopy (Figure 5f). To show this quenching process is not dependent on FITC, we attached a cyanine dye (Cy 5) to the interior as well, and we again observed minimal quenching from the radical (Figures S15−S17).

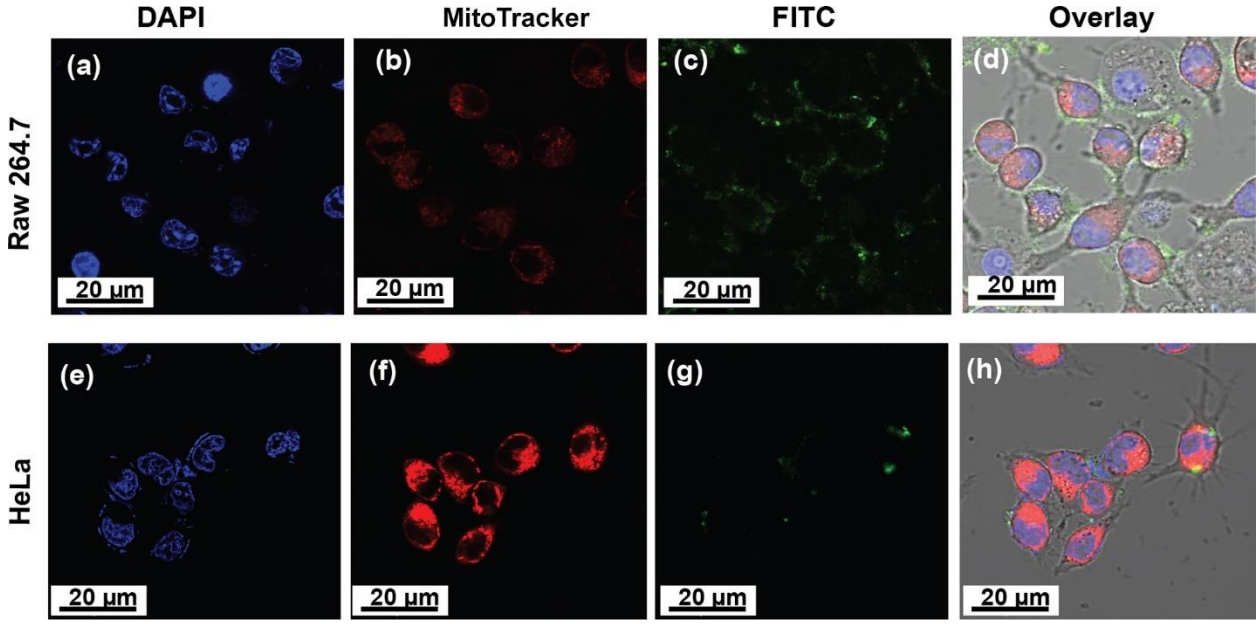

Figure 4.23 Confocal microscopy images of cellular uptake of inFITC-red-exTEMPO-TMV redox probe with (a–d) RAW 264.7 cells and (e,f) HeLa cells. Color code: blue, Hoechst 33342; red, MitoTracker Deep Red; green, inFITC-red-exTEMPO-TMV.

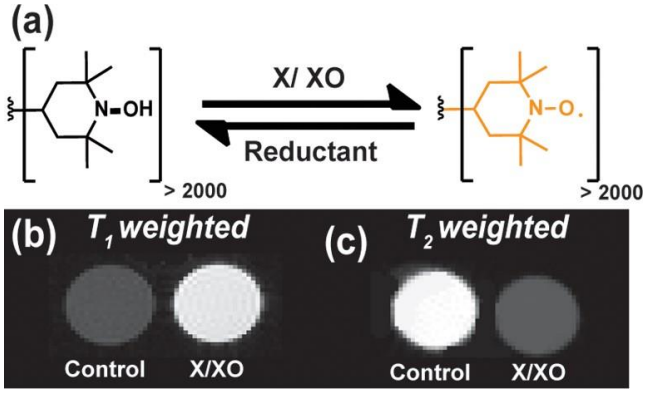

Figure 4.24 (a) Schematic showing the redox behavior of red-exTEMPOTMV. (b) T_1-weighted phantom images and (c) T_2- weighted phantom images before and after addition of X/XO. The concentration of TMV sample was 5.0 mg mL^{-1}, and the reaction mixture consisted of 50% of serum by volume.

Fluorescein and cyanine dyes, like most fluorophores, are known to be quenched by nitroxyl radicals,[33,42,80 336, 345, 382] and the tubelike architecture of TMV allowed us to attach the MRI imaging agent and the fluorescent dye far enough apart to prevent quenching of the fluorescence emission of the dye (Figure 6a). To our satisfaction, we found less than 3% variation in fluorescence when shifting between the oxidized radical to the reduced hydroxylamine (Figure 6b) even after an hour following addition of 100 eq of ascorbate. On the other hand, the EPR spectra (Figure 6c) confirms that the radicals are completely reduced by the ascorbate under these same conditions. We again conducted the same experiment with inCy5-exTEMPO-TMV and confirmed that the oxidation state of the radical does not affect the emission intensity of Cy 5 (Figure S18), showing the generalizability of this approach with different dyes.

In Vitro-inFITC-red-exTEMPO-TMV Studies.

While the ultimate goal is in vivo imaging, in these early studies, we found it important to ascertain their behavior in cells and in serum. Cellular uptake could potentially result in trafficking to organelles normally high in superoxide concentrations, such as mitochondria, and could create an unwanted background signal. Further, uptake by macrophages, which are known to efficiently remove macromolecules and life of these particles and may lead to the formation of antibodies against our probe making their clearance faster.

Studies have shown that macrophages as well as HeLa cells interact less effectively with high aspect ratio nanoparticles, and TMV in particular has been extensively studied.[52,81,82 355, 383, 384] We were curious if we would see uptake with reduced inFITCexTEMPO-TMV (inFITC-red-exTEMPO-TMV) nanoparticles and if this would cause changes in the oxidation state of the ORCA following uptake. We

used confocal microscopy on our “quenchless” system to investigate the interaction between inFITC-red-exTEMPO-TMV and macrophages. The confocal microscopy data shows that inFITC-red-exTEMPO-TMV (Figure 7d) associates with macrophages by adhering to the surface with no obvious fluorescence inside the cells and, in particular, the mitochondria, which are stained red in Figure 7b. We also investigated the cellular uptake of inFITC-redexTEMPO-TMV by HeLa cells (Figure 7e–g) and found no significant fluorescence signal coming from cells (Figure 7g). The lack of interaction with mitochondria was corroborated by EPR spectroscopy. To ensure we would observe signal if any trafficking to mitochondria occurs at all, we stimulated the HeLa and macrophages with the superoxide promotor phorbol 12-myristate 13-acetate (PMA)[83–85 317, 385, 386] and then incubated these cells with red-exTEMPO-TMV for an hour. Cells were collected, and EPR spectra were recorded as a function of time. A lack of an EPR signal over time confirms that redexTEMPO-TMV has not been uptaken by cells (Figure S21). If the red-exTEMPO-TMV had been taken up by the cells and trafficked to an area of ROS activity, we would expect to observe an increase in the EPR signal intensity with time, particularly when the cells were stimulated by PMA.[83 385] These results are promising as it suggests that background signal from cellular metabolism is minimal.

red-exTEMPO-TMV Performance in Serum

Serum is very rich in a variety of proteins that may interfere with superoxide detection either by (i) directly reducing TEMPO to its EPR silent form or (ii) by covering the probe with a layer of protein□commonly called a protein corona□which would inhibit the “turn-on” response. To ascertain if our sensor functions in a biological environment, which might mimic detection of superoxide from tissue damage, for instance, we tested red-exTEMPO-TMV in serum solution using enzymatically produced superoxide. Xanthine/xanthine oxidase (X/XO) was employed as a superoxide generating agent, as it has

been shown[86,87 387, 388] to be a good model of cell-free superoxide generation via EPR/MRI.[1] First, the red-exTEMPO-TMV was made by reduction of exTEMPO-TMV with 0.1 M sodium ascorbate in a suspension of PBS, which was then purged with nitrogen gas to prevent reoxidation. Xanthine (final concentration of 0.05 mM) and red-exTEMPO-TMV (final concentration of 5.0 mg mL^{-1}) were mixed in fetal bovine serum (FBS). Finally, xanthine oxidase (final concentration of 0.1 U/ mL) was added to the mixture. EPR spectra were recorded over 24 h, and MR phantom images were obtained from the same samples. Reoxidation of the probe was evident immediately. The T_1-weighted images and T_2-weighted images for the redexTEMPO-TMV sample with and without X/XO shows a huge contrast difference (Figure 8b,c) clearly indicating that the serum did not prevent detection of superoxide. These changes were confirmed by EPR, which also showed the regeneration of the TEMPO radical by the superoxide formed from X/XO (Figure S22) in the serum solution.

Conclusion

This was a fundamental study of the synthesis, magnetic, and optical characterizations, and in vitro analyses of a new type of a fluorescent/MRI active superoxide sensor that works at both high and low magnetic fields. Our ORCA-conjugated VNPbased nanoparticle probe appears promising for use at both clinical (<3 T) and preclinical (>3 T) MRI fields. Attachment of ORCA to TMV rods resulted in a 10-fold increase in r_1 and a 13-fold increase in r_2 compared to that of the small molecule ORCAs. We have proposed that these increases in relaxivity are ascribed to a decrease in the molecular rotation and diffusional motions brought about by attachment of the ORCA to the large rod-shaped particle. The distinct “inner” and “outer” topology of the TMV permits the creation of a “quenchless” ORCA-based bimodal probe for combined MRI and fluorescence imaging. The probe shows “turn-on” functionality toward enzymatically produced superoxide in the presence of serum, yet does not show appreciable

changes in EPR intensity even when endocytosed by cells, suggesting this probe would be ideal for imaging diffuse tissue injury as may be the case in deep tissue diabetic ulceration or coronary heart disease.

Appendix

Electron Paramagnetic Resonance results of (1) in water and DMF.

As illustrated in Figure S1, below, EPR samples of (**1**) were prepared in both water (trace ***1***) and DMF (trace ***2***) to complement electronic absorption results and verify the (+II) oxidation state and coordination geometry of Co-coordination sphere. The EPR spectrum of aqueous samples of (**1a**) (5 mM) is designated by trace ***1***. This spectrum is consistent with a nearly axial $S = 3/2$ spin state (E/D = 0.05) with observed g-values at 5.5 and 2.04. The line width of this spectrum is dominated by both g-strain and unresolved hyperfine from the ^{59}Co ($I = 7/2$) nucleus. The simulation parameters (*dashed line*) for this species is typical of 5- or 6-coordinate Co(II).[389-393]The temperature-normalized signal intensity for ***1*** decreases with increasing temperature indicating that the $m_s = \pm 1/2$ doublet is the ground state within the $S = 3/2$ spin system. The magnitude of the zero-field splitting parameter (D = 10 ± 3 cm^{-1}) was determined by plotting the EPR signal intensity of this signal versus 1/T and fitting the data to a Boltzmann population distribution for a 2-level system. The EPR simulation (*dashed lines*) for ***1*** shown in Figure 2was calculated using this D-value. For analytical purposes, all data was recorded under non-saturating conditions.

An equivalent sample of (**1b**) (5 mM) prepared in DMF is shown in Figure S4(trace ***2***). Unlike the sample prepared in water, additional features are observed at g-values of 6.40, 5.33, 2.81, 2.04, and 1.70. Additionally, a multiline hyperfine splitting [8.3 mT, 230 MHz] is observed in within the 6.4 <g-value < 4.4 region. These features are reasonably simulated (***S2***) by assuming contributions from two species (***i*** and ***ii***) differing in their rhombicity (E/D-values) of 0.09 and 0.23, respectively. While slightly more rhombic (E/D = 0.09 versus 0.05), the simulation parameters for (***i***) are similar to those obtained for ***S1***. Therefore, it can be concluded that this species is also a 5- or 6-coordinate Co(II)

center. Alternatively, the increased rhombicity (E/D = 0.23) and resolved hyperfine of (***ii***) is **more** consistent with properties reported for tetrahedral Co(II) sites.[389-394]

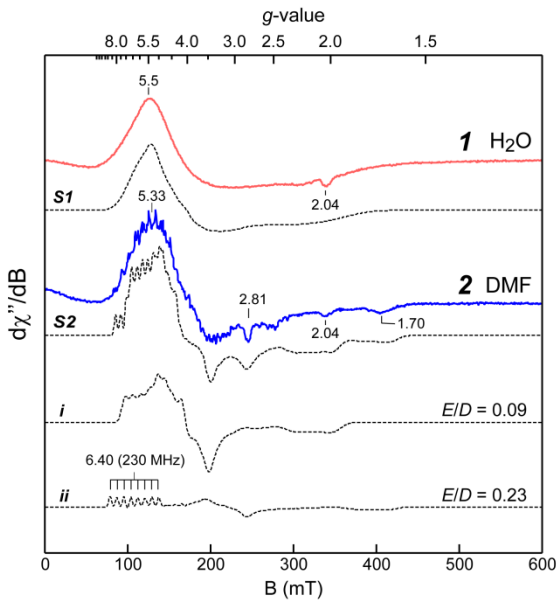

Figure S. 1 10 K X-band EPR spectra of L1-Co and in water (1) and DMF (2). Quantitative simulations (*dashed lines*) for each spectrum are included for comparison. Instrumental parameters: microwave frequency, 9.643 GHz; microwave power, 100 µW; modulation frequency, 0.9 mT; temperature, 10 K. Simulation parameters for each ^{59}Co(II) S = 3/2 (I = 7/2) site:* S1, $g_{x,y,z}$ *(2.01, 2.69, 2.15),* $\sigma_{gx,y,z}$ *(0.09, 0.08, 0.09),* A_{iso}*, (250 MHz),* D *= 10 ± 5 cm^{-1},* E/D *= 0.05;* S2 *(*i*),* $g_{x,y,z}$ *(2.38, 2.34, 2.17),* $\sigma_{gx,y,z}$ *(0.05, 0.05, 0.05),* A_{iso}*, (250 MHz),* D *= 10 ± 5 cm^{-1},* E/D *= 0.09;* (ii), $g_{x,y,z}$ *(2.46, 2.48, 2.04),* $\sigma_{gx,y,z}$ *(0.01, 0.02, 0.03),* A_{iso}*, (230 MHz),* D *= 10 ± 5 cm^{-1},* E/D *= 0.23, 0.1 mT. All simulations utilize a uniform line width (σ_B) of 0.1 mT.

EPR spectroscopy.

X-band (9 GHz) EPR spectra were recorded on a Bruker (Billerica, MA) EMX Plus spectrometer equipped with a bimodal resonator (Bruker model 4116DM). Low-temperature measurements were made using an Oxford ESR900 liquid He/N2cryostat and an Oxford ITC 503 temperature controller.

Unless otherwise noted, a modulation frequency of 100 kHz was used for all EPR measurements. All experimental data used for spin-quantitation were collected under non-saturating conditions as verified by half-power microwave saturation (*P1/2*) measurements. EPR spectra were simulated by diagonalization of the spin Hamiltonian (eq. **1**) using SpinCount ver. 6.1.6682.22252 software (created by Professor M.P. Hendrich, Carnegie Mellon University). Here, ***g*** is the *g*-tensor, and the axial and rhombic zero-field splitting parameters are represented by *D* and *E, respectively*.[14]

$$\mathcal{H} = \mathbf{D}\left[\hat{\mathbf{S}}_{\mathbf{Z}}^{\mathbf{2}} - \frac{S(S+1)}{3}\right] + \mathbf{E}\left(\hat{\mathbf{S}}_{\mathbf{X}}^{\mathbf{2}} + \hat{\mathbf{S}}_{\mathbf{Y}}^{\mathbf{2}}\right) + \beta \boldsymbol{B} \cdot \mathbf{g} \cdot \mathbf{S} \qquad \textbf{(S.1)}$$

This program computes the powder pattern for a uniform spherical distribution of the magnetic field vector *B*, and the transition intensities are calculated using '*Fermi's golden rule*'.[15] The simulations are generated with consideration of all intensity factors, both theoretical and experimental. The concentration of species can be used as a constraint during spectral simulation, which allows quantitative determination of the concentration by comparison of the experimental and simulated signal intensities.[16,17] The only unknown factor relating the spin concentration to signal intensity is an instrumental factor that depends on the microwave detection system. This factor is determined using a Cu(II)EDTA spin standard.[18] Half-power microwave saturation (*P1/2*) values reported for selected samples were determined by collecting scans at increasing microwave power and fixed scan rate and field width. The signal area as a function of microwave power was fit using the SpinCount software package according to eq. **2**.

$$S/\sqrt{P} = \frac{A}{\left(1 + P/P_{1/2}\right)^{b/2}} \qquad \textbf{(S.2)}$$

The software performs least-squares fitting of the normalized derivative signal intensity (*S*) as a function of microwave power (*P*). The A-term represents the normalized maximum signal amplitude. The variable

b is a spectroscopic inhomogeneity factor which is characteristic of the spin packet of the observed resonance. Generally, the signal packet derived from frozen solutions and powders exhibit inhomogeneous line broadening behavior (*b* = 1).

EPR Analysis of S = 1/2 species. As shown in Figure **S3**, panel **A**, samples of $\mathbf{1^0}$ (25 mM in THF) exhibit a broad, nearly isotropic EPR spectrum at *g* = 2.024. This signal exhibits inhomogeneous saturation with a microwave power at half-saturation (P1/2) of 0.7 mW at 10 K. Consistent with an isolated *S* = ½ doublet, no change in the temperature-normalized signal intensity was observed for spectra collected between 4 and 35 K. Spectroscopic simulation (Fig. **S3A**, [***a***], *dashed lines*) of this signal was used to verify the concentration of $\mathbf{1^0}$ present in samples (24.9 mM). Following reduction of $\mathbf{1^0}$, two *S* = ½ signals can be resolved near *g* ~ 2. Similar to trace [***a***], these signals also exhibit Curie-Law behavior within the observed temperature range (4 - 35K). The majority species shown in Fig. **S3B**, (trace [***b***]) exhibits rhombic *g*-values of 2.07, 2.02, and 1.99 and a microwave power at half-saturation (*P1/2*) of 3.6 mW at 10 K. Given that excess reductant (1.3 equiv.) was added to $\mathbf{1^0}$, this (*S* = 1/2) signal, labeled as [***b***] is likely attributed to a fraction of the sample that has decomposed. An additional sharper signal [***c***] can be observed with *g*-values of 2.04, 2.03, and 2.01 (*P1/2* ~ 140 µW at 10 K). Based on similar *g*-values and microwave power saturation behavior, this signal is attributed to the Fe(NO)N2S2 dissociated from $\mathbf{1^-}$.[19,20] Two-component simulations were performed to determine the relative contributions of each species. Following this procedure, the concentration of decomposed complex [***b***] and Fe(NO)N2S2 “free ligand” [***c***] was determined to be 3.01 and 0.14 mM,

respectively. These species account for 12% and 0.6% of the initial complex $\mathbf{1^0}$ concentration and are thus considered minor contaminant.

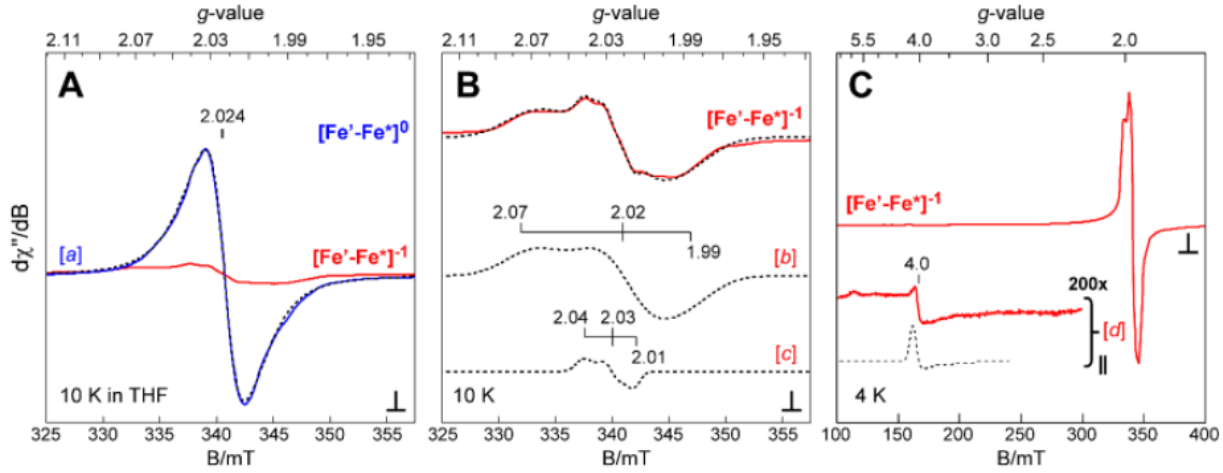

Figure S. 3 X-band spectra of $\mathbf{1^0}$ *(**A**) (blue trace) and* $\mathbf{1^-}$ *(**B** and **C**) (red trace) diiron complexes collected at perpendicular (⊥) and parallel (‖) field polarization. Quantitative simulations were performed for analytic determination of paramagnetic speciation within each sample. The amount of each species and its spectroscopic parameters is provided in **Table S1**. Instrumental conditions: microwave frequency, 9.645GHz (⊥), 9.377 GHz (‖); microwave power, 2 µW (**1⁰**, **A** and **1⁻**, **B**), 0.2mW (**1⁻**, **C**⊥) and 6.3 mW (**1⁻**, **C**‖);modulation amplitude; 9.2 mT; temperature, 10 K (**A** and **B**) and 4.3 K, (**C**). Simulation parameters: Trace [**a**]; S = 1/2; $g_{1,2,3}$ (2.041, 2.023, 2.004); $\sigma_{g1,2,3}$ (0.021, 0.011, 0.019); σ_B, 0.5 mT. Trace [**b**] S = 1/2; $g_{1,2,3}$ (2.073, 2.021, 1.986); $\sigma_{g1,2,3}$ (0.014, 0.010, 0.013); σ_B, 0.5 mT; Trace [**c**], S = 1/2; $g_{1,2,3}$ (2.042,2.027, 2.015); $\sigma_{g1,2,3}$ (0.002 0.002, 0.001); σ_B, 0.5 mT. Trace [**d**], S = 1; D= -35 cm-1; E/D, 0.003; $g_{1,2,3}$(1.974, 1.974, 2.065); σ_D= 0.003; $\sigma_{E/D}$=0.02; σ_B, 0.9 mT.*

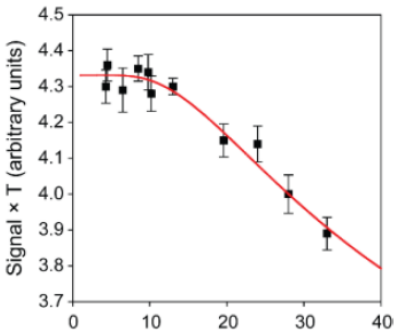

*Figure S. 2 The magnitude of the axial-zero field splitting term (*D *= -35 ± 3 cm⁻¹) for the* $\mathbf{1^-}$ *(*S *= 1) triplet spin-state was determined by fitting the temperature normalized* g ~ *4.0 signal [**d**] observed in parallel mode EPR to a theoretical Boltzmann population distribution for a 2-level system (eq. **3**).The observed decreases in signal intensity with increasing temperature indicating that this transition occurs within the ground state doublet.*

$$Intensity\ x\ T{\sim}n_s = \frac{g_i{\cdot}e^{-\Delta E_i/k_bT}}{\Sigma_j g_j{\cdot}e^{-\Delta E_j/k_bT}} = \frac{(2S_i{+}1){\cdot}e^{-DS_{Z,i}^2/k_bT}}{\Sigma_j(2S_j{+}1){\cdot}e^{-DS_{Z,j}^2/k_bT}} \quad \textbf{(S3)}$$

References

[1] A. Abragam, B. Bleaney. *Electron Paramagnetic Resonance of Transition Ions (International Series of Monographs on Physics)*, (1970).
[2] B. Bennett, R. C. Holz. *Biochemistry*, **36**, (1997).
[3] B. Bennett, R. C. Holz. *J. Am. Chem. Soc.*, **119**, (1997).
[4] P. A. Crawford, K.-W. Yang, N. Sharma, B. Bennett, M. W. Crowder. *Biochemistry*, **44**, (2005).
[5] G. R. Periyannan, A. L. Costello, D. L. Tierney, K.-W. Yang, B. Bennett, M. W. Crowder. *Biochemistry*, **45**, (2006).
[6] H. Yang, M. Aitha, A. R. Marts, A. Hetrick, B. Bennett, M. W. Crowder, D. L. Tierney. *J. Am. Chem. Soc.*, **136**, (2014).
[7] A. Abragam, B. Bleaney. *Electron Paramagnetic Resonance of Transition Ions (International Series of Monographs on Physics)*, (1970).

References

1. Wang, Z.-Q.; Wang, Z.-C.; Zhan, S.; Ye, J.-S., A water-soluble iron electrocatalyst for water oxidation with high TOF. *Applied Catalysis A: General* **2015,** *490*, 128-132.
2. Koch, W. O.; Schünemann, V.; Gerdan, M.; Trautwein, A. X.; Krüger, H.-J., Evidence for an Unusual Thermally Induced Low-Spin (S=1/2) ⇄ Intermediate-Spin (S=3/2) Transition in a Six-Coordinate Iron(III) Complex: Structure and Electronic Properties of a (1,2-Benzenedithiolato)iron(III) Complex Containing N,N′-Dimethyl-2,11-diaza[3.3](2,6)pyridinophane as Ligand. *Chemistry – A European Journal* **1998,** *4* (4), 686-691.
3. McClain II, J. M.; Maples, D. L.; Maples, R. D.; Matz, D. L.; Harris, S. M.; Nelson, A. D. L.; Silversides, J. D.; Archibald, S. J.; Hubin, T. J., Dichloro(4,10-dimethyl-1,4,7,10-tetraazabicyclo[5.5.2]tetradecane)iron(III) hexafluorophosphate. *Acta Crystallographica Section C* **2006,** *62* (11), m553-m555.
4. To, W.-P.; Wai-Shan Chow, T.; Tse, C.-W.; Guan, X.; Huang, J.-S.; Che, C.-M., Water oxidation catalysed by iron complex of N,N′-dimethyl-2,11-diaza[3,3](2,6)pyridinophane. Spectroscopy of iron–oxo intermediates and density functional theory calculations. *Chemical Science* **2015,** *6* (10), 5891-5903.
5. Jones, D. G.; Wilson, K. R.; Cannon-Smith, D. J.; Shircliff, A. D.; Zhang, Z.; Chen, Z.; Prior, T. J.; Yin, G.; Hubin, T. J., Synthesis, Structural Studies, and Oxidation Catalysis of the Late-First-Row-Transition-Metal Complexes of a 2-Pyridylmethyl Pendant-Armed Ethylene Cross-Bridged Cyclam. *Inorganic Chemistry* **2015,** *54* (5), 2221-2234.
6. Majumdar, S.; Majumdar, H. S.; Österbacka, R.; McCarthy, E., Organic Spintronics. In *Reference Module in Materials Science and Materials Engineering*, Elsevier: 2016.
7. Rouault, T., *Volume 1 Characterization, Properties and Applications*. 2017.
8. Abu-Omar, M. M.; Loaiza, A.; Hontzeas, N., Reaction Mechanisms of Mononuclear Non-Heme Iron Oxygenases. *Chemical Reviews* **2005,** *105* (6), 2227-2252.
9. Feig, A. L.; Lippard, S. J., Reactions of Non-Heme Iron(II) Centers with Dioxygen in Biology and Chemistry. *Chemical Reviews* **1994,** *94* (3), 759-805.
10. Nakamura, H.; Matsuda, Y.; Abe, I., Unique chemistry of non-heme iron enzymes in fungal biosynthetic pathways. *Nat Prod Rep* **2018,** *35* (7), 633-645.
11. Hegg, E. L.; Jr, L. Q., The 2-His-1-Carboxylate Facial Triad — An Emerging Structural Motif in Mononuclear Non-Heme Iron(II) Enzymes. *European Journal of Biochemistry* **1997,** *250* (3), 625-629.
12. Bruijnincx, P. C.; van Koten, G.; Klein Gebbink, R. J., Mononuclear non-heme iron enzymes with the 2-His-1-carboxylate facial triad: recent developments in enzymology and modeling studies. *Chem Soc Rev* **2008,** *37* (12), 2716-44.
13. Koehntop, K. D.; Emerson, J. P.; Que, L., Jr., The 2-His-1-carboxylate facial triad: a versatile platform for dioxygen activation by mononuclear non-heme iron(II) enzymes. *J Biol Inorg Chem* **2005,** *10* (2), 87-93.
14. Sazinsky, M. H.; Bard, J.; Di Donato, A.; Lippard, S. J., Crystal structure of the toluene/o-xylene monooxygenase hydroxylase from Pseudomonas stutzeri OX1. Insight into the substrate specificity, substrate channeling, and active site tuning of multicomponent monooxygenases. *J Biol Chem* **2004,** *279* (29), 30600-10.
15. Costas, M.; Mehn, M. P.; Jensen, M. P.; Que, L., Dioxygen Activation at Mononuclear Nonheme Iron Active Sites: Enzymes, Models, and Intermediates. *Chemical Reviews* **2004,** *104* (2), 939-986.
16. Solomon, E. I.; Brunold, T. C.; Davis, M. I.; Kemsley, J. N.; Lee, S.-K.; Lehnert, N.; Neese, F.; Skulan, A. J.; Yang, Y.-S.; Zhou, J., Geometric and Electronic Structure/Function Correlations in Non-Heme Iron Enzymes. *Chemical Reviews* **2000,** *100* (1), 235-350.

17. Solomon, E. I.; Decker, A.; Lehnert, N., Non-heme iron enzymes: Contrasts to heme catalysis. *Proceedings of the National Academy of Sciences* **2003,** *100* (7), 3589.
18. Neidig, M. L.; Solomon, E. I., Structure-function correlations in oxygen activating non-heme iron enzymes. *Chem Commun (Camb)* **2005,** (47), 5843-63.
19. Proshlyakov, D. A.; Henshaw, T. F.; Monterosso, G. R.; Ryle, M. J.; Hausinger, R. P., Direct Detection of Oxygen Intermediates in the Non-Heme Fe Enzyme Taurine/α-Ketoglutarate Dioxygenase. *Journal of the American Chemical Society* **2004,** *126* (4), 1022-1023.
20. Price, J. C.; Barr, E. W.; Hoffart, L. M.; Krebs, C.; Bollinger, J. M., Kinetic Dissection of the Catalytic Mechanism of Taurine:α-Ketoglutarate Dioxygenase (TauD) from Escherichia coli. *Biochemistry* **2005,** *44* (22), 8138-8147.
21. Hoffart, L. M.; Barr, E. W.; Guyer, R. B.; Bollinger, J. M.; Krebs, C., Direct spectroscopic detection of a C-H-cleaving high-spin Fe(IV) complex in a prolyl-4-hydroxylase. *Proceedings of the National Academy of Sciences* **2006,** *103* (40), 14738.
22. Galonić, D. P.; Barr, E. W.; Walsh, C. T.; Bollinger Jr, J. M.; Krebs, C., Two interconverting Fe(IV) intermediates in aliphatic chlorination by the halogenase CytC3. *Nature Chemical Biology* **2007,** *3*, 113.
23. Mbughuni, M. M.; Chakrabarti, M.; Hayden, J. A.; Bominaar, E. L.; Hendrich, M. P.; Münck, E.; Lipscomb, J. D., Trapping and spectroscopic characterization of an Fe^{III}-superoxo intermediate from a nonheme mononuclear iron-containing enzyme. *Proceedings of the National Academy of Sciences* **2010,** *107* (39), 16788.
24. van der Donk, W. A.; Krebs, C.; Bollinger, J. M., Substrate activation by iron superoxo intermediates. *Current Opinion in Structural Biology* **2010,** *20* (6), 673-683.
25. Straganz, G. D.; Nidetzky, B., Variations of the 2-His-1-carboxylate Theme in Mononuclear Non-Heme FeII Oxygenases. *ChemBioChem* **2006,** *7* (10), 1536-1548.
26. Que, L.; Ho, R. Y. N., Dioxygen Activation by Enzymes with Mononuclear Non-Heme Iron Active Sites. *Chemical Reviews* **1996,** *96* (7), 2607-2624.
27. Kovaleva, E. G.; Neibergall, M. B.; Chakrabarty, S.; Lipscomb, J. D., Finding Intermediates in the O2 Activation Pathways of Non-Heme Iron Oxygenases. *Accounts of Chemical Research* **2007,** *40* (7), 475-483.
28. Boyd, D. R.; Bugg, T. D., Arene cis-dihydrodiol formation: from biology to application. *Org Biomol Chem* **2006,** *4* (2), 181-92.
29. Bollinger Jr, J. M.; Price, J. C.; Hoffart, L. M.; Barr, E. W.; Krebs, C., Mechanism of Taurine: α-Ketoglutarate Dioxygenase (TauD) from Escherichia coli. *European Journal of Inorganic Chemistry* **2005,** *2005* (21), 4245-4254.
30. Adams, M. A.; Singh, V. K.; Keller, B. O.; Jia, Z., Structural and biochemical characterization of gentisate 1,2-dioxygenase from Escherichia coli O157:H7. *Molecular Microbiology* **2006,** *61* (6), 1469-1484.
31. Diebold, A. R.; Neidig, M. L.; Moran, G. R.; Straganz, G. D.; Solomon, E. I., The Three-His Triad in Dke1: Comparisons to the Classical Facial Triad. *Biochemistry* **2010,** *49* (32), 6945-6952.
32. Driggers, C. M.; Hartman, S. J.; Karplus, P. A., Structures of Arg- and Gln-type bacterial cysteine dioxygenase homologs. *Protein Science* **2015,** *24* (1), 154-161.
33. Driggers, C. M.; Cooley, R. B.; Sankaran, B.; Hirschberger, L. L.; Stipanuk, M. H.; Karplus, P. A., Cysteine Dioxygenase Structures from pH4 to 9: Consistent Cys-Persulfenate Formation at Intermediate pH and a Cys-Bound Enzyme at Higher pH. *Journal of Molecular Biology* **2013,** *425* (17), 3121-3136.
34. Broderick, J. B., 8.27 - Iron–Sulfur Clusters in Enzyme Catalysis. In *Comprehensive Coordination Chemistry II*, McCleverty, J. A.; Meyer, T. J., Eds. Pergamon: Oxford, 2003; pp 739-757.
35. Korendyaseva, T. K.; Kuvatov, D. N.; Volkov, V. A.; Martinov, M. V.; Vitvitsky, V. M.; Banerjee, R.; Ataullakhanov, F. I., An allosteric mechanism for switching between parallel tracks in mammalian sulfur metabolism. *PLoS Comput Biol* **2008,** *4* (5), e1000076.

36. Griffith, O. W., Mammalian sulfur amino acid metabolism: An overview. In *Methods in Enzymology*, Academic Press: 1987; Vol. 143, pp 366-376.
37. Gaull, G.; Sturman, J. A.; Räihä, N. C. R., Development of Mammalian Sulfur Metabolism: Absence of Cystathionase in Human Fetal Tissues. *Pediatric Research* **1972,** *6* (6), 538-547.
38. Bertini, I., *Biological Inorganic Chemistry: Structure and Reactivity* **2007**.
39. Cavallini, D., Scandurra, R., and De Marco, C., The Enzymatic Oxidation of Cysteamine to Hypotaurine in the Presence of Sulfide. *Journal of Biological Chemistry* **1963,** *238* (9), 2999-3005.
40. Deth, R.; Muratore, C.; Benzecry, J.; Power-Charnitsky, V.-A.; Waly, M., How environmental and genetic factors combine to cause autism: A redox/methylation hypothesis. *NeuroToxicology* **2008,** *29* (1), 190-201.
41. Pean, A. R.; Parsons, R. B.; Waring, R. H.; Williams, A. C.; Ramsden, D. B., Toxicity of sulphur-containing compounds to neuronal cell lines. *Journal of the Neurological Sciences* **1995,** *129*, 107-108.
42. Parsons, R. B., Waring R.H., Ramsden, D. B., Williams, A. C., In vitro effect of the cysteine metabolites homecysteic acid, homocysteine and cysteic acid upon humon neuronal cell lines. *Neurotoxicology* **1998,** *19* (4-5), 599-603.
43. Wu, G.; Fang, Y.-Z.; Yang, S.; Lupton, J. R.; Turner, N. D., Glutathione Metabolism and Its Implications for Health. *The Journal of Nutrition* **2004,** *134* (3), 489-492.
44. Forman, H. J.; Zhang, H.; Rinna, A., Glutathione: overview of its protective roles, measurement, and biosynthesis. *Molecular aspects of medicine* **2009,** *30* (1-2), 1-12.
45. Nobili, V.; Pastore, A.; Gaeta, L. M.; Tozzi, G.; Comparcola, D.; Sartorelli, M. R.; Marcellini, M.; Bertini, E.; Piemonte, F., Glutathione metabolism and antioxidant enzymes in patients affected by nonalcoholic steatohepatitis. *Clinica Chimica Acta* **2005,** *355* (1), 105-111.
46. Mato, J. M.; Martínez-Chantar, M. L.; Lu, S. C., S-adenosylmethionine metabolism and liver disease. *Annals of hepatology* **2013,** *12* (2), 183-189.
47. Park, E.; Park, S. Y.; Dobkin, C.; Schuller-Levis, G., Development of a Novel Cysteine Sulfinic Acid Decarboxylase Knockout Mouse: Dietary Taurine Reduces Neonatal Mortality. *Journal of Amino Acids* **2014,** *2014*, 12.
48. Dominy, J. E., Jr.; Simmons, C. R.; Hirschberger, L. L.; Hwang, J.; Coloso, R. M.; Stipanuk, M. H., Discovery and characterization of a second mammalian thiol dioxygenase, cysteamine dioxygenase. *J Biol Chem* **2007,** *282* (35), 25189-98.
49. Besouw, M.; Masereeuw, R.; van den Heuvel, L.; Levtchenko, E., Cysteamine: an old drug with new potential. *Drug Discovery Today* **2013,** *18* (15), 785-792.
50. Wang, Y.; Griffith, W. P.; Li, J.; Koto, T.; Wherritt, D. J.; Fritz, E.; Liu, A., Cofactor Biogenesis in Cysteamine Dioxygenase: C–F Bond Cleavage with Genetically Incorporated Unnatural Tyrosine. *Angewandte Chemie International Edition* **2018,** *57* (27), 8149-8153.
51. Bailey, C. D. C.; Johnson, G. V. W., The protective effects of cystamine in the R6/2 Huntington's disease mouse involve mechanisms other than the inhibition of tissue transglutaminase. *Neurobiology of Aging* **2006,** *27* (6), 871-879.
52. Dedeoglu, A.; Kubilus, J. K.; Jeitner, T. M.; Matson, S. A.; Bogdanov, M.; Kowall, N. W.; Matson, W. R.; Cooper, A. J. L.; Ratan, R. R.; Beal, M. F.; Hersch, S. M.; Ferrante, R. J., Therapeutic Effects of Cystamine in a Murine Model of Huntington's Disease. *The Journal of Neuroscience* **2002,** *22* (20), 8942.
53. Cherqui, S., Cysteamine therapy: a treatment for cystinosis, not a cure. *Kidney international* **2012,** *81* (2), 127-129.
54. Dunwell, J. M.; Culham, A.; Carter, C. E.; Sosa-Aguirre, C. R.; Goodenough, P. W., Evolution of functional diversity in the cupin superfamily. *Trends in Biochemical Sciences* **2001,** *26* (12), 740-746.
55. Dunwell, J. M.; Purvis, A.; Khuri, S., Cupins: the most functionally diverse protein superfamily? *Phytochemistry* **2004,** *65* (1), 7-17.

56. Xu, D.; Enroth, C.; Lindqvist, Y.; Ballou, D. P.; Massey, V., Studies of the Mechanism of Phenol Hydroxylase: Effect of Mutation of Proline 364 to Serine. *Biochemistry* **2002,** *41* (46), 13627-13636.
57. Sazinsky, M. H.; Lippard, S. J., Methane Monooxygenase: Functionalizing Methane at Iron and Copper. In *Sustaining Life on Planet Earth: Metalloenzymes Mastering Dioxygen and Other Chewy Gases*, Kroneck, P. M. H.; Sosa Torres, M. E., Eds. Springer International Publishing: Cham, 2015; pp 205-256.
58. Pierce, B. S.; Hendrich, M. P., Local and Global Effects of Metal Binding within the Small Subunit of Ribonucleotide Reductase. *Journal of the American Chemical Society* **2005,** *127* (10), 3613-3623.
59. Reig, A. J.; Pires, M. M.; Snyder, R. A.; Wu, Y.; Jo, H.; Kulp, D. W.; Butch, S. E.; Calhoun, J. R.; Szyperski, T.; Solomon, E. I.; DeGrado, W. F., Alteration of the oxygen-dependent reactivity of de novo Due Ferri proteins. *Nat Chem* **2012,** *4* (11), 900-6.
60. Snyder, R. A.; Butch, S. E.; Reig, A. J.; DeGrado, W. F.; Solomon, E. I., Molecular-Level Insight into the Differential Oxidase and Oxygenase Reactivities of de Novo Due Ferri Proteins. *J Am Chem Soc* **2015,** *137* (29), 9302-14.
61. Snyder, R. A.; Betzu, J.; Butch, S. E.; Reig, A. J.; DeGrado, W. F.; Solomon, E. I., Systematic Perturbations of Binuclear Non-heme Iron Sites: Structure and Dioxygen Reactivity of de Novo Due Ferri Proteins. *Biochemistry* **2015,** *54* (30), 4637-51.
62. Jasniewski, A. J.; Que, L., Jr., Dioxygen Activation by Nonheme Diiron Enzymes: Diverse Dioxygen Adducts, High-Valent Intermediates, and Related Model Complexes. *Chem Rev* **2018,** *118* (5), 2554-2592.
63. Lei, Q. P.; Cui, X.; Kurtz, D. M.; Amster, I. J.; Chernushevich, I. V.; Standing, K. G., Electrospray Mass Spectrometry Studies of Non-Heme Iron-Containing Proteins. *Analytical Chemistry* **1998,** *70* (9), 1838-1846.
64. Kaminska, K. H.; Baraniak, U.; Boniecki, M.; Nowaczyk, K.; Czerwoniec, A.; Bujnicki, J. M., Structural bioinformatics analysis of enzymes involved in the biosynthesis pathway of the hypermodified nucleoside ms(2)io(6)A37 in tRNA. *Proteins* **2008,** *70* (1), 1-18.
65. Mathevon, C.; Pierrel, F.; Oddou, J.-L.; Garcia-Serres, R.; Blondin, G.; Latour, J.-M.; Ménage, S.; Gambarelli, S.; Fontecave, M.; Atta, M., The tRNA-modifying MiaE protein from Salmonella typhimurium is a non heme diiron monooxygenase. *Proceedings of the National Academy of Sciences of the United States of America* **2007,** *104*, 13295-300.
66. Corder, A. L.; Subedi, B. P.; Zhang, S.; Dark, A. M.; Foss, F. W., Jr.; Pierce, B. S., Peroxide-shunt substrate-specificity for the Salmonella typhimurium O2-dependent tRNA modifying monooxygenase (MiaE). *Biochemistry* **2013,** *52* (36), 6182-96.
67. McPake, C. B.; Murray, C. B.; Sandford, G., Sequential Continuous Flow Processes for the Oxidation of Amines and Azides by using HOF·MeCN. *ChemSusChem* **2012,** *5* (2), 312-319.
68. Yan, G.; Yang, M., Recent advances in the synthesis of aromatic nitro compounds. *Organic & Biomolecular Chemistry* **2013,** *11* (16), 2554-2566.
69. Kirner, S.; Hammer, P. E.; Hill, D. S.; Altmann, A.; Fischer, I.; Weislo, L. J.; Lanahan, M.; van Pée, K.-H.; Ligon, J. M., Functions Encoded by Pyrrolnitrin Biosynthetic Genes from <em>Pseudomonas fluorescens</em&gt. *Journal of Bacteriology* **1998,** *180* (7), 1939.
70. Lee, J.; Simurdiak, M.; Zhao, H., Reconstitution and characterization of aminopyrrolnitrin oxygenase, a Rieske N-oxygenase that catalyzes unusual arylamine oxidation. *J Biol Chem* **2005,** *280* (44), 36719-27.
71. Simurdiak, M.; Lee, J.; Zhao, H., A new class of arylamine oxygenases: evidence that p-aminobenzoate N-oxygenase (AurF) is a di-iron enzyme and further mechanistic studies. *Chembiochem* **2006,** *7* (8), 1169-72.
72. Makris, T. M.; Vu, V. V.; Meier, K. K.; Komor, A. J.; Rivard, B. S.; Munck, E.; Que, L., Jr.; Lipscomb, J. D., An unusual peroxo intermediate of the arylamine oxygenase of the chloramphenicol biosynthetic pathway. *J Am Chem Soc* **2015,** *137* (4), 1608-17.

73. Komor, A. J.; Rivard, B. S.; Fan, R.; Guo, Y.; Que, L., Jr.; Lipscomb, J. D., Mechanism for Six-Electron Aryl-N-Oxygenation by the Non-Heme Diiron Enzyme CmlI. *J Am Chem Soc* **2016,** *138* (23), 7411-21.
74. Mathevon, C.; Pierrel, F.; Oddou, J. L.; Garcia-Serres, R.; Blondin, G.; Latour, J. M.; Menage, S.; Gambarelli, S.; Fontecave, M.; Atta, M., tRNA-modifying MiaE protein from Salmonella typhimurium is a nonheme diiron monooxygenase. *Proc Natl Acad Sci U S A* **2007,** *104* (33), 13295-300.
75. Choi, Y. S.; Zhang, H.; Brunzelle, J. S.; Nair, S. K.; Zhao, H., In vitro reconstitution and crystal structure of p-aminobenzoate N-oxygenase (AurF) involved in aureothin biosynthesis. *Proc Natl Acad Sci U S A* **2008,** *105* (19), 6858-63.
76. Subedi, B. P.; Corder, A. L.; Zhang, S.; Foss, F. W., Jr.; Pierce, B. S., Steady-state kinetics and spectroscopic characterization of enzyme-tRNA interactions for the non-heme diiron tRNA-monooxygenase, MiaE. *Biochemistry* **2015,** *54* (2), 363-76.
77. Pierce, B. S.; Gardner, J. D.; Bailey, L. J.; Brunold, T. C.; Fox, B. G., Characterization of the Nitrosyl Adduct of Substrate-Bound Mouse Cysteine Dioxygenase by Electron Paramagnetic Resonance: Electronic Structure of the Active Site and Mechanistic Implications. *Biochemistry* **2007,** *46* (29), 8569-8578.
78. Abragam, A.; Bleaney, B., Electron Paramagnetic Resonance of Transition Ions. **1970**.
79. Pierce, B. S.; Subedi, B. P.; Sardar, S.; Crowell, J. K., The "Gln-Type" Thiol Dioxygenase from Azotobacter vinelandii is a 3-Mercaptopropionic Acid Dioxygenase. *Biochemistry* **2015,** *54* (51), 7477-90.
80. Merkx, M.; Kopp, D. A.; Sazinsky, M. H.; Blazyk, J. L.; Müller, J.; Lippard, S. J., Dioxygen Activation and Methane Hydroxylation by Soluble Methane Monooxygenase: A Tale of Two Irons and Three Proteins. *Angewandte Chemie International Edition* **2001,** *40* (15), 2782-2807.
81. Pikus, J. D.; Studts, J. M.; Achim, C.; Kauffmann, K. E.; Münck, E.; Steffan, R. J.; McClay, K.; Fox, B. G., Recombinant Toluene-4-monooxygenase: Catalytic and Mössbauer Studies of the Purified Diiron and Rieske Components of a Four-Protein Complex. *Biochemistry* **1996,** *35* (28), 9106-9119.
82. Davydov, R. M.; Smieja, J.; Dikanov, S. A.; Zang, Y.; Que Jr, L.; Bowman, M. K., EPR properties of mixed-valent μ-oxo and μ-hydroxo dinuclear iron complexes produced by radiolytic reduction at 77 K. *JBIC Journal of Biological Inorganic Chemistry* **1999,** *4* (3), 292-301.
83. Davydov, R.; Valentine, A. M.; Komar-Panicucci, S.; Hoffman, B. M.; Lippard, S. J., An EPR Study of the Dinuclear Iron Site in the Soluble Methane Monooxygenase from Methylococcus capsulatus (Bath) Reduced by One Electron at 77 K: The Effects of Component Interactions and the Binding of Small Molecules to the Diiron(III) Center. *Biochemistry* **1999,** *38* (13), 4188-4197.
84. Hendrich, M. P.; Debrunner, P. G., Integer-spin electron paramagnetic resonance of iron proteins. *Biophysical Journal* **1989,** *56* (3), 489-506.
85. Paulsen, K. E.; Liu, Y.; Fox, B. G.; Lipscomb, J. D.; Munck, E.; Stankovich, M. T., Oxidation-reduction potentials of the methane monooxygenase hydroxylase component from Methylosinus trichosporium OB3b. *Biochemistry* **1994,** *33* (3), 713-722.
86. Elgren, T. E.; Hendrich, M. P.; Que, L., Azide binding to the diferrous clusters of the R2 protein of ribonucleotide reductase from Escherichia coli. *Journal of the American Chemical Society* **1993,** *115* (20), 9291-9292.
87. Winkler, R.; Hertweck, C., Sequential enzymatic oxidation of aminoarenes to nitroarenes via hydroxylamines. *Angew Chem Int Ed Engl* **2005,** *44* (26), 4083-7.
88. Bailey, L. J.; Fox, B. G., Crystallographic and Catalytic Studies of the Peroxide-Shunt Reaction in a Diiron Hydroxylase. *Biochemistry* **2009,** *48* (38), 8932-8939.
89. Dominy, J. E.; Simmons, C. R.; Karplus, P. A.; Gehring, A. M.; Stipanuk, M. H., Identification and Characterization of Bacterial Cysteine Dioxygenases: a New Route of Cysteine Degradation for Eubacteria. *Journal of Bacteriology* **2006,** *188* (15), 5561.

90. Chai, S. C.; Jerkins, A. A.; Banik, J. J.; Shalev, I.; Pinkham, J. L.; Uden, P. C.; Maroney, M. J., Heterologous expression, purification, and characterization of recombinant rat cysteine dioxygenase. *J Biol Chem* **2005,** *280* (11), 9865-9.
91. Stipanuk, M. H., SULFUR AMINO ACID METABOLISM: Pathways for Production and Removal of Homocysteine and Cysteine. *Annual Review of Nutrition* **2004,** *24* (1), 539-577.
92. Ewetz, L.; Sörbo, B., Characteristics of the cysteinesulfinate-forming enzyme system in rat liver. *Biochimica et Biophysica Acta (BBA) - Enzymology and Biological Oxidation* **1966,** *128* (2), 296-305.
93. Cavallini, D., Scandurra, R., De Marco, C., The Enzymatic Oxidation of Cysteamine of Hypotaurine in the Presence of Sulfide. *Biological Chemistry* **1963,** *238* (9), 2999-3005.
94. Reddie, K. G.; Carroll, K. S., Expanding the functional diversity of proteins through cysteine oxidation. *Current Opinion in Chemical Biology* **2008,** *12* (6), 746-754.
95. Winyard, P. G.; Moody, C. J.; Jacob, C., Oxidative activation of antioxidant defence. *Trends in Biochemical Sciences* **2005,** *30* (8), 453-461.
96. Trachootham, D.; Alexandre, J.; Huang, P., Targeting cancer cells by ROS-mediated mechanisms: a radical therapeutic approach? *Nature Reviews Drug Discovery* **2009,** *8*, 579.
97. Devayani, P. B.; Wilson, B. M., III; Kate, S. C., Drug Targets in Mycobacterial Sulfur Metabolism. *Infectious Disorders - Drug Targets* **2007,** *7* (2), 140-158.
98. Heafield, M. T.; Fearn, S.; Steventon, G. B.; Waring, R. H.; Williams, A. C.; Sturman, S. G., Plasma cysteine and sulphate levels in patients with motor neurone, Parkinson's and Alzheimer's disease. *Neuroscience Letters* **1990,** *110* (1), 216-220.
99. James, S. J.; Cutler, P.; Melnyk, S.; Jernigan, S.; Janak, L.; Gaylor, D. W.; Neubrander, J. A., Metabolic biomarkers of increased oxidative stress and impaired methylation capacity in children with autism. *The American Journal of Clinical Nutrition* **2004,** *80* (6), 1611-1617.
100. Pierce, B. S.; Subedi, B. P.; Sardar, S.; Crowell, J. K., The “Gln-Type” Thiol Dioxygenase from Azotobacter vinelandii Is a 3-Mercaptopropionic Acid Dioxygenase. *Biochemistry* **2015,** *54* (51), 7477-7490.
101. Li, W.; Pierce, B. S., Steady-state substrate specificity and O(2)-coupling efficiency of mouse cysteine dioxygenase. *Arch Biochem Biophys* **2015,** *565*, 49-56.
102. Denu, J. M.; Fitzpatrick, P. F., pH and kinetic isotope effects on the oxidative half-reaction of D-amino-acid oxidase. *Journal of Biological Chemistry* **1994,** *269* (21), 15054-15059.
103. Wallace Cleland, W., [22] The use of pH studies to determine chemical mechanisms of enzyme-catalyzed reactions. In *Methods in Enzymology*, Purich, D. L., Ed. Academic Press: 1982; Vol. 87, pp 390-405.
104. Cook, P. F., And Cleland, W. W., Enzyme Kinetics and Mechanisms. **2007**.
105. Glasoe, P. K.; Long, F. A., USE OF GLASS ELECTRODES TO MEASURE ACIDITIES IN DEUTERIUM OXIDE1,2. *The Journal of Physical Chemistry* **1960,** *64* (1), 188-190.
106. Saavedra, J. E.; Southan, G. J.; Davies, K. M.; Lundell, A.; Markou, C.; Hanson, S. R.; Adrie, C.; Hurford, W. E.; Zapol, W. M.; Keefer, L. K., Localizing Antithrombotic and Vasodilatory Activity with a Novel, Ultrafast Nitric Oxide Donor. *Journal of Medicinal Chemistry* **1996,** *39* (22), 4361-4365.
107. Caranto, J. D.; Weitz, A.; Hendrich, M. P.; Kurtz, D. M., The Nitric Oxide Reductase Mechanism of a Flavo-Diiron Protein: Identification of Active-Site Intermediates and Products. *Journal of the American Chemical Society* **2014,** *136* (22), 7981-7992.
108. Kiene, R. P., Taylor, B. F., Biotransformation of organosulphur compounds in sediments via 3-mercaptopropionate. *Nature* **1988,** *332* (6160), 148-150.
109. Bruland, N., Wubbler, J. H., Steinbuchel, A., 3-Mercaptopropionate Dioxygenase, a Cysteine Dioxygease Homologue, Catalyzes the Initial Step of 3-Mercaptopropionate Catabolism in the 3,3-Thiodipropionic acid-degrading Bacterium Variovorax paradoxus. *Journal of Biological Chemistry* **2009,** *284* (1), 660-672.

110. Li, W.; Blaesi, E. J.; Pecore, M. D.; Crowell, J. K.; Pierce, B. S., Second-sphere interactions between the C93-Y157 cross-link and the substrate-bound Fe site influence the O(2) coupling efficiency in mouse cysteine dioxygenase. *Biochemistry* **2013,** *52* (51), 9104-19.
111. Crawford, J. A.; Li, W.; Pierce, B. S., Single turnover of substrate-bound ferric cysteine dioxygenase with superoxide anion: enzymatic reactivation, product formation, and a transient intermediate. *Biochemistry* **2011,** *50* (47), 10241-53.
112. Wanat, A.; Schneppensieper, T.; Stochel, G.; van Eldik, R.; Bill, E.; Wieghardt, K., Kinetics, Mechanism, and Spectroscopy of the Reversible Binding of Nitric Oxide to Aquated Iron(II). An Undergraduate Text Book Reaction Revisited. *Inorganic Chemistry* **2002,** *41* (1), 4-10.
113. Li, M.; Bonnet, D.; Bill, E.; Neese, F.; Weyhermüller, T.; Blum, N.; Sellmann, D.; Wieghardt, K., Tuning the Electronic Structure of Octahedral Iron Complexes [FeL(X)] (L = 1-Alkyl-4,7-bis(4-tert-butyl-2-mercaptobenzyl)-1,4,7-triazacyclononane, X = Cl, CH3O, CN, NO). The S = 1/2 ⇌ S = 3/2 Spin Equilibrium of [FeLPr(NO)]. *Inorganic Chemistry* **2002,** *41* (13), 3444-3456.
114. Sellmann, D.; Blum, N.; Heinemann, F. W.; Hess, B. A., Synthesis, Reactivity, and Structure of Strictly Homologous 18 and 19 Valence Electron Iron Nitrosyl Complexes. *Chemistry – A European Journal* **2001,** *7* (9), 1874-1880.
115. Gardner, J. D.; Pierce, B. S.; Fox, B. G.; Brunold, T. C., Spectroscopic and computational characterization of substrate-bound mouse cysteine dioxygenase: nature of the ferrous and ferric cysteine adducts and mechanistic implications. *Biochemistry* **2010,** *49* (29), 6033-41.
116. Constable, E. C., Coordination Chemistry of Macrocyclic Compounds. **1999**.
117. Bakac, A.; Brynildson, M. E.; Espenson, J. H., Characterization of the structure, properties, and reactivity of a cobalt(II) macrocyclic complex. *Inorganic Chemistry* **1986,** *25* (23), 4108-4114.
118. Busch, D. H., Distinctive coordination chemistry and biological significance of complexes with macrocyclic ligands. *Accounts of Chemical Research* **1978,** *11* (10), 392-400.
119. Hubin, T. J., Synthesis and coordination chemistry of topologically constrained azamacrocycles. *Coordination Chemistry Reviews* **2003,** *241* (1), 27-46.
120. Lincoln, K. M.; Arroyo - Currás, N.; Johnston, H. M.; Hayden, T. D.; Pierce, B. S.; Bhuvanesh, N.; Green, K. N., Chemical characteristics of the products of the complexation reaction between copper(II) and a tetra-aza macrocycle in the presence of chloride ions. *Journal of Coordination Chemistry* **2015,** *68* (16), 2810-2826.
121. Martin, L. Y.; DeHayes, L. J.; Zompa, L. J.; Busch, D. H., Relationship between metal-donor distance and ring size in macrocyclic complexes. *Journal of the American Chemical Society* **1974,** *96* (12), 4046-4048.
122. Sarther, C. M.; Blinn, E. L., Cobalt(II) complexes containing a 12-membered saturated macrocyclic ligand. *Inorganic Chemistry* **1976,** *15* (12), 3083-3086.
123. Bongard, J. E.; Hartsock, R. W.; Stegbauer, W. D.; Streich, F. C.; Barnum, R.; Chang, E. L.; Knight, D. A., Monofunctionalized Tetraazacrowns for Use in Bioconjugation and Catalysis. *Synthesis and Reactivity in Inorganic, Metal-Organic, and Nano-Metal Chemistry* **2005,** *35* (9), 727-731.
124. Choi, K.-Y.; Lee, H.-K.; Kim, K.-J.; Ryu, H.; Lee, K.-C.; Ko, J.; Kim, M.-J., Synthesis and characterization of cobalt(III) tetraaza macrocyclic complexes containing chloro and azido ligands. *Transition Metal Chemistry* **2006,** *31* (8), 1093-1097.
125. Omar, H. A. A.; Moore, P.; Alcock, N. W., Preparation and characterisation of organocobalt(III) complexes of tetraaza macrocyclic ligands. Crystal structures of ethyl- and propyl-cobalt(III) complexes of 3,7,11,17-tetraazabicyclo[11.3.1]heptadeca-1(17),13,15-triene. *Journal of the Chemical Society, Dalton Transactions* **1994,** (18), 2631-2635.
126. Ozay, H.; Baran, Y.; Ishii, Y., Copper and cobalt complexes of octadentate azamacrocycles: Spectrophotometric titration, stopped-flow kinetics and crystallographic study. *Spectrochimica Acta Part A: Molecular and Biomolecular Spectroscopy* **2011,** *83* (1), 525-531.

127. Cabbiness, D. K.; Margerum, D. W., Macrocyclic effect on the stability of copper(II) tetramine complexes. *Journal of the American Chemical Society* **1969,** *91* (23), 6540-6541.
128. Irving, H.; Williams, R. J. P., 637. The stability of transition-metal complexes. *Journal of the Chemical Society (Resumed)* **1953,** (0), 3192-3210.
129. Lincoln, K. M.; Offutt, M. E.; Hayden, T. D.; Saunders, R. E.; Green, K. N., Structural, Spectral, and Electrochemical Properties of Nickel(II), Copper(II), and Zinc(II) Complexes Containing 12-Membered Pyridine- and Pyridol-Based Tetra-aza Macrocycles. *Inorganic Chemistry* **2014,** *53* (3), 1406-1416.
130. Brewer, S. M. a. L., K. M., Manuscript in preparation.
131. Collman, J. P.; Schneider, P. W., Complexes of Cobalt(III) and Rhodium(III) with a Cyclic Tetradentate Secondary Amine. *Inorganic Chemistry* **1966,** *5* (8), 1380-1384.
132. Hubin, T. J.; Alcock, N. W.; Clase, H. J.; Seib, L. L.; Busch, D. H., Synthesis, characterization, and X-ray crystal structures of cobalt(II) and cobalt(III) complexes of four topologically constrained tetraazamacrocycles. *Inorganica Chimica Acta* **2002,** *337*, 91-102.
133. Delgado, R.; Quintino, S.; Teixeira, M.; Zhang, A., Metal complexes of a 12-membered tetraaza macrocycle containing pyridine and N-carboxymethyl groups*Journal of the Chemical Society, Dalton Transactions* **1997,** (1), 55-64.
134. Tait, A. M.; Lovecchio, F. V.; Busch, D. H., A spectrochemical and electrochemical study of complexes of cobalt with macrocyclic ligands having various degrees of unsaturation. *Inorganic Chemistry* **1977,** *16* (9), 2206-2212.
135. Eberhardt, W. H., Electrolysis: H2O and H2O2. *Journal of Chemical Education* **1964,** *41* (8), A591.
136. Koga, N.; Kimizu, T.; Sakamoto, M.; Furukawa, Y., Temperature Effect on Cobalt(II)-Chloride Complex Equilibrium in Aqueous Solution. *The Chemical Educator* **2009,** *14*, 2009.
137. Lever, A. B. P., Charge transfer spectra of transition metal complexes. *Journal of Chemical Education* **1974,** *51* (9), 612.
138. Martins, L. J. A.; da Costa, J. B., Further observations on the cobalt(II)-chloride equilibrium: Effect of changing the chloride ion concentration. *Journal of Chemical Education* **1986,** *63* (11), 989.
139. Nguyen, V. D.; Birdwhistell, K. R., Microwave Mapping Demonstration Using the Thermochromic Cobalt Chloride Equilibrium. *Journal of Chemical Education* **2014,** *91* (6), 880-882.
140. Ophardt, C. E., Cobalt complexes in equilibrium. *Journal of Chemical Education* **1980,** *57* (6), 453.
141. Spears, L. G.; Spears, L. G., Chemical storage of solar energy using an old color change demonstration. *Journal of Chemical Education* **1984,** *61* (3), 252.
142. Siaugue, J.-M.; Segat-Dioury, F.; Sylvestre, I.; Favre-Réguillon, A.; Foos, J.; Madic, C.; Guy, A., Regioselective synthesis of N-functionalized 12-membered azapyridinomacrocycles bearing trialkylcarboxylic acid side chains. *Tetrahedron* **2001,** *57* (22), 4713-4718.
143. Bruker Advanved X-ray Solutions. *APEX2 (Version 2014.9-0)* **2007**.
144. Solutions, B. A. X.-r., SADABS. **2001**.
145. 6.3.1), X. V., Bruker Advanced X-ray Solutions. **2004**.
146. Lichty, J.; Allen, S. M.; Grillo, A. I.; Archibald, S. J.; Hubin, T. J., Synthesis and characterization of the cobalt(III) complexes of two pendant-arm cross-bridged cyclams. *Inorganica Chimica Acta* **2004,** *357* (2), 615-618.
147. Cotton, F. A., Wilkinson, G., Murillo, C. A., Bochmann, M. , Advanced Inorganic Chemistry. **1999**, 817-835.
148. Drago, R. S., Physical Methods in Inorganic Chemistry. **1965**.
149. Dunn, T. M., McClure, D. S., Pearson, R. G.,, Some Aspects of Crystal Field Theory. **1965**, 38-57.
150. Lever, A. B. P., Inorganic Electronic Spectroscopy. **1968**, 306-326.
151. Sherry, B. D.; Fürstner, A., The Promise and Challenge of Iron-Catalyzed Cross Coupling. *Accounts of Chemical Research* **2008,** *41* (11), 1500-1511.
152. Bedford, R. B., Eight irons hit the right spin. *Nature Chemistry* **2016,** *8*, 904.

153. Daifuku, S. L.; Al-Afyouni, M. H.; Snyder, B. E. R.; Kneebone, J. L.; Neidig, M. L., A Combined Mössbauer, Magnetic Circular Dichroism, and Density Functional Theory Approach for Iron Cross-Coupling Catalysis: Electronic Structure, In Situ Formation, and Reactivity of Iron-Mesityl-Bisphosphines. *Journal of the American Chemical Society* **2014,** *136* (25), 9132-9143.
154. Daifuku, S. L.; Kneebone, J. L.; Snyder, B. E. R.; Neidig, M. L., Iron(II) Active Species in Iron–Bisphosphine Catalyzed Kumada and Suzuki–Miyaura Cross-Couplings of Phenyl Nucleophiles and Secondary Alkyl Halides. *Journal of the American Chemical Society* **2015,** *137* (35), 11432-11444.
155. Agata, R.; Iwamoto, T.; Nakagawa, N.; Isozaki, K.; Hatakeyama, T.; Takaya, H.; Nakamura, M., Iron Fluoride/N-Heterocyclic Carbene Catalyzed Cross Coupling- between Deactivated Aryl Chlorides and Alkyl Grignard Reagents with or without β-Hydrogens. *Synthesis* **2015,** *47* (12), 1733-1740.
156. Bedford, R. B.; Brenner, P. B.; Elorriaga, D.; Harvey, J. N.; Nunn, J., The influence of the ligand chelate effect on iron-amine-catalysed Kumada cross-coupling. *Dalton Transactions* **2016,** *45* (40), 15811-15817.
157. Bedford, R. B., Brenner, P. B., Bauer, E. (Ed), Iron Catalysis II. Topics in Organometallic Chemistry. **2015,** *50*, 19-46.
158. Bedford, R. B., How Low Does Iron Go? Chasing the Active Species in Fe-Catalyzed Cross-Coupling Reactions. *Accounts of Chemical Research* **2015,** *48* (5), 1485-1493.
159. Dong, L.; Wen, J.; Qin, S.; Yang, N.; Yang, H.; Su, Z.; Yu, X.; Hu, C., Iron-Catalyzed Direct Suzuki–Miyaura Reaction: Theoretical and Experimental Studies on the Mechanism and the Regioselectivity. *ACS Catalysis* **2012,** *2* (8), 1829-1837.
160. Gustafson, K. P. J.; Guðmundsson, A.; Lewis, K.; Bäckvall, J.-E., Chemoenzymatic Dynamic Kinetic Resolution of Secondary Alcohols Using an Air- and Moisture-Stable Iron Racemization Catalyst. *Chemistry – A European Journal* **2017,** *23* (5), 1048-1051.
161. Bye, N.; Hutt, O. E.; Hinton, T. M.; Acharya, D. P.; Waddington, L. J.; Moffat, B. A.; Wright, D. K.; Wang, H. X.; Mulet, X.; Muir, B. W., Nitroxide-Loaded Hexosomes Provide MRI Contrast in Vivo. *Langmuir* **2014,** *30* (29), 8898-8906.
162. Sun, C.-L.; Li, B.-J.; Shi, Z.-J., Direct C−H Transformation via Iron Catalysis. *Chemical Reviews* **2011,** *111* (3), 1293-1314.
163. He, Y.; Gorden, J. D.; Goldsmith, C. R., Steric Modifications Tune the Regioselectivity of the Alkane Oxidation Catalyzed by Non-Heme Iron Complexes. *Inorganic Chemistry* **2011,** *50* (24), 12651-12660.
164. Bigi, M. A.; Reed, S. A.; White, M. C., Diverting non-haem iron catalysed aliphatic C–H hydroxylations towards desaturations. *Nature Chemistry* **2011,** *3*, 216.
165. Chen, M. S.; White, M. C., Combined Effects on Selectivity in Fe-Catalyzed Methylene Oxidation. *Science* **2010,** *327* (5965), 566.
166. Tseberlidis, G.; Intrieri, D.; Caselli, A., Catalytic Applications of Pyridine-Containing Macrocyclic Complexes. *European Journal of Inorganic Chemistry* **2017,** *2017* (30), 3589-3603.
167. Serrano-Plana, J.; Oloo, W. N.; Acosta-Rueda, L.; Meier, K. K.; Verdejo, B.; García-España, E.; Basallote, M. G.; Münck, E.; Que, L.; Company, A.; Costas, M., Trapping a Highly Reactive Nonheme Iron Intermediate That Oxygenates Strong C—H Bonds with Stereoretention. *Journal of the American Chemical Society* **2015,** *137* (50), 15833-15842.
168. Serrano-Plana, J.; Aguinaco, A.; Belda, R.; García-España, E.; Basallote, M. G.; Company, A.; Costas, M., Exceedingly Fast Oxygen Atom Transfer to Olefins via a Catalytically Competent Nonheme Iron Species. *Angewandte Chemie International Edition* **2016,** *55* (21), 6310-6314.
169. Andris, E.; Navrátil, R.; Jašík, J.; Terencio, T.; Srnec, M.; Costas, M.; Roithová, J., Chasing the Evasive Fe═O Stretch and the Spin State of the Iron(IV)–Oxo Complexes by Photodissociation Spectroscopy. *Journal of the American Chemical Society* **2017,** *139* (7), 2757-2765.

170. Company, A.; Prat, I.; Frisch, J. R.; Mas-Ballesté, D. R.; Güell, M.; Juhász, G.; Ribas, X.; Münck, D. E.; Luis, J. M.; Que Jr, L.; Costas, M., Modeling the cis-Oxo-Labile Binding Site Motif of Non-Heme Iron Oxygenases: Water Exchange and Oxidation Reactivity of a Non-Heme Iron(IV)-Oxo Compound Bearing a Tripodal Tetradentate Ligand. *Chemistry – A European Journal* **2011,** *17* (5), 1622-1634.
171. Bou-Abdallah, F.; McNally, J.; Liu, X. X.; Melman, A., Oxygen catalyzed mobilization of iron from ferritin by iron(iii) chelate ligands. *Chemical Communications* **2011,** *47* (2), 731-733.
172. Hong, S.; Lee, Y.-M.; Cho, K.-B.; Seo, M. S.; Song, D.; Yoon, J.; Garcia-Serres, R.; Clémancey, M.; Ogura, T.; Shin, W.; Latour, J.-M.; Nam, W., Conversion of high-spin iron(iii)–alkylperoxo to iron(iv)–oxo species via O–O bond homolysis in nonheme iron models. *Chemical Science* **2014,** *5* (1), 156-162.
173. Marek, I., Rappoport, Z., Liebman, J. F., Patai, S., The Chemistry of Organoiron Compounds: Fe. **2014**.
174. Bauer, I.; Knölker, H.-J., Iron Catalysis in Organic Synthesis. *Chemical Reviews* **2015,** *115* (9), 3170-3387.
175. Chen, M. S.; White, M. C., A Predictably Selective Aliphatic C–H Oxidation Reaction for Complex Molecule Synthesis. *Science* **2007,** *318* (5851), 783.
176. Talsi, E. P.; Bryliakov, K. P., Chemo- and stereoselective CH oxidations and epoxidations/cis-dihydroxylations with H2O2, catalyzed by non-heme iron and manganese complexes. *Coordination Chemistry Reviews* **2012,** *256* (13), 1418-1434.
177. Lyakin, O. Y.; Ottenbacher, R. V.; Bryliakov, K. P.; Talsi, E. P., Asymmetric Epoxidations with H2O2 on Fe and Mn Aminopyridine Catalysts: Probing the Nature of Active Species by Combined Electron Paramagnetic Resonance and Enantioselectivity Study. *ACS Catalysis* **2012,** *2* (6), 1196-1202.
178. Olivo, G.; Cussó, O.; Borrell, M.; Costas, M., Oxidation of alkane and alkene moieties with biologically inspired nonheme iron catalysts and hydrogen peroxide: from free radicals to stereoselective transformations. *JBIC Journal of Biological Inorganic Chemistry* **2017,** *22* (2), 425-452.
179. Ye, S.; Xue, G.; Krivokapic, I.; Petrenko, T.; Bill, E.; Que Jr, L.; Neese, F., Magnetic circular dichroism and computational study of mononuclear and dinuclear iron(iv) complexes. *Chemical Science* **2015,** *6* (5), 2909-2921.
180. Que, L., The oxo/peroxo debate: a nonheme iron perspective. *JBIC Journal of Biological Inorganic Chemistry* **2004,** *9* (6), 684-690.
181. Wen, J.; Qin, S.; Ma, L.-F.; Dong, L.; Zhang, J.; Liu, S.-S.; Duan, Y.-S.; Chen, S.-Y.; Hu, C.-W.; Yu, X.-Q., Iron-Mediated Direct Suzuki−Miyaura Reaction: A New Method for the ortho-Arylation of Pyrrole and Pyridine. *Organic Letters* **2010,** *12* (12), 2694-2697.
182. Doerwald, Z., Dorwald, F. Z., Side Reactions in Organic Synthesis II: Aromatic Substitutions. **2014**, 61-84.
183. Gribble, G. W.; Fu, L.; Lin, Q.-X., Chapter 3 - Attachment at Ring Positions. In *Pyridines: from lab to production*, Scriven, E. F. V., Ed. Academic Press: Oxford, 2013; pp 153-373.
184. Archibald, S. J., Macrocyclic coordination chemistry. *Annual Reports Section "A" (Inorganic Chemistry)* **2011,** *107* (0), 274-296.
185. Illies, L. N., E., Dixneuf, P. H., Doucet, H. (Ed), C-H Bond Activation and Catalytic Functionalization II. *Springer* **2016,** *56*, 1-18.
186. Kleij, A. W., Martinez-Rodriguez, L., Fiorani, G., Martin, C., North, M. (Ed), Sustainable Catalysis: With Non-Endangered Metals. *Royal Society of Chemistry* **2016**, 373-406.
187. Maes, J., Maes, B. U. W., Scriven, E. F. V., Ramsden, C. A., Heterocyclic Chemistry in the 21st Century. *Elsevier* **2016,** *120*, 137-194.
188. Bai, Y.; Tang, L.; Huang, H.; Deng, G.-J., Synthesis of 2,4-diarylsubstituted-pyridines through a Ru-catalyzed four component reaction. *Organic & Biomolecular Chemistry* **2015,** *13* (15), 4404-4407.

189. Deb, A.; Manna, S.; Maji, A.; Dutta, U.; Maiti, D., Iron-Catalyzed Direct C–H Arylation of Heterocycles and Quinones with Arylboronic Acids. *European Journal of Organic Chemistry* **2013,** *2013* (24), 5251-5256.
190. Du, W.; Zhao, M.-N.; Ren, Z.-H.; Wang, Y.-Y.; Guan, Z.-H., Copper-catalyzed 5-endo-trig cyclization of ketoxime carboxylates: a facile synthesis of 2-arylpyrroles. *Chemical Communications* **2014,** *50* (56), 7437-7439.
191. Ehlers, P.; Petrosyan, A.; Baumgard, J.; Jopp, S.; Steinfeld, N.; Ghochikyan, T. V.; Saghyan, A. S.; Fischer, C.; Langer, P., Synthesis of 2,5-Diarylpyrroles by Ligand-Free Palladium-Catalyzed CH Activation of Pyrroles in Ionic Liquids. *ChemCatChem* **2013,** *5* (8), 2504-2511.
192. Fier, P. S.; Hartwig, J. F., Synthesis and Late-Stage Functionalization of Complex Molecules through C–H Fluorination and Nucleophilic Aromatic Substitution. *Journal of the American Chemical Society* **2014,** *136* (28), 10139-10147.
193. Figueira, C. A.; Lopes, P. S.; Gomes, P. T., Synthesis of 2-arylpyrroles via catalytic dehydrogenation of 2-aryl-1-pyrrolines in the presence of palladium-supported on alumina. *Tetrahedron* **2015,** *71* (25), 4362-4371.
194. Hachiya, H.; Hirano, K.; Satoh, T.; Miura, M., Oxidative Nickel–Air Catalysis in C□H Arylation: Direct Cross-Coupling of Azoles with Arylboronic Acids using Air as Sole Oxidant. *ChemCatChem* **2010,** *2* (11), 1403-1406.
195. Hajipour, A. R.; Azizi, G., Iron-catalyzed cross-coupling reaction: recyclable heterogeneous iron catalyst for selective olefination of aryl iodides in poly(ethylene glycol) medium. *Green Chemistry* **2013,** *15* (4), 1030-1034.
196. Hilton, M. C.; Dolewski, R. D.; McNally, A., Selective Functionalization of Pyridines via Heterocyclic Phosphonium Salts. *Journal of the American Chemical Society* **2016,** *138* (42), 13806-13809.
197. Hirano, K., Miura, Masahiro, Development of carbon-hydrogen bond direct conversion reaction of heteroarenes using first transition elements: Utilization of copper and nickel. *Synthetic Organic Chemistry* **2011,** *69* (3), 252-265.
198. Hirano, K.; Miura, M., Direct Carbon-Hydrogen Bond Functionalization of Heterocyclic Compounds. *Synlett* **2011,** *2011* (03), 294-307.
199. Huang, G.; Sun, H.; Qiu, X.; Jin, C.; Lin, C.; Shen, Y.; Jiang, J.; Wang, L., Ligand-Free Copper-Catalyzed Regioselective C-2 Arylation of Imidazo[2,1-b]thiazoles. *Organic Letters* **2011,** *13* (19), 5224-5227.
200. Huang, Y.; Guan, D.; Wang, L., Direct Arylation of Substituted Pyridines with Arylboronic Acids Catalyzed by Iron(II) Oxalate. *Chinese Journal of Chemistry* **2014,** *32* (12), 1294-1298.
201. Hyodo, I.; Tobisu, M.; Chatani, N., Catalytic Arylation of a C□H Bond in Pyridine and Related Six-Membered N-Heteroarenes Using Organozinc Reagents. *Chemistry – An Asian Journal* **2012,** *7* (6), 1357-1365.
202. Hyodo, I.; Tobisu, M.; Chatani, N., Regioselective C–H bond functionalizations of acridines using organozinc reagents. *Chemical Communications* **2012,** *48* (2), 308-310.
203. Jia, F.; Li, Z., Iron-catalyzed/mediated oxidative transformation of C–H bonds. *Organic Chemistry Frontiers* **2014,** *1* (2), 194-214.
204. Johnston, A. J. S.; Ling, K. B.; Sale, D.; Lebrasseur, N.; Larrosa, I., Direct ortho-Arylation of Pyridinecarboxylic Acids: Overcoming the Deactivating Effect of sp2-Nitrogen. *Organic Letters* **2016,** *18* (23), 6094-6097.
205. Kaewchangwat, N.; Sukato, R.; Vchirawongkwin, V.; Vilaivan, T.; Sukwattanasinitt, M.; Wacharasindhu, S., Direct synthesis of aryl substituted pyrroles from calcium carbide: an underestimated chemical feedstock. *Green Chemistry* **2015,** *17* (1), 460-465.
206. Karadeniz, E.; Zora, M.; Kılıçaslan, N. Z., Facile synthesis of aryl-substituted pyridines via Suzuki–Miyaura approach. *Tetrahedron* **2015,** *71* (47), 8943-8952.

207. Kocaoğlu, E.; Karaman, M. A.; Tokgöz, H.; Talaz, O., Transition-Metal Catalyst Free Oxidative Radical Arylation of N-Methylpyrrole. *ACS Omega* **2017,** *2* (8), 5000-5004.
208. Koley, M.; Wimmer, L.; Schnürch, M.; Mihovilovic, M. D., Pd(0)-Catalyzed Cu(I)-Thiophene-2-carboxylate-mediated Cross-Coupling of Heteroaromatic Thioethers and Boronic Acids—First Liebeskind–Srogl Reaction in Water. *Journal of Heterocyclic Chemistry* **2013,** *50* (6), 1368-1373.
209. Komeyama, K.; Nagao, Y.; Abe, M.; Takaki, K., Scope and Limitation for FeSO4-Mediated Direct Arylation of Heteroarenes with Arylboronic Acids and Its Synthetic Applications. *Bulletin of the Chemical Society of Japan* **2013,** *87* (2), 301-313.
210. Leemans, E.; Colpaert, F.; Mangelinckx, S.; De Brabandere, S.; Denolf, B.; De Kimpe, N., Synthesis of 3-Aryl-3-pyrrolines and 3-Arylpyrroles via Spontaneous Rearrangement of N-Sulfinyl 2-Aryl-2-vinylaziridines. *Synlett* **2011,** *2011* (05), 674-678.
211. Juanhua, L., Kunming, L., Xinfang, D., Jinbiao, L., Recent Progress in Iron Catalyzed C-C Coupling Reactions *Chinese Journal of Organic Chemistry* **2017,** *37* (2).
212. Li, X.; Wang, H.-Y.; Shi, Z.-J., Transition-metal-free cross-dehydrogenative alkylation of pyridines under neutral conditions. *New Journal of Chemistry* **2013,** *37* (6), 1704-1706.
213. Liu, B.; Guo, Q.; Cheng, Y.; Lan, J.; You, J., Palladium-Catalyzed Desulfitative C□H Arylation of Heteroarenes with Sodium Sulfinates. *Chemistry – A European Journal* **2011,** *17* (48), 13415-13419.
214. Ma, Z.; Liu, H.; Zhang, C.; Zheng, X.; Yuan, M.; Fu, H.; Li, R.; Chen, H., One-Pot Synthesis of Symmetrical 2,6-Diarylpyridines via Palladium/Copper-Catalyzed Sequential Decarboxylative and Direct C□H Arylation. *Advanced Synthesis & Catalysis* **2015,** *357* (6), 1143-1148.
215. Maeda, H.; Fukui, A.; Yamakado, R.; Yasuda, N., Dipyrrolyphenol as a precursor of π-electronic anion that forms ion pairs with cations. *Chemical Communications* **2015,** *51* (99), 17572-17575.
216. Marín-Hernández, C.; Santos-Figueroa, L. E.; Moragues, M. E.; Raposo, M. M. M.; Batista, R. M. F.; Costa, S. P. G.; Pardo, T.; Martínez-Máñez, R.; Sancenón, F., Imidazoanthraquinone Derivatives for the Chromofluorogenic Sensing of Basic Anions and Trivalent Metal Cations. *The Journal of Organic Chemistry* **2014,** *79* (22), 10752-10761.
217. Midya, G. C.; Paladhi, S.; Dhara, K.; Dash, J., Iron catalyzed highly regioselective dimerization of terminal aryl alkynes. *Chemical Communications* **2011,** *47* (23), 6698-6700.
218. Midya, G. C.; Parasar, B.; Dhara, K.; Dash, J., Ligand mediated iron catalyzed dimerization of terminal aryl alkynes: scope and limitations. *Organic & Biomolecular Chemistry* **2014,** *12* (11), 1812-1822.
219. Murakami, K.; Yamada, S.; Kaneda, T.; Itami, K., C–H Functionalization of Azines. *Chemical Reviews* **2017,** *117* (13), 9302-9332.
220. Nakao, Y., Transition-Metal-Catalyzed C-H Functionalization for the Synthesis of Substituted Pyridines. *Synthesis* **2011,** *2011* (20), 3209-3219.
221. Nishimoto, Y.; Kondo, H.; Yamaguchi, K.; Yokogawa, D.; Yamaguchi, J.; Itami, K.; Irle, S., Theoretical Elucidation of Potential Enantioselectivity in a Pd-Catalyzed Aromatic C–H Coupling Reaction. *The Journal of Organic Chemistry* **2017,** *82* (9), 4900-4906.
222. Pagar, V. V.; Liu, R.-S., Gold-catalyzed α-furanylations of quinoline N-oxides with alkenyldiazo carbonyl species. *Organic & Biomolecular Chemistry* **2015,** *13* (22), 6166-6169.
223. Pan, F.; Wang, H.; Shen, P.-X.; Zhao, J.; Shi, Z.-J., Cross coupling of thioethers with aryl boroxines to construct biaryls via Rh catalyzed C–S activation. *Chemical Science* **2013,** *4* (4), 1573-1577.
224. Partyka, D. V., Transmetalation of Unsaturated Carbon Nucleophiles from Boron-Containing Species to the Mid to Late d-Block Metals of Relevance to Catalytic C–X Coupling Reactions (X = C, F, N, O, Pb, S, Se, Te). *Chemical Reviews* **2011,** *111* (3), 1529-1595.
225. Perumgani, P. C.; Parvathaneni, S. P.; Keesara, S.; Mandapati, M. R., Recyclable Pd(II)complex catalyzed oxidative sp2 CH bond acylation of 2-aryl pyridines with toluene derivatives. *Journal of Organometallic Chemistry* **2016,** *822*, 189-195.

226. Qian, Y. Y.; Wong, K. L.; Zhang, M. W.; Kwok, T. Y.; To, C. T.; Chan, K. S., Catalytic C–H arylation of unactivated heteroaromatics with aryl halides by cobalt porphyrin. *Tetrahedron Letters* **2012,** *53* (13), 1571-1575.
227. Batchu, V. R.; Romero-Estudillo, I.; Boto, A.; Miguélez, J., Metal-free, one-pot conversion of proline derivatives into 2-aryl-3-iodo pyrrolidines by a sequential scission–iodination–arylation process. *Organic & Biomolecular Chemistry* **2014,** *12* (47), 9547-9556.
228. Rossi, R.; Lessi, M.; Manzini, C.; Marianetti, G.; Bellina, F., Transition Metal-Free Direct C□H (Hetero)arylation of Heteroarenes: A Sustainable Methodology to Access (Hetero)aryl-Substituted Heteroarenes. *Advanced Synthesis & Catalysis* **2015,** *357* (18), 3777-3814.
229. Shang, R.; Ilies, L.; Nakamura, E., Iron-Catalyzed C–H Bond Activation. *Chemical Reviews* **2017,** *117* (13), 9086-9139.
230. Shirakawa, E.; Nishikawa, R.; Uchiyama, N.; Hata, I.; Hayashi, T., Copper-catalyzed Oxidative C–C, C–O, and C–N Bond Forming Reactions of Arylboronic Acids. *Chemistry Letters* **2013,** *42* (3), 269-271.
231. Singh, P. P.; Aithagani, S. K.; Yadav, M.; Singh, V. P.; Vishwakarma, R. A., Iron-catalyzed Cross-Coupling of Electron-Deficient Heterocycles and Quinone with Organoboron Species via Innate C–H Functionalization: Application in Total Synthesis of Pyrazine Alkaloid Botryllazine A. *The Journal of Organic Chemistry* **2013,** *78* (6), 2639-2648.
232. Uchiyama, N.; Shirakawa, E.; Nishikawa, R.; Hayashi, T., Iron-catalyzed oxidative coupling of arylboronic acids with benzene derivatives through homolytic aromatic substitution. *Chemical Communications* **2011,** *47* (42), 11671-11673.
233. Vakuliuk, O.; Koszarna, B.; Gryko, D. T., Base-Mediated Direct Arylation of Pyrrole Derivatives. *Advanced Synthesis & Catalysis* **2011,** *353* (6), 925-930.
234. Wang, H. B.; Hu, Y.-L.; Li, D.-J., Facile and efficient Suzuki–Miyaura coupling reaction of aryl halides catalyzed by Pd2(dba)3 in ionic liquid/supercritical carbon dioxide biphasic system. *Journal of Molecular Liquids* **2016,** *218*, 429-433.
235. Wang, H.-Y.; Mueller, D. S.; Sachwani, R. M.; Kapadia, R.; Londino, H. N.; Anderson, L. L., Regioselective Synthesis of 2,3,4- or 2,3,5-Trisubstituted Pyrroles via [3,3] or [1,3] Rearrangements of O-Vinyl Oximes. *The Journal of Organic Chemistry* **2011,** *76* (9), 3203-3221.
236. Wang, J.; Wang, S.; Wang, G.; Zhang, J.; Yu, X.-Q., Iron-mediated direct arylation with arylboronic acids through an aryl radical transfer pathway. *Chemical Communications* **2012,** *48* (96), 11769-11771.
237. Wen, J.; Zhang, R.-Y.; Chen, S.-Y.; Zhang, J.; Yu, X.-Q., Direct Arylation of Arene and N-Heteroarenes with Diaryliodonium Salts without the Use of Transition Metal Catalyst. *The Journal of Organic Chemistry* **2012,** *77* (1), 766-771.
238. Xu, J.; Shao, L.-D.; Li, D.; Deng, X.; Liu, Y.-C.; Zhao, Q.-S.; Xia, C., Construction of Tetracyclic 3-Spirooxindole through Cross-Dehydrogenation of Pyridinium: Applications in Facile Synthesis of (±)-Corynoxine and (±)-Corynoxine B. *Journal of the American Chemical Society* **2014,** *136* (52), 17962-17965.
239. Yagoubi, M.; Cruz, A. C. F.; Nichols, P. L.; Elliott, R. L.; Willis, M. C., Cascade Palladium-Catalyzed Direct Intramolecular Arylation/Alkene Isomerization Sequences: Synthesis of Indoles and Benzofurans. *Angewandte Chemie International Edition* **2010,** *49* (43), 7958-7962.
240. Yamaguchi, K.; Kondo, H.; Yamaguchi, J.; Itami, K., Aromatic C–H coupling with hindered arylboronic acids by Pd/Fe dual catalysts. *Chemical Science* **2013,** *4* (9), 3753-3757.
241. Yılmaz, Ü.; Deniz, S.; Küçükbay, H.; Şireci, N., Microwave Assisted Suzuki-Miyaura and Ullmann Type Homocoupling Reactions of 2- and 3-Halopyridines Using a Pd(OAc)2/Benzimidazolium Salt and Base Catalyst System. *Molecules* **2013,** *18* (4).
242. Yu, X.; Li, X.; Wan, B., Palladium-catalyzed desulfitative arylation of azoles with arylsulfonyl hydrazides. *Organic & Biomolecular Chemistry* **2012,** *10* (37), 7479-7482.

243. Zhang, B., Zhou, Q., Chen, R., Jiang, H., Transition-Metal-Catalyzed Functionalization of Pyridines. *Chinese Journal of Organic Chemistry* **2012,** *32*, 1653-1665.
244. Zhang, Q.; Li, C.; Yang, F.; Li, J.; Wu, Y., Palladium-catalyzed ortho-acylation of 2-arylbenzoxazoles. *Tetrahedron* **2013,** *69* (1), 320-326.
245. Zhang, Q.; Yang, F.; Wu, Y., Palladium-catalyzed ortho-acylation of 2-aryl pyridine derivatives using arylmethyl amines as new acyl sources. *Chemical Communications* **2013,** *49* (61), 6837-6839.
246. Zhu, T.; Li, X.; Chang, H.; Gao, W.; Wei, W., Nano-Pd/Al(OH)3-Catalyzed Suzuki–Miyaura Coupling Reaction of Potassium Aryl- and Heteroaryltrifluoroborates with Electrophiles in Alcohols. *Synlett* **2016,** *27* (06), 880-887.
247. Zhuo, F.-F.; Xie, W.-W.; Yang, Y.-X.; Zhang, L.; Wang, P.; Yuan, R.; Da, C.-S., TMEDA-Assisted Effective Direct Ortho Arylation of Electron-Deficient N-Heteroarenes with Aromatic Grignard Reagents. *The Journal of Organic Chemistry* **2013,** *78* (7), 3243-3249.
248. Najafpour, M. M.; Safdari, R.; Ebrahimi, F.; Rafighi, P.; Bagheri, R., Water oxidation by a soluble iron(iii)–cyclen complex: new findings. *Dalton Transactions* **2016,** *45* (6), 2618-2623.
249. Chen, G.; Chen, L.; Ng, S.-M.; Man, W.-L.; Lau, T.-C., Chemical and Visible-Light-Driven Water Oxidation by Iron Complexes at pH 7–9: Evidence for Dual-Active Intermediates in Iron-Catalyzed Water Oxidation. *Angewandte Chemie International Edition* **2013,** *52* (6), 1789-1791.
250. Raffard, N.; Carina, R.; Simaan, A. J.; Sainton, J.; Rivière, E.; Tchertanov, L.; Bourcier, S.; Bouchoux, G.; Delroisse, M.; Banse, F.; Girerd, J.-J., Biomimetic Catalysis of Catechol Cleavage by O2 in Organic Solvents − Role of Accessibility of O2 to FeIII in 2,11-Diaza[3,3](2,6)pyridinophane-Type Catalysts. *European Journal of Inorganic Chemistry* **2001,** *2001* (9), 2249-2254.
251. Fulmer, G. R.; Miller, A. J. M.; Sherden, N. H.; Gottlieb, H. E.; Nudelman, A.; Stoltz, B. M.; Bercaw, J. E.; Goldberg, K. I., NMR Chemical Shifts of Trace Impurities: Common Laboratory Solvents, Organics, and Gases in Deuterated Solvents Relevant to the Organometallic Chemist. *Organometallics* **2010,** *29* (9), 2176-2179.
252. Ferraudi, G., Photochemistry of high-spin iron(III) complexes of the macrocyclic ligands [15]pydieneN5 and [15]pyaneN5. An investigation of the charge-transfer processes. *Inorganic Chemistry* **1980,** *19* (2), 438-444.
253. Wakelin, L. P. G.; Bu, X.; Eleftheriou, A.; Parmar, A.; Hayek, C.; Stewart, B. W., Bisintercalating Threading Diacridines: Relationships between DNA Binding, Cytotoxicity, and Cell Cycle Arrest. *Journal of Medicinal Chemistry* **2003,** *46* (26), 5790-5802.
254. Rakowski, M. C.; Rycheck, M.; Busch, D. H., Synthesis and characterization of transition metal complexes containing a pentadentate macrocyclic ligand. *Inorganic Chemistry* **1975,** *14* (5), 1194-1200.
255. Kálmán, F. K.; Végh, A.; Regueiro-Figueroa, M.; Tóth, É.; Platas-Iglesias, C.; Tircsó, G., H4octapa: Highly Stable Complexation of Lanthanide(III) Ions and Copper(II). *Inorganic Chemistry* **2015,** *54* (5), 2345-2356.
256. de Sá, A.; Bonnet, C. S.; Geraldes, C. F. G. C.; Tóth, É.; Ferreira, P. M. T.; André, J. P., Thermodynamic stability and relaxation studies of small, triaza-macrocyclic Mn(ii) chelates. *Dalton Transactions* **2013,** *42* (13), 4522-4532.
257. Nelson, S. M.; Busch, D. H., Seven-coordination in some mononuclear and binuclear iron(III) complexes containing a pentadentate macrocyclic ring. *Inorganic Chemistry* **1969,** *8* (9), 1859-1863.
258. Hodgkinson, L. C.; Johnson, M. R.; Leigh, S. J.; Spencer, N.; Sutherland, I. O.; Newton, R. F., Formation of complexes between aza derivatives of crown ethers and primary alkylammonium salts. Part 4. Diaza-18-crown-6 derivatives. *Journal of the Chemical Society, Perkin Transactions 1* **1979,** (0), 2193-2202.
259. B.A.X.-R Solutions, A., (Version 2014.9-0), **2007**.
260. B.A.X.-R Solutions, X., (Version 6.3.1), **2004**.
261. Abragam, A., Bleaney, B., Electron Paramagentic Resonance of Transition Ions. **1970**.

262. Alcock, N. W., Busch, D. H., Liu, C. Y., , Private Communication **2007**.
263. Chow, T. W.-S.; Wong, E. L.-M.; Guo, Z.; Liu, Y.; Huang, J.-S.; Che, C.-M., cis-Dihydroxylation of Alkenes with Oxone Catalyzed by Iron Complexes of a Macrocyclic Tetraaza Ligand and Reaction Mechanism by ESI-MS Spectrometry and DFT Calculations. *Journal of the American Chemical Society* **2010,** *132* (38), 13229-13239.
264. Shannon, R., Revised effective ionic radii and systematic studies of interatomic distances in halides and chalcogenides. *Acta Crystallographica Section A* **1976,** *32* (5), 751-767.
265. Koch, W. O.; Barbieri, A.; Grodzicki, M.; Schünemann, V.; Trautwein, A. X.; Krüger, H.-J., Eight-Coordinate Iron(II) and Iron(III) Ions in Complexes with Distorted Dodecahedral FeN8 Environments: Synthesis and Structures of Bis(2,11-diaza[3.3](2,6)pyridinophane)iron Complexes. *Angewandte Chemie International Edition in English* **1996,** *35* (4), 422-424.
266. Lincoln, K. M.; Gonzalez, P.; Richardson, T. E.; Julovich, D. A.; Saunders, R.; Simpkins, J. W.; Green, K. N., A potent antioxidant small molecule aimed at targeting metal-based oxidative stress in neurodegenerative disorders. *Chemical Communications* **2013,** *49* (26), 2712-2714.
267. Bard, A. J., Faulkner, L. R., Leddy, J., Zoski, C. G., Electrochemical Methods: Fundamentals and Applications. **2001**.
268. Hua, W. S.; Ajiboye, S. I.; Haining, G.; McGhee, L.; Peacock, R. D.; Peattie, G.; Siddique, R. M.; Winfield, J. M., Co-ordination chemistry of iodine(I) with tetraazamacrocycles or monodentate ligands. Comparisons with bromine(I) and with some d-block metals. *Journal of the Chemical Society, Dalton Transactions* **1995,** (23), 3837-3841.
269. Enemark, J. H.; Feltham, R. D., Principles of structure, bonding, and reactivity for metal nitrosyl complexes. *Coordination Chemistry Reviews* **1974,** *13* (4), 339-406.
270. Hoffmann, R.; Chen, M. M. L.; Thorn, D. L., Qualitative discussion of alternative coordination modes of diatomic ligands in transition metal complexes. *Inorganic Chemistry* **1977,** *16* (3), 503-511.
271. Ye, S.; Neese, F., The Unusual Electronic Structure of Dinitrosyl Iron Complexes. *Journal of the American Chemical Society* **2010,** *132* (11), 3646-3647.
272. Hauser, C.; Glaser, T.; Bill, E.; Weyhermüller, T.; Wieghardt, K., The Electronic Structures of an Isostructural Series of Octahedral Nitrosyliron Complexes {Fe−NO}6,7,8 Elucidated by Mössbauer Spectroscopy. *Journal of the American Chemical Society* **2000,** *122* (18), 4352-4365.
273. Vanin, A. F., Bioorganometallic Chemistry. **2015**, 202-238.
274. Hickok, J. R.; Sahni, S.; Shen, H.; Arvind, A.; Antoniou, C.; Fung, L. W. M.; Thomas, D. D., Dinitrosyliron complexes are the most abundant nitric oxide-derived cellular adduct: biological parameters of assembly and disappearance. *Free Radical Biology and Medicine* **2011,** *51* (8), 1558-1566.
275. Wyllie, G. R. A.; Scheidt, W. R., Solid-State Structures of Metalloporphyrin NOx Compounds. *Chemical Reviews* **2002,** *102* (4), 1067-1090.
276. Pellegrino, J.; Bari, S. E.; Bikiel, D. E.; Doctorovich, F., Successful Stabilization of the Elusive Species {FeNO}8 in a Heme Model. *Journal of the American Chemical Society* **2010,** *132* (3), 989-995.
277. Goodrich, L. E.; Roy, S.; Alp, E. E.; Zhao, J.; Hu, M. Y.; Lehnert, N., Electronic Structure and Biologically Relevant Reactivity of Low-Spin {FeNO}8 Porphyrin Model Complexes: New Insight from a Bis-Picket Fence Porphyrin. *Inorganic Chemistry* **2013,** *52* (13), 7766-7780.
278. Hu, B.; Li, J., One Electron Makes Differences: From Heme {FeNO}7 to {FeNO}8. *Angewandte Chemie* **2015,** *127* (36), 10725-10728.
279. Kundakarla, N.; Lindeman, S.; Rahman, M. H.; Ryan, M. D., X-ray Structure and Properties of the Ferrous Octaethylporphyrin Nitroxyl Complex. *Inorganic Chemistry* **2016,** *55* (5), 2070-2075.
280. Serres, R. G., Grapperhaus, C. A., Bothe, E., Bill, E., Weyhermuller T., Neese, F., Wieghardt, K., Structural, Spectroscopic, and Computational Study of an Octahedral, Non-Heme $\{Fe{-}NO0\}^{6-8}$ Series: $[Fe(NO)(cyclam\text{-}ac)]^{2+/+/0}$. *Journal of the American Chemical Society* **2004,** *125*, 12509-12513.

281. Speelman, A. L.; Lehnert, N., Characterization of a High-Spin Non-Heme {FeNO}8 Complex: Implications for the Reactivity of Iron Nitroxyl Species in Biology. *Angewandte Chemie* **2013,** *125* (47), 12509-12513.
282. Confer, A. M.; McQuilken, A. C.; Matsumura, H.; Moënne-Loccoz, P.; Goldberg, D. P., A Nonheme, High-Spin {FeNO}8 Complex that Spontaneously Generates N2O. *Journal of the American Chemical Society* **2017,** *139* (31), 10621-10624.
283. Kupper, C.; Rees, J. A.; Dechert, S.; DeBeer, S.; Meyer, F., Complete Series of {FeNO}8, {FeNO}7, and {FeNO}6 Complexes Stabilized by a Tetracarbene Macrocycle. *Journal of the American Chemical Society* **2016,** *138* (25), 7888-7898.
284. Denny, J. A.; Darensbourg, M. Y., Metallodithiolates as Ligands in Coordination, Bioinorganic, and Organometallic Chemistry. *Chemical Reviews* **2015,** *115* (11), 5248-5273.
285. Can, M.; Armstrong, F. A.; Ragsdale, S. W., Structure, Function, and Mechanism of the Nickel Metalloenzymes, CO Dehydrogenase, and Acetyl-CoA Synthase. *Chemical Reviews* **2014,** *114* (8), 4149-4174.
286. Darnault, C.; Volbeda, A.; Kim, E. J.; Legrand, P.; Vernède, X.; Lindahl, P. A.; Fontecilla-Camps, J. C., Ni-Zn-[Fe4-S4] and Ni-Ni-[Fe4-S4] clusters in closed and open α subunits of acetyl-CoA synthase/carbon monoxide dehydrogenase. *Nature Structural & Molecular Biology* **2003,** *10* (4), 271-279.
287. Hsieh, C.-H.; Ding, S.; Erdem, Ö. F.; Crouthers, D. J.; Liu, T.; McCrory, C. C. L.; Lubitz, W.; Popescu, C. V.; Reibenspies, J. H.; Hall, M. B.; Darensbourg, M. Y., Redox active iron nitrosyl units in proton reduction electrocatalysis. *Nature Communications* **2014,** *5*, 3684.
288. Ding, S.; Ghosh, P.; Darensbourg, M. Y.; Hall, M. B., Interplay of hemilability and redox activity in models of hydrogenase active sites. *Proceedings of the National Academy of Sciences* **2017,** *114* (46), E9775.
289. Ghosh, P.; Ding, S.; Chupik, R. B.; Quiroz, M.; Hsieh, C.-H.; Bhuvanesh, N.; Hall, M. B.; Darensbourg, M. Y., A matrix of heterobimetallic complexes for interrogation of hydrogen evolution reaction electrocatalysts. *Chemical Science* **2017,** *8* (12), 8291-8300.
290. Karlin, K. D.; Lippard, S. J., Sulfur-bridged binuclear iron(II) complexes. Effect of ligand constraints on their physical properties; reactions with carbon monoxide and alkyl isocyanides. *Journal of the American Chemical Society* **1976,** *98* (22), 6951-6957.
291. Karlin, K. D.; Rabinowitz, H. N.; Lewis, D. L.; Lippard, S. J., Synthesis and characterization of the pentacoordinate mononitrosyliron complexes Fe(NO)[SCH2CH2N(CH3)(CH2)nN(CH3)CH2CH2S], n = 2,3. *Inorganic Chemistry* **1977,** *16* (12), 3262-3267.
292. Hsieh, C.-H.; Darensbourg, M. Y., A {Fe(NO)3}10 Trinitrosyliron Complex Stabilized by an N-Heterocyclic Carbene and the Cationic and Neutral {Fe(NO)2}9/10 Products of Its NO Release. *Journal of the American Chemical Society* **2010,** *132* (40), 14118-14125.
293. Hsieh, C.-H.; Brothers, S. M.; Reibenspies, J. H.; Hall, M. B.; Popescu, C. V.; Darensbourg, M. Y., Ambidentate Thiocyanate and Cyanate Ligands in Dinitrosyl Iron Complexes. *Inorganic Chemistry* **2013,** *52* (4), 2119-2124.
294. Butler, A. R.; Megson, I. L., Non-Heme Iron Nitrosyls in Biology. *Chemical Reviews* **2002,** *102* (4), 1155-1166.
295. Chiang, C.-Y.; Miller, M. L.; Reibenspies, J. H.; Darensbourg, M. Y., Bismercaptoethanediazacyclooctane as a N2S2 Chelating Agent and Cys−X−Cys Mimic for Fe(NO) and Fe(NO)2. *Journal of the American Chemical Society* **2004,** *126* (35), 10867-10874.
296. Tannoudji, C. C., Quantum Mechanics. **1977**.
297. Gupta, R.; Lacy, D. C.; Bominaar, E. L.; Borovik, A. S.; Hendrich, M. P., Electron Paramagnetic Resonance and Mössbauer Spectroscopy and Density Functional Theory Analysis of a High-Spin FeIV–Oxo Complex. *Journal of the American Chemical Society* **2012,** *134* (23), 9775-9784.

298. Hendrich, M. P.; Munck, E.; Fox, B. G.; Lipscomb, J. D., Integer-spin EPR studies of the fully reduced methane monooxygenase hydroxylase component. *Journal of the American Chemical Society* **1990,** *112* (15), 5861-5865.
299. Lacy, D. C.; Gupta, R.; Stone, K. L.; Greaves, J.; Ziller, J. W.; Hendrich, M. P.; Borovik, A. S., Formation, Structure, and EPR Detection of a High Spin FeIV—Oxo Species Derived from Either an FeIII—Oxo or FeIII—OH Complex. *Journal of the American Chemical Society* **2010,** *132* (35), 12188-12190.
300. Yamaguchi, K.; Yamanaka, S.; Nishino, M.; Takano, Y.; Kitagawa, Y.; Nagao, H.; Yoshioka, Y., Symmetry and broken symmetries in molecular orbital descriptions of unstable molecules II. Alignment, flustration and tunneling of spins in mesoscopic molecular magnets. *Theoretical Chemistry Accounts* **1999,** *102* (1), 328-345.
301. Addison, A. W.; Rao, T. N.; Reedijk, J.; van Rijn, J.; Verschoor, G. C., Synthesis, structure, and spectroscopic properties of copper(II) compounds containing nitrogen–sulphur donor ligands; the crystal and molecular structure of aqua[1,7-bis(N-methylbenzimidazol-2'-yl)-2,6-dithiaheptane]copper(II) perchlorate. *Journal of the Chemical Society, Dalton Transactions* **1984,** (7), 1349-1356.
302. Sun, N.; Liu, L. V.; Dey, A.; Villar-Acevedo, G.; Kovacs, J. A.; Darensbourg, M. Y.; Hodgson, K. O.; Hedman, B.; Solomon, E. I., S K-Edge X-Ray Absorption Spectroscopy and Density Functional Theory Studies of High and Low Spin {FeNO}7 Thiolate Complexes: Exchange Stabilization of Electron Delocalization in {FeNO}7 and {FeO2}8. *Inorganic Chemistry* **2011,** *50* (2), 427-436.
303. Mingos, D. M. P., Structure and Bonding. *Springer* **2014**, 1-44.
304. Bakalova, R.; Georgieva, E.; Ivanova, D.; Zhelev, Z.; Aoki, I.; Saga, T., Magnetic Resonance Imaging of Mitochondrial Dysfunction and Metabolic Activity, Accompanied by Overproduction of Superoxide. *ACS Chemical Neuroscience* **2015,** *6* (12), 1922-1929.
305. Sabharwal, S. S.; Schumacker, P. T., Mitochondrial ROS in cancer: initiators, amplifiers or an Achilles' heel? *Nature Reviews Cancer* **2014,** *14*, 709.
306. Desideri, E.; Vegliante, R.; Ciriolo, M. R., Mitochondrial dysfunctions in cancer: Genetic defects and oncogenic signaling impinging on TCA cycle activity. *Cancer Letters* **2015,** *356* (2, Part A), 217-223.
307. Pinto, M.; Moraes, C. T., Mitochondrial genome changes and neurodegenerative diseases. *Biochimica et Biophysica Acta (BBA) - Molecular Basis of Disease* **2014,** *1842* (8), 1198-1207.
308. Yadav, A.; Agrawal, S.; Kant Tiwari, S.; K Chaturvedi, R., Mitochondria: Prospective Targets for Neuroprotection in Parkinson's Disease. *Current pharmaceutical design* **2014,** *20*.
309. Giacco, F.; Brownlee, M., Oxidative stress and diabetic complications. *Circulation research* **2010,** *107* (9), 1058-1070.
310. Lowell, B. B.; Shulman, G. I., Mitochondrial Dysfunction and Type 2 Diabetes. *Science* **2005,** *307* (5708), 384.
311. Campuzano, V.; Montermini, L.; Moltò, M. D.; Pianese, L.; Cossée, M.; Cavalcanti, F.; Monros, E.; Rodius, F.; Duclos, F.; Monticelli, A.; Zara, F.; Cañizares, J.; Koutnikova, H.; Bidichandani, S. I.; Gellera, C.; Brice, A.; Trouillas, P.; De Michele, G.; Filla, A.; De Frutos, R.; Palau, F.; Patel, P. I.; Di Donato, S.; Mandel, J.-L.; Cocozza, S.; Koenig, M.; Pandolfo, M., Friedreich's Ataxia: Autosomal Recessive Disease Caused by an Intronic GAA Triplet Repeat Expansion. *Science* **1996,** *271* (5254), 1423.
312. Mascialino, B.; Leinonen, M.; Meier, T., Meta-analysis of the prevalence of Leber hereditary optic neuropathy mtDNA mutations in Europe. *European Journal of Ophthalmology* **2011,** *22* (3), 461-465.
313. Montagna, P.; Gallassi, R.; Medori, R.; Govoni, E.; Zeviani, M.; Di Mauro, S.; Lugaresi, E.; Andermann, F., MELAS syndrome: Characteristic migrainous and epileptic features and maternal transmission. *Neurology* **1988,** *38*, 751-4.
314. Wallace, D. C. Z., X.; Lott, M. T.; Shoffner, J. M.; Hodge, J. A.; Kelley, R. I.; Epstein, C. M., Familial mitochondrial encephalomyopathy (MERRF): Genetic, pathophysiological, and biochemical characterization of a mitochondrial DNA disease. *Cell* **1988,** *55* (4), 601-610.

315. Hayashi, G. C., G., Oxidative stress in inherited mitochondrial diseases. *Free Radical Biology and Medicine* **2015,** *88* (Pt A), 10-17.
316. Rahman, S. B., R. B.; Dahl, H. H.; Danks, D. M.; Kirby, D. M.; Chow, C. W.; Christodoulou, J.; Thorburn, D. R., Leigh syndrome: clinical features and biochemical and DNA abnormalities. *Annual Neurology* **1996,** *39* (3), 343-351.
317. Abbas, K.; Hardy, M.; Poulhès, F.; Karoui, H.; Tordo, P.; Ouari, O.; Peyrot, F., Detection of superoxide production in stimulated and unstimulated living cells using new cyclic nitrone spin traps. *Free Radical Biology and Medicine* **2014,** *71*, 281-290.
318. Mrakic-Sposta, S. G., M.; Montorsi, M.; Porcelli, S.; Vezzoli, A., Assessment of a standardized ROS production profile in humans by electron paramagnetic resonance. *Oxidative Medicine and Cell Longevitiy* **2012,** *2012*, 973927.
319. Krotz, F. S., H. Y.; Pohl, U., Reactive oxygen species: players in the platelet game. *Arteriosclerosis, Thrombosis, and Vascular Biology* **2004,** *24* (11), 1988-1996.
320. Apel, K. H., H., Reactive oxygen species: metabolism, oxidative stress, and signal transduction. *Annual Review of Plant Biology* **2004,** *55*, 373-399.
321. Kanofsky, J. R., Singlet oxygen production by biological systems. *Chemico-Biological Interactions* **1989,** *70* (1-2), 1-28.
322. Kayama, Y. R., U.; Jagger, A.; Adam, M.; Schellinger, I. N.; Sakamoto, M.; Suzuki, H.; Toyama, K.; Spin, J. M.; Tsao, P. S., Diabetic Cardiovascular Disease Induced by Oxidative Stress. *International Journal of Molecular Science* **2015,** *16* (10), 25234-25263.
323. Cai, L. W., J.; Li, Y.; Sun, X.; Wang, L.; Zhou, Z.; Kang, Y. J., Inhibition of Superoxide Generation and Associated Nitrosative-Damage Is Involved in Metallothionein Prevention of Diabetic Cardiomyopathy. *Diabetes* **2005,** *54* (6), 1829-1837.
324. Woods, M. W., D. E.; Sherry, A. D., Paramagnetic lanthanide complexes as PARACEST agents for medical imaging. *Chemical Society Reviews* **2006,** *35* (6), 500-511.
325. Viswanathan, S. K., Z.; Green, K. N.; Ratnakar, S. J.; Sherry, A. D., Alternatives to gadolinium-based metal chelates for magnetic resonance imaging. *Chemical Reviews* **2010,** *110* (5), 2960-3018.
326. Sherry, A. D. W., M., Chemical exchange saturation transfer contrast agents for magnetic resonance imaging. *Annual Review of Biomedical Engineering* **2008,** *10*, 391-441.
327. Ivan, S., Electron Paramagnetic Resonance - A Powerful Tool of Medical Biochemistry in Discovering Mechanisms of Disease and Treatment Prospects. *Journal of Medical Biochemistry* **2010,** *29* (3), 175-188.
328. Ratnakar, S. J.; Soesbe, T. C.; Lumata, L. L.; Do, Q. N.; Viswanathan, S.; Lin, C.-Y.; Sherry, A. D.; Kovacs, Z., Modulation of CEST Images in Vivo by T1 Relaxation: A New Approach in the Design of Responsive PARACEST Agents. *Journal of the American Chemical Society* **2013,** *135* (40), 14904-14907.
329. Zhang, L.; Martins, A. F.; Zhao, P.; Wu, Y.; Tircsó, G.; Sherry, A. D., Lanthanide-Based T2ex and CEST Complexes Provide Insights into the Design of pH Sensitive MRI Agents. *Angewandte Chemie International Edition* **2017,** *56* (52), 16626-16630.
330. Zhang, L.; Martins, A. F.; Mai, Y.; Zhao, P.; Funk, A. M.; Clavijo Jordan, M. V.; Zhang, S.; Chen, W.; Wu, Y.; Sherry, A. D., Imaging Extracellular Lactate In Vitro and In Vivo Using CEST MRI and a Paramagnetic Shift Reagent. *Chemistry – A European Journal* **2017,** *23* (8), 1752-1756.
331. Song, B.; Wu, Y.; Yu, M.; Zhao, P.; Zhou, C.; Kiefer, G. E.; Sherry, A. D., A europium(iii)-based PARACEST agent for sensing singlet oxygen by MRI. *Dalton Transactions* **2013,** *42* (22), 8066-8069.
332. Do, Q. N.; Ratnakar, J. S.; Kovács, Z.; Sherry, A. D., Redox- and Hypoxia-Responsive MRI Contrast Agents. *ChemMedChem* **2014,** *9* (6), 1116-1129.
333. Hyodo, F.; Matsumoto, K.-i.; Matsumoto, A.; Mitchell, J. B.; Krishna, M. C., Probing the Intracellular Redox Status of Tumors with Magnetic Resonance Imaging and Redox-Sensitive Contrast Agents. *Cancer Research* **2006,** *66* (20), 9921.

334. Prescott, C.; Bottle, S. E., Biological Relevance of Free Radicals and Nitroxides. *Cell Biochemistry and Biophysics* **2017,** *75* (2), 227-240.
335. Liu, S.; Zhou, N.; Chen, Z.; Wei, H.; Zhu, Y.; Guo, S.; Zhao, Q., Using a redox-sensitive phosphorescent probe for optical evaluation of an intracellular redox environment. *Optics Letters* **2017,** *42* (1), 13-16.
336. Sowers, M. A.; McCombs, J. R.; Wang, Y.; Paletta, J. T.; Morton, S. W.; Dreaden, E. C.; Boska, M. D.; Ottaviani, M. F.; Hammond, P. T.; Rajca, A.; Johnson, J. A., Redox-responsive branched-bottlebrush polymers for in vivo MRI and fluorescence imaging. *Nature Communications* **2014,** *5*, 5460.
337. Merbach, A., Helm, L., Toth, E., The Chemistry of Contrast Agents in Medical Magnetic Resonance Imaging. **2013,** *2nd Ed*.
338. Nguyen, H. V. T.; Chen, Q.; Paletta, J. T.; Harvey, P.; Jiang, Y.; Zhang, H.; Boska, M. D.; Ottaviani, M. F.; Jasanoff, A.; Rajca, A.; Johnson, J. A., Nitroxide-Based Macromolecular Contrast Agents with Unprecedented Transverse Relaxivity and Stability for Magnetic Resonance Imaging of Tumors. *ACS Central Science* **2017,** *3* (7), 800-811.
339. Garmendia, S.; Mantione, D.; Alonso-de Castro, S.; Jehanno, C.; Lezama, L.; Hedrick, J. L.; Mecerreyes, D.; Salassa, L.; Sardon, H., Polyurethane based organic macromolecular contrast agents (PU-ORCAs) for magnetic resonance imaging. *Polymer Chemistry* **2017,** *8* (17), 2693-2701.
340. Chan, J. M. W.; Wojtecki, R. J.; Sardon, H.; Lee, A. L. Z.; Smith, C. E.; Shkumatov, A.; Gao, S.; Kong, H.; Yang, Y. Y.; Hedrick, J. L., Self-Assembled, Biodegradable Magnetic Resonance Imaging Agents: Organic Radical-Functionalized Diblock Copolymers. *ACS Macro Letters* **2017,** *6* (2), 176-180.
341. Haugland, M. M.; Anderson, E. A.; Lovett, J. E., Tuning the properties of nitroxide spin labels for use in electron paramagnetic resonance spectroscopy through chemical modification of the nitroxide framework. In *Electron Paramagnetic Resonance: Volume 25*, The Royal Society of Chemistry: 2017; Vol. 25, pp 1-34.
342. Rajca, A.; Wang, Y.; Boska, M.; Paletta, J. T.; Olankitwanit, A.; Swanson, M. A.; Mitchell, D. G.; Eaton, S. S.; Eaton, G. R.; Rajca, S., Organic Radical Contrast Agents for Magnetic Resonance Imaging. *Journal of the American Chemical Society* **2012,** *134* (38), 15724-15727.
343. Yamada, K.-i.; Mito, F.; Matsuoka, Y.; Ide, S.; Shikimachi, K.; Fujiki, A.; Kusakabe, D.; Ishida, Y.; Enoki, M.; Tada, A.; Ariyoshi, M.; Yamasaki, T.; Yamato, M., Fluorescence probes to detect lipid-derived radicals. *Nature Chemical Biology* **2016,** *12*, 608.
344. Anderson, E. A.; Isaacman, S.; Peabody, D. S.; Wang, E. Y.; Canary, J. W.; Kirshenbaum, K., Viral Nanoparticles Donning a Paramagnetic Coat: Conjugation of MRI Contrast Agents to the MS2 Capsid. *Nano Letters* **2006,** *6* (6), 1160-1164.
345. Chen, Z.; Li, N.; Li, S.; Dharmarwardana, M.; Schlimme, A.; Gassensmith, J. J., Viral chemistry: the chemical functionalization of viral architectures to create new technology. *Wiley Interdisciplinary Reviews: Nanomedicine and Nanobiotechnology* **2016,** *8* (4), 512-534.
346. Scholthof, K.-B. G.; Adkins, S.; Czosnek, H.; Palukaitis, P.; Jacquot, E.; Hohn, T.; Hohn, B.; Saunders, K.; Candresse, T.; Ahlquist, P.; Hemenway, C.; Foster, G. D., Top 10 plant viruses in molecular plant pathology. *Molecular Plant Pathology* **2011,** *12* (9), 938-954.
347. Harrison, B. D.; Wilson, T. M. A., Milestones in the Research on Tobacco Mosaic Virus. *Philosophical Transactions: Biological Sciences* **1999,** *354* (1383), 521-529.
348. Klug, A., The tobacco mosaic virus particle: structure and assembly. *Philosophical transactions of the Royal Society of London. Series B, Biological sciences* **1999,** *354* (1383), 531-535.
349. Sitasuwan, P.; Lee, L. A.; Li, K.; Nguyen, H. G.; Wang, Q., RGD-conjugated rod-like viral nanoparticles on 2D scaffold improve bone differentiation of mesenchymal stem cells. *Frontiers in chemistry* **2014,** *2*, 31-31.

350. Miller, R. A.; Stephanopoulos, N.; McFarland, J. M.; Rosko, A. S.; Geissler, P. L.; Francis, M. B., Impact of Assembly State on the Defect Tolerance of TMV-Based Light Harvesting Arrays. *Journal of the American Chemical Society* **2010,** *132* (17), 6068-6074.
351. Datta, A.; Hooker, J. M.; Botta, M.; Francis, M. B.; Aime, S.; Raymond, K. N., High Relaxivity Gadolinium Hydroxypyridonate−Viral Capsid Conjugates: Nanosized MRI Contrast Agents1. *Journal of the American Chemical Society* **2008,** *130* (8), 2546-2552.
352. Schlick, T. L.; Ding, Z.; Kovacs, E. W.; Francis, M. B., Dual-Surface Modification of the Tobacco Mosaic Virus. *Journal of the American Chemical Society* **2005,** *127* (11), 3718-3723.
353. Li, S.; Dharmarwardana, M.; Welch, R. P.; Ren, Y.; Thompson, C. M.; Smaldone, R. A.; Gassensmith, J. J., Template-Directed Synthesis of Porous and Protective Core–Shell Bionanoparticles. *Angewandte Chemie International Edition* **2016,** *55* (36), 10691-10696.
354. Li, S.; Dharmarwardana, M.; Welch, R. P.; Benjamin, C. E.; Shamir, A. M.; Nielsen, S. O.; Gassensmith, J. J., Investigation of Controlled Growth of Metal–Organic Frameworks on Anisotropic Virus Particles. *ACS Applied Materials & Interfaces* **2018,** *10* (21), 18161-18169.
355. Bruckman, M. A.; Randolph, L. N.; Gulati, N. M.; Stewart, P. L.; Steinmetz, N. F., Silica-coated Gd(DOTA)-loaded protein nanoparticles enable magnetic resonance imaging of macrophages. *Journal of materials chemistry. B* **2015,** *3* (38), 7503-7510.
356. Hu, H.; Zhang, Y.; Shukla, S.; Gu, Y.; Yu, X.; Steinmetz, N. F., Dysprosium-Modified Tobacco Mosaic Virus Nanoparticles for Ultra-High-Field Magnetic Resonance and Near-Infrared Fluorescence Imaging of Prostate Cancer. *ACS Nano* **2017,** *11* (9), 9249-9258.
357. Bruckman, M. A.; Hern, S.; Jiang, K.; Flask, C. A.; Yu, X.; Steinmetz, N. F., Tobacco mosaic virus rods and spheres as supramolecular high-relaxivity MRI contrast agents. *Journal of materials chemistry. B* **2013,** *1* (10), 1482-1490.
358. Bruckman, M. A.; Jiang, K.; Simpson, E. J.; Randolph, L. N.; Luyt, L. G.; Yu, X.; Steinmetz, N. F., Dual-Modal Magnetic Resonance and Fluorescence Imaging of Atherosclerotic Plaques in Vivo Using VCAM-1 Targeted Tobacco Mosaic Virus. *Nano Letters* **2014,** *14* (3), 1551-1558.
359. Prasuhn, J. D. E.; Yeh, R. M.; Obenaus, A.; Manchester, M.; Finn, M. G., Viral MRI contrast agents: coordination of Gd by native virions and attachment of Gd complexes by azide–alkyne cycloaddition. *Chemical Communications* **2007,** (12), 1269-1271.
360. Liepold, L.; Anderson, S.; Willits, D.; Oltrogge, L.; Frank, J. A.; Douglas, T.; Young, M., Viral capsids as MRI contrast agents. *Magnetic Resonance in Medicine* **2007,** *58* (5), 871-879.
361. Garimella, P. D.; Datta, A.; Romanini, D. W.; Raymond, K. N.; Francis, M. B., Multivalent, High-Relaxivity MRI Contrast Agents Using Rigid Cysteine-Reactive Gadolinium Complexes. *Journal of the American Chemical Society* **2011,** *133* (37), 14704-14709.
362. Hooker, J. M.; Datta, A.; Botta, M.; Raymond, K. N.; Francis, M. B., Magnetic Resonance Contrast Agents from Viral Capsid Shells: A Comparison of Exterior and Interior Cargo Strategies. *Nano Letters* **2007,** *7* (8), 2207-2210.
363. Raymond, K. N.; Pierre, V. C., Next Generation, High Relaxivity Gadolinium MRI Agents. *Bioconjugate Chemistry* **2005,** *16* (1), 3-8.
364. Allen, M.; Bulte, J. W. M.; Liepold, L.; Basu, G.; Zywicke, H. A.; Frank, J. A.; Young, M.; Douglas, T., Paramagnetic viral nanoparticles as potential high-relaxivity magnetic resonance contrast agents. *Magnetic Resonance in Medicine* **2005,** *54* (4), 807-812.
365. Qazi, S.; Liepold, L. O.; Abedin, M. J.; Johnson, B.; Prevelige, P.; Frank, J. A.; Douglas, T., P22 Viral Capsids as Nanocomposite High-Relaxivity MRI Contrast Agents. *Molecular Pharmaceutics* **2013,** *10* (1), 11-17.
366. Bruckman, M. A.; Steinmetz, N. F., Chemical Modification of the Inner and Outer Surfaces of Tobacco Mosaic Virus (TMV). In *Virus Hybrids as Nanomaterials: Methods and Protocols*, Lin, B.; Ratna, B., Eds. Humana Press: Totowa, NJ, 2014; pp 173-185.

367. Hong, V.; Presolski, S. I.; Ma, C.; Finn, M. G., Analysis and Optimization of Copper-Catalyzed Azide–Alkyne Cycloaddition for Bioconjugation. *Angewandte Chemie International Edition* **2009,** *48* (52), 9879-9883.
368. Bruckman, M. A.; Kaur, G.; Lee, L. A.; Xie, F.; Sepulveda, J.; Breitenkamp, R.; Zhang, X.; Joralemon, M.; Russell, T. P.; Emrick, T.; Wang, Q., Surface Modification of Tobacco Mosaic Virus with "Click" Chemistry. *ChemBioChem* **2008,** *9* (4), 519-523.
369. Franchi, P.; Lucarini, M.; Pedrielli, P.; Pedulli, G. F., Nitroxide Radicals as Hydrogen Bonding Acceptors. An Infrared and EPR Study. *ChemPhysChem* **2002,** *3* (9), 789-793.
370. Caravan, P.; Farrar, C. T.; Frullano, L.; Uppal, R., Influence of molecular parameters and increasing magnetic field strength on relaxivity of gadolinium- and manganese-based T1 contrast agents. *Contrast Media & Molecular Imaging* **2009,** *4* (2), 89-100.
371. Maliakal, A. J.; Turro, N. J.; Bosman, A. W.; Cornel, J.; Meijer, E. W., Relaxivity Studies on Dinitroxide and Polynitroxyl Functionalized Dendrimers: Effect of Electron Exchange and Structure on Paramagnetic Relaxation Enhancement. *The Journal of Physical Chemistry A* **2003,** *107* (41), 8467-8475.
372. Halle, B.; Wennerström, H. k., Nearly exponential quadrupolar relaxation. A perturbation treatment. *Journal of Magnetic Resonance (1969)* **1981,** *44* (1), 89-100.
373. of proton exchange T_e, tumbling, and chemical shift that is proportional the magnetic field. , T. n. c. i. d. f. t. s. w. o. o. t. t. p. o. t. i.-s. *T.* a. *T.* c. t. o. o. t. s. d. o. t. r.
374. Luchinat, C., Bertini, I., NMR of Paramagnetic Molecules in Biological Systems. *Physical Bioinorganic Chemistry Series* **1986**.
375. Vander Elst, L.; Roch, A.; Gillis, P.; Laurent, S.; Botteman, F.; Bulte, J. W. M.; Muller, R. N., Dy-DTPA derivatives as relaxation agents for very high field MRI: The beneficial effect of slow water exchange on the transverse relaxivities. *Magnetic Resonance in Medicine* **2002,** *47* (6), 1121-1130.
376. Caravan, P.; Greenfield, M. T.; Bulte, J. W. M., Molecular factors that determine Curie spin relaxation in dysprosium complexes†. *Magnetic Resonance in Medicine* **2001,** *46* (5), 917-922.
377. Swift, T. J., Connick, R. E., NMR-Relaxation Mechanisms of O^{17} in Aqueous Solutions of Paramagnetic Cations and the Lifetime of Water Molecules in the First Coordination Sphere. *Journal of Chemical Physics* **1962,** *37* (2), 307-320.
378. Bertini, I. L., C.; Parigi, G.; Ravera, E., NMR of Paramagnetic Molecules Applications to Metallobiomolecules and Model, 2nd Ed. **2017**.
379. Pereira, G. A.; Ananias, D.; Rocha, J.; Amaral, V. S.; Muller, R. N.; Elst, L. V.; Tóth, É.; Peters, J. A.; Geraldes, C. F. G. C., NMR relaxivity of Ln3+-based zeolite-type materials. *Journal of Materials Chemistry* **2005,** *15* (35-36), 3832-3837.
380. Hyodo, F.; Soule, B. P.; Matsumoto, K.-i.; Matusmoto, S.; Cook, J. A.; Hyodo, E.; Sowers, A. L.; Krishna, M. C.; Mitchell, J. B., Assessment of tissue redox status using metabolic responsive contrast agents and magnetic resonance imaging. *Journal of Pharmacy and Pharmacology* **2008,** *60* (8), 1049-1060.
381. Bobko, A. A.; Kirilyuk, I. A.; Grigor'ev, I. A.; Zweier, J. L.; Khramtsov, V. V., Reversible reduction of nitroxides to hydroxylamines: Roles for ascorbate and glutathione. *Free Radical Biology and Medicine* **2007,** *42* (3), 404-412.
382. Sato, S.; Endo, S.; Kurokawa, Y.; Yamaguchi, M.; Nagai, A.; Ito, T.; Ogata, T., Synthesis and fluorescence properties of six fluorescein-nitroxide radical hybrid-compounds. *Spectrochimica Acta Part A: Molecular and Biomolecular Spectroscopy* **2016,** *169*, 66-71.
383. Shukla, S.; Eber, F. J.; Nagarajan, A. S.; DiFranco, N. A.; Schmidt, N.; Wen, A. M.; Eiben, S.; Twyman, R. M.; Wege, C.; Steinmetz, N. F., The Impact of Aspect Ratio on the Biodistribution and Tumor Homing of Rigid Soft-Matter Nanorods. *Advanced Healthcare Materials* **2015,** *4* (6), 874-882.
384. Liu, X.; Wu, F.; Tian, Y.; Wu, M.; Zhou, Q.; Jiang, S.; Niu, Z., Size Dependent Cellular Uptake of Rod-like Bionanoparticles with Different Aspect Ratios. *Scientific Reports* **2016,** *6*, 24567.

385. Dikalov, S. I.; Kirilyuk, I. A.; Voinov, M.; Grigor'ev, I. A., EPR detection of cellular and mitochondrial superoxide using cyclic hydroxylamines. *Free Radical Research* **2011,** *45* (4), 417-430.
386. Yapici, N. B.; Jockusch, S.; Moscatelli, A.; Mandalapu, S. R.; Itagaki, Y.; Bates, D. K.; Wiseman, S.; Gibson, K. M.; Turro, N. J.; Bi, L., New Rhodamine Nitroxide Based Fluorescent Probes for Intracellular Hydroxyl Radical Identification in Living Cells. *Organic Letters* **2012,** *14* (1), 50-53.
387. Fridovich, I., Quantitative Aspects of the Production of Superoxide Anion Radical by Milk Xanthine Oxidase. *Journal of Biological Chemistry* **1970,** *245* (16), 4053-4057.
388. McCord, J. M.; Fridovich, I., The Reduction of Cytochrome c by Milk Xanthine Oxidase. *Journal of Biological Chemistry* **1968,** *243* (21), 5753-5760.
389. Bennett, B.; Holz, R. C., Spectroscopically Distinct Cobalt(II) Sites in Heterodimetallic Forms of the Aminopeptidase from Aeromonas proteolytica: Characterization of Substrate Binding. *Biochemistry* **1997,** *36* (32), 9837-9846.
390. Bennett, B.; Holz, R. C., EPR Studies on the Mono- and Dicobalt(II)-Substituted Forms of the Aminopeptidase from Aeromonas proteolytica. Insight into the Catalytic Mechanism of Dinuclear Hydrolases. *J. Am. Chem. Soc.* **1997,** *119* (8), 1923-1933.
391. Crawford, P. A.; Yang, K.-W.; Sharma, N.; Bennett, B.; Crowder, M. W., Spectroscopic Studies on Cobalt(II)-Substituted Metallo-β-lactamase ImiS from Aeromonas veronii bv. sobria†. *Biochemistry* **2005,** *44* (13), 5168-5176.
392. Periyannan, G. R.; Costello, A. L.; Tierney, D. L.; Yang, K.-W.; Bennett, B.; Crowder, M. W., Sequential Binding of Cobalt(II) to Metallo-β-lactamase CcrA†. *Biochemistry* **2006,** *45* (4), 1313-1320.
393. Yang, H.; Aitha, M.; Marts, A. R.; Hetrick, A.; Bennett, B.; Crowder, M. W.; Tierney, D. L., Spectroscopic and Mechanistic Studies of Heterodimetallic Forms of Metallo-β-lactamase NDM-1. *J. Am. Chem. Soc.* **2014,** *136* (20), 7273-7285.
394. Abragam, A.; Bleaney, B., *Electron Paramagnetic Resonance of Transition Ions (International Series of Monographs on Physics)*. 1970; p 912 pp.